

Electronic Thesis and Dissertation Repository

5-26-2017 12:00 AM

Automated Vascular Smooth Muscle Segmentation, Reconstruction, Classification and Simulation on Whole-Slide Histology

Yiwen Xu, *The University of Western Ontario*

Supervisor: Aaron D. Ward, *The University of Western Ontario*

Joint Supervisor: J. Geoffrey Pickering, *The University of Western Ontario*

A thesis submitted in partial fulfillment of the requirements for the Doctor of Philosophy degree
in Medical Biophysics

© Yiwen Xu 2017

Follow this and additional works at: <https://ir.lib.uwo.ca/etd>



Part of the [Circulatory and Respiratory Physiology Commons](#), and the [Medical Biophysics Commons](#)

Recommended Citation

Xu, Yiwen, "Automated Vascular Smooth Muscle Segmentation, Reconstruction, Classification and Simulation on Whole-Slide Histology" (2017). *Electronic Thesis and Dissertation Repository*. 4566.
<https://ir.lib.uwo.ca/etd/4566>

This Dissertation/Thesis is brought to you for free and open access by Scholarship@Western. It has been accepted for inclusion in Electronic Thesis and Dissertation Repository by an authorized administrator of Scholarship@Western. For more information, please contact wlsadmin@uwo.ca.

Abstract

Histology of the microvasculature depicts detailed characteristics relevant to tissue perfusion. One important histologic feature is the smooth muscle component of the microvessel wall, which is responsible for controlling vessel caliber. Abnormalities can cause disease and organ failure, as seen in hypertensive retinopathy, diabetic ischemia, Alzheimer's disease and improper cardiovascular development. However, assessments of smooth muscle cell content are conventionally performed on selected fields of view on 2D sections, which may lead to measurement bias. We have developed a software platform for automated (1) 3D vascular reconstruction, (2) detection and segmentation of muscularized microvessels, (3) classification of vascular subtypes, and (4) simulation of function through blood flow modeling. Vessels were stained for α -actin using 3,3'-Diaminobenzidine, assessing both normal (n=9 mice) and regenerated vasculature (n=5 at day 14, n=4 at day 28). 2D locally adaptive segmentation involved vessel detection, skeletonization, and fragment connection. 3D reconstruction was performed using our novel nucleus landmark-based registration. Arterioles and venules were categorized using supervised machine learning based on texture and morphometry. Simulation of blood flow for the normal and regenerated vasculature was performed at baseline and during demand based on the structural measures obtained from the above tools. Vessel medial area and vessel wall thickness were found to be greater in the normal vasculature as compared to the regenerated vasculature ($p < 0.001$) and a higher density of arterioles was found in the regenerated tissue ($p < 0.05$). Validation showed: a Dice coefficient of 0.88 (compared to manual) for the segmentations, a 3D reconstruction target registration error of $4 \mu m$, and area under the receiver operator curve of 0.89 for vessel classification. We found 89% and 67% decreases in the blood flow through the network for the regenerated vasculature during increased oxygen demand as compared to the normal vasculature, respectively for 14 and 28 days post-ischemia. We developed a software platform for automated vasculature histology analysis involving 3D reconstruction, segmentation, and arteriole vs. venule classification. This advanced the knowledge of conventional histology sampling compared to whole slide analysis, the morphological and density differences in the regenerated vasculature, and the effect of the differences on blood flow and function.

Keywords: Microvasculature, Regeneration, Vascular Smooth Muscle, Whole-slide Imaging, Histology, Immunohistochemistry, Reconstruction, Simulation, Segmentation, Machine Learning

Co-Authorship Statement

This thesis is presented in an integrated article format, the chapters of which are based on the following publications that are either published or in preparation for submission. My contributions to the first author peer-reviewed manuscripts included all aspects of the studies, including manuscript preparation and submission. Specifically, this involved algorithm development, designing research questions, and implementing experiments, as well as drafting, revising, and submission of all manuscripts. The work was performed under the supervision of Dr. Aaron Ward and Dr. J. Geoffrey Pickering who provided ongoing guidance and were responsible for study conception, defining the research questions, designing and analyzing the experiments; interpreting the results and drafting the manuscript. The histological tissues were processed by Caroline O’Neil, Hao Yin, and Zengxuan Nong. For each manuscript contained in this thesis, all other co-authors contributed to reviewing and editing the manuscript and their specific contributions are described below.

Chapter 2 is an original research article entitled “A method for 3D histopathology reconstruction supporting mouse microvasculature analysis” and was published in PlosONE in May 2015. This manuscript was co-authored by J. Geoffrey Pickering, Zengxuan Nong, Eli Gibson, John-Michael Arpino, Hao Yin, and Aaron Ward. Zengxuan Nong, John-Michael Arpino, and Hao Yin aided in the procurement of samples, histological processing and interpretation of the results. Eli Gibson provided an implementation for registration error calculation and interpretation of the results.

Chapter 3 is an original research article entitled “Segmentation of digitized histological sections for quantification of the muscularized vasculature in the mouse hind limb” and was published in the Journal of Microscopy in February 2017. This manuscript was co-authored by J. Geoffrey Pickering, Zengxuan Nong, and Aaron Ward. Zengxuan Nong aided in the procurement of samples and histological processing.

Chapter 4 is an original research article entitled “Differentiation of arterioles from venules in mouse histology images using machine learning” and was published in the Journal of Medical Imaging in February 2017. This manuscript was co-authored by J. Sachi Elkerton, J. Geoffrey Pickering, and Aaron Ward. As the joint first author, J. Sachi Elkerton was involved in designing and analyzing the experiments; interpreting the results and drafting the manuscript.

Chapter 5 titled “High throughput analysis of microvascular smooth muscle reveals deficient wrapping and impaired blood flow reserve” involved J. Geoffrey Pickering, Daniel Goldman, Zengxuan Nong, and Aaron Ward. Daniel Goldman provided an implementation for the blood flow simulation, aided in designing research experiments, and interpretation of the results. Zengxuan Nong aided in the procurement of samples and histological processing.

Acknowledgements

This work would not have been possible without the support of the following individuals.

I am exceptionally grateful to both my supervisors, both of whom provided different perspectives, insights and mentorship. Dr. Aaron Ward not only provided detailed directions on the projects but has gone above and beyond in mentorship, such that I am not only a stronger researcher but a professional with valuable communication skills. Dr. Geoffrey Pickering's dedication and passion for discovery is unparalleled. I always come out of our brainstorming sessions with more insights to pursue.

I would like to thank the members of my advisory committee. I am grateful for Dr. Aaron Fenster's guidance and support throughout my studies. His pursuit of innovation and his confidence in my expertise was very motivating. Dr. Daniel Goldman provided expert guidance when he came on my advisory committee for which I am grateful for. I would also like to thank Dr. Charles McKenzie for his guidance from the very start of my graduate degree.

This collaborative project has given me the opportunity to interact with groups of remarkably perceptive and thoughtful colleagues both at the Baines Imaging Laboratory and Robarts and Research Institute. This ability to communicate with individuals from different scientific backgrounds was the key to the success of the projects. I could brainstorm around solutions to software but also fundamental processes in vascular biology.

Members of the department of Medical Biophysics are a very intellectual and supportive group. I cannot enumerate the number of people whom I've had a positive interaction with throughout these past years.

I would also like to thank my family and friends for always providing me with their kindness and support.

Contents

Abstract	i
Co-Authorship Statement	ii
Acknowledgements	iii
List of Figures	viii
List of Tables	xiii
List of Appendices	xiv
List of Abbreviations	xv
1 Introduction	1
1.1 Vasculature development	2
1.1.1 Vasculogenesis	4
1.1.2 Arteriogenesis	4
1.1.3 Angiogenesis	4
1.1.4 The mature vasculature	6
1.2 Vascular disease	6
1.2.1 Atherosclerosis	7
1.2.2 Current treatments	7
1.2.3 Diagnostic methods	8
1.3 Post-ischemic regeneration	9
1.4 Hind limb ischemia model	10
1.4.1 Surgical ligation	10
1.4.2 Assessment of the ischemia model	11
1.5 Role and regulation of SMC Function	11
1.6 Vascular assessment	12
1.6.1 Micro CT	12
1.6.2 Vascular Casting	14
1.6.3 Frozen section block face imaging	15
1.6.4 Confocal microscopy	16
1.6.5 Immunohistochemistry	17
Stain standardization	19
IHC assessment	19

1.7	Image Analysis Techniques	20
1.7.1	Image registration	20
1.7.2	Image segmentation	22
1.7.3	Machine Learning	25
1.8	State of the Art in Histology Image Analysis	28
1.9	Thesis Outline	30
	Chapter 2: A method for 3D histopathology reconstruction supporting mouse microvasculature analysis	31
	Chapter 3: Segmentation of digitized histological sections for quan- tification of the muscularized vasculature in the mouse hind limb	31
	Chapter 4: Differentiation of arterioles from venules in mouse histol- ogy images using machine learning	32
	Chapter 5: High content analysis of the microvasculature in the post- ischemic skeletal muscle reveals the emergence of abnor- mally thin-walled arteries and arterioles: Implications for flow reserve in regenerated muscle	32
2	A method for 3D histopathology reconstruction supporting mouse microvascu- lature analysis	46
2.1	Introduction	46
2.2	Materials and Methods	49
2.2.1	Animal model	49
	Ethics Statement	50
2.2.2	Image registration and validation approach	50
2.2.3	Experimental methods	52
2.2.4	Intensity-based registration	54
2.2.5	Nucleus feature extraction, correspondence, and registration	54
	Evaluation of registration accuracy	58
	Evaluation of image similarity metrics	59
2.3	Results	60
2.3.1	Vessel reconstruction properties	60
	Registration technique comparisons	62
2.3.2	Evaluation of registration accuracy	62
2.3.3	Evaluation of image similarity metrics	66
2.4	Discussion	66
2.4.1	Evaluation of registration accuracy	69
2.4.2	Evaluation of image similarity metrics	72
2.4.3	Limitations	72
2.5	Conclusion	73
3	Segmentation of digitized histological sections for quantification of the muscu- larized vasculature in the mouse hind limb	78
3.1	Introduction	78
3.1.1	Previous Techniques	79

3.1.2	Our Technique	80
3.2	Materials	80
3.3	Methods	82
3.3.1	Vessel Fragment Detection	84
3.3.2	Vessel Fragment Connection	86
3.3.3	Locally Adaptive Segmentation Refinement	87
3.4	Experimental Design	88
3.4.1	Evaluation of Segmentation Accuracy	88
3.4.2	Field of View Sampling Simulation	89
3.4.3	Vessel Measurement and Statistical Analysis	89
3.5	Experimental Results	91
3.5.1	Segmentation Validation	93
3.5.2	Field of View Sampling Simulation	95
3.6	Discussion	98
3.6.1	Whole-slide Imaging	98
3.6.2	Segmentation Validation	98
3.6.3	Field of View Sampling Simulation	99
3.6.4	Biological Validity	100
3.6.5	Limitations	101
3.7	Conclusion	102
4	Differentiation of Arterioles from Venules in Mouse Histology Images Using Machine Learning	106
4.1	Introduction	106
4.2	Materials and Methods	108
4.2.1	Materials	108
4.2.2	Methods overview	110
4.2.3	Feature extraction	111
4.2.4	Feature selection	111
4.2.5	Supervised machine learning	111
4.2.6	Validation	112
4.2.7	Classifier Confidence	112
4.2.8	Statistics	113
4.3	Results	113
4.3.1	Experiment 1	113
4.3.2	Experiment 2	119
4.4	Discussion	123
4.5	Conclusions	126
5	Muscularized microvascular analysis	132
5.1	Introduction	132
5.2	Methods	134
5.2.1	Materials	134
5.2.2	Vessel segmentation summary	135
5.2.3	Vascular measurements	135

5.2.4	Blood flow simulation	135
5.2.5	Statistical analysis	136
5.3	Results	137
5.3.1	Increase in density of muscularized vasculature	137
5.3.2	Decrease in vascular SMC wrapping in regenerated skeletal muscle	138
5.3.3	Lower blood flow in the regenerated arteriolar network	142
5.4	Discussion	145
5.5	Conclusion	147
6	Conclusions and Future Directions	152
6.1	Thesis contributions	152
6.1.1	Technological advancements	153
	A 3D histology reconstruction algorithm was developed using intrinsic landmarks within the tissue, which results in more accurate registration compared to conventional intensity based registration for tissue reconstruction.	153
	An automated segmentation algorithm for the muscularized microvasculature was developed for examining the distribution of vascular morphology in a biological system.	154
	A machine learning platform was developed to separate arterioles from the rest of the vasculature automatically for analysis.	155
6.1.2	Knowledge advancements	155
	How does conventional field of view sampling compare to our developed 2D whole tissue section analysis, with respect to vascular assessment?	155
	What are the main differences in smooth muscle cell content in the post ischemic arteriolar microvasculature compared to the normal tissue?	156
	How do these structural differences affect blood flow and function?	156
6.2	Applications and future directions	157
6.2.1	Vascular analysis in different organs and stains	157
6.2.2	Adaptation of developed techniques for additional applications	157
6.2.3	Potential applications for immunohistochemistry (IHC) analysis	158
6.3	Remaining gaps in automated histology analysis	159
A	Permission for Reproduction of Scientific Articles	164
B	Curriculum Vitae	172
	Curriculum Vitae	172

List of Figures

1.1	Vessel wall components of the (a) endothelial tube, (b) capillary, (d) arteriole and venule, as well as the wall of larger vessels (d). Adapted from Jian, 2003. Nature medicine by Nature Publishing Company Reproduced with permission of NATURE PUBLISHING GROUP in the format Republish in a thesis/dissertation via Copyright Clearance Center.	2
1.2	Stages of vascular development including vasculogenesis, arteriogenesis and angiogenesis. Adapted from Herbert et al. 2011. Nature Reviews Molecular Cell Biology by Nature Publishing Company Reproduced with permission of NATURE PUBLISHING GROUP in the format Republish in a thesis/dissertation via Copyright Clearance Center.	3
1.3	Vascular and skeletal muscle structure after hind limb ischemia (HLI, right panels) as compared to the control (left panels). A (artery) and V (vein) in (a,b) indicates the collateral vessels. Multicellular infiltrations reside in the location of the arrowhead in (d), where there are also muscle cells without nuclei. There is an increase in capillary density post ischemia within the skeletal muscle tissue (e,f). Scale bars: 100 μ m. Adapted from Limbourg et al. 2009. Nature Protocols by Nature Publishing Company Reproduced with permission of NATURE PUBLISHING GROUP in the format Republish in a thesis/dissertation via Copyright Clearance Center.	5
1.4	Micro-CT angiograms of Matrigel implants. Adapted from Frontini et al. 2011. Nature biotechnology by Nature Publishing Company Reproduced with permission of NATURE PUBLISHING GROUP in the format Republish in a thesis/dissertation via Copyright Clearance Center.	14
1.5	Fluorescent confocal images of vascular constructs stained for the endothelium and vascular smooth muscle of the vessel wall. Adapted from Frontini et al. 2011. Nature biotechnology by Nature Publishing Company Reproduced with permission of NATURE PUBLISHING GROUP in the format Republish in a thesis/dissertation via Copyright Clearance Center.	17
1.6	Immunohistochemistry targeting vascular smooth muscle in the mouse hind limb with the arteriole and venules indicated by the arrows.	18
1.7	First order intensity measure (mean) and second order texture measure (uniformity) of a synthetic dataset. The uniformity is decreasing from left to right and the mean is increasing, where the middle panels are indistinguishable by the first order intensity measure.	26

2.1	Regenerated hind limb tissue following ischemic damage.	The tissue was immunostained with smooth muscle α -actin and DAB chromogen and counterstained with hematoxylin. Blue arrows indicate nuclei and black arrows indicate the stained arteriole. Scale bar (A) 500 μm , (B) 100 μm	50
2.2	Diagram depicting the registration methods.	The flow diagram in (A) depicts the overall experimental process, with (B) and (C) giving exploded views of the intensity-based and nucleus-based registration steps. Both approaches were initialized with a rigid, low-resolution intensity-based registration. The intensity-based registrations (B) were done using a standard iterative optimization loop. The nucleus-based registration (C) was computed non-iteratively in closed form based on automatically segmented and corresponded nucleus landmarks. Both methods were executed pairwise on each adjacent section pair, and as a final step these pairwise registrations were composed to form the final 3D reconstructed volume.	51
2.3	Comparison of the alignment of bisected nuclei when measuring the accumulated registration error.	(A) The ideal error-free reference reconstruction, with bisected nuclei aligned with minimum residual error (a pairwise target registration error between corresponding halves of bisected nuclei of zero is depicted). (B) A reconstruction aligning nuclei with spatially unbiased error; but vessel connectedness (topology) and angle (geometry) are mostly conserved. (C) A reconstruction optimizing pairwise alignment of salient structures (the vessel cross sections in this example) preserves vessel topology but not geometry. Note that the pairwise target registration errors in (B) and (C) are similar, despite the lack of geometry preservation in C. The accumulated target registration error does capture the difference between (B) and (C); the plots in the bottom row indicate increasing accumulated error through the stack of sections.	53
2.4	Separate set of mouse hind limb tissues that were not used for the experiments reported in this chapter. These tissues were used to determine nucleus size and colour for nucleus extraction. Scale bar 100 μm		55
2.5	Nucleus segmentation method.	(A) The segmented nucleus labeled blue on the histology section stained with DAB and hematoxylin counter stain. (B) The surrounding region (white) of each nucleus was defined by morphological dilation and used to evaluate whether the extracted nucleus was within the tissue, or was instead a false positive corresponding to debris on a white background outside of the tissue, indicated with the white arrows. Scale bar 50 μm	56

2.6	Nucleus correspondence method. (An illustration depicting the approach to establishing correspondence of nucleus p in section I with its best matching nucleus in adjacent section J . In this example, the candidate nuclei on section J are p' , q_1 , and q_2 , lying within a dashed circle of radius T centred on p (only 3 of the 18 candidate nuclei within the circle are illustrated here for simplicity). The candidate nucleus with the most similar surrounding tissue appearance is selected to correspond to p . Surrounding tissue appearance similarity is measured using the MSE image similarity metric, comparing the local square region $I(p)$ centered on p with the local square regions $J(p')$, $J(q_1)$, and $J(q_2)$ centered on the candidates p' , q_1 , and q_2 . In this example, since $MSE(I(p), J(p')) < MSE(I(p), J(q_1))$ and $MSE(I(p), J(p')) < MSE(I(p), J(q_2))$, p is corresponded with p'	57
2.7	3D and 2D histology comparisons. 2D histology sections (pixel size $0.25 \mu m \times 0.25 \mu m$) and corresponding 3D reconstruction (voxel size of $0.25 \mu m \times 0.25 \mu m \times 5 \mu m$) of serial histology sections of a normal (A-D) and regenerated mouse (E-H) TA post-femoral artery excision, immunostained for smooth muscle alpha-actin. A and E are registered using affine intensity based registration. B and F are registered using affine nucleus based registration. Within each column, the dashed lines indicate correspondence (according to colour) between parts of the 2D sections and their locations on the 3D views. Also within each column, the lower case letter labels indicate correspondence between vessel cross sections on the 2D sections and their homologous locations within the 3D views. Blue arrows indicate incorrect vessel wall discontinuities arising from reconstruction error. The insets in the red boxes show 2D and 3D diameter measurements of the same vessel; note that the 2D measurement overestimates the 3D measurement by a factor of > 6 . Scale bars $100 \mu m$	61
2.8	Registration accuracy measurement values. Box plots of the rigid and affine target registration error (TRE) computed for each adjacent pair of sections (pairwise) and propagated throughout the 3D reconstruction (accumulated).	65
3.1	Mouse hind limb tissue immunostained with an antibody to smooth muscle α -actin and DAB chromogen and counter-stained with hematoxylin.	81
3.2	A block diagram depicting each step in the automated vessel segmentation algorithm starting with whole slide histology images and resulting in vessel wall contours and measurements. The main steps include vessel fragment detection (a), vessel fragment connection (b), locally adaptive segmentation refinement (c) and vessel measurement (d).	83
3.3	Colour deconvolution of the immunostained bright field image (a) separating the haematoxylin (b) and DAB (c) channel, also shown in grayscale (d).	85
3.4	Vessel fragment component connection for locally adaptive segmentation. The binary image (c) from the global threshold of the grayscale DAB channel (b) of the bright field image (a) was skeletonized (d). The skeleton endpoints were connected to define each vessel as a single unit and created bounding boxes (e) for locally adaptive segmentation refinement.	87

3.5	Automatic vessel smooth muscle morphological and density measures. The vessel measures were aggregated by median values for each mouse for vessel count per tissue area (a), smooth muscle layer area (b), lumen area (c), lumen perimeter (d), smooth muscle layer thickness (e), and standard deviation (SD) (f) for all vessels and separated by vessel diameter. Each glyph represents one mouse sample.	93
3.6	Contours of manually delineated (a) and automatically segmented (b) vessel walls in the mouse hind limb stained with DAB for α -actin smooth muscle. . .	94
3.7	Bland-Altman plots depicting the differences between the smooth muscle (SM) layer area, thickness and lumen perimeter measurements derived from manual and automated segmentations. Difference: (automated - manual segmentation measure), Average: (automated + manual segmentation measure)/2.	95
3.8	The percent difference in vessel measures of the simulated fields of view (FOV) - the whole slide for each tissue section. The vessel measures were aggregated by median values for each FOV for vessel count per tissue area (a), smooth muscle layer area (b), lumen area (c), lumen perimeter (d), smooth muscle layer thickness (e), and variance (f) for all tissue sections (n = 69). Boxplots include the median, 25th, 75th percentiles, and whiskers at the 5th and 95th percentiles. Distribution of measurement simulations (n = 100) extrapolated from FOVs for each mouse tissue section.	96
3.9	The distribution of vessel measures when taking 6 fields of view (FOV) from each tissue section and compared to the whole slide measurement (median shown in grey) for each of the 5 samples. The vessel measures were aggregated by median values for each mouse for vessel count per tissue area (a), smooth muscle layer area (b), lumen area (c), lumen perimeter (d), smooth muscle layer thickness (e), and variance (f) for all tissue sections (n = 69). Boxplots include the median, 25th, 75th percentiles, and whiskers at the 5th and 95th percentiles. Distribution of measurement simulations (n = 400) extrapolated from 6 FOVs for each mouse tissue section.	97
4.1	Arteriole with the DAB stain (a), and the binary mask (b) output from the automated segmentation. Scale bar is 50 μm	109
4.2	Arterioles and venules are shown in the normal and regenerated tissues. The microvessels have distinguishable differences in the normal vasculature where the smooth muscle layer is thicker and more pronounced on the arteriolar side and have a visibly darker stain. Venules also appear to have a more tortuous vessel wall. This difference is less apparent in the regenerated vasculature. . .	109
4.3	Block diagram to demonstrate the method followed in this experiment for a leave-one-mouse-out cross validation.	110
4.4	AUC (a) and error rate (b) as a function of number of features used for classification. The error bars represent the standard error of the mean. All features were chosen using a forward feature selection and classifiers were trained with a LOMO cross validation.	114
4.5	Three features chosen from forward feature selection over the 10 cross validations.	114

4.6	Receiver operating characteristic curves for each of the classifiers trained on 2 features. LOGLC AUC: 0.89, SVM AUC: 0.89, RFC AUC: 0.84.	115
4.7	Histogram of the confidences from the LOGLC (a,b), SVM (c,d) and RFC (e,f) classification using 2 features with their respective confidence thresholds, where “none” indicates no confidence threshold was applied and all vessels were categorized.	117
4.8	AUC (a) and error rate (b) as a function of number of features used for classification. All features were chosen using a forward feature selection and classifiers were trained with an independent training set.	119
4.9	Receiver operating characteristic curves for each of the classifiers from classifier trained on 2 features. LOGLC AUC: 0.91, SVM AUC: 0.92, RFC AUC: 0.89.	120
4.10	Histogram of the confidences from the LOGLC (a,b), SVM (c,d) and RFC (e,f) classifications with their respective confidence thresholds.	122
4.11	Incorrectly (a-e) and correctly (f-j) classified arterioles by the LOGLC. Scale bar is 20 μm	123
5.1	Normal (a) and regenerated (day 28) (b) hind limb tissue following ischemic damage, immunostained with an antibody to smooth muscle α -actin and DAB chromogen and counter-stained with hematoxylin. Distribution of density (c) with regards to the vessel diameter where All indicates where the total distribution is represented in the boxplots. The boxes represent the median and interquartile range values and the whiskers are at the 5th and 95th percentile. Significance in the form of a Kruskal-Wallis and post-hoc test is indicated for $p < 0.05$ for density (n for number of mice). Scale bar 50 μm	138
5.2	Normal (a-d) and regenerated (e-h) hind limb tissue following ischemic damage, immunostained with an antibody to smooth muscle α -actin and DAB chromogen and counter-stained with hematoxylin. Scale bar 50 μm for full vessels, 10 μm for vessel walls.	140
5.3	Distribution of morphological values with regards to the vessel diameter where All indicates where the total distribution is represented in the boxplots. The boxes represent the median and interquartile range values and the whiskers are at the 5th and 95th percentile. Significance in the form of a Kruskal-Wallis and post-hoc test is indicated for $p < 0.0026$ (n for number of vessels).	141
5.4	Distribution of vessel measurements between the normal and regenerated vessel media at day 14 and day 28 post-ischemia. The media area with respect to the lumen area (a) and the median vessel wall thickness with respect to the vessel diameter (b) are represented with the three distributions.	142
5.5	Simulated blood flow in the normal (a, b) and regenerated (c, d) networks for vessel diameters at baseline (a, c) and when the tissues are in the state of perfusion demand where the vessel diameter is dilated. Vessel diameter at baseline ranges from 12 to 120 μm	144

List of Tables

1.1	A summary of previous studies on registration for 3D vascular histology reconstruction (work presented in this thesis in boldface).	29
1.2	A summary of previous studies on segmentation of vasculature in histology (work presented in this thesis in boldface).	30
2.1	Pairwise affine registration errors (μm) of the reference nucleus landmarks . . .	63
2.2	Pairwise and accumulated target registration error (TRE) values (μm) of the rigid and affine intensity-based and nucleus-based landmark registration (best in boldface)	63
2.3	Mean and SD of maximum pairwise and accumulated target registration error (TRE), observed on each section for the rigid and affine intensity-based and nucleus-based landmark registration (best results in boldface)	64
2.4	The displacement of the optimal mean squared error transformation from the affine nucleus-based registration	66
3.1	Summary of the histology samples used for each experiment	82
3.2	Descriptive statistics of vessel count and density	91
3.3	Automated morphological measures of the smooth muscle layer	92
3.4	Segmentation validation metrics	94
3.5	Field of view sampling simulation	95
4.1	Performance metrics from cross validation using 2 features from forward feature selection (mean \pm SD) All Vessels	116
4.2	The classification errors from the 2 featured forward feature selection with a LOMO cross validation as the confidence threshold increases and vessels are eliminated.	118
4.3	Performance metrics using 2 features from forward feature selection.	121
4.4	List of all the features extracted from each vessel image.	127
4.5	List of all the features extracted from each vessel image.	128
5.1	Vessel density of the muscularized microvasculature (N indicates number of mice)	137
5.2	Morphological measures of the smooth muscle (SM) layer (N indicates number of vessels)	139
5.3	Simulated blood flow measures and network parameters	143
5.4	Smooth muscle (SM) layer thickness binned based on vessel diameter(d_B) in the normal (T_{norm}) and regenerated (T_{reg}) vasculature	147

List of Appendices

Appendix A Permission for Reproduction of Scientific Articles	164
Appendix B Curriculum Vitae	172

List of Abbreviations

2D	Two-dimensional
3D	Three-dimensional
ABI	ankle-brachial index
ANCOVA	analysis of covariance
AUC	area under the receiver operating characteristic curve
CMYK	cyan-magenta-yellow-black
CT	computed tomography
CVD	cardiovascular disease
DAB	3,3'-Diaminobenzidine chromogen
DSC	Dice similarity coefficient
EC	endothelial cell
ECM	extracellular matrix
EDL	extensor digitorum longus
EDRF	endothelium derived relaxing factor
FNR	false negative rate
FOV	fields of view
FPR	false positive rate
FRE	fiducial registration error
GLCM	gray-level co-occurrence matrix
H&E	hematoxylin and eosin
HRP	horseradish peroxidase
HSV	hue saturation and value
ICP	iterative closest point
IHC	immunohistochemistry
IQR	interquartile range
ITK	Insight Segmentation and Registration Toolkit Version
LOGLC	logistic linear classifier
LOMO	leave-one-mouse-out
LOOCV	leave-one-out cross validation
MAD	mean absolute boundary distance
MSE	mean squared error
NCC	normalized cross correlation

NMI	normalized mutual information
NO	nitric oxide
OD	optical density
PAD	peripheral arterial disease
PL	peroneus longus
PVD	peripheral vascular disease
SM	smooth muscle
RMS	root mean square error
ROC	receiver operating characteristic
SD	standard deviation
SIFT	scale-invariant feature transform
SM	smooth muscle
SMC	smooth muscle cell
SNS	sympathetic nervous system
SVM	support vector machine
TA	tibialis anterior
TMA	tissue microarrays
TRE	target registration error

Chapter 1

Introduction

The vascular circulatory system is essential for fluid flow throughout the human body. It provides a network for the delivery of oxygen, nutrients, and minerals to cells, enabling the survival of organs within the system. Vessel walls generally have a similar structure throughout the network with varying distributions of sizes and composition including the intima, media and adventitia. (Fig. 1.1) The intimal layer lines the lumina of all vessel walls and is composed of endothelial cells (ECs) with varying permeability depending on the location. The basement membrane on which the ECs reside is composed of laminin, collagen and nidogen. [1] The internal elastic lamina is comprised of elastin fibers, which separate the intima and the media. It contributes to the elasticity of the vessel wall and the capacitance in lieu of pressure changes. [2] The media is comprised of smooth muscle cells (SMCs) and, in small vessels, pericytes and contributes to the structural integrity and contractility of the vessel wall. [3] The external elastic lamina is another sheet of elastic fibers, which resides between the media and the adventitia. The adventitia is the outermost layer of the vessel wall and is composed of mainly collagen, thus giving the vessel structural integrity and connectivity to the surrounding tissue. [4] Vessels of different sizes have different compositions and therefore different roles in the vascular network. Studies have been focused on the macrovasculature and capillaries with very few works focused on arterioles that controls local blood flow.

One of the main components that contribute to the stability and the dynamic structure of the vasculature is the vascular SMC. They are the most abundant components of the vessel wall and have both structural and physiological functions. One of their features is contractility enabling control of vessel tone. [5] This is performed in order to provide peripheral blood flow resistance at the level of arteries and arterioles in order to regulate blood pressure. [3] SMC are quiescent in their developed form and provide the capacity to withstand blood pressure throughout the circulatory system. There is a need for quantitative understanding of the muscularized microvasculature. They are involved in many processes including vascular

development, regeneration after injury and control of local blood flow. [3], [6]–[8]

The broad goal of my research was to characterize the SMC content in microvasculature to study the effects of ischemia on vascular morphology and function. My studies focus on addressing the technology gap in automated quantitative histology assessment and the measurement of SMC changes after skeletal tissue regeneration post-ischemia. To address this goal, my objectives are to develop an automated software system for comprehensive vascular histology quantitation and use the developed system to infer differences in the regenerated vasculature as compared to uninjured tissues.

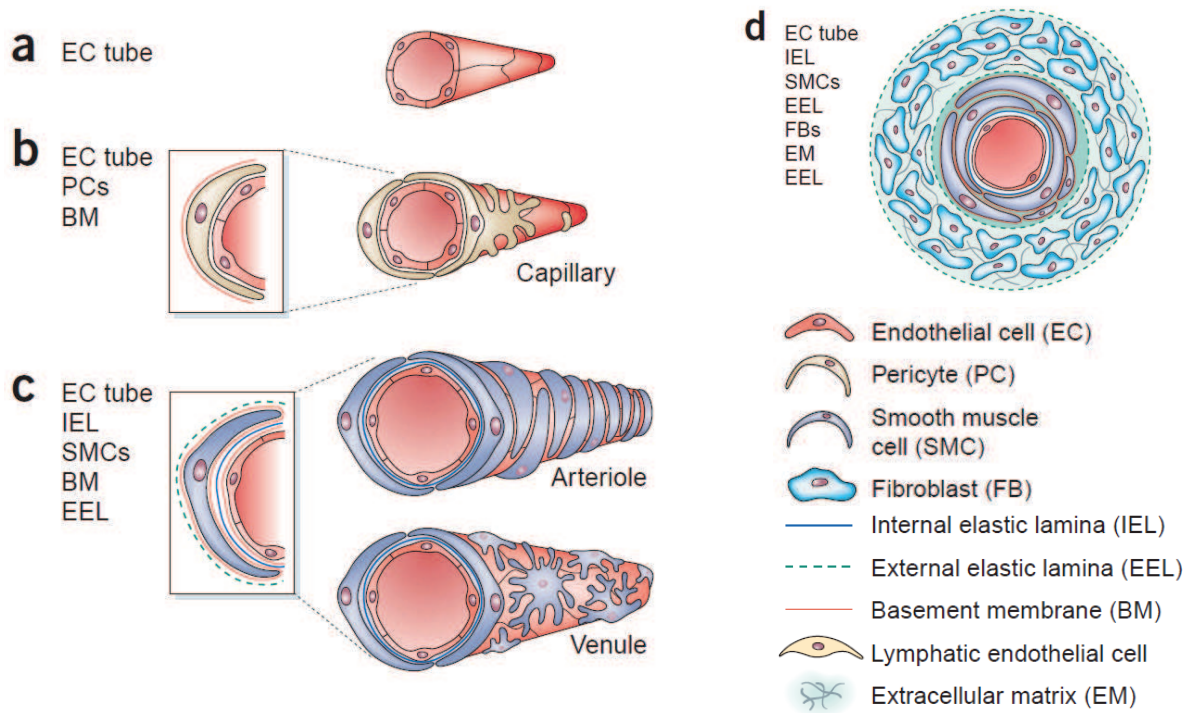


Figure 1.1: Vessel wall components of the (a) endothelial tube, (b) capillary, (d) arteriole and venule, as well as the wall of larger vessels (d). Adapted from Jian, 2003. Nature medicine by Nature Publishing Company Reproduced with permission of NATURE PUBLISHING GROUP in the format Republish in a thesis/dissertation via Copyright Clearance Center.

1.1 Vasculature development

Development of a functional vascular system is essential to organ morphogenesis, and thus initiates at the stage of embryonic development. [7] The tissues need oxygen and nutrients to grow and mature, as well as receive signals for differentiation. The vasculature is developed de novo through mechanisms of vasculogenesis, arteriogenesis and angiogenesis at the early

stages of life. (Fig. 1.2) [9] Each mechanism encompasses stages of creating a vascular network that is stable in adulthood. The vessels are derived from endothelial precursor cells, in the form of angioblasts, derived from hematopoietic progenitors. [2] This links the development of the vasculature to the red blood cells within the network and is essential for angiogenic repair in the mature vascular system. [7]

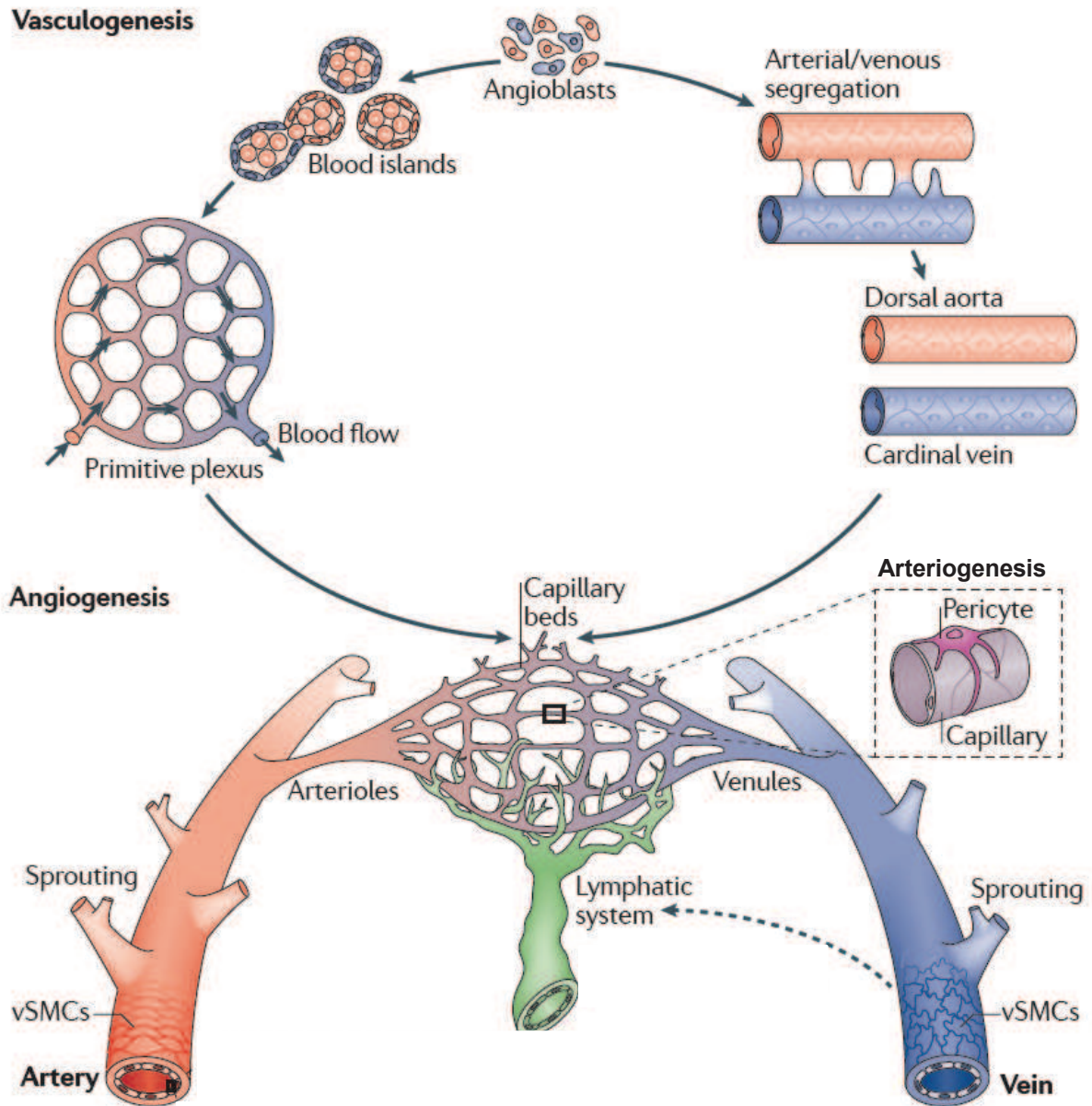


Figure 1.2: Stages of vascular development including vasculogenesis, arteriogenesis and angiogenesis. Adapted from Herbert et al. 2011. Nature Reviews Molecular Cell Biology by Nature Publishing Company Reproduced with permission of NATURE PUBLISHING GROUP in the format Republish in a thesis/dissertation via Copyright Clearance Center.

1.1.1 Vasculogenesis

Vasculogenesis involves the formation of the endothelium and the initial formation of the vascular plexus. [2] Development of the overall vascular network through vasculogenesis occurs at the stage of embryonic development. [10] This process generates the initial vascular plexus through the migration of angioblasts. It involves the differentiation of the ECs through sprouting, after the condensation of the primary vascular network. Although unstable, the network cells have arterial or venous fate and are remodeling into an organized network of arteries, capillaries, and veins. [11] The network model's objective is to achieve homeostasis through adaptation to the environmental, physiological and pathological conditions. At this stage, the vasculature does not involve mural cells.

1.1.2 Arteriogenesis

Arteriogenesis leads to the stabilization and maturation of the developing embryonic vascular network. [6] This involves interactions between the pre-existing ECs and the recruitment of mural cells to the network. [12] During EC remodeling, factors such as platelet derived growth factor B are released and attract pericytes, which then migrate towards the vasculature. [6] The factors act as chemo-attractants in the recruitment process of mural cells. The cells then have direct contact with the endothelium of the vasculature and act to stabilize the network by promoting EC survival. [8] The mural cells also differentiate into SMCs at the level of arteries and into pericytes at the pre-capillary level. They sheath the vasculature at the arterial and venous side. This results in vascular quiescence. [13]

1.1.3 Angiogenesis

Angiogenesis, commonly known as the growth of the vasculature, is specifically the expansion of the pre-existing vasculature through vessel sprouting. [14], [15] This occurs at the embryonic stage and in adulthood. The expansion of the vascular plexus at the embryonic stage involves remodeling in the form of growth, as well as pruning and differentiation. [16] At this stage, the networking structure is becoming highly organized and is being stabilized by pericytes and SMCs. In the mature vasculature, angiogenesis is driven by hypoxia in ischemic tissues. [11] This could be caused by a blockage in the blood flow or in the case of tumour development. With respect to oncology, the rapid tissue growth increases the demand for oxygen, through hypoxia, triggering the angiogenic switch. [17] Angiogenesis can occur in ischemic muscle tissue to compensate for hypoxia.

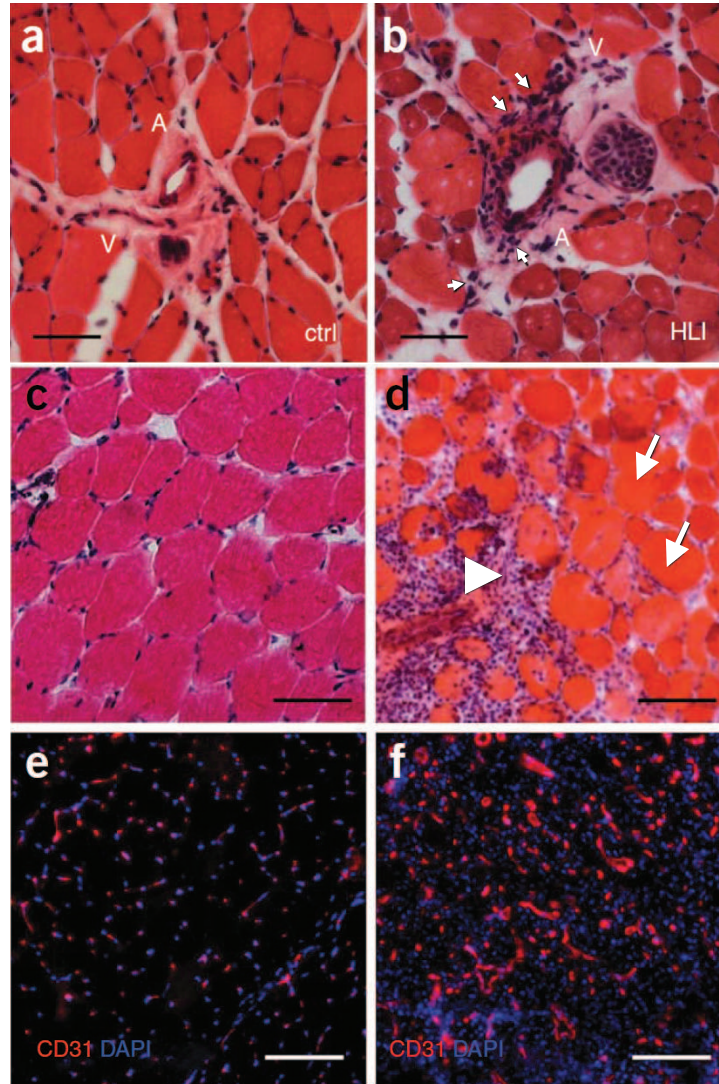


Figure 1.3: Vascular and skeletal muscle structure after hind limb ischemia (HLI, right panels) as compared to the control (left panels). A (artery) and V (vein) in (a,b) indicates the collateral vessels. Multicellular infiltrations reside in the location of the arrowhead in (d), where there are also muscle cells without nuclei. There is an increase in capillary density post ischemia within the skeletal muscle tissue (e,f). Scale bars: $100\mu\text{m}$. Adapted from Limbourg et al. 2009. Nature Protocols by Nature Publishing Company Reproduced with permission of NATURE PUBLISHING GROUP in the format Republish in a thesis/dissertation via Copyright Clearance Center.

1.1.4 The mature vasculature

In the mature vasculature, the demand for remodeling through the disruption of homeostasis can promote arteriogenesis. [18] This disruption can be in the form of hypoxia in ischemic tissues. Pro-angiogenic signals, including those that can reverse the stabilization of the mature vasculature, are initiated to facilitate vascular remodeling. [14] This involves the detachment of mural cells for plasticity. [5] In the case of ischemia caused by blockage of main arteries, our vascular system contains collateral arteries. They redirect flow and increase perfusion to the organ, for the rescue of ischemic tissues. [19] The opening and remodeling of collateral vessels are a response from an increase in shear stress on the vasculature, due to the artery blockage. (Fig. 1.3b) [20] Wall tension and shear stress can cause an increase in lumen diameter and the thickening of the vessel wall. [19] The growth involves angiogenic growth factors, including signaling from ECs for the recruitment of mural cells. Arteriogenesis also takes place during the formation of new vasculature in adulthood. [6] However, the histopathology in this process is understudied in the context of microvascular arteriole morphology and density.

1.2 Vascular disease

The vasculature, through development or aging, can succumb to disease. Cardiovascular disease (CVD) is one of the leading causes of death in industrialized countries. [20] Atherosclerosis, or the occlusion of blood vessels through asymmetrical thickening of the artery intima, is one of the dominant causes of CVD. [21] Occlusion of vessels leads to myocardial infarction, coronary artery disease, stroke and claudication in the form of pain during exercise. The risk factors for these disorders include hypertension, smoking, and diabetes. [10] One particular disease that effects the extremities is peripheral arterial disease (PAD). Diabetes specifically has a role in causing claudication PAD. [22] This leads to a leg amputation due to diabetes every 20 seconds in the world. PAD is in up to 50% of this patient population. [22] The chronic blockage leads to intermittent claudication, characterized by ischemic pain and weakness during locomotion and relief at rest. [23] The initiation of this disorder may be undetected, as 50% of the elderly population with PAD may not be symptomatic due to immobility from other comorbidities, such as arthritis. Asymptomatic patients simply may not have the capability to walk fast enough to induce claudication. [23] Patients with severe blockage may not have sufficient blood flow at rest and thus experience chronic pain even at rest. [12] This is accompanied by tissue loss due to the ischemic state of the limb, which develops at the level of the ankle, heel, or leg starting with ulceration in > 80% of cases and eventually leads to gangrene and amputation if not treated. [22] As individuals with diabetes have reduced capacity

for wound healing, there is a higher risk for amputation. [22]

1.2.1 Atherosclerosis

Atherosclerosis is an inflammatory disease that involves stages of plaque accumulation, infiltration of inflammatory cells, and fibrosis. The lesions consist of small necrotic cells, connective tissue, lipids and debris. [10], [21] The lesion, or specifically atheroma, is located in the middle of the intimal layer of the artery wall. [21] They are especially likely to occur at artery bifurcations. The atherosclerotic lesion is induced by blood flow such that regions with higher shear stress, like bifurcations, are especially prone. ECs may express atheroprotective genes along the intimal layer of the vessel wall and areas of low or normal shear stress are generally protected. [10] The immune system plays a key role in thickening of the artery, which occurs asymmetrically and locally. The adventitia or outermost layer of the vasculature facilitates the infiltration of lymphocytes. This leads to a cascade of immune competent cells, promoting inflammation and buildup of debris. [10]

The core cells involved in the progression of atherosclerosis are inflammatory, blood borne immune, endothelial and SMCs. The initiation of an atheroma may occur during youth and is preceded by a fatty streak. [24] This streak is the accumulation of cells beneath the endothelium, which are especially lipid laden, [25] such as macrophages and T cell lymphocytes, but may eventually disappear or initiate the development of an occlusion. [21], [26] The lesion is initialized with the activation of ECs in the presence of expressive adhesion molecules. These adhesion molecules facilitate the attachment of monocytes and T cells to the ECs and penetrate the intimal layer of the vasculature. [10] Other cell types, which may also be present in the lesion, are dendritic cells, mast cells and neutrophils. SMCs can change in phenotype and migrate from the media into the intima, contributing to the growing lesion. The distribution of cells within the region includes foam cells and lipid droplets in the core. The SMC and collagen rich matrix caps the lesion and the cell infiltrates shoulder the region of growth. [21]

1.2.2 Current treatments

Treatment options for a compromised blood supply due to complications of cardiovascular and metabolic disease can be non-invasive through pharmacological drugs. [27] Anti-inflammatory and immunosuppressant agents can be used to combat acute coronary syndromes. Immunosuppressant agents can be administered to block the activation of T cell lymphocytes and SMC proliferation, which are some of the main components of the atheroma. Anti-inflammatory agents include inhibitors that decrease lipid levels. Statins can inhibit antigen dependent T-cell activation. [21] One type of statin is Atorvastatin, which can also be used for arthritis because

of its anti-inflammatory effects. [28] They also reduce platelet activity by EC nitric oxide production, causing vasodilation and fibrinolysis, which is the breakdown of blood clots. [29]

Depending on the severity of PAD, rehabilitation or surgical salvage of the limb may be necessary. In the case of mild ischemia and when the patient has the capability of wound healing, rehabilitation through exercise and foot care may manage the symptoms of intermittent claudication. [23] However, when PAD is hindering the ability to heal wounds or claudication is interfering with quality of life, revascularization through endovascular repair or bypass is recommended. There are risks associated with revascularization and thus this procedure is generally not performed on frail patients or those who have a short life expectancy. [30] This includes individuals with pre-existing impairments, such that an amputation would not decrease the quality of life. If patients have a large volume of unsalvageable necrotic tissue, the only option would be amputation. Limb salvage rates for those who qualify for revascularization are at 80-85%, with 60% of ulcerations healing within one year. [30] Follow ups involve the assessment of the entire lower extremity circulation, where the arteries are visualized in detail below the knee. The goal of the procedure is to restore pulsatile flow to the arteries in the foot. [30]

1.2.3 Diagnostic methods

Diagnosis of PAD severity can decide if salvage surgery is necessary. This involves the assessment of the blood flow to the lower extremities and the identification of a history of PAD symptoms. [30] Blood flow is measured using hand held Doppler ultrasound at the level of the foot arteries. The ankle-brachial index (ABI) or toe-brachial index is measured to determine the ratio of blood pressure measured at the ankle compared to the pressure at the arm. Thus, a lower ABI can indicate a blockage or a narrowing of the arteries in the lower extremities. An ABI of > 0.9 indicates that PAD is likely. Symptoms of ischemia, with an ABI of > 0.6 , indicates mild PAD and wound healing is assessed after 6 weeks of care. [30] Follow up when wound healing is poor may involve an angiography. Other examinations may include palpation of the carotid and abdomen, as well as inspection of the feet for discolouration, temperature, and skin integrity, such as trophic skin changes and ulcerations. [23] In order to advance the methods of diagnosis and treatment, there needs to be further understanding of the regeneration process involved in tissue healing at the microvascular level.

1.3 Post-ischemic regeneration

Several vascular diseases occur at the level of the arteries. Improper perfusion leads to ischemia and tissue damage downstream of the aberration. The issues could be caused by several factors, such as atherosclerosis, lead by an occlusion of the artery, diabetes and hypertension. [27] This occlusion, or lack of blood flow, causes ischemia and potentially tissue death due to the reduction in oxygen supply. [20] The vasculature compensates for the hypoxic conditions through arteriogenesis and angiogenesis. However, unlike the mechanism behind vascular development at the embryonic stage, the underlying mechanism is not known. [10]

There are several animal models indicating compensation for the lack of tissue perfusion during post-ischemia regeneration. [9] At the macro scale, depending on the level of ischemia and tissue perfusion, the effect can range from no necrosis to toe necrosis. [31] At the level of arteries, collateral vessels open and remodel, which may compensate for hypoxia. This process involves increasing lumen diameter and smooth muscle wrapping to increase flow and stabilize the vessel. (Fig. 1.3b) The changes in the femoral collateral arteries initiate around day 3 post femoral artery ligation. [11]

Arteriogenesis is initiated by factors that are independent of ischemia severity. Most organs in the body have pre-existing collateral vessels in adulthood, which can open up in case there is a blockage in the conductance artery. [32] Blockage in the large conductance artery initiates the process of arteriogenesis, when the blood flow is redirected and thus causes an increase in pressure to the collateral vessels. [12] The resistance to blood flow increases and there are changes in the biomechanical forces within the vasculature. The path of least resistance is now at the collateral vessels, thus the blood flow is redirected to open up the reserve vasculature. [20] The blood flow within the pre-existing collaterals causes shear stress against the ECs. The recruitment process of the SMC through signaling from the ECs is initiated, thickening the collateral vessel wall. [33], [34] The release of nitric oxide by the ECs also causes the relaxation of the SMC, dilating the collateral arterial network. [20]

With the reperfusion of the tissues post collateral opening, there is a combination of pre-existing vasculature reperfusion and angiogenesis. [11] The understanding of angiogenesis has been defined at the embryonic stage when a new vasculature is being developed, but the mechanism is not known at the stage of repair from an ischemic event. After perfusion of the skeletal muscles by the collateral vasculature, there is an increase in capillary density, (Fig. 1.3f) compared to tissue in the non-ischemic state (Fig. 1.3e). [11]

1.4 Hind limb ischemia model

To assess mechanisms of vascular reperfusion after ischemia, involving angiogenesis and arteriogenesis, animal models have been developed based on human conditions of disease, involving arterial blockages. [9] This provides a model that enables assessment and understanding of therapies prior to clinical trials. Investigations can be performed on the mechanisms behind arterial disease and the roles of cells and various factors, which may affect the regeneration process. [11] These models were initiated with unilateral hind limb ischemia in the rabbit and have progressed to the more commonly used model in mice. Genetically engineered mouse models can provide insights into methods of vascular adaptation. Increasing levels of ischemia can be induced to model the severity of disease.

Models have been developed at different sites to model states of ischemia. The result of the femoral artery ligation or excision changes the state of the network and results in development of the collateral vasculature. This is similar to human PAD and can model similar states of ischemia at other sites. The blockage of the main conductance artery causes an increase in blood flow distal to the origin of the deep branch. This change remodels the collateral vessels into main conductance vessels through arteriogenesis. [34] It is a simpler surgical operation than other processes, such as ligation of the arterial supply to the ear. Ligation of carotid arteries can be performed for the assessment of cerebral arteriogenesis. One of the few methods of studying angiogenesis after the embryonic stage is to analyse the developing retina after birth. [11]

1.4.1 Surgical ligation

The most common limb ischemia model in the literature is the surgical ligation of the femoral artery. [11] The vascular structure at this level of the arterial system includes the common femoral artery, which goes into the deep branch (*arteria profunda femoris*). This divides into collateral vessels that are interarterial connections residing in the proximal limb. They are closed and dormant prior to the induction of ischemia. Unilateral hind limb ischemia is induced by exposing the vessel at the location of the femoral artery through incision of the skin, which covers the middle portion of the hind limb. This is typically performed on the left limb of the mouse. [9], [11], [32] For example, the proximal end of this femoral artery could be permanently ligated along with the distal saphenous artery. The side branches and arteries in this region are excised to prevent flow along the main network. There is impaired flow in this model after surgery. [11]

1.4.2 Assessment of the ischemia model

The hind limb model can be assessed at different stages of recovery through histological and blood flow measurement processes. The assessment of recovery from ischemia can be performed at different time points after surgery to analyse the development process. Longitudinal studies can be performed using laser Doppler imaging to analyse the level of reperfusion. Measures can be taken at the suggested time points; days 3, 7, 14, 21 and 28 post artery ligation. [11] The oxygen saturation can be measured within the ischemic muscle with an inserted probe. The level of necrosis can be measured with the number of necrotic toes distal to the ligated limb. Histologic tissues can be used to measure the capillary density at certain time points to assess the level of angiogenesis. Due to muscle atrophy, the number of capillaries per muscle fibre is more representative of the microvessel density than the number of capillaries per area. (Fig. 1.3f) [11], [32], [35] Immunohistochemistry can also be used to visualize regions of hypoxia.

1.5 Role and regulation of SMC Function

The control of vascular tone by SMCs is essential to proper organ function through the maintenance of homeostasis. The inability to control and the lack of vascular tone is incompatible with life. [5] The control of the blood flow through the dilation and contraction of the SMC enables the direction of flow to organs in demand locally. Improper control through excessive contractile tone can lead to high levels of blood pressure. The individual cells communicate for proper function. This communication between the vascular SMCs and ECs, which line the vessel lumen, enables the ability for contraction and dilation. The communication initiates at the stage of vessel formation during embryonic development. [2]

Communication within the mature vasculature, through signaling, maintains blood flow within the network. Signaling begins at the stage of embryogenesis throughout the processes of vessel formation, and this continues to regulate tone and blood pressure. Vessel relaxation is regulated by calcium dependent factors. Endothelium derived relaxing factors (EDRFs) include soluble and secreted molecules. [3] The EC and SMC are adjacent and thus enables efficient signaling between the cells. The endothelial factors, which are diffused or secreted, include nitric oxide (NO), prostacyclin and hyperpolarizing agents.

The main relaxing factor released by the endothelium is NO, previously known as EDRF. The endothelium can be stimulated by biological factors to release NO, but NO can also be used exogenously to create vasodilation independently of the endothelium. Stimuli including acetylcholine, serotonin, thrombin, bradykinin and shear stress causes hyperpolarization of the ECs, involving the influx of calcium ions. This influx activates endothelial nitric oxide

synthase, which generates NO within the ECs. [3] The NO diffuses into the vascular SMCs and causes vasodilation through the guanylate cyclase pathway. The NO stimulates the generation of cyclic guanosine monophosphate, which then causes the relaxation of the smooth muscle and dilates the vessel. [36] NO can cause vasodilation exogenously, so treatments that release NO, such as nitroglycerin and sodium nitroprusside, are effective dilators. [36] Compounds can release NO directly or it can be released through an enzymatic reaction to treat hypertension and congestive heart failure. [36]

The contractile ability of the vasculature in order to maintain tone is controlled by the sympathetic nervous system (SNS). [5] The SNS is responsible for increasing blood flow to compensate for metabolic demand. Blood flow can be redirected locally to organs in the demand state. The detection of luminal pressure leads to the contractile response. The extracellular matrix (ECM) surrounding the SMC facilitates the detection of pressure through mechanotransduction. [5] The strain on the ECM, or the elastin where present, stretches the SMC. The contraction of the resistance arteries leads to a reduction in vessel lumen diameter. The mechanotransduction and contractility mechanisms are dependent on myosin light chain phosphorylation. The interactions between actin and myosin generate contractions in the SMC. Hormones through other pathways also stimulate the phosphorylation process, along with proteins, such as calponins and caldesmons. EDRFs, endothelin and angiotensin II, are released by the endothelium and increase vasal tone. [2] Thus, it is important to understand the SMC content that the microvascular level as they are involved in control of local blood flow.

1.6 Vascular assessment

Several methods exist for assessing the vasculature either in vivo or through histological approaches. The network structure of the vascular lumen can be visualized through techniques involving vascular casts and micro-CT in three dimensions. Other modalities are used for imaging two dimensional (2D) structures, with stains on the feature of interest. Cryomicrotomes facilitate the visualization of stains on the block face of tissues. Confocal microscopy penetrates tissues below the surface. [9] Histology involves sectioning and staining for tissue features at high resolutions in 2D. Each modality has its strengths and limitations, which makes them applicable to certain studies and not others.

1.6.1 Micro CT

Micro-computed tomography (CT) enables the visualization of the anatomical vascular structure in 3D, at high resolutions. There is an increase in the availability of micro-CT systems

with applications to preclinical imaging. This is due to the commercial availability of the systems and the ability to perform in vivo and ex vivo imaging. The 3D image volumes have a higher spatial resolution than clinical CT systems, with an isotropic voxel size of $100 \text{ } \mu\text{m}^3$, for the visualization of the reconstructed 2D slices and structures segmented in 3D. [37] Specific to the assessment of vasculature, contrast agents can be perfused in the lumen to provide visualization.

Micro-CT systems are like conventional CT systems, including similar methodologies and components. Image reconstruction is performed using filtered back projection or iterative algorithms. In biological specimens, there is generally poor tissue contrast, as there is not a large difference in the attenuation of x-rays within soft tissues. To differentiate organs, or sites of interest within the tissue, higher attenuating contrast agents are introduced to the system. Osmium staining is used to phenotype mouse embryos ex vivo. [38] Less toxic stains, such as iodine and phosphotungstic acid, can be an alternative for staining. Specific to vascular imaging, contrast agents can be perfused within the vasculature to visualize the lumen, thus the network structure. Clinical CT imaging contrast agents, such as Omnipaque (GE Healthcare), are iodine based and are also used in preclinical rodent studies. [37] However, due to the low molecular weight, it clears the mouse vascular system within seconds. Iodine based blood pooling can last much longer in the rodent system, with durations from minutes to hours. [39] Passive and active targeting nanoparticles are now under development and may provide functional information on a molecular level. For high resolution micro-CT images, there is higher amounts of exposure to radiation of the subject or pre-clinical specimens. In the mouse, $135 \text{ } \mu\text{m}$ resolution requires a whole-body dose of 0.25Gy and $65 \text{ } \mu\text{m}$ resolution requires 5Gy. This is feasible because the lethal dose 50/30 in mice ranges between 5-7.6Gy, and they recover below this lethal dose. [37]

Micro-CT can be applied to image the biological system with regards to bone, lung, cancer, and the cardiovascular system. [37] With regards to the vasculature, ex vivo imaging of the vessel lumen can be performed with a silicon based contrast agent; MICROFIL (FlowTech, Inc., Carver, MA, USA). (Fig. 1.4) This results in the enhanced contrast within the coronary arteries, for example, for cardiac vascular 3D visualization. [38] Similarly, this could also be perfused in the mouse hind limb to visualize the 3D network vasculature of the extremities. In vivo cardiac imaging can be performed using blood pool contrast agents to differentiate the blood and the myocardial tissue. Functional data can be acquired using 4D-CT. [40] This system is limited by long scanning times for high resolution and the radiation dose. For microvasculature applications, the perfusion of the vessels is limited at a fine scale for contrast agents, with limited soft tissue contrast to discern the vessel wall.

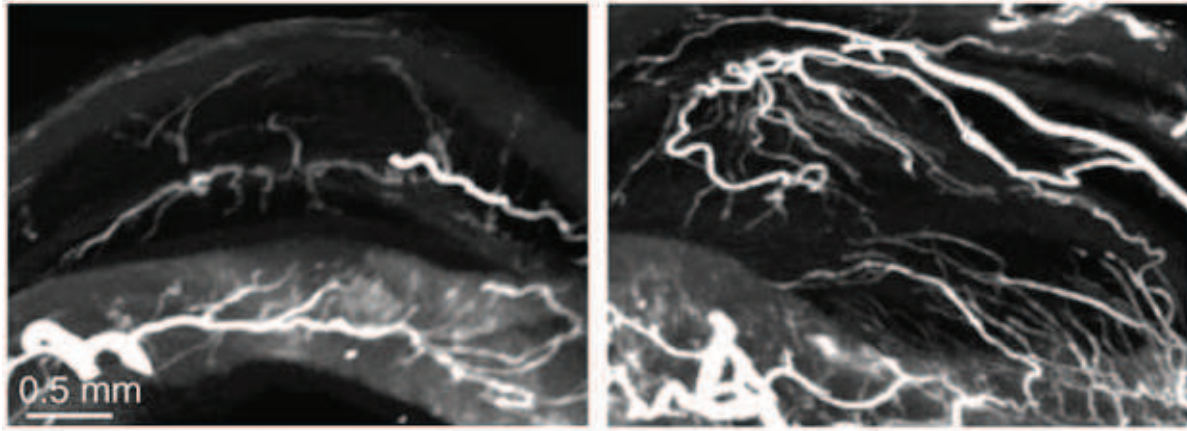


Figure 1.4: Micro-CT angiograms of Matrigel implants. Adapted from Frontini et al. 2011. Nature biotechnology by Nature Publishing Company Reproduced with permission of NATURE PUBLISHING GROUP in the format Republish in a thesis/dissertation via Copyright Clearance Center.

1.6.2 Vascular Casting

Vascular casts are a conventional method for visualizing the three-dimensional (3D) vessel network through the perfusion of the vessel lumen. Overall, the method involves injecting the specimen with a material that will harden, such as a coloured gelatin, latex or plastic. [41] Vascular casting can involve visualizing the vasculature at this stage or further processing through corrosion casting. The tissue surrounding the material is later digested to visualize the network structure. The casting processing involves perfusion of the vasculature through cannulating the feeder artery of the vascular bed. [42] The blood is then removed and the vessels flushed with a buffer solution. The vasculature is then infused with a polymerizing material with contrast, so that the vascular bed can be visualized. The casting material penetrates several centimeters into the capillary bed, enabling the visualization of connections from the arterioles to the venules and the parallel connections between the capillaries. Features such as vessel diameter, length and branching can be measured under light or electron microscopy after vascular casting. However, when there is a high density of capillaries in the vascular bed, the depth of view is limited to 1mm. [41]

Corrosion casting is used for the visualization of intra-organ vasculature. The vessel network can be replicated by digesting the surrounding tissue. [41] After the perfusion of the vasculature with casting material, the surrounding tissue is removed through maceration with a corrosive solution, such as a concentrated acid or base. The visualization of the network structures can lead to the measurement of the capillary density in the heart, to assess changes in the normal and hypertensive states. The description of the vascular anatomy, including branching

angles, diameters and lengths, can be input into simulations for vessel function. The vessel density again can affect the measurement of the vascular network over long distances. However, the vessels can be trimmed down to the arteriolar level to visualize vessels of interest. Casting at non-physiological pressures is a potential source of error in the final replicated vasculature. Other variables that may affect the quality and accuracy of the cast is the polymer dilution, and may affect the viscosity when perfusing the network. The presence of air bubbles in the casting resin is also an issue. Because the reaction involved is exothermic, the cast can shrink during the polymerization process.

1.6.3 Frozen section block face imaging

The imaging cryomicrotome, or episcopic microtome, is used for the visualization of 3D vasculature through reconstruction of block face histological images. [41] This process involves imaging separate histological slices and aligning the images in 3D to create an image volume. The histological images are taken from the block face of the tissue after each tissue section is removed. This process overcomes the distortions of the tissue from sectioning. [43] The resulting image volume can provide structural or functional measurements though the use of high resolution fluorescence imaging, typically imaged at an isotropic voxel resolution of 25 μm . The fluorescent probes enable the visualization of vasculature or specific cells of interest within the tissues. Many probes can be targeted with fluorescence and visualized all at once through spectral unmixing. [41] 3D reconstruction of the features of interest within the tissue can be performed with post processing for quantitative assessments. Segmentation of the vasculature, for example, can be performed for the detection of connecting vessel nodes, vessel angles, and diameters. Methods such as skeletonization can then be applied to find the vessel centerlines for the vessel segments. This process is also used in angiography; however, cryomicrotomes provide more extensive information with regards to tissue content.

There are several limitations to this technique. There is a trade-off between the resolution and field of view, as with other imaging techniques, and this affects the ability to visualize vessels smaller than arterioles. Whole organ and whole mouse imaging can be performed with a large FOV; however, the resolution is limited. Paraffin embedding enables visualization of histological tissues at higher resolutions of 0.5 to 5 μm . With vessel lumen filling methods for vessel visualization, this limits the ability to differentiate between arteries and veins. Distortions to the images can be caused by blurring of the lens, optical noise and artifacts created by the fluorescence beneath the surface of the tissue block. [44] Post-processing of the images for quantification is then dependent on the quality of the image volume. Validation of the technique through histological assessment of the tissue section can be limited.

1.6.4 Confocal microscopy

Confocal fluorescence microscopy is an optical technique for imaging tissue at high resolutions, in 3D. Thin optical sections can be taken for a 2D image, or serial optical sections can be combined for a 3D volume of thick fluorescent tissues or whole cell imaging. (Fig. 1.5) The planes of view do not have to be orthogonal to the line of sight and advancements have been made to penetrate deep ($100\ \mu\text{m}$) into tissues. [45] Multiple fluorophores can be targeted and registered for an image encompassing multiple cellular components into one image. [46] The technique, for reconstructing images, involves a point light source in the form of a laser at the frequency appropriate for the fluorophore of interest. One location is illuminated at a time in the specimen to avoid scatter from the surrounding tissue, which will cause blurring. [47] This results in light reflected from a single focal plane. The specimen is scanned at locations on one focal plane for a 2D image. Multiple planes can be captured at different depths and combined for a 3D image. [45] Confocal microscopy does have the disadvantage of being more labour intensive than bright field microscopy for acquiring an image. It also does not incorporate imaging components of tissues or cells, which were not targeted by fluorophores. In general, the fluorescent probes are only active for a set period. However, with the advancement of hardware and software, whole slide fluorescence confocal scanners will also be widely available.

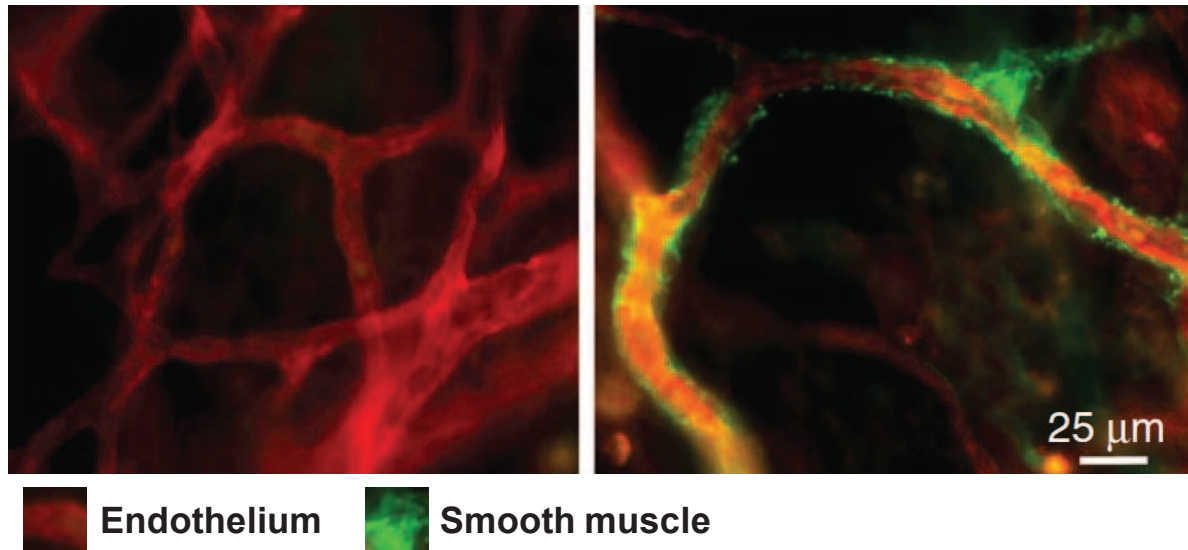


Figure 1.5: Fluorescent confocal images of vascular constructs stained for the endothelium and vascular smooth muscle of the vessel wall. Adapted from Frontini et al. 2011. Nature biotechnology by Nature Publishing Company Reproduced with permission of NATURE PUBLISHING GROUP in the format Republish in a thesis/dissertation via Copyright Clearance Center.

1.6.5 Immunohistochemistry

Histology is used as a gold standard in both clinical diagnostics and animal model research. To visualise tissue morphology and protein expression, tissue can be removed from the body and specimen for assessment through histological techniques. (Fig. 1.6) The tissues are generally immersed in a fixative to stop the autolysis process and cut small enough for fast penetration. The solution will be based on the stain that will be applied, such as formalin, a 4% solution of formaldehyde, or a zinc based fixative. [48] Formalin is the most widely used fixative because it is inexpensive, easily stored and readily available. It also preserves morphological detail. [49] One of the contributors to staining intensity variability in the histological tissue is fixation. The duration of fixation can vary from 6 hours to longer than a day, and the fixative may not be freshly prepared. [50] This, in addition to the different rates of penetration of the tissues, can lead to variability in the final image and is uncontrolled due to the need for transporting the slides and the volume of samples one pathology lab can get at a time. The tissues are then embedded in paraffin and sectioned, usually at the thickness of 5 μm. [50] The deparaffinising process involves heating and treating the tissue with chemicals. Then the tissues are ready for staining, whether it is conventional hematoxylin and eosin (H&E), a Movat cocktail of several

stains, or immunostains targeting a specific antigen. [48]

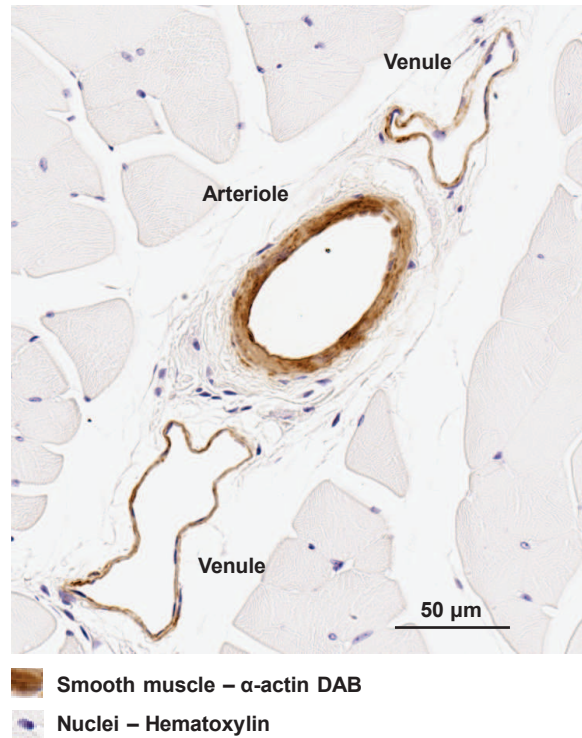


Figure 1.6: Immunohistochemistry targeting vascular smooth muscle in the mouse hind limb with the arteriole and venules indicated by the arrows.

Immunohistochemistry (IHC) involves exposing the antigen and application of antibodies to visualize and interpret the protein distribution within tissues. [51] Antigen retrieval is performed to unmask the antigens, which was affected by the fixation process. Most of the variation in staining occurs due to incomplete antigen exposure. [52] This procedure involves heating the sample in acid buffers in the form of pressure cooking, microwaving or a water bath. [53] Enzyme treatments can also be performed. The application of the primary antibody that binds to the antigen, can be at different concentrations. [54] The antibody, produced by mouse or rabbit immunization processes, is then washed off to remove unbound residuals. [48] The secondary antibody binds specifically to the primary antibody. It comprises of a tag such as horseradish peroxidase or is conjugated to biotin. The final detection phase to visualise the targeted protein involves applying a chromogen or a fluorescently tagged molecule.

This process contains several stages and thus many opportunities for staining intensity variation. There is variability at stages of fixation, tissue treatments, the reagents, the concentration of the reagents, detection methods, and how the final histology image is interpreted. [55]–[57] At the fixation stage, if the tissues are not optimally treated then the subsequent stages of

antigen retrieval are affected. The process of antigen retrieval itself does not have a standardized protocol within all labs. This can lead to insufficient retrieval being interpreted as low or negative results. [58] The differences in the dilution of the antibodies can make comparisons difficult between different labs or even between experiments. Not only the dilution, but the antibody itself can be different and thus have different levels of sensitivity and specificity of protein detection.

Stain standardization

Standardization processes can be implemented to mitigate components of intensity variation in IHC staining for quantification. [59], [60] Automated immunostainers have been developed but are still prone to variation and are not yet widely available. [50] When comparing IHC to other assays, it is similar to the quantitative enzyme lined immunoabsorbent assay. [50] The same reagents are used for both processes. However, because IHC is distributed on a tissue section, it is viewed as a stain. Standardization techniques can be applied and protocols developed for variables, such as the heating processes, temperature, time and pH for antigen retrieval. [51] Because the protocols by the reagent providers are not identical to the procedure followed in the lab, the validation metrics are not relevant. Each lab may want to standardize using their own validation measures for each type of immunostain and tissue. [50] Measurement is generally performed semi-quantitatively without reference standards, but methods have been developed for internal standardization of IHC. [61]

IHC assessment

Assessment of IHC can be challenging due to the differences in reactivity of the reagents involved and the method used for assessment. The IHC target can vary in location within the tissue. The target protein can be within the membrane, cytoplasm, nucleus or stroma. The assessments can vary ranging from manual quantification through counting to the quick eye-ball. The intensity of the stain itself can vary by batch. [58] It is usually not assessed quantitatively and can be inconsistent. In the clinic, observations are subjective to the operator, with the reference point being experience. Diaminobenzidine (DAB) IHC is also nonlinear with respect to the relationship between intensity and amount of protein in the tissues. This needs to be considered, especially at high levels of intensity. [62] The perceived ratio of large cells compared to relatively small cells can be used for a grading system. Reference standards are used to make judgements, however the inter-observer variability for references is 60%. [63] Semi-quantitative assessment could lead to tissue measurements, such as area and intensity, or simply as positive or negative for the stain. Common measurements include positive cell

counts and percentage of staining in a select field of view within the whole tissue section. The data are can be stratified in to ranges for scoring.

With standardization, IHC can be viewed as an assay and be quantified through semi-quantitative and computer assisted methods. [64], [65] H&E can also be interpreted differently by individuals, but has components that have been quantitatively assessed. IHC variability is even higher in interpretation. Under controlled settings, image analysis methods can be superior to manual observation. Commercially available solutions do exist to aid semi-quantitation of the tissues; however they may not be available to smaller labs or academia due to cost or lack of expertise. [50] As semi-automated software requires user input from experienced individuals, such as pathologists, it would take more time out of their hectic schedule. [50] Previously, there were hardware and software deficiencies with respect to cameras and management of large file types. However, with recent advancements on both fronts and further standardization of the specimen through image analysis, accurate and reliable quantification is feasible in IHC.

1.7 Image Analysis Techniques

1.7.1 Image registration

Within structures, such as the vasculature, it is important to assess and visualize morphologies of the tissues in the 3D context. Bright field histology enables the visualization and measurement cellular and subcellular components with various stains, but it is conventionally 2D. There are several key features that cannot be measured or may be misinterpreted in the 2D context when the features of interest are inherently 3D. [66] For example, the vasculature contains bifurcations where there will be infiltration of specific cell types, which are of interest to analyze. [67] The points of bifurcation cannot be identified in 2D. Another related feature is the branching of the vasculature. Without the 3D context, we do not have the capability of following individual vessels from one histology section to another to assess the changes in vessel wall composition, as the vessel increases in vessel order. Vascular tortuosity would also be lost in 2D analysis. For example, a tortuous vessel weaving in and out of one section could increase the vessel density count when measurements are performed in 2D. Stereology, the ability to infer 3D information from 2D representations, has been previously applied to infer structure of the vasculature. [68], [69] However, manual stereological measurements may not be feasible for the whole-slide assessments to be conducted in this work.

Reconstruction of 2D histology involves registration of serial sections in order to define a coordinate system where histological features are aligned and represented in a volume. [70], [71] This would result in the continuity of structures of interest within the tissue for purposes of

quantification and visualization in 3D. [72]–[74] Registration can involve image-based registration and feature-based registration. Both involve mapping the target image into the coordinate system of the reference image. [75] Image-based approaches involve measuring the alignment through quantitative measures of intensities within the image. The conventional registration scheme involves a similarity metric between the images that are being compared, an optimization technique for the metric, a transformation, and an interpolator. Feature-based registration involves the definition of an image transform from corresponding points or features between two images. [76]

Image-based registration may involve a wide range of image similarity metrics and the types used will depend on the properties of the images involved in the alignment process. In the case of histology sections, when the images have been stained consistently with the same stain, the mean square error (MSE) metric would be reasonable to use. MSE metric measures the direct differences in pixel intensity between the two images. The MSE metric assumes the target and reference images have the same intensity ranges and that the objects within the image have the same intensity. [75] When there is a potential overstaining of the tissue or increase in stain from one section to another, normalized cross correlation (NCC) would be useful, as it takes linear intensity displacements into account. [76] In cases where it is of interest to align histology images with different types of stains, normalized mutual information (NMI) may be used. For NMI to be effective, the intensities in the reference image can be mapped to the intensity of the target image in the same object. This mapping does not need to be linear. [77] NMI requires computation of a joint intensity histogram, causing it to be more computationally intensive than MSE and NCC.

The optimal image similarity measure can be computed by brute force by transforming the target image through all possible transformations through space, but this is not feasible due to the length of time required for image transformations and the computation of the similarity metrics. Optimizers are thus used to find the globally optimal metric value by traversing through the solution space, which is defined by the image similarity metric and the image pairs to be registered. [75] For the optimizer to not be trapped at a local minimum, parameters such as the step size in a gradient decent optimizer need to be considered. Registration is performed at multiple resolutions through an image pyramid for initialization and prevention of the optimizer finding a local minimum not representative of the globally optimal solution. [78] Coarse alignment is performed at lower resolutions, which would also reduce the search space of the objective function. Optimization can contain first order properties, such as the gradient descent or ascent optimizer, which has linear convergence properties. There are also higher order and derivative free approaches to optimization.

The goal of registration is to align homologous points in two or more images. When the

images sample different tissues, care must be taken in identifying truly homologous points, and they can be sparse. In the case of two histology sections obtained from immediately adjacent loci in the tissue, a homologous point pair can be defined by a single structure that appears on both sections and is oriented orthogonally to the sectioning plane. Thus, for instance, cross sections of a vessel oriented 45 degrees to the sectioning plane are not truly homologous; if a registration algorithm were to align them, the result would be a vessel falsely reoriented to be orthogonal to the sectioning plane. This issue poses a particular challenge to intensity-based approaches, which will tend to align large and salient structures regardless of whether they are oriented orthogonally to the sectioning plane. This causes the well-known banana-into-cylinder effect observed in some histology reconstruction algorithms. [66] In order to preserve geometry, features unbiased in their orientation can be used within the tissues. [79] The features can be corresponded using a variety of techniques to define a transformation. Landmarks can be corresponded independently of the image through iterative closest point. [80]–[82] Scale-invariant feature transform can be used to identify and correspond matching features. [83]

Depending on the deformation of the target image to the source image, different types of image transformations can be applied. The transformations can be derived from image based and feature based techniques. Linear transformations include rigid, similarity and affine transformations, which have increasing degrees of freedom. In cases where the deformation of the image, that needs to be registered, cannot be compensated by a linear transform, deformable registration can be performed. [84] Transformations such as thin-plate spline lead to local deformations. [75]

Registration techniques require accuracy measurement for assessment and validation. There are several metrics that may involve a set of gold standard landmarks, which are placed or validated manually. [85]–[87] Other methods of assessing the quality of the 3D histology reconstructions may involve measures of smoothness from one serial section to another, such as the Haralick contrast feature. [88] Other measures include calculating the target and fiducial registration error of the landmarks. [85], [86] Common metrics used in the assessment of histology reconstruction and registration have been the Hausdorff distance, [89] root mean square error and accumulated error. However, some studies are using visual validation for the assessment of registration accuracy. [90]

1.7.2 Image segmentation

To perform assessments on features within histology, in the form of morphology and stain intensity, the structures need to be detected and segmented. [91]–[93] The detection and seg-

mentation can be performed manually, and at different levels of automation. [50] This could be performed fully manually. For example, the vessel diameter is measured or the number of vessels in a field of view is counted, such that a density measure is calculated. [94] Fully manual techniques have inter- and intra-operator variability and are limited to small regions of histological tissue because whole-slide analysis is labour intensive. [58] Techniques have been performed in a semi-automated approach, which may involve initializing an automated process or correcting the process manually through post-processing. [50] For example, the user would define a threshold for each field of view to detect vessels, and the final number detected may be assessed again by the user. Fully automatic approaches have no input from the operator. This may be in the form of inputting an image into an algorithm with predefined parameters, with the output of defined measures. This type of analysis increases the throughput of image analysis because the algorithm can quantify whole-slide histology images without the need to extrapolate from small fields of view. [95]

The current state of the art in histology assessment involves quantification and qualitative assessment on bright field microscopes, on small fields of view. [94], [96] This could then involve extrapolating the measurement. For large vessels, such as the aorta, this involves taking sections at locations along the vessel, and assessing the components within the individual vessel wall. [25] This is feasible to perform manually, as there are usually a few vessels to visually assess per sample, or there is only one large vessel, and any quantitative measurements can be performed on a small sample size. A common measurement in studying the vasculature, in the context of vascular disease or oncological related studies, is to assess the capillary density. [97] This is typically assessed by taking random fields of view within the tissue section at representative locations to get an assessment or quantitative measure for the density of the capillaries. [94], [98], [99] This is also performed with cell count or the positive number of cells.

At the level of arterioles containing SMCs, where there are many vessels on the slide, there is interest in the morphology of the vasculature. Density is the main feature of interest when assessing capillaries. However, the arterioles contain a smooth muscle layer with differences in distributions, which needs to be measured. [100] They are also much larger in numbers when compared to large arteries or the aorta, [6] so manually assessing a distribution large enough to represent the population would be tedious. Thus, there is a need to assess the distribution of vascular smooth muscle along the vessel wall on whole slide histology, and encompassing all vasculature within the section. This would involve detection of the vessels on high resolution images and segmenting them automatically to measure the morphological differences between disease models. The segmentation method needs to be comparable to operator variability, and represent the differences found between sample groups of interest accurately. [50]

The segmentation method has to take into account the input image size and in a histological context, this could vary depending on the imaging technique and method of analysis. [101] Three main groups of image types are; bright field images from conventional microscopes, scanned tissue microarrays (TMAs) and scanned whole-slide images. The typical workflow involves images taken from a charge-coupled device camera mounted on top of a bright field microscope. These images usually enable quantification within fields of view, thus there is a trade-off between the magnification of the image and the amount of tissue represented in the image. The resulting images are relatively small and can be assessed in a manual or automated fashion. The user has the option to manually stitch together the images to reconstruct a larger field of view. [102] TMAs can be analyzed in the same way or through whole slide scanning. They represent a small portion of the tissue and are commonly generated through biopsies. [103], [104] The largest representation of the sample are whole-section images. Because histology images are in colour and currently can be scanned at an isotropic pixel size of $0.25 \mu\text{m}$, they result in images of larger than 1 gigabyte. Thus, the segmentation algorithm needs to adapt to the size of the input images because the full image cannot be processed within the working memory of a computer. [105] One way to overcome this obstacle would be to detect the features of interest in a downsampled image, and then performed the segmentation locally at full resolution, in the image region applicable to the feature.

Assessment of the vasculature would involve defining a contour around the inner and outer boundary of the vessel wall through segmentation. The type of segmentation technique will depend on the features within the image and the object to be segmented. There are many techniques that all group mainly into low-level and model-based segmentations. [101] These two categories differ in that low-level segmentation methods rely on features in the image and model-based methods, which takes a-priori knowledge of shape into account. Both results in boundaries around the objects of interest. [106]

Low-level segmentation approaches involve methods such as thresholding, watershed transformations and region growing. [107] Thresholding creates a boundary between different pixel values, where positive values are within the segmented region. The threshold level can be determined manually or automatically using techniques such as Otsu's method [108] and k-means clustering. [109] One or multiple levels of thresholding can be determined. Methods such as watershed segmentation involve calculating the gradient within the image in order to locate the edges of the contours of the object. [110] Region growing is another commonly used method. The algorithm is initialized with a seed and compares the neighbouring pixels to include similar pixel values within the same region. [107]

Model-based segmentation methods can be used when there is a-priori knowledge of the objects of interest, such as boundary smoothness, shape and appearance. This includes active

contour models (snakes) [111] and level set methods. [112] Both methods involve, and can be sensitive to, the initialization curve of the segmentation. Snakes involve optimizing an energy function, which incorporates features of the curve itself and features within the image. Each object to be segmented needs an individual initialization. [111] This may not be the best approach for segmenting features that have variability in the curvature of their contours. The resulting vessel wall segmentations have different curvatures and smoothness to their contours, which is why it is of interest to analyse them. Level set segmentations are represented through a signed distance to the boundary of the object to be segmented. [112] They have the capability of implicitly defining the boundary and provide different topologies. [106]

With colour images, one can extract the feature of interest through colour separation, to use a simpler low-level segmentation method. Colour deconvolution can be performed to represent the colour of interest in one greyscale image. [113], [114] In general, IHC is in colour, due to the oxidization process, and through colour deconvolution. We can rescale the colours such that they represent the stain. This could make the segmentation process more generalizable for various stain types due to the initial step of stain separation. For example, another commonly used secondary antibody is Fast Red in IHC, which results in a red colour. Potentially, the same segmentation algorithm could be used to automatically contour features that have been stained for Fast Red and the typical brown DAB because colour deconvolution extracts the intensity of the decomposed image for the same scale.

1.7.3 Machine Learning

The vasculature involves several calibres of vessels, as a part of a continuous network, comprising of dynamic components within the vascular wall. For convenience, they are categorised and labeled as arteries, and veins, with capillaries in between. There are several tiers of the vasculature from the aorta to arteries and arterioles. [6] At the level of microvessels, vasculature primarily contains a layer of mural wrapping or simply one layer of endothelium for perfusion. [7] With IHC targeting the SMC component of the vasculature, both inflow and draining vessels are visible. The inflow vessels in the form of arteries and arterioles are functionally and structurally different from veins and venules. Our interest is at the level of the arterioles because they can control local blood flow, thus the venules should be separated in a different category for comprehensive quantification.

To automatically differentiate the categories of vessel after segmentation, features or quantitative measures can be extracted from the vessels of interest. The features could include the vessel morphology, based on the geometric measures of the segmented vessel wall. [115] Measures can also be extracted from the intensity distribution in the IHC stained SMC. This can

include first order and second order intensity statistics. First order statistics are independent of the pixel location. (Fig. 1.7) Higher order features account for neighbouring pixel relationships.

Bright field histology is represented in colour, as the values are within the visible spectrum, thus the intensity features can have different representations. The standard colour channels include red-green-blue (RGB), cyan-magenta-yellow-black (CMYK), hue-saturation-value (HSV), and Lab space. [116] This could be performed for the stain typically used for IHC, which is the DAB precipitate, resulting in a brown hue. The other stains could be extracted in the same process. Features such as nuclei could also be extracted from the image, with the selection of the blue-purple hue of hematoxylin, and has been performed in previous works. [117]

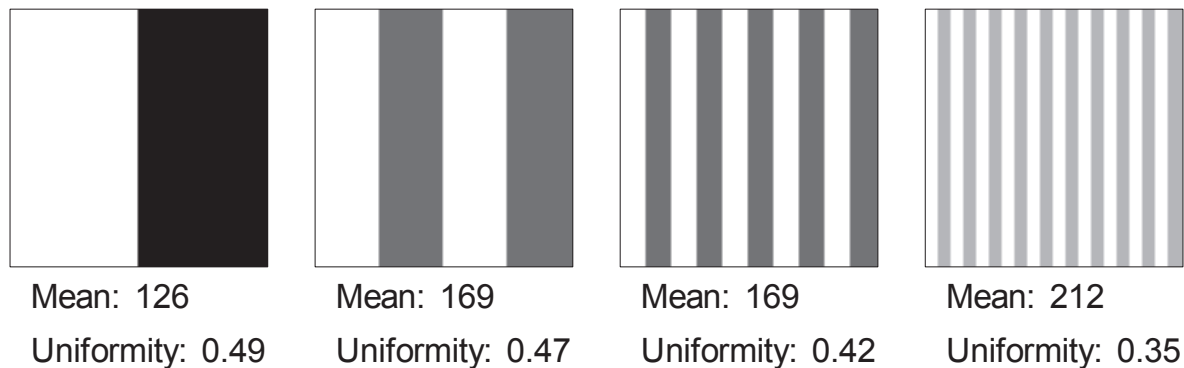


Figure 1.7: First order intensity measure (mean) and second order texture measure (uniformity) of a synthetic dataset. The uniformity is decreasing from left to right and the mean is increasing, where the middle panels are indistinguishable by the first order intensity measure.

First and second order statistics could then be calculated, as measures of the intensity values, to differentiate between the categories of vessels. [118] First order statistics do not involve the spatial relations between the pixels within an image. These values include measures such as the mean, median, and grey level skewness, on all the grey levels within an image, or within the segmented vessel wall. [115], [119] Higher order statistics take into account the neighbouring pixel relations to measure texture within the greyscale representation of each colour channel. [119] One method to calculate higher order features is through creating a high order histogram in the form of a grey-level-co-occurrence matrix (GLCM). [88], [120], [121] This is created through measuring the correlation of neighbouring pixel pairs. The neighbour could be defined at any direction or distance away from the current pixel. This results in a GLCM that incorporates the paired pixel directions and the intensity of the pixel pairs. [122] Measures can be derived from the GLCM and be used as features, such as contrast, dissimilarity and entropy.

Classifiers can be built from combinations of features automatically through machine learn-

ing. [122] Through this process the system can predict outcomes through models dependent on characteristics of the input. Supervised machine learning is when the data being input are labeled and the features are directly mapped into the output. [123] Unsupervised machine learning recognises patterns within the input without the user providing labels. An example of a supervised system with a binary outcome is the input of features contained within two classes, arterioles and venules. Each sample is labeled as a feature of either category. The output can then be either one of the two labels. However, machine learning can also encompass continuous outputs, such as providing a probability of a certain circumstance. This may involve the process of selecting the optimal set of features and using different classification methods. [123]

Feature selection is a means to sift relevant features and incorporate them into the machine learning algorithm. This process enables the ability to remove redundant and correlated features in multivariate methods, in order to prevent overfitting. [124] Through this process, features can be ranked based on their performance. Features that work well in combination with others can be included as well, even if they are unable to separate the classes on their own. Thus, through feature selection, the optimal subsets of features are chosen for class separation, avoiding overfitting to the dataset. This involves two main groups of methods; wrappers and filters. [125] Wrappers score features based on their predictive power. These are typically greedy search techniques and are robust to overfitting. Nested subsets of feature are created using methods such as forward selection. The top predictive features are continuously added to the feature set. [125] This also includes backward elimination. In this case, all the features are used at first, and the least predictive or redundant variables are removed. Filters are another method that involves pre-processing to select the features and is not dependent on the classifier. These techniques are used to prevent overfitting and false positive classifications.

Machine learning involves creating classifiers through algorithms. Classifiers form decision boundaries between the classes in feature space. [122] This can be in the form of linear classifiers in the form of a line, plane, or hyperplane. [126] Other techniques include higher order hyperplanes, support vector machines (SVMs), naive Bayes, and decision trees. [127] A commonly used classifier is the SVM, as it maximizes the margin between the classes in feature space. [128] SVM is a linear classifier; however, features can be transformed, such that they can be linearly separated in feature space.

The classifiers created need to be evaluated based on their performance, and there are methods of validation. [129] In the case of arteriole and venule separation, a binary classification can be compared to user determined labels, through measures such as the true positive, true negative, false positive and false negative values. Error rates can be derived from these values, such as the precision, sensitivity and specificity of the system. The area under the operator

receiver curve can be measured to determine the trade-off between true and false positive classification. Cross-validations can be performed, with subsets of samples are left out, such that the machine learning algorithm is blind to those datasets. They could also be externally validated on samples from different centers.

1.8 State of the Art in Histology Image Analysis

The work described in this thesis involves development of automated software modules for the analysis of vascular histology, in the context of microvascular regeneration, at the level of the arterioles. Other studies have approached similar problems, with different solutions, for histology image registration (Table 1.1) and segmentation (Table 1.2). Developed solutions in both fields involve applications of either manual, semi-automated, or fully automated methods enabling the analysis of vasculature or their feature of interest, within the histological context. They demonstrated the feasibility of developing an automated system and the need for such approaches.

One of the main focuses of histology registration involves alignment of 2D serial sections for 3D volume reconstruction. Table 1.1 shows a summary of works for 3D reconstruction with application for the vasculature. The work by Steiniger et al. demonstrated the need for 3D reconstruction. They performed manual reconstruction of the capillary network in the spleen in order to assess the network structure and the arterial microvascular ends, suggesting an open circulatory system. [130] Semi-automatic reconstructions involve initializing the serial histology sections using a revolving microscope or Photoshop to roughly align the images prior to intensity based registration. [72], [131] Manual or automatic methods may not have been validated through measures such as the registration error. [132]–[134] When they were measured, metrics such as the Hausdorff distance, root mean squared error, and quantitative smoothness measures were used to assess accuracy on either synthetic or sample data sets. Our technique results in fully automatic 3D reconstructions of arterioles on whole-slide histology.

The vascular segmentation in the histological context mainly focuses on IHC, which is demonstrated by Table 1.2. Unlike H&E staining, which results in magenta coloured tissues, IHC provides contrast for the vasculature in the form of capillaries, arterioles and arteries. The techniques developed involve semi-automated methods, developed as early as 1998 by Van der Laak et al. [135] Since then, other semi- and fully automated methods have been developed, mainly focusing on the capillaries, and aim to achieve an accurate density measure. [131], [136]–[140] Segmentation of vessel wall, not simply the outer boundary of the vessel, has been performed. This enabled the measurement of the vessel wall area compared to the lumen. [138] Depending on the hardware available, the samples included TMAs, field of views taken

Table 1.1: A summary of previous studies on registration for 3D vascular histology reconstruction (work presented in this thesis in boldface).

Year	1st Author	Stain	Tissue	Calibre	Method	Image	Automation
2005	Gijtenbeek	IHC	Patients	Arteriole/ Capillary	Manual/ intensity based	Conventional Microscope	Semi
2006	Gilhuis	IHC	Patients	Capillary	Manual/ intensity based	Conventional Microscope	Semi
2011	Feuerstein	H&E	Rat	Artery	Markov random field	Whole- slide	Fully
2011	Steiniger	IHC	Patients	Capillary	Image overlays	Conventional Microscope	Manual
2013	Song	H&E	Patients	Artery	Intensity based	Whole- slide	Fully
2013	Schwier	H&E	Rat	Artery	Iterative best fit	Whole- slide	Fully
2014	Galambos	H&E/ IHC	Patients	Artery/ arteriole	Manual alignment	Conventional Microscope	Manual
2015	Wang	H&E	Patients	Artery	Manual/ Photoshop	Whole- slide	Semi
2015	Xu	IHC	Mice	Artery/ arteriole	Landmark based	Whole- slide	Fully

from a conventional microscope, and whole-slide imaging. The steps involved with the segmentation process typically involved thresholding, either at a user given value, or using Otsu's method. Post-processing steps were performed, such as smoothing, skeletonization and separating attached vessels through watershed segmentation. [138] Validation of the segmentation techniques involved comparison between manual assessments. The accuracy of detection and segmentation was reported in some studies. Our technique results in fully automatic segmentations of the arteriole wall on whole-slide histology.

Automated image analysis techniques in the context of histology are not restricted to the study of vasculature. Other developed methods can be adapted for the assessment of vessels. Reconstructions of serial histological sections have been performed on the brain, [71], [141] liver, glomerulus and whole mouse embryos. [142] Registration of serial tissue sections with different stains has been performed for co-localisation of positivity, which would require both registration and segmentation of the stains of interest. [132], [143] Oncological applications

Table 1.2: A summary of previous studies on segmentation of vasculature in histology (work presented in this thesis in boldface).

Year	1st Author	Stain	Tissue	Calibre	Segmented	Image	Automation
1998	Van der Laak	IHC	Patients	Capillary	Stain	Conventional Microscope	Semi
2003	Chantrain	IHC	Patients	Capillary	Stain	Whole-slide	Semi
2005	Gijtenbeek	IHC	Patients	Arteriole/ capillary	Endothelial cells and pericytes	Conventional Microscope	Semi
2008	Hu	IHC	Porcine	Aorta	Stain	Conventional Microscope	Semi
2009	Sullivan	IHC	Patients	Capillary	Stain	Tissue Microarray	Fully
2011	Reyes-Aldasoro	IHC	Patients/ Mice	Capillary	Vessel wall	Conventional Microscope	Fully
2013	Fernandez-Carrobles	IHC	Mice	Capillary	Vessel outer boundary	Tissue Microarray	Fully
2014	Galambos	H&E/ IHC	Patients	Artery/ arteriole	Vessel	Conventional Microscope	Manual
2015	Kather	IHC	Patients	Capillary	Vessel wall	Whole-slide	Fully
2016	Xu	IHC	Mice	Arteriole	Vessel wall	Whole- slide	Fully

have been at the forefront for applications of histology tissue segmentation, and there has been a special focus on the accurate detection of nuclei. [144]

1.9 Thesis Outline

To address the technology gap, with respect to the comprehensive assessment of muscularized microvasculature, the overarching objective of this thesis is to develop an automated software platform to assess the differences in morphology of the post-ischemic vasculature compared to normal and its impact on function. The central research questions of this thesis are:

1. Does using 2D whole tissue section analysis result in different vasculature measurements of morphology and density as compared to conventional field of view sampling?
2. Are there differences in SMC content with respect to density and morphology between post ischemic and normal arterioles?

3. Do the differences in SMC content between post ischemic and normal arterioles affect blood flow and function?

To answer these research questions, this thesis has the following five aims:

1. To develop an automated registration software module for 3D vascular reconstruction
2. To develop an automated detection and segmentation software module for vessel contours
3. To classify arterioles from venules using a machine learning platform
4. To compare morphology measurements between regenerated and normal vasculature
5. To infer difference in local blood flow control of SMC through modeling

Chapter 2: A method for 3D histopathology reconstruction supporting mouse microvasculature analysis

The purpose of this work was to develop an automated registration method, for whole-slide serial histology sections, to reconstruct 3D histological volumes for the visualization of the microvasculature. The developed technique aims to preserve the topology and geometry of the vessels with accuracy, high enough for the microvessels down to the level of precapillary arterioles. This would enable the visualization of structural abnormalities in the post-ischemic hind limb compared to the normal. We aim to use fiducial markers within the tissue section for registration to avoid deformation of the features within the tissue. We hypothesized that a fully automated nucleus landmark based registration algorithm can be developed to perform high accuracy 3D histology reconstruction for the visualization of the microvasculature.

Chapter 3: Segmentation of digitized histological sections for quantification of the muscularized vasculature in the mouse hind limb

The objective of this work was to develop a fully automated software algorithm for the detection and segmentation of vascular smooth muscle containing microvasculature. Chapter 2 provided the visualization of the vessels of interest, but delineations are necessary to provide a mode for quantification. Up to hundreds of arterioles and venules are present within each section, and thus a comprehensive measurement requires automated accurate detection and segmentation without field of view sampling. We hypothesized that a fully automated detection and segmentation algorithm can be developed with high accuracy compared to manual delineations, for quantification of vasculature on whole slide histology images.

Chapter 4: Differentiation of arterioles from venules in mouse histology images using machine learning

The objective of this work was to automatically classify arterioles separately from venules. Chapter 3 described the developed automated segmentation of vessels containing vascular smooth muscle. However, arterioles and venules are functionally and morphologically different, thus valuable quantitation cannot be performed unless they are analyzed separately. Morphological and intensity based features were extracted from the segmented vasculature to define a classifier to separate the feeder and draining vessels in both the normal and post-ischemic mouse model, through machine learning. We hypothesized that automated and accurate classification of arterioles and venules is feasible with a machine learning platform.

Chapter 5: High content analysis of the microvasculature in the post-ischemic skeletal muscle reveals the emergence of abnormally thin-walled arteries and arterioles: Implications for flow reserve in regenerated muscle

The purpose of this work was to characterise the differences in morphology and function of the vascular smooth muscle distribution between the post-ischemic and normal vasculature. Chapters 2-4 encompass the development of a platform for a comprehensive analysis of the muscularized microvasculature. This enabled the quantitative analysis of the difference in vessel wall morphology in the post-ischemic stage. The morphology could then be used as parameters for functional modeling of the blood flow through the network. Our hypothesis was that the comprehensive quantification of the vasculature would result in the detection of differences in the morphology of the vessel wall in the post-ischemic mice, as compared to the normal, and functional modeling will demonstrate deficiencies in the injured vascular network.

References

- [1] A. Palotie, K. Tryggvason, L. Peltonen, and H. Seppa, "Components of subendothelial aorta basement membrane. immunohistochemical localization and role in cell attachment," *Laboratory investigation; a journal of technical methods and pathology*, vol. 49, no. 3, pp. 362–370, 1983.
- [2] B. Lilly, "We have contact: Endothelial cell-smooth muscle cell interactions," *Physiology*, vol. 29, no. 4, pp. 234–241, 2014.
- [3] K. A. Dora, "Cell-cell communication in the vessel wall," *Vascular Medicine*, vol. 6, no. 1, pp. 43–50, 2001.

- [4] J. N. Passman, X. R. Dong, S.-P. Wu, C. T. Maguire, K. A. Hogan, V. L. Bautch, and M. W. Majesky, "A sonic hedgehog signaling domain in the arterial adventitia supports resident *sc1+* smooth muscle progenitor cells," *Proceedings of the National Academy of Sciences*, vol. 105, no. 27, pp. 9349–9354, 2008.
- [5] P. Lacolley, V. Regnault, A. Nicoletti, Z. Li, and J.-B. Michel, "The vascular smooth muscle cell in arterial pathology: A cell that can take on multiple roles," *Cardiovascular research*, vol. 95, no. 2, pp. 194–204, 2012.
- [6] S. P. Herbert and D. Y. Stainier, "Molecular control of endothelial cell behaviour during blood vessel morphogenesis," *Nature reviews Molecular cell biology*, vol. 12, no. 9, pp. 551–564, 2011.
- [7] P. Carmeliet, "Angiogenesis in life, disease and medicine," *Nature*, vol. 438, no. 7070, pp. 932–936, 2005.
- [8] R. K. Jain, "Molecular regulation of vessel maturation," *Nature medicine*, vol. 9, no. 6, pp. 685–693, 2003.
- [9] T. Couffignal, P. Dufourcq, L. Barandon, L. Leroux, and C. Duplaa, "Mouse models to study angiogenesis, vasculogenesis and arteriogenesis in the context of cardiovascular diseases," *France. Institut National de la Sante et de la Recherche Meidicale*, 2010.
- [10] J. Frostegard, "Immunity, atherosclerosis and cardiovascular disease," *BMC medicine*, vol. 11, no. 1, p. 117, 2013.
- [11] A. Limbourg, T. Korff, L. C. Napp, W. Schaper, H. Drexler, and F. P. Limbourg, "Evaluation of postnatal arteriogenesis and angiogenesis in a mouse model of hind-limb ischemia," *Nature protocols*, vol. 4, no. 12, pp. 1737–1748, 2009.
- [12] M. H. Vries, A. Wagenaar, S. E. Verbruggen, D. G. Molin, and M. J. Post, "Cxcl1 promotes arteriogenesis through enhanced monocyte recruitment into the peri-collateral space," *Angiogenesis*, 2014.
- [13] K. Gaengel, G. Genove, A. Armulik, and C. Betsholtz, "Endothelial-mural cell signaling in vascular development and angiogenesis," *Arterioscler Thromb Vasc Biol*, vol. 29, no. 5, pp. 630–638, 2009.
- [14] P. Carmeliet and R. K. Jain, "Molecular mechanisms and clinical applications of angiogenesis," *Nature*, vol. 473, no. 7347, pp. 298–307, 2011.
- [15] R. H. Adams and K. Alitalo, "Molecular regulation of angiogenesis and lymphangiogenesis," *Nature Reviews Molecular Cell Biology*, vol. 8, no. 6, pp. 464–478, 2007.

- [16] T. P. Zhong, S. Childs, J. P. Leu, and M. C. Fishman, "Gridlock signalling pathway fashions the first embryonic artery," *Nature*, vol. 414, no. 6860, pp. 216–220, 2001.
- [17] F. C. White, S. M. Carroll, and M. P. Kamps, "Vegf mrna is reversibly stabilized by hypoxia and persistently stabilized in vegf-overexpressing human tumor cell lines," *Growth Factors*, vol. 12, no. 4, pp. 289–301, 1995.
- [18] W.-J. Cai, E. Kocsis, D. Scholz, X. Luo, W. Schaper, and J. Schaper, "Presence of cx37 and lack of desmin in smooth muscle cells are early markers for arteriogenesis," *Molecular and cellular biochemistry*, vol. 262, no. 1, pp. 17–23, 2004.
- [19] E. Deindl, I. Buschmann, I. E. Hoefler, T. Podzuweit, K. Boengler, S. Vogel, N. van Royen, B. Fernandez, and W. Schaper, "Role of ischemia and of hypoxia-inducible genes in arteriogenesis after femoral artery occlusion in the rabbit," *Circulation research*, vol. 89, no. 9, pp. 779–786, 2001.
- [20] C. Arnold, A. Feldner, L. Pfisterer, M. Hodebeck, K. Troidl, G. Genove, T. Wieland, M. Hecker, and T. Korff, "Rgs5 promotes arterial growth during arteriogenesis," *EMBO Mol Med*, vol. 6, no. 8, pp. 1075–1089, 2014.
- [21] G. K. Hansson, "Inflammation, atherosclerosis, and coronary artery disease," *New England Journal of Medicine*, vol. 352, no. 16, pp. 1685–1695, 2005.
- [22] R. Hinchliffe, G. Andros, J. Apelqvist, K. Bakker, S. Fiedrichs, J. Lammer, M. Lepantalo, J. L. Mills, J. Reekers, and C. Shearman, "A systematic review of the effectiveness of revascularization of the ulcerated foot in patients with diabetes and peripheral arterial disease," *Diabetes/metabolism research and reviews*, vol. 28, no. S1, pp. 179–217, 2012.
- [23] W. S. Aronow, "Office management of peripheral arterial disease," *The American journal of medicine*, vol. 123, no. 9, pp. 790–792, 2010.
- [24] H. C. Stary, A. B. Chandler, S. Glagov, J. R. Guyton, W. Insull, M. E. Rosenfeld, S. A. Schaffer, C. J. Schwartz, W. D. Wagner, and R. W. Wissler, "A definition of initial, fatty streak, and intermediate lesions of atherosclerosis. a report from the committee on vascular lesions of the council on arteriosclerosis, american heart association," *Circulation*, vol. 89, no. 5, pp. 2462–2478, 1994.
- [25] H. C. Stary, A. B. Chandler, R. E. Dinsmore, V. Fuster, S. Glagov, W. Insull, M. E. Rosenfeld, C. J. Schwartz, W. D. Wagner, and R. W. Wissler, "A definition of advanced types of atherosclerotic lesions and a histological classification of atherosclerosis," *Circulation*, vol. 92, no. 5, pp. 1355–1374, 1995.

- [26] K. A. Campbell, M. J. Lipinski, A. C. Doran, M. D. Skafien, V. Fuster, and C. A. McNamara, "Lymphocytes and the adventitial immune response in atherosclerosis," *Circulation research*, vol. 110, no. 6, pp. 889–900, 2012.
- [27] A. Matsakas, V. Yadav, S. Lorca, R. M. Evans, and V. A. Narkar, "Revascularization of ischemic skeletal muscle by estrogen-related receptor- γ ," *Circulation research*, vol. 110, no. 8, pp. 1087–1096, 2012.
- [28] D. W. McCarey, I. B. McInnes, R. Madhok, R. Hampson, O. Scherbakova, I. Ford, H. A. Capell, and N. Sattar, "Trial of atorvastatin in rheumatoid arthritis (tara): Double-blind, randomised placebo-controlled trial," *The Lancet*, vol. 363, no. 9426, pp. 2015–2021, 2004.
- [29] M. Takemoto and J. K. Liao, "Pleiotropic effects of 3-hydroxy-3-methylglutaryl coenzyme a reductase inhibitors," *Arteriosclerosis, thrombosis, and vascular biology*, vol. 21, no. 11, pp. 1712–1719, 2001.
- [30] N. Schaper, G. Andros, J. Apelqvist, K. Bakker, J. Lammer, M. Lepantalo, J. L. Mills, J. Reekers, C. Shearman, and R. Zierler, "Specific guidelines for the diagnosis and treatment of peripheral arterial disease in a patient with diabetes and ulceration of the foot 2011," *Diabetes/metabolism research and reviews*, vol. 28, no. S1, pp. 236–237, 2012.
- [31] R. A. Brenes, C. C. Jadowiec, M. Bear, P. Hashim, C. D. Protack, X. Li, W. Lv, M. J. Collins, and A. Dardik, "Toward a mouse model of hind limb ischemia to test therapeutic angiogenesis," *Journal of vascular surgery*, vol. 56, no. 6, pp. 1669–1679, 2012.
- [32] D. Scholz, T. Ziegelhoeffer, A. Helisch, S. Wagner, C. Friedrich, T. Podzuweit, and W. Schaper, "Contribution of arteriogenesis and angiogenesis to postocclusive hindlimb perfusion in mice," *Journal of molecular and cellular cardiology*, vol. 34, no. 7, pp. 775–787, 2002.
- [33] B. G. Halloran, M. P. Lilly, E. J. Cohn, and W. R. Flinn, "Arterial remodeling in the rabbit: Structural changes in response to chronic hindlimb ischemia," *Journal of Vascular and Interventional Radiology*, vol. 10, no. 7, pp. 987–988, 1999.
- [34] A. Lutun, M. Tjwa, L. Moons, Y. Wu, A. Angelillo-Scherrer, F. Liao, J. A. Nagy, A. Hooper, J. Priller, and B. De Klerck, "Revascularization of ischemic tissues by plgf treatment, and inhibition of tumor angiogenesis, arthritis and atherosclerosis by anti-flt1," *Nature medicine*, vol. 8, no. 8, pp. 831–840, 2002.

- [35] T. Couffinhal, M. Silver, L. P. Zheng, M. Kearney, B. Witztenbichler, and J. M. Isner, “Mouse model of angiogenesis,” *The American journal of pathology*, vol. 152, no. 6, p. 1667, 1998.
- [36] H. L. Gornik and M. A. Creager, “Arginine and endothelial and vascular health,” *The Journal of nutrition*, vol. 134, no. 10, 2880S–2887S, 2004.
- [37] D. Clark and C. Badea, “Micro-ct of rodents: State-of-the-art and future perspectives,” *Physica medica*, vol. 30, no. 6, pp. 619–634, 2014.
- [38] S. J. Schambach, S. Bag, L. Schilling, C. Groden, and M. A. Brockmann, “Application of micro-ct in small animal imaging,” *Methods*, vol. 50, no. 1, pp. 2–13, 2010.
- [39] F. Hallouard, N. Anton, P. Choquet, A. Constantinesco, and T. Vandamme, “Iodinated blood pool contrast media for preclinical x-ray imaging applications-a review,” *Biomaterials*, vol. 31, no. 24, pp. 6249–6268, 2010.
- [40] C. T. Badea, S. M. Johnston, Y. Qi, and G. A. Johnson, “4d micro-ct for cardiac and perfusion applications with view under sampling,” *Physics in medicine and biology*, vol. 56, no. 11, p. 3351, 2011.
- [41] J. P. van den Wijngaard, J. C. Schwarz, P. van Horssen, M. G. van Lier, J. G. Dobbe, J. A. Spaan, and M. Siebes, “3d imaging of vascular networks for biophysical modeling of perfusion distribution within the heart,” *Journal of Biomechanics*, vol. 46, no. 2, pp. 229–239, 2013.
- [42] M. J. Levesque, J. F. Cornhill, and R. M. Nerem, “Vascular casting a new method for the study of the arterial endothelium,” *Atherosclerosis*, vol. 34, no. 4, pp. 457–467, 1979.
- [43] Q. H. Hogan, “Lumbar epidural anatomy. a new look by cryomicrotome section,” *Anesthesiology*, vol. 75, no. 5, pp. 767–775, 1991.
- [44] N. Hakimzadeh, P. van Horssen, M. G. van Lier, J. P. van den Wijngaard, C. Belterman, R. Coronel, J. J. Piek, H. J. Verberne, J. A. Spaan, and M. Siebes, “Detection and quantification methods of monocyte homing in coronary vasculature with an imaging cryomicrotome,” *Journal of molecular and cellular cardiology*, vol. 76, pp. 196–204, 2014.
- [45] S. Inoué, “Foundations of confocal scanned imaging in light microscopy,” in *Handbook of biological confocal microscopy*, Springer, 2006, pp. 1–19.
- [46] K. Fujita, M. Kobayashi, S. Kawano, M. Yamanaka, and S. Kawata, “High-resolution confocal microscopy by saturated excitation of fluorescence,” *Physical review letters*, vol. 99, no. 22, p. 228 105, 2007.

- [47] I. Cox, C. J. Sheppard, and T. Wilson, "Super-resolution by confocal fluorescent microscopy," *Optik*, vol. 60, no. 4, pp. 391–396, 1982.
- [48] M. Cregger, A. J. Berger, and D. L. Rimm, "Immunohistochemistry and quantitative analysis of protein expression," *Archives of Pathology & Laboratory Medicine*, vol. 130, no. 7, pp. 1026–1030, 2006.
- [49] M. Werner, A. Chott, A. Fabiano, and H. Battifora, "Effect of formalin tissue fixation and processing on immunohistochemistry," *The American journal of surgical pathology*, vol. 24, no. 7, pp. 1016–1019, 2000.
- [50] C. Taylor and R. Levenson, "Quantification of immunohistochemistry - issues concerning methods, utility and semiquantitative assessment ii," *Histopathology*, vol. 49, no. 4, pp. 411–424, 2006.
- [51] S.-R. Shi, R. J. Cote, and C. R. Taylor, "Antigen retrieval techniques current perspectives," *Journal of Histochemistry & Cytochemistry*, vol. 49, no. 8, pp. 931–937, 2001.
- [52] A. J. Norton, S. Jordan, and P. Yeomans, "Brief, high-temperature heat denaturation (pressure cooking): A simple and effective method of antigen retrieval for routinely processed tissues," *The Journal of pathology*, vol. 173, no. 4, pp. 371–379, 1994.
- [53] G. Cattoretti, S. Pileri, C. Parravicini, M. H. Becker, S. Poggi, C. Bifulco, G. Key, L. D'Amato, E. Sabattini, and E. Feudale, "Antigen unmasking on formalin-fixed, paraffin-embedded tissue sections," *The Journal of pathology*, vol. 171, no. 2, pp. 83–98, 1993.
- [54] D. McCormick, C. Yu, C. Hobbs, and P. Hall, "The relevance of antibody concentration to the immunohistological quantification of cell proliferation-associated antigens," *Histopathology*, vol. 22, no. 6, pp. 543–547, 1993.
- [55] A. Rhodes, B. Jasani, A. J. Balaton, D. M. Barnes, E. Anderson, L. G. Bobrow, and K. D. Miller, "Study of interlaboratory reliability and reproducibility of estrogen and progesterone receptor assays in europe," *American Journal of Clinical Pathology*, vol. 115, no. 1, pp. 44–58, 2001.
- [56] R. von Wasielewski, M. Mengel, B. Wiese, T. Rudiger, H. K. Muller-Hermelink, and H. Kreipe, "Tissue array technology for testing interlaboratory and interobserver reproducibility of immunohistochemical estrogen receptor analysis in a large multicenter trial," *American Journal of Clinical Pathology*, vol. 118, no. 5, pp. 675–682, 2002.

- [57] M. Mengel, R. von Wasielewski, B. Wiese, T. Rudiger, H. K. Muller-Hermelink, and H. Kreipe, “Inter-laboratory and inter-observer reproducibility of immunohistochemical assessment of the ki-67 labelling index in a large multi-centre trial,” *The Journal of pathology*, vol. 198, no. 3, pp. 292–299, 2002.
- [58] R. Walker, “Quantification of immunohistochemistry-issues concerning methods, utility and semiquantitative assessment i,” *Histopathology*, vol. 49, no. 4, pp. 406–410, 2006.
- [59] S. R. Shi, R. J. Cote, B. Chaiwun, L. L. Young, Y. Shi, D. Hawes, T. Chen, and C. R. Taylor, “Standardization of immunohistochemistry based on antigen retrieval technique for routine formalin-fixed tissue sections,” *Applied Immunohistochemistry*, vol. 6, no. 2, pp. 89–96, 1998.
- [60] C. R. Taylor and R. J. Cote, *Immunomicroscopy: a diagnostic tool for the surgical pathologist*. WB Saunders Company, 2006.
- [61] A. Rhodes, B. Jasani, E. Anderson, A. R. Dodson, and A. J. Balaton, “Evaluation of her-2/neu immunohistochemical assay sensitivity and scoring on formalin-fixed and paraffin-processed cell lines and breast tumors,” *American Journal of Clinical Pathology*, vol. 118, no. 3, pp. 408–417, 2002.
- [62] P. Fritz, X. Wu, H. Tuzek, H. Mulhaupt, and P. Schwarzmann, “Quantitation in immunohistochemistry. a research method or a diagnostic tool in surgical pathology?” *Pathologica*, vol. 87, no. 3, pp. 300–309, 1995.
- [63] J. O. Armitage, “A clinical evaluation of the international lymphoma study group classification of non-hodgkin’s lymphoma,” *Blood*, vol. 89, no. 11, pp. 3909–3918, 1997.
- [64] R. L. Camp, G. G. Chung, and D. L. Rimm, “Automated subcellular localization and quantification of protein expression in tissue microarrays,” *Nature medicine*, vol. 8, no. 11, pp. 1323–1328, 2002.
- [65] S. Chen, M. Zhao, G. Wu, C. Yao, and J. Zhang, “Recent advances in morphological cell image analysis,” *Computational and mathematical methods in medicine*, vol. 1, 2012.
- [66] Y. Xu, J. G. Pickering, Z. Nong, E. Gibson, J.-M. Arpino, H. Yin, and A. D. Ward, “A method for 3d histopathology reconstruction supporting mouse microvasculature analysis,” *PloS One*, vol. 10, no. 5, e0126817, 2015.
- [67] S. Lang, B. Muller, M. D. Dominiotto, P. C. Cattin, I. Zanette, T. Weitkamp, and S. E. Hieber, “Three-dimensional quantification of capillary networks in healthy and cancerous tissues of two mice,” *Microvascular research*, vol. 84, no. 3, pp. 314–322, 2012.

- [68] M. Guo, S. D. Ricardo, J. A. Deane, M. Shi, L. Cullen-McEwen, and J. F. Bertram, "A stereological study of the renal glomerular vasculature in the db/db mouse model of diabetic nephropathy," *Journal of Anatomy*, vol. 207, no. 6, pp. 813–821, 2005.
- [69] P. Dockery and J. Fraher, "The quantification of vascular beds: A stereological approach," *Experimental and molecular pathology*, vol. 82, no. 2, pp. 110–120, 2007.
- [70] S. Ourselin, A. Roche, G. Subsol, X. Pennec, and N. Ayache, "Reconstructing a 3d structure from serial histological sections," *Image and Vision Computing*, vol. 19, no. 1-2, pp. 25–31, 2001.
- [71] S. Gaffling, V. Daum, and J. Hornegger, "Landmark-constrained 3-d histological imaging: A morphology-preserving approach.," in *VMV*, Citeseer, 2011, pp. 309–316.
- [72] H. J. Gilhuis, J. A. van der Laak, J. Pomp, A. C. Kappelle, J. M. Gijtenbeek, and P. Wesseling, "Three-dimensional (3d) reconstruction and quantitative analysis of the microvasculature in medulloblastoma and ependymoma subtypes," *Angiogenesis*, vol. 9, no. 4, pp. 201–208, 2006.
- [73] T. Kurien, R. W. Boyce, E. C. Paish, J. Ronan, J. Maddison, E. A. Rakha, A. R. Green, and I. O. Ellis, "Three dimensional reconstruction of a human breast carcinoma using routine laboratory equipment and immunohistochemistry," *Journal of clinical pathology*, vol. 58, no. 9, pp. 968–972, 2005.
- [74] A. H. Boag, L. A. Kennedy, and M. J. Miller, "Three-dimensional microscopic image reconstruction of prostatic adenocarcinoma," *Archives of Pathology & Laboratory Medicine*, vol. 125, no. 4, pp. 562–566, 2001.
- [75] B. Zitova and J. Flusser, "Image registration methods: A survey," *Image and Vision Computing*, vol. 21, no. 11, pp. 977–1000, 2003.
- [76] L. G. Brown, "A survey of image registration techniques," *ACM computing surveys (CSUR)*, vol. 24, no. 4, pp. 325–376, 1992.
- [77] F. Maes, A. Collignon, D. Vandermeulen, G. Marchal, and P. Suetens, "Multimodality image registration by maximization of mutual information," *IEEE Transactions on Medical Imaging*, vol. 16, no. 2, pp. 187–198, 1997.
- [78] P. Thevenaz and M. Unser, "Optimization of mutual information for multiresolution image registration," *IEEE Transactions on Image Processing*, vol. 9, no. 12, pp. 2083–2099, 2000.

- [79] J. Lotz, J. Olesch, B. Muller, T. Polzin, P. Galuschka, J. Lotz, S. Heldmann, H. Laue, M. Gonzalez-Vallinas, and A. Warth, "Patch-based nonlinear image registration for gigapixel whole slide images," *IEEE Transactions on Biomedical Engineering*, vol. 63, no. 9, pp. 1812–1819, 2016.
- [80] P. J. Besl and N. D. McKay, "A method for registration of 3-d shapes," *Pattern Analysis and Machine Intelligence, IEEE Transactions on*, vol. 14, no. 2, pp. 239–256, 1992.
- [81] M. Chen and B. Yan, "Registration algorithm research for work-pieces based on affine invariant," in *International Conference on Optical Instruments and Technology (OIT2011)*, International Society for Optics and Photonics, 2011, 82011Q.
- [82] S. Du, N. Zheng, L. Xiong, S. Ying, and J. Xue, "Scaling iterative closest point algorithm for registration of m-d point sets," *Journal of Visual Communication and Image Representation*, vol. 21, no. 5-6, pp. 442–52, 2010.
- [83] D. G. Lowe, "Object recognition from local scale-invariant features," in *Computer vision, 1999. The proceedings of the seventh IEEE international conference on*, IEEE, vol. 2, 1999, pp. 1150–1157.
- [84] J. A. Maintz and M. A. Viergever, "A survey of medical image registration," *Medical image analysis*, vol. 2, no. 1, pp. 1–36, 1998.
- [85] E. Gibson, C. Crukley, M. Gaed, J. A. Gomez, M. Moussa, J. L. Chin, G. S. Bauman, A. Fenster, and A. D. Ward, "Registration of prostate histology images to ex vivo mr images via strand-shaped fiducials," *Journal of Magnetic Resonance Imaging*, vol. 36, no. 6, pp. 1402–1412, 2012.
- [86] E. Gibson, M. Gaed, J. A. Gomez, M. Moussa, C. Romagnoli, J. L. Chin, C. Crukley, G. S. Bauman, A. Fenster, and A. D. Ward, "3d prostate histology reconstruction: An evaluation of image-based and fiducial-based algorithms," in *Medical Imaging 2013: Digital Pathology*, M. N. Gurcan and A. Madabhushi, Eds., ser. Proceedings of SPIE. 2013, vol. 8676.
- [87] A. D. Ward, C. Crukley, C. A. McKenzie, J. Montreuil, E. Gibson, C. Romagnoli, J. A. Gomez, M. Moussa, J. Chin, G. Bauman, *et al.*, "Prostate: Registration of digital histopathologic images to in vivo mr images acquired by using endorectal receive coil," *Radiology*, vol. 263, no. 3, pp. 856–864, 2012.
- [88] R. M. Haralick and K. Shanmugam, "Textural features for image classification," *IEEE Transactions on systems, man, and cybernetics*, vol. 3, no. 6, pp. 610–621, 1973.

- [89] D. P. Huttenlocher, G. A. Klanderman, and W. J. Rucklidge, "Comparing images using the hausdorff distance," *IEEE Transactions on Pattern Analysis and Machine Intelligence*, vol. 15, no. 9, pp. 850–863, 1993.
- [90] K. Mosaliganti, T. Pan, R. Ridgway, R. Sharp, L. Cooper, A. Gulacy, A. Sharma, O. Irfanoglu, R. Machiraju, T. Kurc, A. de Bruin, P. Wenzel, G. Leone, J. Saltz, and K. Huang, "An imaging workflow for characterizing phenotypical change in large histological mouse model datasets," *Journal of Biomedical Informatics*, vol. 41, no. 6, pp. 863–873, 2008.
- [91] Y.-Y. Wang, S.-C. Chang, L.-W. Wu, S.-T. Tsai, and Y.-N. Sun, "A color-based approach for automated segmentation in tumor tissue classification," in *Engineering in Medicine and Biology Society, 2007. EMBS 2007. 29th Annual International Conference of the IEEE*, IEEE, 2007, pp. 6576–6579.
- [92] S. P. Zehntner, M. M. Chakravarty, R. J. Bolovan, C. Chan, and B. J. Bedell, "Synergistic tissue counterstaining and image segmentation techniques for accurate, quantitative immunohistochemistry," *Journal of Histochemistry & Cytochemistry*, vol. 56, no. 10, pp. 873–880, 2008.
- [93] S. Di Cataldo, E. Ficarra, A. Acquaviva, and E. Macii, "Automated segmentation of tissue images for computerized ihc analysis," *Comput Methods Programs Biomed*, vol. 100, no. 1, pp. 1–15, 2010.
- [94] J. E. Holley, J. Newcombe, J. L. Whatmore, and N. J. Gutowski, "Increased blood vessel density and endothelial cell proliferation in multiple sclerosis cerebral white matter," *Neuroscience letters*, vol. 470, no. 1, pp. 65–70, 2010.
- [95] M. G. Rojo, G. Bueno, and J. Slodkowska, "Review of imaging solutions for integrated quantitative immunohistochemistry in the pathology daily practice," *Folia Histochem Cytobiol*, vol. 47, no. 3, pp. 349–54, 2009.
- [96] A. Mavrou, K. Brakspear, M. Hamdollah-Zadeh, G. Damodaran, R. Babaei-Jadidi, J. Oxley, D. A. Gillatt, M. R. Lodomery, S. J. Harper, and D. O. Bates, "Serine arginine protein kinase 1 (srpk1) inhibition as a potential novel targeted therapeutic strategy in prostate cancer," *Oncogene*, vol. 34, no. 33, pp. 4311–4319, 2015.
- [97] A. A. Van der Veldt, M. Lubberink, I. Bahce, M. Walraven, M. P. de Boer, H. N. Greuter, N. H. Hendrikse, J. Eriksson, A. D. Windhorst, and P. E. Postmus, "Rapid decrease in delivery of chemotherapy to tumors after anti-vegf therapy: Implications for scheduling of anti-angiogenic drugs," *Cancer cell*, vol. 21, no. 1, pp. 82–91, 2012.

- [98] G. Lin, R. Yang, L. Banie, G. Wang, H. Ning, L.-C. Li, T. F. Lue, and C.-S. Lin, “Effects of transplantation of adipose tissue-derived stem cells on prostate tumor,” *The Prostate*, vol. 70, no. 10, pp. 1066–1073, 2010.
- [99] N. Steeghs, T. Rabelink, J. Op’t Roodt, E. Batman, F. Cluitmans, N. Weijl, E. de Koning, and H. Gelderblom, “Reversibility of capillary density after discontinuation of bevacizumab treatment,” *Annals of oncology*, vol. 21, no. 5, pp. 1100–1105, 2010.
- [100] J. M. Marieb PB Wilhelm, *Human Anatomy*, 6th ed. San Francisco: Pearson Benjamin Cummings, 2012.
- [101] J. C. Russ, *The image processing handbook*. CRC press, 2016.
- [102] V. Rankov, R. J. Locke, R. J. Edens, P. R. Barber, and B. Vojnovic, “An algorithm for image stitching and blending,” in *Biomedical Optics 2005*, International Society for Optics and Photonics, 2005, pp. 190–199.
- [103] A. Erbersdobler, H. Isbarn, K. Dix, I. Steiner, T. Schlomm, M. Mirlacher, G. Sauter, and A. Haese, “Prognostic value of microvessel density in prostate cancer: A tissue microarray study,” *World journal of urology*, vol. 28, no. 6, pp. 687–692, 2010.
- [104] A. Hoos and C. Cordon-Cardo, “Tissue microarray profiling of cancer specimens and cell lines: Opportunities and limitations,” *Laboratory investigation*, vol. 81, no. 10, pp. 1331–1338, 2001.
- [105] A. Madabhushi, “Digital pathology image analysis: Opportunities and challenges,” *Imaging in Medicine*, vol. 1, no. 1, pp. 7–10, 2009.
- [106] R. M. Haralick and L. G. Shapiro, “Image segmentation techniques,” *Computer vision, graphics, and image processing*, vol. 29, no. 1, pp. 100–132, 1985.
- [107] R. Adams and L. Bischof, “Seeded region growing,” *IEEE Transactions on Pattern Analysis and Machine Intelligence*, vol. 16, no. 6, pp. 641–647, 1994.
- [108] N. Otsu, “A threshold selection method from gray-level histogram,” *IEEE Transactions on Systems, Man and Cybernetics*, vol. 9, no. 1, pp. 62–66, 1979.
- [109] J. A. Hartigan and M. A. Wong, “Algorithm as 136: A k-means clustering algorithm,” *Journal of the Royal Statistical Society. Series C (Applied Statistics)*, vol. 28, no. 1, pp. 100–108, 1979.
- [110] L. Shafarenko, M. Petrou, and J. Kittler, “Automatic watershed segmentation of randomly textured color images,” *IEEE Transactions on Image Processing*, vol. 6, no. 11, pp. 1530–1544, 1997.

- [111] M. Kass, A. Witkin, and D. Terzopoulos, "Snakes: Active contour models," *International Journal of Computer Vision*, vol. 1, no. 4, pp. 321–331, 1988.
- [112] S. Osher and J. A. Sethian, "Fronts propagating with curvature-dependent speed: Algorithms based on hamilton-jacobi formulations," *Journal of computational physics*, vol. 79, no. 1, pp. 12–49, 1988.
- [113] P. Haub and T. Meckel, "A model based survey of colour deconvolution in diagnostic brightfield microscopy: Error estimation and spectral consideration," *Scientific reports*, vol. 5, 2015.
- [114] A. C. Ruifrok and D. A. Johnston, "Quantification of histochemical staining by color deconvolution," *Anal Quant Cytol Histol*, vol. 23, no. 4, pp. 291–9, 2001.
- [115] M. H. Bharati, J. J. Liu, and J. F. MacGregor, "Image texture analysis: Methods and comparisons," *Chemometrics and intelligent laboratory systems*, vol. 72, no. 1, pp. 57–71, 2004.
- [116] J. C. Russ and R. P. Woods, *The image processing handbook*, 1995.
- [117] S. Petushi, F. U. Garcia, M. M. Haber, C. Katsinis, and A. Tozeren, "Large-scale computations on histology images reveal grade-differentiating parameters for breast cancer," *BMC medical imaging*, vol. 6, no. 1, p. 14, 2006.
- [118] C.-h. Chen, *Handbook of pattern recognition and computer vision*. World Scientific, 2015.
- [119] I. o. Electrical and E. Engineers, *IEEE Standards Glossary of Image Processing and Pattern Recognition Terminology*. IEEE, 1990.
- [120] R. M. Haralick, "Statistical and structural approaches to texture," *Proceedings of the IEEE*, vol. 67, no. 5, pp. 786–804, 1979.
- [121] M. M. Galloway, "Texture analysis using gray level run lengths," *Computer graphics and image processing*, vol. 4, no. 2, pp. 172–179, 1975.
- [122] C. M. Bishop, *Pattern recognition and machine learning*. springer, 2006.
- [123] K. Ron and P. Foster, "Special issue on applications of machine learning and the knowledge discovery process," *Journal of Machine Learning*, vol. 30, pp. 271–274, 1998.
- [124] M. L. Bermingham, R. Pong-Wong, A. Spiliopoulou, C. Hayward, I. Rudan, H. Campbell, A. F. Wright, J. F. Wilson, F. Agakov, and P. Navarro, "Application of high-dimensional feature selection: Evaluation for genomic prediction in man," *Scientific reports*, vol. 5, 2015.

- [125] I. Guyon and A. Elisseeff, “An introduction to variable and feature selection,” *Journal of machine learning research*, vol. 3, no. Mar, pp. 1157–1182, 2003.
- [126] G.-X. Yuan, C.-H. Ho, and C.-J. Lin, “Recent advances of large-scale linear classification,” *Proceedings of the IEEE*, vol. 100, no. 9, pp. 2584–2603, 2012.
- [127] L. Breiman, “Random forests,” *Machine learning*, vol. 45, no. 1, pp. 5–32, 2001.
- [128] C. Cortes and V. Vapnik, “Support-vector networks,” *Machine learning*, vol. 20, no. 3, pp. 273–297, 1995.
- [129] I. H. Witten, E. Frank, M. A. Hall, and C. J. Pal, *Data Mining: Practical machine learning tools and techniques*. Morgan Kaufmann, 2016.
- [130] B. Steiniger, M. Bette, and H. Schwarzbach, “The open microcirculation in human spleens: A three-dimensional approach,” *The journal of histochemistry and cytochemistry : official journal of the Histochemistry Society*, vol. 59, no. 6, pp. 639–648, 2011.
- [131] J. M. Gijtenbeek, P. Wesseling, C. Maass, L. Burgers, and J. A. van der Laak, “Three-dimensional reconstruction of tumor microvasculature: Simultaneous visualization of multiple components in paraffin-embedded tissue,” *Angiogenesis*, vol. 8, no. 4, pp. 297–305, 2005.
- [132] Y. Song, D. Treanor, A. J. Bulpitt, and D. R. Magee, “3d reconstruction of multiple stained histology images,” *Journal of pathology informatics*, vol. 4, no. S7, p. 3539.109864, 2013.
- [133] M. Feuerstein, H. Heibel, J. Gardiazabal, N. Navab, and M. Groher, “Reconstruction of 3-d histology images by simultaneous deformable registration,” no. Journal Article, pp. 582–589, 2011.
- [134] M. Schwier, T. Bohler, H. K. Hahn, U. Dahmen, and O. Dirsch, “Registration of histological whole slide images guided by vessel structures,” *Journal of pathology informatics*, vol. 4, no. Suppl, S10–3539.109868. Print 2013, 2013.
- [135] J. Van der Laak, J. R. Westphal, L. J. Schalkwijk, M. M. Pahlplatz, D. Ruiter, R. De Waal, and P. De Wilde, “An improved procedure to quantify tumor vascularity using true color image analysis: Comparison with the manual hot-spot procedure in a human melanoma xenograft model,” *J Pathol*, vol. 184, pp. 136–143, 1998.
- [136] C. F. Chantrain, Y. A. DeClerck, S. Groshen, and G. McNamara, “Computerized quantification of tissue vascularization using high-resolution slide scanning of whole tumor sections,” *J Histochem Cytochem*, vol. 51, no. 2, pp. 151–8, 2003.

- [137] C. Sullivan, S. Ghosh, I. Ocal, R. Camp, D. L. Rimm, and G. Chung, "Microvessel area using automated image analysis is reproducible and is associated with prognosis in breast cancer," *Human pathology*, vol. 40, no. 2, pp. 156–165, 2009.
- [138] C. C. Reyes-Aldasoro, L. J. Williams, S. Akerman, C. Kanthou, and G. M. Tozer, "An automatic algorithm for the segmentation and morphological analysis of microvessels in immunostained histological tumour sections," *Journal of Microscopy*, vol. 242, no. 3, pp. 262–278, 2011.
- [139] M. M. Fernandez-Carrobles, I. Tadeo, G. Bueno, R. Noguera, O. Deniz, J. Salido, and M. Garcia-Rojo, "Tma vessel segmentation based on color and morphological features: Application to angiogenesis research," *Scientific World Journal*, vol. 2013, p. 263 190, 2013.
- [140] J. N. Kather, A. Marx, C. C. Reyes-Aldasoro, L. R. Schad, F. G. Zollner, and C.-A. Weis, "Continuous representation of tumor microvessel density and detection of angiogenic hotspots in histological whole-slide images," *Oncotarget*, vol. 6, no. 22, p. 19 163, 2015.
- [141] A. Cifor, L. Bai, and A. Pitiot, "Smoothness-guided 3-d reconstruction of 2-d histological images," *NeuroImage*, vol. 56, no. 1, pp. 197–211, 2011.
- [142] N. Roberts, D. Magee, Y. Song, K. Brabazon, M. Shires, D. Crellin, N. M. Orsi, R. Quirke, P. Quirke, and D. Treanor, "Toward routine use of 3d histopathology as a research tool," *The American journal of pathology*, vol. 180, no. 5, pp. 1835–1842, 2012.
- [143] X. M. Lopez, P. Barbot, Y.-R. Van Eycke, L. Verset, A.-L. Trepant, L. Larbanoix, I. Salmon, and C. Decaestecker, "Registration of whole immunohistochemical slide images: An efficient way to characterize biomarker colocalization," *Journal of the American Medical Informatics Association*, amiajnl-2014-002710, 2014.
- [144] B. Nielsen, F. Albrechtsen, and H. E. Danielsen, "Automatic segmentation of cell nuclei in feulgen-stained histological sections of prostate cancer and quantitative evaluation of segmentation results," *Cytometry.Part A : the journal of the International Society for Analytical Cytology*, vol. 81, no. 7, pp. 588–601, 2012.

Chapter 2

A method for 3D histopathology reconstruction supporting mouse microvasculature analysis

The contents of this chapter were previously published in the journal Plos One:

Xu Y, Pickering JG, Nong Z, Gibson E, Arpino JM, Yin H, Ward AD. A method for 3D histopathology reconstruction supporting mouse microvasculature analysis. Plos One. 2015 May 29; 10(5): e0126817. Permission to reproduce this article was granted by Plos One and is provided in Appendix A.

2.1 Introduction

The microvasculature constitutes the complex distal end of the vascular tree, the structure of which is vital to ensuring optimal delivery of oxygenated blood throughout the tissue. Microvascular structure is inherently 3D, as the vessels are arranged as a highly branched network that courses throughout the tissue. Understanding the microvessel network organization, and its rearrangement during pathology, could thus be critical to dissecting the basis of organ dysfunction during disease. A structural appreciation of the vessel wall components of the microvascular tree is also vital. This is particularly important for assessing arterioles and venules, vessels that are wrapped to varying extents by vascular smooth muscle cells. The smooth muscle layer of the vessel wall determines vascular tone and thus blood pressure and flow rate. Thickening of the smooth muscle layer can lead to hypertension [1] and the arrangement of the smooth muscle layers with respect to vessel density, organization, and circumferential wrapping are vital to downstream flow in capillary beds. [2]

Conventional 2D histology provides planar information on microvessels and is useful for identifying components of the vessel wall. However, 3-dimensional architectural information cannot be ascertained. Moreover, 2D assessment of the microvasculature may lead to misinterpretations, particularly in the setting of restructured microvasculature during disease, where vessel and network morphometry cannot be predicted. In contrast to large and medium-sized vessels that can be embedded and sectioned in specific directions, the orientation of arterioles and venules of the microvasculature cannot be determined from standard histologic sections. Because of this, branching, bifurcations, and tortuosity of microvessels are difficult to interpret in conventional histology sections and misleading interpretations could arise from the 2D assessment of complex 3D structures. Focal pathology (e.g. occurring at bifurcation points and subregions of the vessel wall) can be better detected in a 3D volume of reconstructed tissue. Thus, there is a need for a highly accurate 3D reconstruction [3] to visualize and measure the microvasculature architecture in normal and diseased conditions.

There are various modalities with which to image the vasculature with 3D spatial information; however, most lack the sensitivity to assess fine pathological perturbations. Traditional light microscopy imaging of histology sections provides detailed information on tissue components and structure in 2D at high resolutions, but lacks the 3D context necessary for assessing structural aspects of pathologies in the vasculature. [4] Micro-CT allows for the spatial visualization of the lumina of the vessels after injection of a contrast agent. The surrounding soft tissue components, such as the vessel walls and connective tissues, are poorly resolved using this imaging modality due to lack of soft tissue contrast and retention of the contrast agent within the lumina. Casting the vasculature provides excellent lumen detail but is limited by the fact that the casting agent does not always perfuse throughout the microvasculature, and depiction of the vessel wall and surrounding tissue components is not possible. [5] Confocal fluorescence microscopy imaging is a powerful tool but has a limited spectrum of molecules which can be visualized, according to probe availability. This modality is also limited by the field of view and depth of penetration of the probes into the tissue. [6]

3D histology reconstruction of the microvasculature has been explained in a few contexts and proven to be useful. Steiniger et al undertook a 3D histology assessment of the spleen vasculature to reveal the terminal microvessel nodules. However, the alignment procedure used was performed manually and was therefore subject to the accompanying labour and operator variability. [7] 3D confocal microscopy has been used to observe microvascular branching patterns in diabetic models, but the authors noted there was possible bias in the results due to the limited depth of field. [8] Also using 3D confocal microscopy, capillary vessels in the skeletal muscle have been evaluated for vessel tortuosity, orientation, and mean capillary length. However the authors highlighted that the problem of variable visualization of capillaries “is

even more pronounced [in thick sections], because antibodies and dyes have to travel longer distance[s] from the boundary of the sample.” They noted that new strategies in microscopy would be useful. [9] 3D reconstructions of histological tissues may also aid in the validation of high resolution 3D imaging techniques.

Accurate 3D visualization of histology could allow for obtaining features of the vessel wall, the surrounding tissue features, and the inherent spatial configuration of the vasculature. The lack of 3D spatial context in 2D histology may lead to misinterpretations of several different aspects of the vasculature, including vessel angle, vessel size, and vessel wall thickness. 3D reconstruction of 2D histology sections renders these types of measurements readily available and unambiguous. In previous work, 3D histology reconstruction has been performed using section-by-section pairwise registrations optimizing a feature or image similarity metric for adjacent section pairs, assuming that co-registration of similar structures in the 2D space of the pairwise images yields an accurate reconstruction. [10] This assumption is challenged by the fact that adjacent sections sample different tissue, and an accurate 3D reconstruction may not result in the section-to-section alignment of structures having similar appearance, such as two adjacent cross sections of a blood vessel. This notion is clear when one considers the case of a blood vessel oriented non-perpendicularly to the tissue section; in a correct 3D reconstruction, on any adjacent pair of sections, the blood vessel cross sections will not be exactly aligned in the 2D space of the histology sections to account for the non-perpendicular angular direction of the vessel in 3D. In general, 3D reconstruction techniques must be designed to avoid forcing curved or non-section-orthogonal structures to be orthogonal to the tissue sections [3], also known as the “banana-into-cylinder” problem [11], in order to preserve the original orientation of the vasculature for accurate assessment.

The objective of this work was to design, implement, and evaluate a method for 3D reconstruction of 2D histology sections of mouse tissue that is sufficiently accurate to enable interpretation of 3D arteriolar and venular networks. To address the banana-into-cylinder problem, the reconstruction method uses a section pairwise landmark-based registration, where the landmarks were homologous nuclei that were bisected by the microtome blade during sectioning. This choice of landmark type is based on the insight that cell nuclei, approximately $5\mu\text{m}$ in diameter [12], are unlikely to appear on more than two adjacent sections. We conjectured that the use of such landmarks may address the banana-into-cylinder problem due to their appearance on not more than two consecutive sections, and their lack of orientational bias. This is in contrast to, for instance, the use of vessel centerlines to define landmarks; vessels will appear on many consecutive tissue sections and their angles of orientation through multiple tissue sections are coherent and smoothly varying. In general, there is a lack of bias in the centroid to centroid vectors of bisected nuclei across adjacent slides, compared to multi-slice non-section-

orthogonal objects (such as the previously described vessels) that are smoothly varying at the scale of the section thickness. Also, nuclei are roughly spherically symmetric, so arbitrary cuts through nuclei should yield section-orthogonal centroid-to-centroid orientations. We compared the reconstruction error of the proposed nucleus-based registration to that given by more conventional intensity based registration. The registration algorithms were evaluated based on reference standard homologous nucleus features on adjacent sections to determine registration accuracy.

2.2 Materials and Methods

2.2.1 Animal model

The experiments were conducted on tissue samples of the upper one third tibialis anterior (TA) hind limb muscle from 11 wild type C57BL/J6 mice. In 5 of the 11 mice, tissue was collected two weeks after induction of hind limb ischemia by femoral artery excision; these samples were expected to contain regenerated vasculature. This particular muscle segment was selected because of the consistent development of microvessels of diverse caliber following hindlimb ischemia. The remaining 6 mice were not subjected to hind limb ischemia; these samples were expected to contain normal vasculature. There were between 9 and 14 serial sections obtained from each sample.

The mice were perfused with saline post-mortem to remove the red blood cells from the vessel lumina and then perfusion-fixed at physiological pressure with 4% paraformaldehyde. The tissues were processed and paraffin-embedded after harvesting, then cut into 7×5 mm blocks and sectioned at 5 μm . To visualize the smooth muscle distribution down to the level of the arterioles and venules, sections were immunostained with smooth muscle (SM) α -actin using the monoclonal antibody (DAKO, M0851), and bound primary antibody detected with horseradish peroxidase (HRP)-conjugated secondary antibody and 3,3'-Diaminobenzidine chromogen (DAB, Vector Laboratories, SK-4100). This marked the smooth muscle layer of the vasculature (resulting in the vessel walls being stained with a brown colour) which is shown in Figure 2.1. The tissue was then counter stained with hematoxylin, resulting in blue-stained nuclei. The stained sections were then imaged with a ScanScope CS (Aperio Technologies, Vista, CA, USA) bright field slide scanner, at 20 \times objective with the 2 \times magnification engaged, resulting in a 0.25 μm isotropic pixel size.

Ethics Statement

All experiments in this study were approved by the Animal Care and Veterinary Service Committee at The University of Western Ontario (Protocol # 2010-244) and were carried out in accordance with their requirements. Surgeries were performed under isoflurane anesthesia.

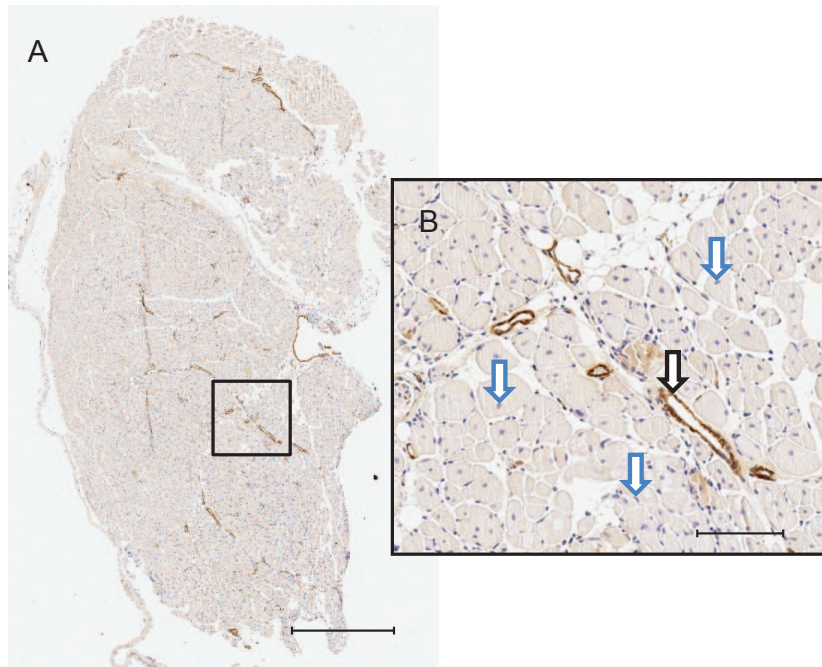


Figure 2.1: **Regenerated hind limb tissue following ischemic damage.** The tissue was immunostained with smooth muscle α -actin and DAB chromogen and counter-stained with hematoxylin. Blue arrows indicate nuclei and black arrows indicate the stained arteriole. Scale bar (A) $500 \mu\text{m}$, (B) $100\mu\text{m}$.

2.2.2 Image registration and validation approach

A high level overview of the methods is shown in Figure 2.2. All processing was performed using custom software developed in MATLAB 7.13 (The Mathworks Inc., Natick, MA, USA) except where otherwise indicated. Pairwise non-rigid affine nucleus landmark and intensity based registration was performed between serial sections of tissue in two dimensions and used to create a three dimensional volume. Two non-rigid affine registration methods were compared: high-resolution intensity-based registration using a mean squared error (MSE) image similarity metric, and the affine nucleus landmark-based registration that is the main contribution of this paper. A non-rigid affine registration involves rotation, translation, scaling and skew for non-rigid alignment of the moving image to the fixed image. The registrations were

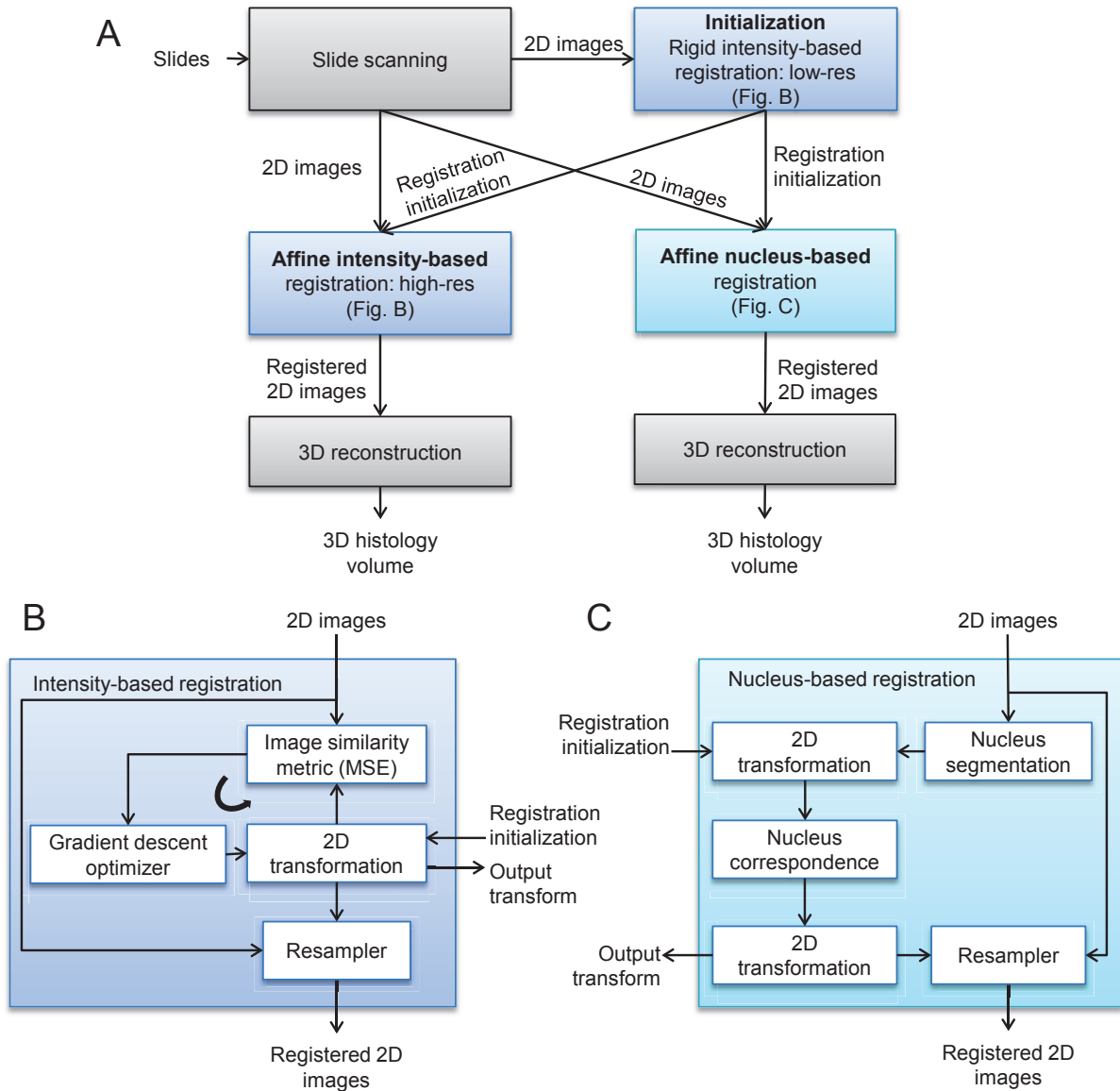


Figure 2.2: **Diagram depicting the registration methods.** The flow diagram in (A) depicts the overall experimental process, with (B) and (C) giving exploded views of the intensity-based and nucleus-based registration steps. Both approaches were initialized with a rigid, low-resolution intensity-based registration. The intensity-based registrations (B) were done using a standard iterative optimization loop. The nucleus-based registration (C) was computed non-iteratively in closed form based on automatically segmented and corresponded nucleus landmarks. Both methods were executed pairwise on each adjacent section pair, and as a final step these pairwise registrations were composed to form the final 3D reconstructed volume.

initialized with a rigid registration, which involves only rotation and translation of the moving image. MSE is the mean of the squared intensity differences between each pair of overlapping pixels in the fixed and moving comparison images. The ideal value of MSE is zero, and a

gradient descent optimizer was used to find the optimal registration yielding an MSE closest to zero. Both methods are provided with the same initialization from a coarse, intensity-based rigid registration performed on low-resolution (downsampled) images using the MSE metric. This coarse 3D reconstruction was first performed via pairwise registration of adjacent tissue sections using an intensity-based registration, on low-resolution images (with extents of 172×264 pixels) obtained by downsampling using bilinear interpolation. This coarse registration yielded an initial alignment that was provided to both tested registration algorithms. For the landmark-based registration, nucleus landmarks were automatically extracted based on size and the hematoxylin stain colour, and corresponded across adjacent sections according to similarity metric measures of the surrounding local image neighborhood. After pairwise adjacent section registration, the tissues were rendered into a 3D volume by a stacking process to visualize the histological vasculature.

2.2.3 Experimental methods

A set of homologous reference nucleus landmarks were located with the segmentation algorithm. The landmarks were manually verified for accuracy, corresponded in pairs on adjacent sections, and used to evaluate the registrations. This set of nucleus landmarks was not used in registering the images (i.e. the reference landmarks were specifically excluded in the computations described in the Section 2.5). A reference reconstruction using these reference landmarks provides a surrogate for an ideal reconstruction (Figure 2.3A) that preserves both topology and geometry. Topology preservation maintains connectedness of structures and geometry preservation maintains the original positions and orientations of structures in the reconstruction.

Our need for high-accuracy reconstructions requires that we evaluate our method against a reference standard providing precision of $< 10 \mu m$, with accuracy measured throughout all regions of the tissue. These requirements preclude the use of a 3D reference image obtained using CT or MRI as these imaging modalities do not provide the necessary resolution and/or soft tissue contrast to resolve the necessary small, homologous point landmarks to measure reconstruction error throughout the spatial extents of the volume. Micro CT of contrast-enhanced vasculature could provide sufficient landmarking precision at vessel bifurcation points, but this would spatially concentrate reconstruction error measurements around these points, precluding error measurement throughout all other tissue regions.

An ideal reference against which to evaluate our reconstructions would be a set of dense and evenly distributed landmarks, localizable with the necessary precision and accuracy. As it would be impractical to introduce a set of extrinsic landmarks meeting these criteria, we turn to a close intrinsic surrogate: the small, highly localizable cell nuclei distributed throughout

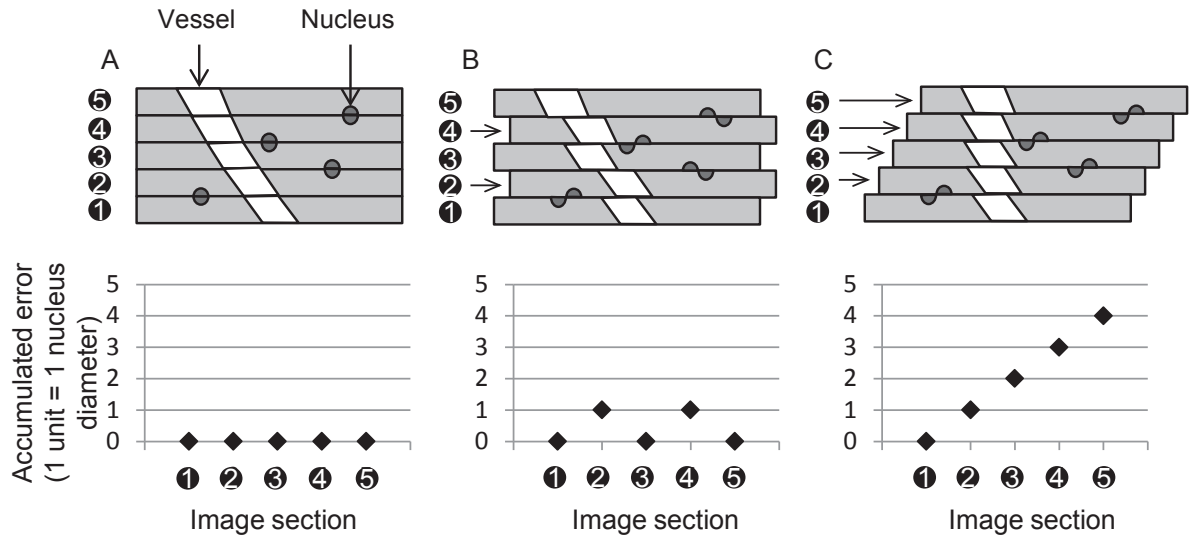


Figure 2.3: **Comparison of the alignment of bisected nuclei when measuring the accumulated registration error.** (A) The ideal error-free reference reconstruction, with bisected nuclei aligned with minimum residual error (a pairwise target registration error between corresponding halves of bisected nuclei of zero is depicted). (B) A reconstruction aligning nuclei with spatially unbiased error; but vessel connectedness (topology) and angle (geometry) are mostly conserved. (C) A reconstruction optimizing pairwise alignment of salient structures (the vessel cross sections in this example) preserves vessel topology but not geometry. Note that the pairwise target registration errors in (B) and (C) are similar, despite the lack of geometry preservation in C. The accumulated target registration error does capture the difference between (B) and (C); the plots in the bottom row indicate increasing accumulated error through the stack of sections.

the tissue. Specifically, we manually localized the subset of nuclei that were bisected by the microtome blade; these nuclei appear on homologous points on adjacent tissue sections. By aligning these bisected nuclei on adjacent sections throughout the volume, we re-established the spatial tissue homology that was broken during the tissue cutting process, yielding a reference 3D reconstruction that depicts the geometric and topological configuration of the tissue before it was cut.

It is important to note that although the method for constructing the reference reconstruction and the method for performing automatic reconstruction are both based on nuclei, there are two important differences that justify the use of this validation approach. First, as is typical in landmark-based registration evaluation, the landmarks used for the reference reconstruction are not used by the registration algorithm. Thus, the algorithm is validated using a completely different set of landmarks than those used to perform the reconstruction. Second, the landmarks used for the reference reconstruction were all manually verified by an operator for truth of

correspondence and localisation, whereas for the reconstruction process, the landmarks were fully automatically identified and not checked by an operator.

2.2.4 Intensity-based registration

The histology images were obtained from the Scanscope CS slide scanner with isotropic $0.25 \mu\text{m}$ pixels and had extents of 17135×26398 pixels. To support faster processing for the intensity-based registration only, these images were downsampled to obtain images with isotropic $4 \mu\text{m}$ pixels using bilinear interpolation, resulting in an image size of 1071×1650 pixels. These downsampled images were then converted into greyscale images by averaging of the RGB colour channels.

Figure 2.2B describes the intensity-based registration algorithm we tested. The images were registered using custom C++ software built on the Insight Segmentation and Registration Toolkit Version 4.4.1 (ITK) [13]¹². In the interests of computational efficiency, we used the MSE image similarity metric because this is a mono-modality image registration problem and tissue staining is anticipated to be consistent within a set of serial sections. The space of 2D rigid transformations was searched to minimize MSE using a regular step gradient descent optimizer initialized with zero rotation and translation. Non-rigid affine registration was applied after the rigid intensity based registration with the optimizer initialized using the rigid registration parameters. After optimization, MATLAB's `imtransform` function was used to apply the resulting set of 2D affine spatial transformations. This mapped the full resolution RGB histology image of each section to that of its adjacent section, yielding a 3D reconstruction from the intensity-based registration.

2.2.5 Nucleus feature extraction, correspondence, and registration

Figure 2.2C describes our nucleus landmark-based registration algorithm. Cell nuclei were automatically extracted from the images based on combined criteria of colour and size. To determine the colour and size criteria to be used for nucleus extraction, we used a separate set of mouse hind limb tissues that were not used for the experiments reported in this chapter.

¹For the low-resolution registration used as initialization, the `itk::RegularStepGradientDescentOptimizer` optimizer was tuned for scale differences in transformation parameters using its `SetScales()` function; scales were set to be 10^2 and 10^{-2} for the rotational and the translational components of the transformation, respectively. The maximum (i.e. initial) and minimum (i.e. defining convergence criterion) step sizes were set to 4 and 0.1, respectively, using the optimizer's `SetMaximumStepLength()` and `SetMinimumStepLength()` functions. For the high resolution registration, these parameters were adjusted to 0.01 and 0.001, respectively, to refine convergence to the local optimum found by the low-resolution registration.

²Parameters were chosen on experimentation with a sample not included in this study and not tuned for the samples in the study.

On this separate set of tissues, we manually delineated nuclei which were counter stained with hematoxylin with varying degrees of staining (Figure 2.4). Based on these manual delineations, a threshold value of $< 80\%$ in the green channel of the red-green-blue (RGB) colour space and an area range of $6 \mu\text{m}^2 - 160 \mu\text{m}^2$ were determined as the criteria for defining nuclei.² Both the colour and area criteria needed to be met for detection of each nucleus; samples of extracted nucleus points are shown in Figure 2.5A. Debris can occur in the blank/white space of the microscope slide surrounding the tissue and can have similar colour and size criteria as nuclei. This debris was automatically excluded as nuclei by determining whether the surrounding area had similar appearance to the measured slide background. The surrounding area is defined by a $5 \mu\text{m}$ disk-shaped morphological dilation² seen in Figure 2.5B. The area was compared to a mean green channel of $> 95\%$, standard deviation of $< 4\%$, which were chosen according to the typical appearance of the clear glass slide regions.² The centroids of the extracted nuclei were used as the nucleus landmarks for registration.

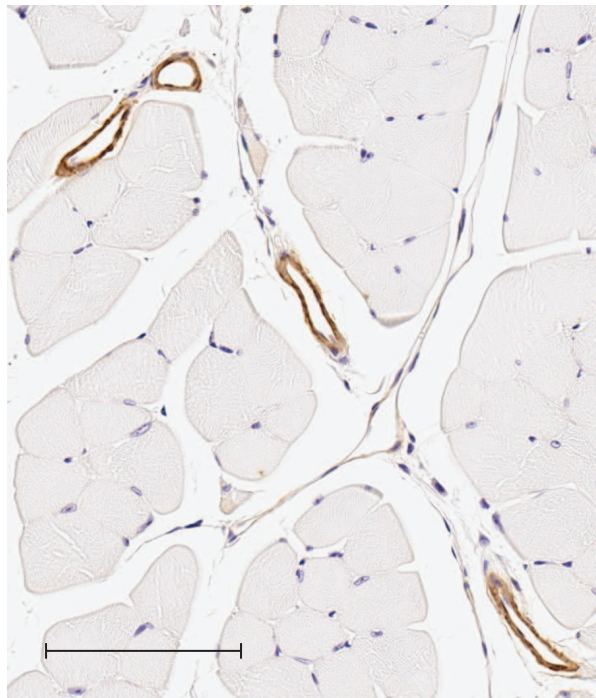


Figure 2.4: Separate set of mouse hind limb tissues that were not used for the experiments reported in this chapter. These tissues were used to determine nucleus size and colour for nucleus extraction. Scale bar $100 \mu\text{m}$.

Next, we estimated a correspondence between bisected homologous nuclei appearing on adjacent sections, in order to define an affine transformation registering each pair. Our approach to correspondence establishment is inspired by block matching-based image registration [14], and is based on the conjecture that for a given nucleus on a section, if a homologous

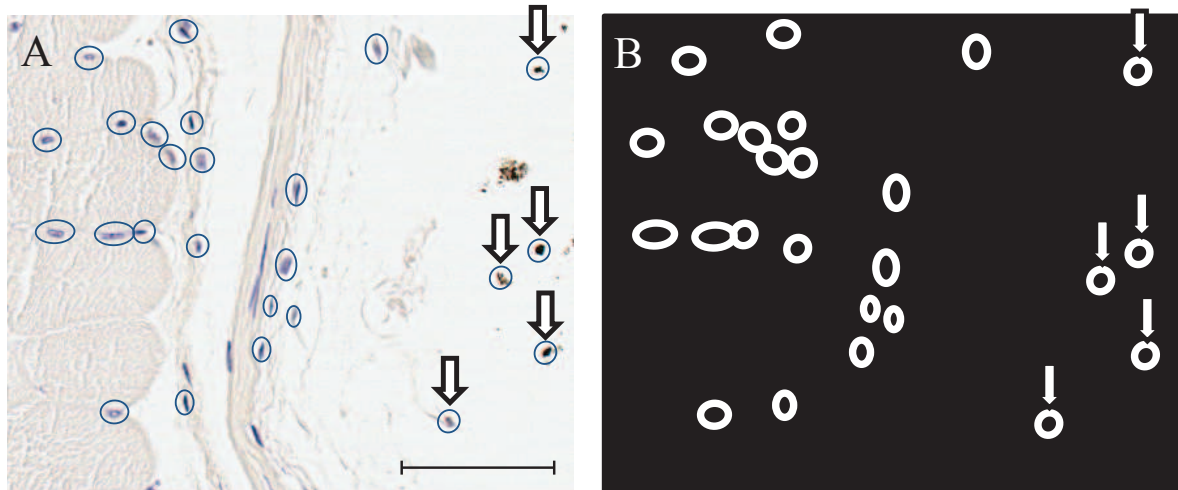


Figure 2.5: **Nucleus segmentation method.** (A) The segmented nucleus labeled blue on the histology section stained with DAB and hematoxylin counter stain. (B) The surrounding region (white) of each nucleus was defined by morphological dilation and used to evaluate whether the extracted nucleus was within the tissue, or was instead a false positive corresponding to debris on a white background outside of the tissue, indicated with the white arrows. Scale bar $50 \mu m$.

nucleus exists within a local neighbourhood on a neighbouring section, it will be surrounded by tissue having similar appearance. All of the tunable parameters in our method were chosen based on experimentation with a sample not used in the study. Our approach to estimating correspondence for each detected nucleus involves defining a set of candidate nuclei within a defined local neighbourhood on the adjacent section. An image similarity metric is then evaluated within a local region surrounding each candidate to find the candidate with the most similar surrounding tissue. A square local region was used to compare the neighbourhoods of candidate nucleus landmark correspondences (Figure 2.6). The green channel of the square image was used and the window/level was adjusted (by software, without human interaction) to the window of 14 and level of 235 to enhance tissue-background contrast.² The neighbourhood image $I(p)$ has a side length² of $250 \mu m$ and surrounds each nucleus \mathbf{p} on section I . We calculated the mean-squared error (MSE in the equation below) image similarity metric between $I(p)$ and the local image neighbourhoods $J(q)$ surrounding all candidate nuclei \mathbf{q} (within $T = 100 \mu m$ of p)² on adjacent section J . We corresponded each nucleus \mathbf{p} on each section to the best matching nucleus \mathbf{p}' on the adjacent section, with the best match defined as the one having the smallest MSE as defined above. Precisely,

$$\mathbf{p}' = \arg \min_{\mathbf{q} \in \{\mathbf{x}_j^i, \forall i | D(\mathbf{p}, \mathbf{x}_j^i) < T\}} MSE(I(\mathbf{p}), J(\mathbf{q})) \quad (2.1)$$

where \mathbf{x}_{ij} is defined to be the i^{th} nucleus on image J and D is defined to be the 2D Euclidean distance function. For each adjacent section pair, we defined a rigid transformation minimizing the residual error between the corresponding nuclei (i.e. the established $\mathbf{p} \rightarrow \mathbf{p}'$ correspondences) having the best (smallest) 100 MSE values² found for that section pair. We retain only the best correspondences to define the registration since there will undoubtedly be many nuclei that do not have a homologous nucleus on the adjacent section, since not all nuclei are bisected by the microtome blade. The composition of these transformations, both rigid and affine, for each section pair yielded the 3D nucleus landmark reconstruction.

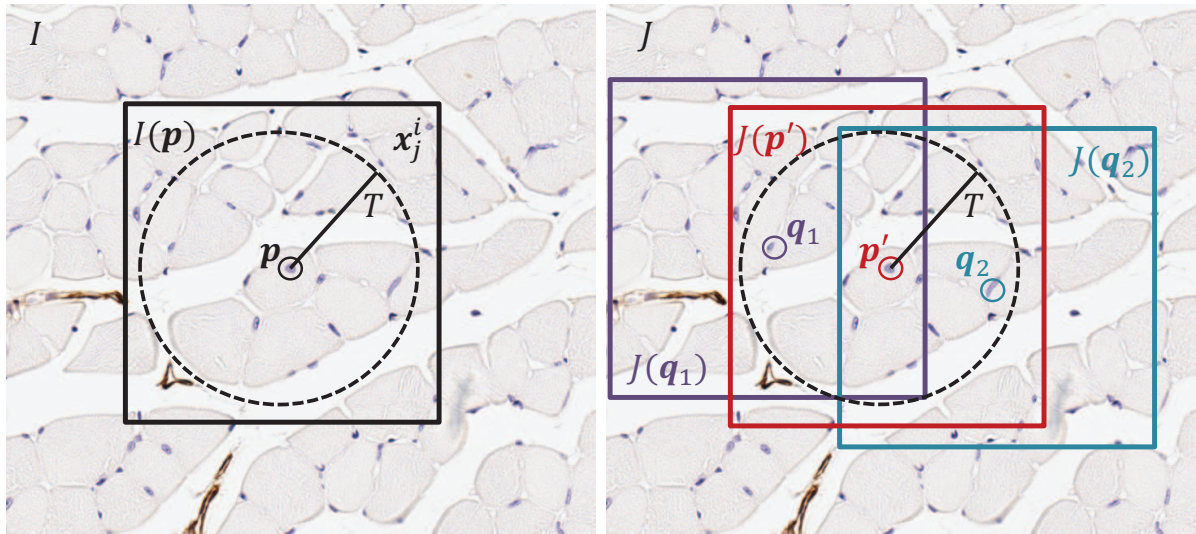


Figure 2.6: **Nucleus correspondence method.** (An illustration depicting the approach to establishing correspondence of nucleus p in section I with its best matching nucleus in adjacent section J . In this example, the candidate nuclei on section J are p' , q_1 , and q_2 , lying within a dashed circle of radius T centred on p (only 3 of the 18 candidate nuclei within the circle are illustrated here for simplicity). The candidate nucleus with the most similar surrounding tissue appearance is selected to correspond to p . Surrounding tissue appearance similarity is measured using the MSE image similarity metric, comparing the local square region $I(p)$ centered on p with the local square regions $J(p')$, $J(q_1)$, and $J(q_2)$ centered on the candidates p' , q_1 , and q_2 . In this example, since $MSE(I(p), J(p')) < MSE(I(p), J(q_1))$ and $MSE(I(p), J(p')) < MSE(I(p), J(q_2))$, p is corresponded with p' .

Evaluation of registration accuracy

The registration accuracy was measured in terms of topology (i.e. preservation of structural connectivity) and geometry (i.e. preservation of distances and angles between structures). Accuracy was measured based on reference reconstructions of the tissues. For each sample, the reference reconstruction was determined by reference nucleus landmarks, which formed a separate set of corresponded nuclei not used to define the automated registration. To ensure the correctness of the reference reconstructions, every reference landmark correspondence was verified manually and any incorrect correspondences were discarded. We measured the pairwise registration error as the post-registration misalignment of reference nuclei on each section with the homologous corresponding reference nuclei on the next adjacent section. Thus, the pairwise registration error for a single nucleus is measured within the 2D spatial context of a section on which it appears. We also measured the accumulated registration error as the difference between the position of a reference nucleus given by a registration algorithm and its position within the reference registration. Thus, the accumulated registration error for a single nucleus is measured within the 3D spatial context of the reference reconstruction. This captures accumulation of error propagated through the series of pairwise section registrations. The pairwise error characterizes the performance of the reconstruction algorithm for each pairwise registration of adjacent sections independently. However, the accumulated error provides information about spatial bias in the pairwise error that may result in a reconstruction that is more erroneous than the pairwise error would suggest. This scenario is depicted in Figure 2.3. Although the scenarios depicted in Figures 2.3B and 2.3C have the same pairwise registration error and both preserve topology, the reconstruction Figure in 2.3B better preserves geometry and this is reflected in a lower accumulated registration error. Errors measured in these two spatial contexts are thus complementary, with the pairwise registration error capturing errors in topology of the reconstructed vasculature, and accumulated registration error capturing geometric errors.

Within the different spatial contexts described above, we measured two different types of registration error: the target registration error (TRE) and fiducial registration error (FRE). The “targets” and “fiducials” refer to reference points. Both the TRE and FRE are measured as the post-registration Euclidean distance between homologous fiducial pairs. Since, in an ideal registration, these homologous fiducial pairs should be perfectly aligned, the ideal value of TRE and FRE is zero. The difference between the FRE and TRE is in the choice of fiducials used. To calculate the FRE, the same nucleus landmarks that were used to define the registration are used to calculate the error. To calculate the TRE, the nucleus landmarks that were used to define the registration are not used to calculate the error; the separate set of reference landmarks, to which the algorithm is blinded, are used instead. Thus, the FRE provides sense of

the best-case performance of the algorithm since the algorithm optimized the alignment of the same landmarks used to calculate the error, and the TRE provides a more realistic measure of performance. We evaluated the intensity-based and nucleus-based reconstructions separately by calculating the pairwise and accumulated TREs for each algorithm on each of both normal and regenerated mouse tissues. To determine the appropriate statistical tests for comparing the TREs generated by the different approaches, Kolmogorov-Smirnov normality tests were performed on the TRE distributions. We tested the null hypothesis that the median pairwise TRE of the intensity-based registration was the same as the median pairwise TRE of the nucleus-based registration using the non-parametric Wilcoxon sign rank test. A similar null hypothesis for the accumulated TRE was also tested.

We undertook several steps to give context to our measured registration errors. As a best-case estimate of fidelity of the reference reconstruction to a hypothetical ideal reconstruction, we measured the pairwise FRE of the reference reconstruction based on manually validated nucleus landmark correspondences. This measure reflects the amount of tissue distortion that was not compensated by our affine transformation model, which gives a sense of the discrepancy between the reference reconstruction and an ideal reconstruction. To provide context for interpretation of the pairwise TREs from the tested algorithms, we also measured the pairwise TRE using the reference nuclei using leave-one-out cross validation (LOOCV). Using this technique, one of the reference landmark pairs is removed (“left out”) and the registration is defined based on the remaining pairs. The registration error for the removed pair is calculated. This is performed N times for each of the N reference fiducial pairs, yielding N distinct TRE measurements which are averaged. Since the algorithm is only blinded to one reference landmark pair at a time, the pairwise TRE measured by LOOCV over the reference nuclei provides an optimistic measure of registration performance against which to compare the TRE calculated when the algorithm is blinded to all of the reference nuclei.

Evaluation of image similarity metrics

Any observed differences in error values observed between the intensity-based and nucleus-based reconstructions could be attributed to two main sources. The first is that the transformation yielding the MSE similarity metric optimum may not be coincident with the nucleus landmark-based transformation as defined by

$$T_{MSE} = \arg \min_T MSE(I, J) \quad (2.2)$$

where I and J are images of adjacent sections. The second is that the intensity-based registration optimizer could fail to converge to the desired optimum. If the optimum is not

coincident with the landmark-based transformation, one could assert that the reconstructions given by the nucleus landmark-based approach would be different from those given by the intensity-based approach. This would be the case even with the use of a hypothetical ideal optimizer. If the intensity-based registration did not converge to the optimum, one could assert that the intensity-based approach using the MSE metric could perform equally as well as the nucleus landmark-based approach, given improvements to optimization. To gain insight into the reasons behind any such observed differences in error, we calculated the MSE image similarity metric in the spatial neighbourhood of the transformations yielded by the nucleus-based reconstruction. This exploration could determine that the MSE optimum and nucleus landmark optimum are not coincident (i.e. if there exists a transformation with a lower MSE value than that given by the nucleus landmark transformation); in this case, a hypothetical ideal optimizer would not yield a reconstruction based on the MSE metric that would be equivalent to the nucleus-based reconstruction.

In this experiment, we explored the space of translations along the x and y directions separately, within ranges of $20 \mu m$ from the nucleus-based optimum, in increments of $0.5 \mu m$. This experiment was performed on full resolution serial section images. For each of the x and y directions we found the optimal translation yielding the lowest MSE and recorded this value as a displacement from the nucleus landmark registration (i.e. a displacement of $0 \mu m$ reflects an MSE optimum coincident with a nucleus landmark registration optimum). We calculated the 95% prediction intervals of these displacements and recorded the upper bounds of these intervals to obtain an estimate of the expected translational offset between the nucleus based registrations and the registrations one could obtain via optimization of the MSE image similarity metric within the local neighbourhood of the nucleus based registration. Under some assumptions (discussed in the penultimate paragraph of this paper), this allows a comparison between the nucleus-based reconstructions and reconstructions that could be achieved without the need for explicit localization and correspondence of nucleus landmarks (e.g. using robust optimization of MSE in a multi-resolution framework).

2.3 Results

2.3.1 Vessel reconstruction properties

Images of the 3D reconstructed volumes were rendered using 3D Slicer 4.1.1 (Harvard SPL, Boston, MA, USA), with a voxel size of $0.25 \mu m \times 0.25 \mu m \times 5 \mu m$. [15] Regions of interest from whole-slide reconstructions of both normal and regenerated vasculature are shown in Figure 2.7, with selected corresponding 2D histological sections; both nucleus landmark-based

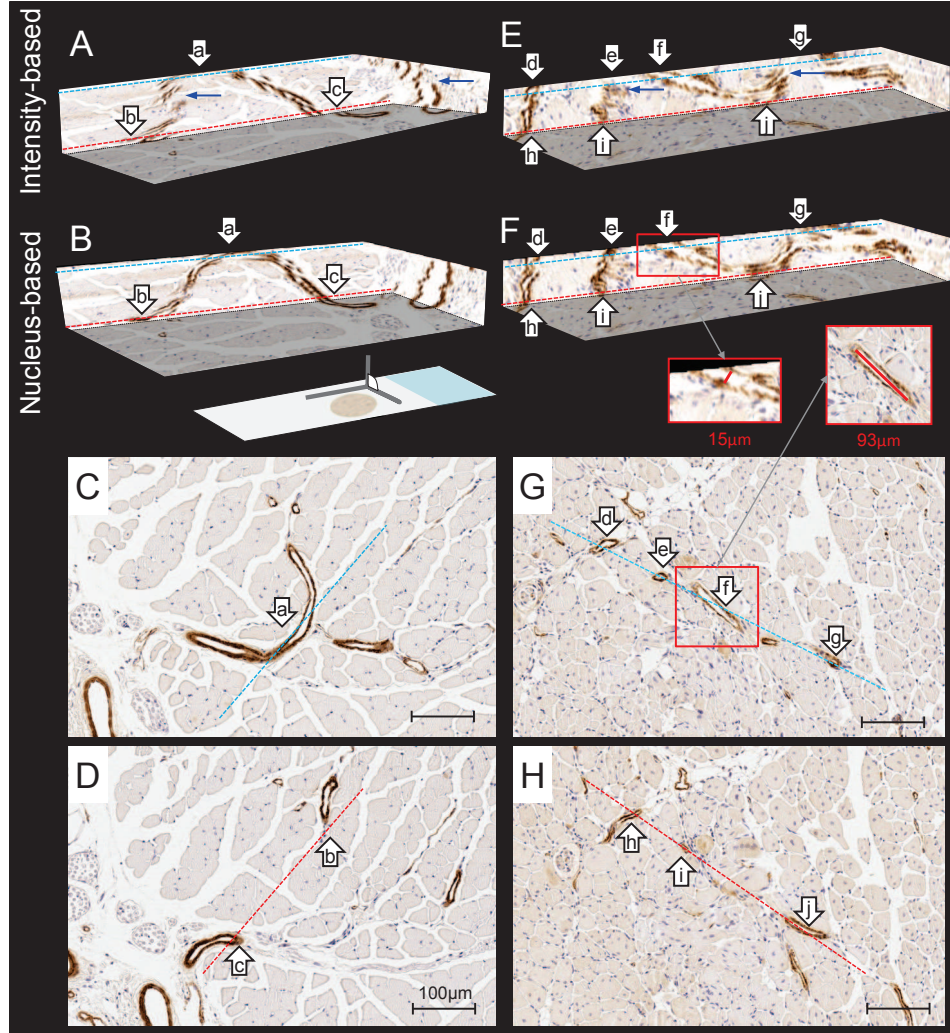


Figure 2.7: **3D and 2D histology comparisons.** 2D histology sections (pixel size $0.25 \mu\text{m} \times 0.25 \mu\text{m}$) and corresponding 3D reconstruction (voxel size of $0.25 \mu\text{m} \times 0.25 \mu\text{m} \times 5 \mu\text{m}$) of serial histology sections of a normal (A-D) and regenerated mouse (E-H) TA post-femoral artery excision, immunostained for smooth muscle alpha-actin. A and E are registered using affine intensity based registration. B and F are registered using affine nucleus based registration. Within each column, the dashed lines indicate correspondence (according to colour) between parts of the 2D sections and their locations on the 3D views. Also within each column, the lower case letter labels indicate correspondence between vessel cross sections on the 2D sections and their homologous locations within the 3D views. Blue arrows indicate incorrect vessel wall discontinuities arising from reconstruction error. The insets in the red boxes show 2D and 3D diameter measurements of the same vessel; note that the 2D measurement overestimates the 3D measurement by a factor of > 6 . Scale bars $100 \mu\text{m}$.

and intensity-based reconstructions are shown. In Figure 2.7C, a distinct vessel cross section is visible on one histology section, labeled as a. Figure 2.7D depicts another section taken $60 \mu\text{m}$ deeper into the tissue, showing two vessel cross sections, labeled as b and c. If only

2D histology images were available, one might conclude that these three vessel cross sections correspond to multiple distinct vessels. However, the 3D reconstruction shown in Figure 2.7B reveals that a, b, and c are in fact all connected within the same vessel. Figures 2.7G and H depict two sections taken $50 \mu\text{m}$ apart, with seven vessel cross sections indicated with labels d through j. Based on inspection of only these 2D sections, one might conclude that there were four distinct vessels represented: one vessel d appearing on only one section, and three more vessels connecting e to h, f to i, and g to j, respectively. However, the 3D reconstruction of this tissue shown in Figure 2.7F reveals that in fact the connectivity is d to h, e to i, and an undulating vessel connecting f, j, and g. Thus, both the number of distinct vessels and their connectivity would be incorrectly estimated based on 2D sections alone. Additionally, the undulation creates the appearance of incorrectly large vessel lumina in 2D, which is demonstrated particularly for cross sections labeled f and j, arising from the fact that the plane of sectioning runs nearly parallel to the direction of the vessel in these areas. We compared spatially corresponding 2D and 3D manual diameter measurements of a total of 40 randomly chosen vessels from all 11 mouse samples. This yielded 40 paired differences (2D diameter - 3D diameter), the median \pm interquartile range of which was $21.09 \pm 27.95 \mu\text{m}$. We also calculated the 2D diameter / 3D diameter ratio for each of the 40 vessels and found a median \pm interquartile range of 1.6 ± 1.2 . For each of the 40 vessels, the 2D diameter was larger than the 3D diameter.

Registration technique comparisons

We observed qualitative differences between the different reconstruction approaches, with a smoother reconstruction in the nucleus landmark registration. Volumes depicting 3D reconstructions of normal and regenerated vasculature are shown in Figure 2.7. The intensity based reconstruction was generally observed to preserve vessel topology/connectedness for larger vessels but more geometric disruptions were qualitatively observed, compared to the nucleus-based reconstructions as seen in Figure 2.7A and 2.7E (intensity-based reconstruction), compared to Figure 2.7B and 2.7F (nucleus-based reconstruction), respectively.

2.3.2 Evaluation of registration accuracy

In all of our experiments, the TRE values were found to be non-normally distributed ($p < .01$), therefore non-parametric testing (Wilcoxon sign rank test) of null hypotheses of equivalent medians was performed, and descriptive statistics were reported as the median \pm interquartile range (IQR). For reference in terms of the best possible performance using non-rigid affine registration, the measured pairwise FRE and the TRE of the reference reconstruction are shown in Table 2.1.

Table 2.1: Pairwise affine registration errors (μm) of the reference nucleus landmarks

	Normal	Median \pm IQR	CI 95%
FRE		3.42 \pm 4.44	[3.32,3.52]
TRE		3.54 \pm 4.63	[3.42,3.63]
Regenerated			
FRE		2.49 \pm 4.44	[2.43,2.57]
TRE		2.57 \pm 4.63	[2.50,2.65]

Table 2.2 shows both the pairwise and accumulated TRE values for normal and regenerated samples, with 95% confidence intervals on the medians. Intensity-based registration at low resolution was also reported, which was used to initialize the subsequent high-resolution intensity- and nucleus landmark-based registrations.

Table 2.2: Pairwise and accumulated target registration error (TRE) values (μm) of the rigid and affine intensity-based and nucleus-based landmark registration (best in boldface)

		Rigid Registration		Affine Registration	
		Normal	Regenerated	Normal	Regenerated
Pairwise TRE (μm)					
Intensity-based (low-res)	Median \pm IQR	12.90 \pm 13.85	10.31 \pm 13.03		
	CI	[12.6,13.3]	[10.1,10.6]		
Intensity-based (high-res)	Median \pm IQR	9.07 \pm 14.96	6.70 \pm 7.39	7.70 \pm 12.41	4.73 \pm 6.33
	CI	[8.81,9.34]	[6.53,6.89]	[7.43,7.99]	[4.61,4.87]
Nucleus based	Median \pm IQR	6.54 \pm 8.02	5.93 \pm 7.68	4.97 \pm 5.75	4.54 \pm 6.67
	CI	[6.36,6.76]	[5.74,6.07]	[4.87,5.12]	[4.41,4.68]
Accumulated TRE (μm)					
Intensity-based (low-res)	Median \pm IQR	34.43 \pm 42.49	31.58 \pm 32.70		
	CI	[33.4,35.6]	[30.8,32.4]		
Intensity-based (high-res)	Median \pm IQR	33.70 \pm 40.48	17.95 \pm 23.71	22.49 \pm 38.59	13.62 \pm 20.19
	CI	[32.8,34.7]	[17.3,18.5]	[21.7,23.2]	[13.1,14.1]
Nucleus based	Median \pm IQR	12.67 \pm 15.84	12.42 \pm 12.91	9.78 \pm 17.09	9.81 \pm 15.71
	CI	[12.3,13.1]	[12.0,12.7]	[9.4,10.2]	[9.4,10.1]

Table 2.2 also shows the pairwise and accumulated TRE values for these subsequent rigid and non-rigid affine registrations for both high resolution intensity based registration and nucleus landmark registration. The intensity based registrations were performed on grayscale images; no significant differences were found between these reported error values and those measured when the registration was performed on the red, green or blue channels separately. Since the TRE values were found to be non-normally distributed, these confidence intervals

were computed non-parametrically as $[L, U]$, with lower bound L and upper bound U defined as the TRE values having ranks of $n/2 - 1.96 / 2$ and $n/2 + 1.96 / 2$, respectively, in the sorted list of TREs. [16] There was a statistically significant difference in the median pairwise TRE values between the intensity-based and the nucleus-based registrations for normal and regenerated mouse tissues ($p < .001$). The medians of the accumulated TRE were also statistically significantly different between the intensity-based and the nucleus-based registrations for both normal and regenerated tissues ($p < .001$). For both normal and regenerated tissues, we also calculated the maximum post-registration distance between any pair of homologous nucleus landmarks used for the TRE calculation. Table 2.3 reports the mean and standard deviation of these maximum differences.

Table 2.3: Mean and SD of maximum pairwise and accumulated target registration error (TRE), observed on each section for the rigid and affine intensity-based and nucleus-based landmark registration (best results in boldface)

	Pairwise (Mean \pm SD)		Accumulated (Mean \pm SD)	
	Normal	Regenerated	Normal	Regenerated
Rigid Registration TRE (μm)				
Intensity-based (low-res)	49.02 \pm 32.19	31.73 \pm 17.65		
Intensity-based (high-res)	47.47 \pm 38.51	26.96 \pm 19.26	46.47 \pm 35.40	24.06 \pm 15.34
Nucleus based	38.89 \pm 30.68	24.32 \pm 15.43	35.87 \pm 32.06	24.49 \pm 21.67
Affine Registration TRE (μm)				
Intensity-based (low-res)	90.22 \pm 52.86	66.22 \pm 38.74		
Intensity-based (high-res)	90.87 \pm 79.05	37.14 \pm 22.20	78.63 \pm 65.44	41.78 \pm 25.31
Nucleus based	43.06 \pm 34.71	28.47 \pm 12.80	30.05 \pm 23.52	39.41 \pm 48.03

Box plots of the distributions of the TRE values are shown in Figure 2.8 for the high resolution affine intensity based registration and the affine nucleus landmark based registration. These plots provide a more detailed view of the error measurements, and showing the distributions of pairwise and accumulated TRE values at every section in the reconstruction. For the pairwise TRE, Figure 2.8 shows the TRE distributions for each section pair, where the number on the horizontal axis indicates the larger of the two section numbers in the pair (e.g. at horizontal axis point 2, the pairwise TRE distribution for sections 1 and 2 is shown). For the accumulated TRE, Figure 2.8 shows the TRE distributions for each section number as indicated on the horizontal axis. For the pairwise TRE, the horizontal axis value of one clearly has no

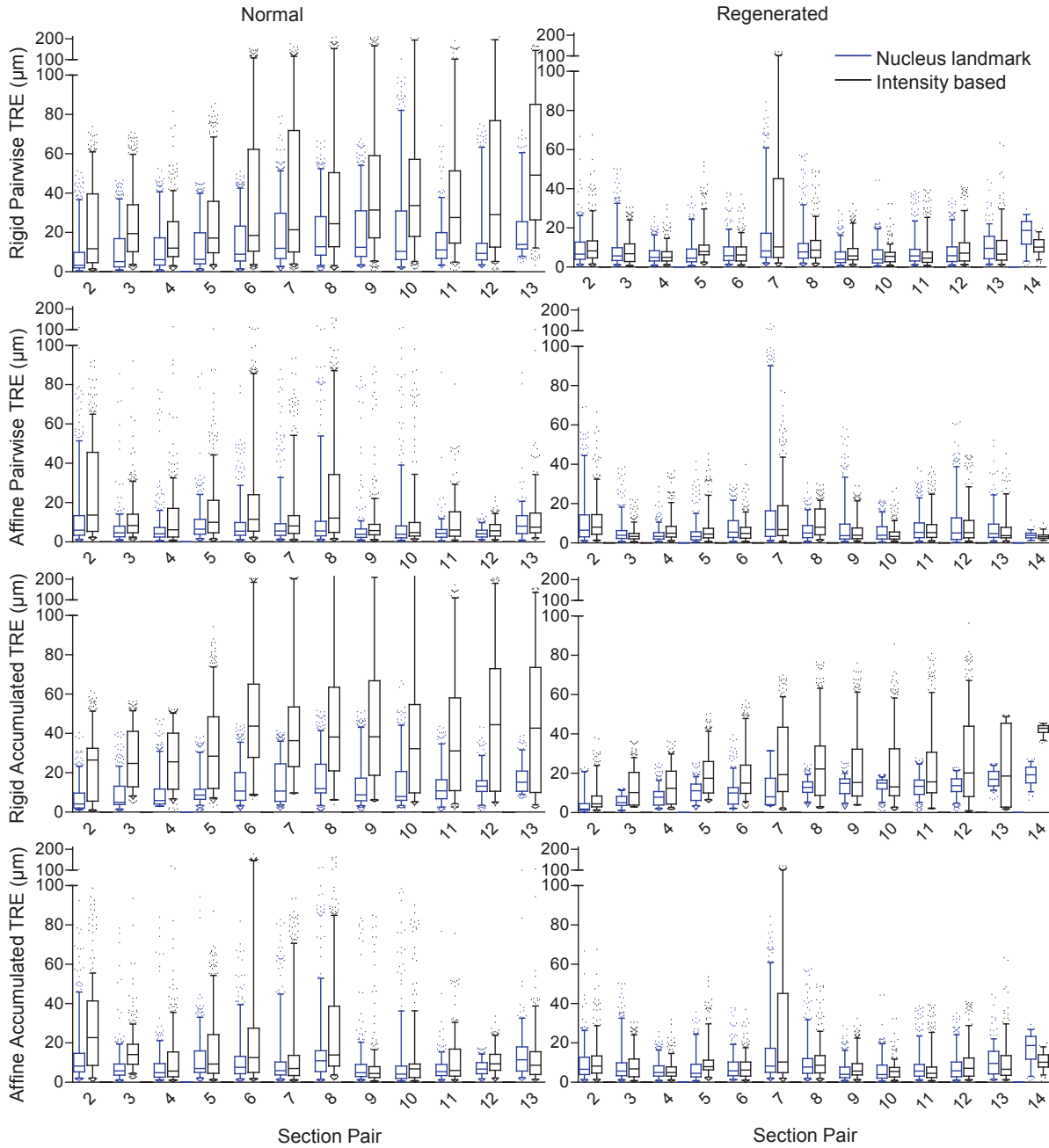


Figure 2.8: **Registration accuracy measurement values.** Box plots of the rigid and affine target registration error (TRE) computed for each adjacent pair of sections (pairwise) and propagated throughout the 3D reconstruction (accumulated).

defined TRE distribution, and for the accumulated TRE at this point on the horizontal axis all TREs are zero (since section 1 is an untransformed reference section forming the basis of the reconstruction). It is for this reason that the horizontal axes begin at section 2 in Figure 2.8. For the rigid transformation model, we observed a more pronounced trend toward increasing

accumulated TRE values with increasing section number for the intensity-based reconstruction, as compared with the nucleus-based reconstruction. For most sections, concordant with the observations in Tables 2.2 and 2.3, we observed larger error magnitude and variability using intensity-based registration. Overall, the affine transformation model outperformed the rigid transformational model and suffered fewer effects of accumulation of error.

2.3.3 Evaluation of image similarity metrics

Table 2.4 shows the medians and interquartile ranges of the displacements described in the experimental methods along the x and y directions for normal and regenerated samples, and for all samples in aggregate. The upper bounds of the associated prediction intervals are also shown. As these samples were found to be non-normally distributed, a non-parametric approach to calculating the prediction interval was used, where the maximum TRE value observed in the sample defined the upper bound of the $P\%$ prediction interval, where $P = (N - 1)/(N + 1)$. [17] For all the samples in aggregate, an upper bound of not more than $10\ \mu m$ was observed in the 98% prediction interval, suggesting that with robust optimization of the MSE image similarity metric on full resolution images, the resulting pairwise registrations are unlikely to be displaced more than $10\ \mu m$ from those given by the nucleus-based registration.

Table 2.4: The displacement of the optimal mean squared error transformation from the affine nucleus-based registration

Sample	Displacement direction (μm)	Median IQR	Upper bound of non-parametric $P\%$ prediction interval (μm)	P (%)
Normal	X	1.50 ± 2.25	9.58	97
	Y	1.00 ± 1.50	5.37	97
Regenerated	X	1.50 ± 2.00	6.5	97
	Y	1.50 ± 2.00	8.87	97
All Values	X	1.50 ± 2.38	10	98
	Y	1.50 ± 1.50	8.52	98

2.4 Discussion

Vascular abnormalities perturb organ perfusion and could lead to damage and tissue dysfunction. The microvasculature which underlies tissue perfusion is inherently 3D and aspects of the vascular pathology may be unaccounted for when assessing the vessels in conventional 2D histology. Visualizations in 3D could remove potential ambiguities in the interpretation of the

histological samples. This is demonstrated by our results in Figure 2.7, where several different types of misinterpretations may potentially occur. The density of vessels in one region could be misinterpreted and the branching or structural detail at the bifurcation point is lost. The reconstructed normal tissue in (B) demonstrates the connectivity of the vessels shown in the cross sections (C) and (D). Without the 3D image, the interpretation of the connectivity of microvasculature can be challenging. Cross sections $50\ \mu\text{m}$ apart in Figure 2.7G and H demonstrate regenerated vessels, portions of which (indicated by f and i) run nearly parallel to the section plane. In this example, the vessels could be misinterpreted to have larger lumina and have a higher vessel count in plane due to multiple views in cross section of one vessel. For example, the vessel labeled f in Figure 2.7G is connected to the vessel labeled g on the same figure due to the tortuosity of the vessel. When quantifying vessel features within 2D sections, this tortuosity could lead to an erroneously high vessel density count. In the corresponding reconstruction (F), connectivity, tortuosity and thickness of the vessel are visualized. Errors in 2D measurement of vessel diameter arising from non-orthogonality of vessels to sections can be resolved in a 3D reconstruction. This is demonstrated with an example in Figure 2.7, where the measured lumen diameter in 2D is $93\ \mu\text{m}$ due to the vessel running nearly parallel to the section plane. In the 3D reconstruction, we are able to measure the diameter of the vessel in a direction perpendicular to the vessel's 3D centerline, yielding a lumen diameter of $15\ \mu\text{m}$. Our experiment comparing 2D and 3D measurements on 40 different vessels revealed that 2D measurements are biased to overestimate vessel diameter, with overestimations of 50% or more occurring frequently. These observations are clear in the 3D reconstruction but nearly impossible to make with only the ambiguous 2D histology.

Previous work on 3D imaging of vessel wall components has been performed using phase-contrast computed tomography (CT) imaging in order to differentiate the soft tissue layers of the human carotid artery and potentially characterize arterial plaque. [18] The authors showed that several layers of formalin-fixed carotid artery could be differentiated using a conventional X-ray tube with $100\ \mu\text{m}$ resolution, using radiation doses much higher than those used for clinical CT imaging. Although $100\ \mu\text{m}$ resolution is insufficient for microvasculature visualization (where vessel sizes are approximately $10\ \mu\text{m}$ and vessel wall components are even smaller), our 3D histology reconstruction approach could be used to address the authors' stated difficulty in obtaining a precise co-registration between their 2D histologic sections (used for CT imaging validation) and the 3D CT images. Our approach is also complementary in its ability to provide 3D reconstructions of specific structures and proteins revealed by histology stains, complementing the vessel wall layer information provided by phase-contrast CT.

These recent investigations make clear the need for highly accurate, automated, repeatable 3D reconstructions of thin histology sections both as a complement to confocal microscopy

and as an independent means of answering important research questions involving microvasculature analysis and quantification. The automatic registration of the serial sections would speed up the process of manual alignment for volume reconstruction by increasing the sample size with a minimal corresponding increase in manual labour and time. The smooth muscle surrounding the vasculature was stained using the smooth muscle α -actin primary antibody in the samples of this study, but other tissue components could also be stained and incorporated into the 3D reconstruction. Multiple stains could be applied to the tissue to visualize different components; e.g., vascular endothelial cells and smooth muscle could be stained to visualise both components. [19] The reconstruction of histology into the 3D context could also facilitate co-registration with 3D in vivo imaging (as has been done at the millimeter scale in human imaging [20]–[22]) such as micro-CT, where co-registered 3D histology could provide complementary information to the vessel lumina visualized using the iodinated CT contrast agent.

In this study, we evaluated intensity-based and nucleus landmark-based 3D reconstruction methods on TA muscle samples of wild type mice under both normal and hind limb ischemic conditions. Our hybrid approach uses a coarse initialization from on a low-resolution intensity-based registration, followed by a refinement using a landmark-based registration defined using bisected cell nuclei appearing on adjacent tissue sections. Our approach is inspired by previously published methods that applied intensity-based coarse registration followed by landmark-based registration refinement, [4] but differs from previous work in two primary respects. First, in contrast to methods relying on the introduction of extrinsic landmarks (e.g. needles) into the tissue, [23] our approach automatically extracts and corresponds intrinsic cell nuclei, resulting in a more streamlined workflow and reduced tissue disruption. Second, our specific choice of landmark type (cell nuclei) differs from landmark types used in previous work and has demonstrated high accuracy for 3D reconstruction both in terms of pairwise and accumulated TRE. This is based on the observation that the accuracy of a 3D reconstruction using landmark-based registration depends on the characteristics of the landmarks used to define the registration transformation. This issue is especially important in the context of a 3D reconstruction that is defined as a composition of multiple pairwise registrations; any spatial bias in pairwise landmark correspondence error can propagate through the pairwise registrations and result in a large accumulated error in the reconstruction. Our choice of small cell nuclei as landmarks mitigates this issue as nucleus orientation in our specimens would not be expected to have a spatial bias that would contribute to such error propagation. It is for this reason that our method can overcome the issue of error propagation and the banana-into-cylinder effect, as evidenced by our reported accumulated TRE values. Due to the abundance of nuclei in the tissue, the registration is robust to the accuracy of segmentation of the cell nuclei when the majority of nuclei present are segmented (as is the case using our algorithm). The number of

nucleus landmark correspondences obtained by our algorithm far exceeds the number of pairs necessary for defining an affine or rigid registration.

Our interest in ischemia and reperfusion is due to the critical need to understand the regeneration process of the vasculature, as this has important therapeutic potential for patients with vascular disease. However, this potential has yet to be fully realized and understanding the 3D relationships amongst the neovasculature and the surrounding ischemic and/or regenerating tissue will be important in advancing this field. [24] We anticipate that in a larger study of these mice, renderings of 3D reconstructed histology will clearly show the microvasculature connectivity at the level of the arterioles and venules, which would not be apparent in conventional 2D histology analysis (Figure 2.7). We also anticipate that 3D histology reconstructions will permit more reliable quantifications of important surrounding tissue components that can affect tissue perfusion, such as the volume and surface area of the nearby skeletal muscle fibers. [25] In addition, vessel surface area cannot be measured in 2D histology, whereas it is straightforward to measure in 3D on a segmented vessel network. As another illustration, due to variability in the angle of sectioning, the medial wall thickness and vessel diameter can be difficult to interpret. For example, if the tissue was sectioned off-orthogonal to the vessel, the lumen would likely be measured to have a larger area than the correct area that would be measured if the tissue were sectioned orthogonal to the vessel direction (Figure 2.7G). We speculate that vascular measurements, such as the vessel wall thickness, may be more consistent in 3D, especially when malformations cause structural changes.

2.4.1 Evaluation of registration accuracy

It is helpful to the interpretation of registration errors in comparison to the reference reconstruction to note that the lower bound of an arteriole microvessel diameter in the mouse is approximately $10\ \mu\text{m}$. [26] Imaging the tissue prior to sectioning may generate a volume which does not have resolution high enough to resolve microvascular structures, thus a surrogate reference was used. The reference reconstruction generated through manually validated, intrinsic nucleus landmarks provides a surrogate for an ideal 3D reference volume, where the intrinsic landmarks are not subject to orientation bias. The pairwise and accumulated TREs indicate that in the normal and regenerated tissue, the 95% confidence intervals on the median TRE were lower than $5.2\ \mu\text{m}$ for the affine nucleus landmark registration (Table 2.2), which suggests accurate reconstruction of both microvessel topology and geometry in these samples. The reference FRE shown in Table 2.1 provides a sense of the best-case registration that can be achieved using an affine transformation of the manually validated reference landmarks; the FRE thus provides insight into the amount of residual deformation in the tissue.

The intensity-based reconstruction did not provide 95% confidence intervals of less than $10 \mu\text{m}$ for the accumulated TRE values. This, combined with the observation that the nucleus-based reconstruction provided lower accumulated TRE for both the normal and the regenerated tissues, suggests that this nucleus landmark-based registration is valuable for 3D histology reconstruction of microvasculature. To place our results within the context of a comparable, recently published method investigating the accuracy of 3D histology reconstructions based on semi-automatic non-rigid B-spline registration [10], we calculated and compared results analogous to those presented in [10] (Table 2.3). The authors of [10] demonstrated reconstructions of metastatic colorectal carcinoma in human liver tissue, cirrhotic human liver tissue infected with hepatitis C, and a rat glomerulus. Reconstruction error was quantified in terms of Hausdorff distance, and reported mean \pm SD pairwise Hausdorff distance errors of $49 \pm 31 \mu\text{m}$ and $54 \pm 37 \mu\text{m}$ respectively for two specimens. Corresponding reported mean \pm SD accumulated Hausdorff distance errors (over 10 sections) were $112 \pm 71 \mu\text{m}$ and $120 \pm 88 \mu\text{m}$, respectively. By comparison, for our fully-automatic affine nucleus-based landmark registration, we observed mean \pm SD accumulated maximum per-section TREs of $30 \pm 24 \mu\text{m}$ and $39 \pm 48 \mu\text{m}$ for normal and regenerated tissues respectively (Table 2.3).

The authors of [6], [27] proposed an intensity-based registration approach for 3D histology reconstruction of tumor microvasculature using iterative optimization of an image similarity metric to align a series of adjacent section pairs; our tested intensity-based method is similar in these respects. The accuracy of the registrations in [6], [27] was evaluated by the authors using qualitative inspection of the reconstructed volumes; our work extends this work by quantitatively measuring the registration error using intensity-based registration. The method described in [28] intended for alignment of individual cells used a multi-resolution intensity-based registration. On their data sets consisting of serial sections, the majority of registration errors were between 10 and $30 \mu\text{m}$; this is concordant with our mean intensity-based registration errors (Table 2.2). The method described in [29] is intended for human liver tissue reconstruction used a block-matching intensity-based registration approach to align sections with the same type of stain. Their results presented Hausdorff distance errors most frequently lying between 50 and $150 \mu\text{m}$ on a single specimen, which is concordant with our maximum observed intensity-based registration errors (Table 2.3). Although the work presented in [30] was not intended for microvasculature reconstruction, it has similarities to our work in that structures of interest are segmented and used to refine an initial intensity-based registration for reconstruction of mammary gland tissue. Reconstruction accuracy on real image data in [31] was assessed by qualitative inspection of the 3D volumes. Similarly, the accuracies of the feature-based reconstruction methods proposed in [4], [7], [32] were not measured quantitatively on real image data, challenging the assessment of their utility for microvasculature reconstruction and anal-

ysis where the requirements for accuracy are stringent. A block matching method proposed in [14] reported a pairwise root mean square error (RMS) of $23.25 \mu m$, which is larger than our pairwise nucleus landmark-based registration RMS TRE values of $14.25 \mu m$. Our work extends these investigations by providing a rigorous quantitative assessment of reconstruction error for a feature-based registration approach in the context of microvasculature assessment in the mouse.

As intensity-based registration is driven by optimization of an image-similarity metric computed over the entire image domain, misalignment of large, salient structures produces a larger penalty to the optimizer and thus the tendency is to provide a registration aligning such structures from one section to the next. Registration of salient structures may propagate pairwise error through the reconstructed volume, and this pairwise error may appear negligible unless the salient structures have spatial bias. One example could be due to a large blood vessel oriented non-orthogonally to the section. The result can be a non-negligible accumulation of error throughout the reconstructed volume. This accumulation of registration error across multiple sections has been previously observed in other intensity based pairwise registration methods. [4], [10], [29] Knowledge of accurate structural orientation can be vital to differentiation between pathological models. These geometric measurements could be perturbed by pairwise registration of salient features, which may force non-orthogonal features to be straight and section-orthogonal. In the hind limb skeletal muscle tissues, the vasculature flows parallel to muscle fibers, [32] and the tissue sections were taken in the transverse plane. In this case, forcing the salient muscle fibres to align pairwise and run orthogonal to the plane of sectioning may have been expected to result accurate 3D reconstructions. However, the accumulated TRE values (Table 2.2) and the reconstructed volumes (Figure 2.7) for the intensity-based registration indicate otherwise. This accumulation of error may pose an even greater problem in tissues with salient features which are not orthogonal to the plane of sectioning, such as muscle fibers in the heart which have a helical configuration. Our results suggest that landmark-based registration of small features such as cell nuclei may aid in the alignment of tissues where geometry preservation is a priority.

The non-negligible accumulation of error in the reconstructed volumes could lead to vessel structure misinterpretations. As seen in Figure 2.7, although the differences in intensity-based and landmark-based registration of the adjacent sections are not visually salient, the impact of these differences is clear in the 3D reconstructions of the normal and regenerated mice. The bias in the intensity based registration to align large, salient features on the adjacent sections is disruptive to the preservation of microvasculature continuity.

2.4.2 Evaluation of image similarity metrics

Based on the upper bound of the 95% prediction interval across all three samples, global MSE optimization would transform the moving image to be not more than $10 \mu m$ - 100% of the typical diameter of a microvessel - from the transformed moving image given by nucleus-based registration. It could therefore be expected that such differences could be disruptive to useful 3D histology reconstructions for microvasculature analysis. This suggests that this image similarity metric may not be suitable for this problem. In our informal initial experiments, we did not observe reduced error using the normalized cross correlation or mutual information image similarity metrics, so we opted to test the MSE metric in the interests of computational efficiency for this mono-modality registration problem. The use of MSE seems particularly appropriate given that each of our samples was processed in one preparation to mitigate any potential effects of staining variability, with variables such as the concentration of the solutions and the incubation time controlled.

2.4.3 Limitations

The scope of this study was to perform a technical evaluation of intensity-based and nucleus landmark-based registration algorithms on the two types of mice: those with normal vasculature, and those with post-ischemic regenerated vasculature. The differences observed between the nucleus landmark and intensity based registrations were consistent with both the normal and regenerated vasculature, with consistently higher accuracy using the nucleus landmark registration technique. Comparison of vessel structure in the two types of mice is of interest and the subject of future work; the work presented in this chapter is a critical first step toward this future aim.

The results of this study need to be considered in the context of its strengths and limitations. Although two distinct tissue types were studied, the sample size is small and thus new insights may be expected to arise with additional samples. Moreover, the approach can be adapted for variation in anatomy, pathology or stain. The key observation was the use of small structures not spanning more than two adjacent sections could reduce the banana-into-cylinder problem without the use of costly equipment. Serial sections cut by the microtome can be technically challenging, but in the case of missed sections, a fine scale alignment of the tissue conserving structural context can be used for exploration of the overall tissue. The local neighbourhood size $T = 100 \mu m$ was chosen (based on experimentation with a sample not included in this study) to encompass the observed pairwise TREs from the intensity-based registration, in an effort to ensure that corresponding nuclei lay within this neighbourhood. However, this parameter represents a brittle aspect of our algorithm; if a correctly corresponding nucleus is outside

of this range, correct correspondence cannot occur. Our informal experimentation suggests that the algorithm is not particularly sensitive to this neighbourhood size, but nevertheless this is an important parameter that may need to be modified when adapting this algorithm to other contexts, according to the observed error in the intensity-based registration. Finally, our conclusions regarding the performance of intensity-based registration for this task must take into account the limitations of our experimental design; we tested only the MSE image similarity metric and used gradient descent optimization. Although our results demonstrated that ideal optimization of the MSE metric would yield reconstructions different from those given by our nucleus landmark-based approach, we cannot conclude from this that a more suitable image similarity metric (e.g. an approach based on M-estimators [14]) could not be devised that would be suitable for this problem, and this would be a useful avenue of future work in this area.

2.5 Conclusion

We have demonstrated that accurate 3D reconstructions of serial histology sections of mouse hindlimb tissue can avoid potential misinterpretations of the vasculature arising from assessment of 2D histology sections without 3D context. Such misinterpretations may relate to vessel size, tortuosity, connectivity, and bifurcation, all of which are important to understand pathologies of the vascular network at the arteriolar and venular levels. Our results demonstrated that a 3D reconstruction algorithm based on section pairwise registrations using small, homologous landmarks spanning not more than two tissue sections may support 3D reconstruction of digital histology images with sufficient accuracy to provide acceptable registration for the arterioles and venules. This technique avoids the otherwise problematic banana-into-cylinder effect where conventional intensity-based registration methods optimize the pairwise alignment of large, salient structures, forcing them to be section-orthogonal. Our results demonstrated that 3D digital histology reconstruction of mouse hind-limb tissue stained for vascular smooth muscle cells and hematoxylin could be performed accurately and fully automatically via a cascaded approach beginning with pairwise low-resolution intensity based registration of adjacent tissue sections, and refined by a landmark-based registration using corresponding nuclei that were bisected by the microtome blade during sectioning. Intensity-based reconstructions driven by larger, more salient features appear to preserve vascular topology but not geometry; the use of nuclei for refinement of the reconstruction achieves both ends. With our ongoing validation and refinement of this system on a larger data set, we aim to provide a valuable tool for scientists conducting studies requiring high-throughput, high-accuracy ($<10 \mu\text{m}$ error) 3D histology reconstructions for analysis of 3D microvasculature and surrounding tissue components in small

animal models.

References

- [1] G. G. Pietra, F. Capron, S. Stewart, O. Leone, M. Humbert, I. M. Robbins, L. M. Reid, and R. M. Tuder, “Pathologic assessment of vasculopathies in pulmonary hypertension,” *J Am Coll Cardiol*, vol. 43, no. 12 Suppl S, 25S–32S, 2004.
- [2] B. Csernus, L. Ficsor, B. Molnar, and Z. Sapi, “Comparison of the vasculature of myxofibrosarcoma and myxoid liposarcoma using 3d histological reconstruction,” *Histopathology*, vol. 53, no. Journal Article, pp. 410–411, 2008.
- [3] A. Cifor, L. Bai, and A. Pitiot, “Smoothness-guided 3-d reconstruction of 2-d histological images,” *NeuroImage*, vol. 56, no. 1, pp. 197–211, 2011.
- [4] M. Schwier, T. Bohler, H. K. Hahn, U. Dahmen, and O. Dirsch, “Registration of histological whole slide images guided by vessel structures,” *Journal of pathology informatics*, vol. 4, no. Suppl, S10–3539.109868. Print 2013, 2013.
- [5] E. J. Walker, F. Shen, W. L. Young, and H. Su, “Cerebrovascular casting of the adult mouse for 3d imaging and morphological analysis,” *J Vis Exp*, no. 57, 2011.
- [6] J. M. Gijtenbeek, P. Wesseling, C. Maass, L. Burgers, and J. A. van der Laak, “Three-dimensional reconstruction of tumor microvasculature: Simultaneous visualization of multiple components in paraffin-embedded tissue,” *Angiogenesis*, vol. 8, no. 4, pp. 297–305, 2005.
- [7] B. Steiniger, M. Bette, and H. Schwarzbach, “The open microcirculation in human spleens: A three-dimensional approach,” *The journal of histochemistry and cytochemistry : official journal of the Histochemistry Society*, vol. 59, no. 6, pp. 639–648, 2011.
- [8] M. Jirkovska, T. Kucera, J. Kalab, M. Jadrnicek, V. Niedobova, J. Janacek, L. Kubinova, M. Moravcova, Z. Zizka, and V. Krejci, “The branching pattern of villous capillaries and structural changes of placental terminal villi in type 1 diabetes mellitus,” *Placenta*, vol. 33, no. 5, pp. 343–351, 2012.
- [9] E. Janacek Jiriand Cvetko, L. Kubinova, L. Travnik, and I. Erzen, “A novel method for evaluation of capillarity in human skeletal muscles from confocal 3d images,” *Microvascular research*, vol. 81, no. 2, pp. 231–238, 2011.
- [10] N. Roberts, D. Magee, Y. Song, K. Brabazon, M. Shires, D. Crellin, N. M. Orsi, R. Quirke, P. Quirke, and D. Treanor, “Toward routine use of 3d histopathology as a research tool,” *The American journal of pathology*, vol. 180, no. 5, pp. 1835–1842, 2012.

- [11] S. Gaffling, V. Daum, and J. Hornegger, "Landmark-constrained 3-d histological imaging: A morphology-preserving approach.," in *VMV*, Citeseer, 2011, pp. 309–316.
- [12] J. M. Marieb PB Wilhelm, *Human Anatomy*, 6th ed. San Francisco: Pearson Benjamin Cummings, 2012.
- [13] T. S. Yoo, M. J. Ackerman, W. E. Lorensen, W. Schroeder, V. Chalana, S. Aylward, D. Metaxas, and R. Whitaker, "Engineering and algorithm design for an image processing api: A technical report on itk—the insight toolkit," *Studies in health technology and informatics*, vol. 85, no. Journal Article, pp. 586–592, 2002.
- [14] S. Ourselin, A. Roche, G. Subsol, X. Pennec, and N. Ayache, "Reconstructing a 3d structure from serial histological sections," *Image and Vision Computing*, vol. 19, no. 1-2, pp. 25–31, 2001.
- [15] A. Fedorov, R. Beichel, J. Kalpathy-Cramer, J. Finet, J. C. Fillion-Robin, S. Pujol, C. Bauer, D. Jennings, F. Fennessy, M. Sonka, J. Buatti, S. Aylward, J. V. Miller, S. Pieper, and R. Kikinis, "3d slicer as an image computing platform for the quantitative imaging network," *Magnetic resonance imaging*, vol. 30, no. 9, pp. 1323–1341, 2012.
- [16] M. J. Campbell and M. J. Gardner, "Statistics in medicine - calculating confidence-intervals for some non-parametric analyses," *British Medical Journal*, vol. 296, no. 6634, pp. 1454–1456, 1988, Campbell, mj gardner, mj.
- [17] T. Ryan, *Modern Engineering Statistics*. John Wiley & Sons, Inc., 2007.
- [18] T. Saam, J. Herzen, H. Hetterich, S. Fill, M. Willner, M. Stockmar, K. Achterhold, I. Zanette, T. Weitkamp, and U. Schuller, "Translation of atherosclerotic plaque phase-contrast ct imaging from synchrotron radiation to a conventional lab-based x-ray source," *PloS One*, vol. 8, no. 9, e73513, 2013.
- [19] E. van der Veer, Z. Nong, C. O’Neil, B. Urquhart, D. Freeman, and J. G. Pickering, "Pre-b-cell colony-enhancing factor regulates nad+-dependent protein deacetylase activity and promotes vascular smooth muscle cell maturation," *Circ Res*, vol. 97, no. 1, pp. 25–34, 2005.
- [20] E. Gibson, C. Crukley, M. Gaed, J. A. Gomez, M. Moussa, J. L. Chin, G. S. Bauman, A. Fenster, and A. D. Ward, "Registration of prostate histology images to ex vivo mr images via strand-shaped fiducials," *Journal of Magnetic Resonance Imaging*, vol. 36, no. 6, pp. 1402–1412, 2012.

- [21] E. Gibson, M. Gaed, J. A. Gomez, M. Moussa, C. Romagnoli, J. L. Chin, C. Crukley, G. S. Bauman, A. Fenster, and A. D. Ward, "3d prostate histology reconstruction: An evaluation of image-based and fiducial-based algorithms," in *Medical Imaging 2013: Digital Pathology*, M. N. Gurcan and A. Madabhushi, Eds., ser. Proceedings of SPIE. 2013, vol. 8676.
- [22] A. D. Ward, C. Crukley, C. A. McKenzie, J. Montreuil, E. Gibson, C. Romagnoli, J. A. Gomez, M. Moussa, J. Chin, G. Bauman, *et al.*, "Prostate: Registration of digital histopathologic images to in vivo mr images acquired by using endorectal receive coil," *Radiology*, vol. 263, no. 3, pp. 856–864, 2012.
- [23] C. Hughes, O. Rouviere, F. Mege-Lechevallier, R. Souchon, and R. Prost, "Robust alignment of prostate histology slices with quantified accuracy," *IEEE Trans Biomed Eng*, vol. 60, no. 2, pp. 281–91, 2013.
- [24] M. J. Frontini, Z. Nong, R. Gros, M. Drangova, C. O'Neil, M. N. Rahman, O. Akawi, H. Yin, C. G. Ellis, and J. G. Pickering, "Fibroblast growth factor 9 delivery during angiogenesis produces durable, vasoresponsive microvessels wrapped by smooth muscle cells," *Nature biotechnology*, vol. 29, no. 5, pp. 421–427, 2011.
- [25] E. Ichinose, T. Kurose, D. Daitoku, and S. Kawamata, "The skeletal muscle vascular supply closely correlates with the muscle fiber surface area in the rat," *Archives of Histology and Cytology*, vol. 71, no. 1, pp. 45–57, 2008.
- [26] M. Gleeson, "Scott-brown's otorhinolaryngology: Head and neck surgery.," in, G. Browning, Ed. United Kingdom: Hodder Arnold, 2008, pp. 111–112.
- [27] H. J. Gilhuis, J. A. van der Laak, J. Pomp, A. C. Kappelle, J. M. Gijtenbeek, and P. Wesseling, "Three-dimensional (3d) reconstruction and quantitative analysis of the microvasculature in medulloblastoma and ependymoma subtypes," *Angiogenesis*, vol. 9, no. 4, pp. 201–208, 2006.
- [28] X. M. Lopez, P. Barbot, Y.-R. Van Eycke, L. Verset, A.-L. Trepant, L. Larbanoix, I. Salmon, and C. Decaestecker, "Registration of whole immunohistochemical slide images: An efficient way to characterize biomarker colocalization," *Journal of the American Medical Informatics Association*, amiajnl-2014-002710, 2014.
- [29] Y. Song, D. Treanor, A. J. Bulpitt, and D. R. Magee, "3d reconstruction of multiple stained histology images," *Journal of pathology informatics*, vol. 4, no. S7, p. 3539.109864, 2013.

- [30] I. Arganda-Carreras, R. Fernandez-Gonzalez, A. Munoz-Barrutia, and C. Ortiz-De-Solorzano, “3d reconstruction of histological sections: Application to mammary gland tissue,” *Microscopy research and technique*, vol. 73, no. 11, pp. 1019–1029, 2010.
- [31] M. Feuerstein, H. Heibel, J. Gardiazabal, N. Navab, and M. Groher, “Reconstruction of 3-d histology images by simultaneous deformable registration,” no. Journal Article, pp. 582–589, 2011.
- [32] E. Eriksson and R. Myrhage, “Microvascular dimensions and blood flow in skeletal muscle,” *Acta Physiologica Scandinavica*, vol. 86, no. 2, pp. 211–222, 1972.

Chapter 3

Segmentation of digitized histological sections for quantification of the muscularized vasculature in the mouse hind limb

The contents of this chapter were previously published in the Journal of Microscopy: Xu Y, Pickering JG, Nong Z, Ward AD. Segmentation of digitized histological sections for quantification of the muscularized vasculature in the mouse hind limb. Journal of Microscopy. 2017 Apr 1; 266(1): 89-103. Permission to reproduce this article was granted by John Wiley and Sons and is provided in Appendix A.

3.1 Introduction

Vascular restructuring is a prominent feature of wound healing, tissue regeneration, ischemic disease and hypertension. The specifics of the vascular remodeling response can profoundly impact tissue perfusion and organ function. To visualize and identify the features of interest, histology is used to stain and visualize specific vessel wall components. Immunohistochemistry (IHC) is a routine method for identifying cell types and localizing protein distributions at high resolutions. [1] The vessel medial layer is comprised of smooth muscles. Differences in smooth muscle cell distribution may be prominent in the blood vessels that redistribute during tissue remodeling as well as ischemic and hypertensive conditions. [2] This variation in the amount of smooth muscle cell wrapping around the vessel may modulate vasoreactivity, and thus flow rate and tissue perfusion, which is imperative to organ function. Differences in smooth muscle

cell distribution may be prominent in the blood vessels that remodel and/or regenerate during ischemic conditions. [3] A robust measurement of vascular features throughout whole tissue sections could enable the routine detection of focal pathologies, furthering our understanding of vascular smooth muscle distributions.

It is particularly important to be able to obtain such measurements in the networks containing microvessels (arterioles and venules) immediately proximal to the capillaries. [4] These networks are important because they contain the smallest vessels wrapped with smooth muscle and are thus responsible for differentially directing blood to and away from capillary beds to deliver oxygen and nutrients according to different tissue demands at any given time. Since arterioles and venules can be as small as $10\ \mu\text{m}$ in diameter [5] and there may exist hundreds on even a small tissue section from a mouse, they are particularly difficult to comprehensively quantify manually or automatically.

3.1.1 Previous Techniques

Assessment of cell type and protein content based on IHC has been performed using manual and semi-automatic methods. [6] For instance, measurement of the number of positively stained endothelial cells [7] has enabled capillary density estimation. [6] In the immediately higher order vessels such as arterioles and venules, the vascular morphology is of interest, requiring not only vessel counting but individual vessel morphometry measurement. However, morphological characteristics can be challenging to measure manually, and some measurements, such as the varying thickness of the arteriole wall, exceed the limits of practicality of manual measurement when considering the fact that there could be hundreds of vessels in one sample. Consequently, manual measurements are generally taken in a limited number of fields of view (FOVs) and extrapolated to the whole tissue section, potentially introducing error and inter-observer variability. Several semi-automatic approaches to quantifying histology use global thresholding followed by post-processing to remove artefacts. [1], [8], [9] However, global approaches on 2D sections are challenged by within-section staining variability; lack of standardization of IHC staining is a barrier to automated or manual quantification. [1]

Recent approaches to processing whole-slide histology images have been performed both on conventional hematoxylin and eosin (H&E) as well as IHC images, with the main focus on oncological applications. Features have been extracted from prostate histology in order to determine the Gleason grade of prostate cancer. [10]. Modeling of colorectal adenocarcinoma histology on H&E has been performed to assess tissue morphology parameters. [11] Regarding IHC, vascular endothelial cell detection has been performed in order to assess tumour microvessel density in previous work. [12], [13] Segmentation is a common method used in

whole-slide assessment of histology, including the segmentation of nuclei in breast histology. [14] Even without the process of whole-slide scanning, segmentation approaches for muscle cell bundles allow for the assessment of growth, atrophy and repair. [15]

3.1.2 Our Technique

To address the issues of sparse sampling through field of view analysis and semi-automated approaches, we have developed an automated segmentation method that uses three stages of computations involving spatial localization to compensate for within-slide staining variability. The first stage involves extraction of the vessel fragment boundaries after colour deconvolution. [16] The second stage bridges non-artefactual fragments belonging to vessels according to the spatial concordance of their topological skeletons [17], in order to form full vessel units. The third stage of locally adaptive segmentation refinement creates fully-formed vessel boundaries. Vessel density, wall area, perimeter, and thickness were measured on mouse hind limb samples. We evaluated segmentation and measurement accuracy by comparison to manually-delineated vessel walls.

3.2 Materials

The experiments were conducted on a total of 9 C57BL/J6 mice. Between 2 and 19 serial tissue sections were obtained per mouse; all sections were used for analysis in this study. The design of the experiment involved two tissues samples of C57BL/J6 mouse hindlimb tissue, independent of the samples within this study. Validation of segmentation and detection was performed on a subset of mice within this study (Table 3.1). The mice were sacrificed by overdose of isoflurane. After the blood was flushed by intraventricular perfusion with phosphate buffered saline, the tissues were fixed by intraventricular perfusion with formalin. The anterior calf bundle, which contains tibialis anterior, extensor digitorum longus, and peroneus longus muscles, was isolated. The tissues were then fixed in formalin for another 48 hours. The tissues were processed and paraffin-embedded, and then cut into blocks and sectioned at $5 \mu\text{m}$. To visualize the smooth muscle distribution within the arterioles and venules, sections were immunostained for smooth muscle (SM) α -actin using the monoclonal antibody (DAKO, M0851), and bound primary antibody detected with horseradish peroxidase (HRP)-conjugated secondary antibody and 3,3'-Diaminobenzidine chromogen (DAB, Vector Laboratories, SK-4100). This marked the smooth muscle layer of the vasculature, resulting in the vessel walls being stained with a brown colour (Fig. 3.1). The tissue was then counter stained with hematoxylin, resulting in blue-stained nuclei. The sections were imaged with a ScanScope CS (Aperio Technologies,

Vista, CA, USA) bright field slide scanner, at 20× objective with 2× magnification engaged, resulting in 0.25 μm isotropic pixels. This yielded images with extents ranging from 12341 - 26398 pixels in the vertical dimension and 9000 to 17135 pixels in the horizontal dimension.

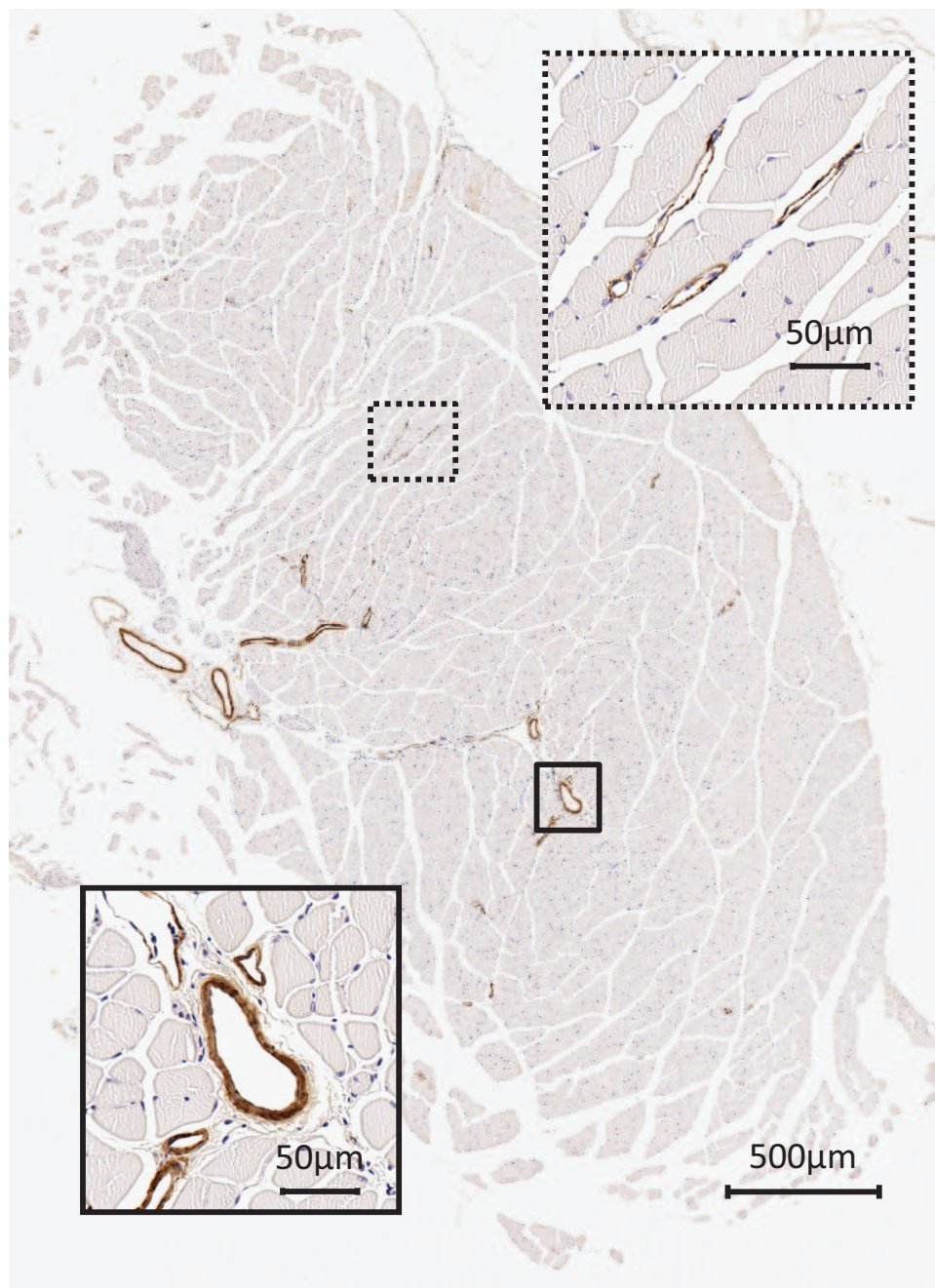


Figure 3.1: Mouse hind limb tissue immunostained with an antibody to smooth muscle α -actin and DAB chromogen and counter-stained with hematoxylin.

Table 3.1: Summary of the histology samples used for each experiment

	Samples Used	Number of sections
Algorithm design	Two external samples	Two sections from each
Measurements	9 mouse samples	All sections
Validation	3 mouse samples	One section from each
FOV Simulation	9 mouse samples	All sections

All experiments in this study were approved by the Animal Care and Veterinary Service Committee at The University of Western Ontario (Protocol # 2010-244) and were carried out in accordance with their requirements. Surgeries were performed under isoflurane anesthesia.

3.3 Methods

The main steps in the automated vessel segmentation algorithm are vessel fragment detection, vessel fragment connection, locally adaptive segmentation refinement, and vessel measurement (Fig. 3.2). The detection and segmentation was validated with manual detection of vessels as well as manual contours on a subset of vessels. Measurements of the vascular smooth muscle layer were compared between the manual and automated segmentations.

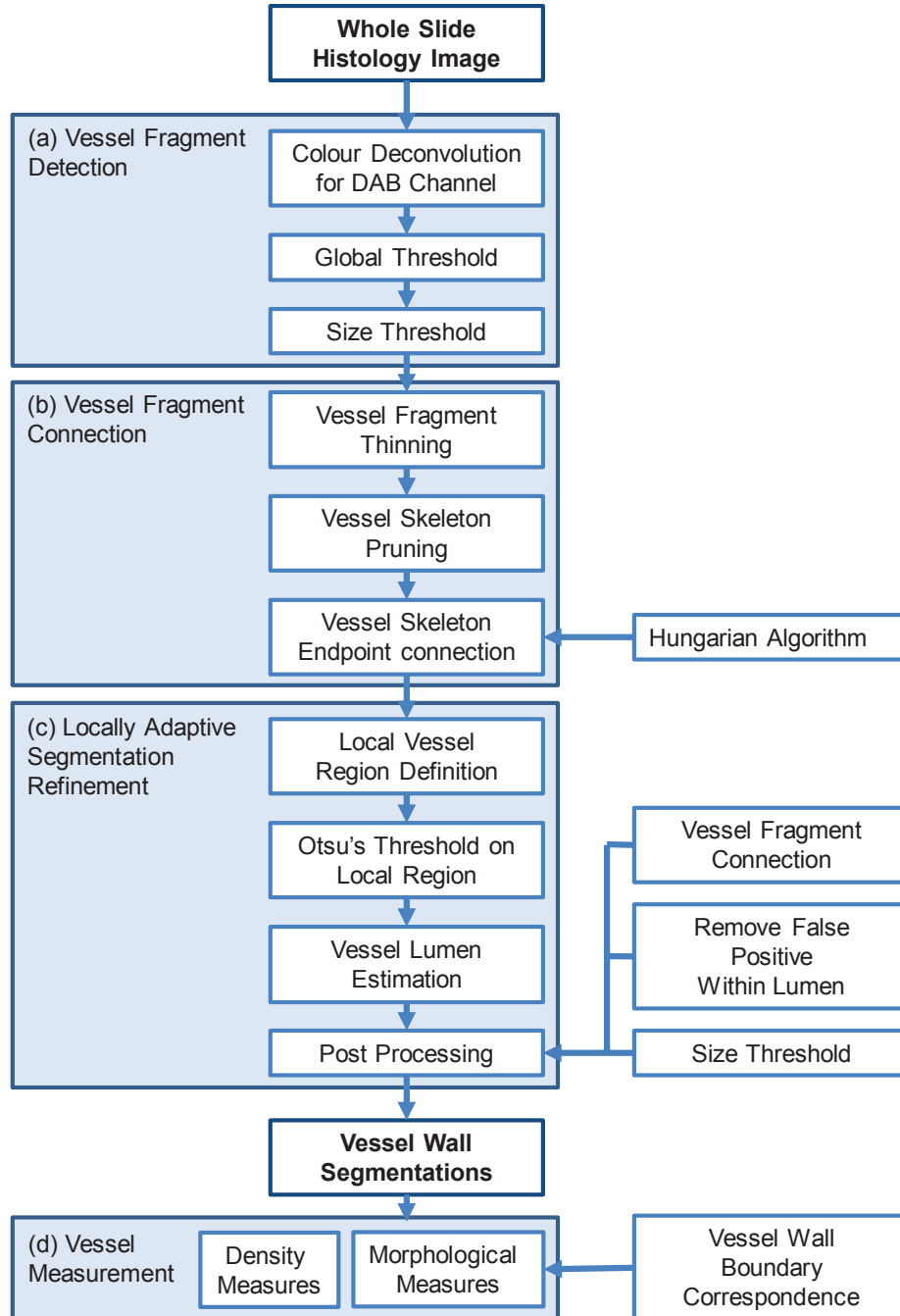


Figure 3.2: A block diagram depicting each step in the automated vessel segmentation algorithm starting with whole slide histology images and resulting in vessel wall contours and measurements. The main steps include vessel fragment detection (a), vessel fragment connection (b), locally adaptive segmentation refinement (c) and vessel measurement (d).

3.3.1 Vessel Fragment Detection

Colour deconvolution [16] was performed to extract the features stained by DAB, resulting in a brown colour on the smooth muscle component of the vessel, into a single channel (Fig. 3.3). The colour deconvolution previously described by Ruifrok et al. is based on the RGB model of optical density (OD), defined as

$$OD_C = -\log_{10}(I_C/I_{0,C}) = A * c_C \quad (3.1)$$

where $I_{0,C}$ is the intensity of light entering the specimen, I_C is the intensity of the light detected after passing through the specimen, and A is the amount of stain with the absorption factor c . The subscript C indicates the detection channel. The pure stain channels are specified by the OD in each RGB channel. [16] A 3 by 1 vector describes each stain. The vector value is proportional to $A * c_C$. In the case of RGB for 3 colour channels, the matrix is

$$\begin{bmatrix} p_{11} & p_{12} & p_{13} \\ p_{21} & p_{22} & p_{23} \\ p_{31} & p_{32} & p_{33} \end{bmatrix}.$$

The absorption factor is normalized for each stain prior to an orthonormal transformation. [16] The normalization of the first column of the OD matrix is

$$\hat{p}_{11} = p_{11} / \sqrt{p_{11}^2 + p_{12}^2 + p_{13}^2} \quad (3.2)$$

$$\hat{p}_{21} = p_{21} / \sqrt{p_{21}^2 + p_{22}^2 + p_{23}^2} \quad (3.3)$$

$$\hat{p}_{31} = p_{31} / \sqrt{p_{31}^2 + p_{32}^2 + p_{33}^2} \quad (3.4)$$

with similar normalization for the other columns, to obtain the normalized matrix \mathbf{N}

$$\begin{bmatrix} \hat{p}_{11} & \hat{p}_{12} & \hat{p}_{13} \\ \hat{p}_{21} & \hat{p}_{22} & \hat{p}_{23} \\ \hat{p}_{31} & \hat{p}_{32} & \hat{p}_{33} \end{bmatrix}.$$

Thus the stain amount vector \mathbf{C} is defined as

$$\mathbf{C} = \mathbf{D}[y] \quad (3.5)$$

where $\mathbf{D} = \mathbf{N}^{-1}$ and y is the OD at each pixel.

The greyscale colour deconvolution image \mathbf{C} representing the intensity of the DAB stain was then thresholded at 50% of the maximum image intensity value, yielding binary images. The threshold level was chosen arbitrarily from a subset of images independent of our dataset (Table 3.1). The colour deconvolution was performed using block processing and the resulting greyscale image was reconstructed at full resolution. The binary image was then processed at full resolution on the whole tissue section level. Positive foreground objects not in the region of the tissue were masked out. In order to create the masks, the tissue section region was defined by downsampling the grayscale slide image to $4 \mu\text{m}$ isotropic pixel size, and thresholding to remove the white slide background. Morphological image closing and filling of holes in the mask were performed in order to close any gaps in the skeletal muscle of the anterior bundle.

After thresholding, foreground objects (eg. vessel fragments) were filtered according to size in order to remove actin-positive cells unrelated to the smooth muscle wall. Any object smaller than half the approximate size of a nucleus ($5 \mu\text{m}$ in diameter or $19.6 \mu\text{m}^2$) was removed from the foreground. This was introduced to remove spurious DAB precipitate and cells, which may express smooth muscle α -actin, so that they are not candidates for vessel fragment connection. Blue nuclei within the vessel walls can cause holes in the DAB channel, thus any holes in the foreground objects smaller than the approximate size of a nucleus ($5 \mu\text{m}$ in diameter or $19.6 \mu\text{m}^2$) were therefore filled.

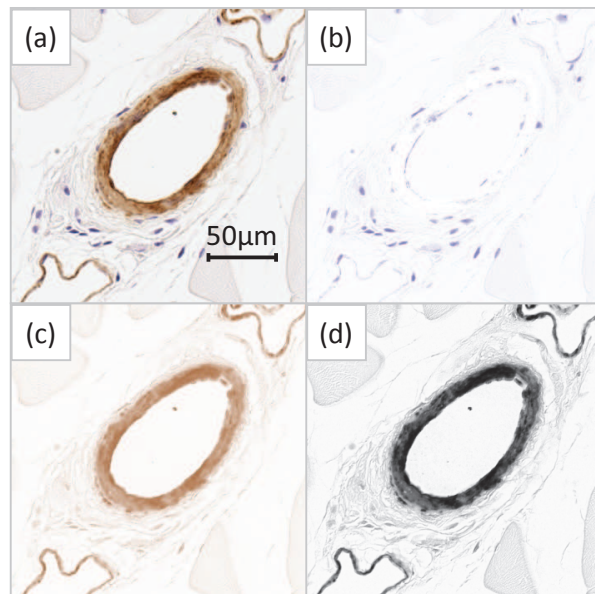


Figure 3.3: Colour deconvolution of the immunostained bright field image (a) separating the haematoxylin (b) and DAB (c) channel, also shown in grayscale (d).

3.3.2 Vessel Fragment Connection

Due to variation in the intensity of the DAB stain throughout the whole slide image and within some vessel walls, the preceding operations yield a set of foreground objects consisting of some fully-formed vessels, and some neighbouring vessel fragments that require reconstitution into fully-formed vessels. For instance, vessels with relatively weak staining in portions of the vessel wall can be fragmented by the global threshold, causing disconnections in the smooth muscle boundary (Fig. 3.4(c)). Foreground objects with an Euler characteristic or Euler number of one do not have holes or lumina in the case of vessels, and thus were considered as vessel fragments potentially requiring connection. [18] Other foreground objects were considered as complete vessels as they contain lumina and would not be considered for vessel connection.

The discontinuous vessel fragments were connected to form complete vessel walls using the topological skeletons computed by thinning the vessel fragments using the thinning operation presented in [17] in order to prevent spurious branches. Pruning was performed on the remaining branches to yield skeletons with no branch points. The selected pruned skeleton was defined as

$$S = \arg \max_{S_i \in \{S_E, S_G\}} DSC(R(S_i), F) \quad (3.6)$$

where S_E and S_G are the pruned skeletons with the longest Euclidean and geodesic distances between their endpoints, respectively; R is a function that produces a binary image of an object by reconstruction from its skeleton; F is the binary image of the vessel fragment prior to skeletonization; and DSC is the Dice similarity coefficient. Intuitively, of the two pruned skeletons, this approach chooses the one yielding the highest fidelity reconstruction of the vessel fragment.

The endpoints of the pruned skeletons (Fig. 3.4(d)) were considered for connection to join vessel fragments and form complete vessels. Endpoint pairs separated by less than $25 \mu m$ were considered as candidates for connection; this is based on the sizes of arterioles and venules being within the range of around 15 to $40 \mu m$. [5] Among these candidates, the optimal assignment was determined by solving the resulting bipartite graph matching problem using the Hungarian algorithm [19] minimizing the Euclidean distances between the endpoint pairs (Fig. 3.4(e)). A graph G is defined as a set of edges E and vertices V such that $G = (E, V)$, where each individual edge e has two vertices u and v . A bipartite graph has two sets of vertices, where a vertex cannot be connected by an edge to another vertex in the same set. In our case, the endpoints of the skeletons are the vertices. The edges matching the vertices is determined by the Hungarian algorithm, which assigns matches based on a cost matrix formed between the two sets of vertices. In this case, the cost is the Euclidean distance between the vertices or

skeleton endpoints, and the assignment is created by minimizing the cost.

The automatic segmentation A_{glob} of each vessel based on global thresholding was defined as the union of the vessel fragments and the connected skeleton S .

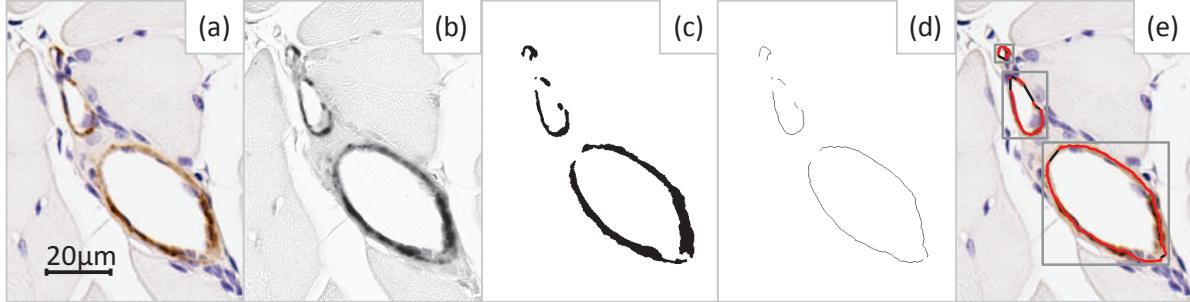


Figure 3.4: Vessel fragment component connection for locally adaptive segmentation. The binary image (c) from the global threshold of the greyscale DAB channel (b) of the bright field image (a) was skeletonized (d). The skeleton endpoints were connected to define each vessel as a single unit and created bounding boxes (e) for locally adaptive segmentation refinement.

3.3.3 Locally Adaptive Segmentation Refinement

To compensate for staining variation within the tissue sections, adaptive thresholding was performed on each vessel using Otsu's method. [20] This method involves minimizing cumulative moments in a gray-level histogram, represented by

$$\sigma_W^2 = \omega_0\sigma_0^2 + \omega_1\sigma_1^2 \quad (3.7)$$

$$\sigma_B^2 = \sigma^2 - \sigma_W^2 \quad (3.8)$$

$$= \omega_0(\mu_0 - \mu_T)^2 + \omega_1(\mu_1 - \mu_T)^2 \quad (3.9)$$

$$= \omega_0\omega_1(\mu_1 - \mu_0)^2 \quad (3.10)$$

which are the within- (σ_W) and between- (σ_B) class variances.

Otsu segmentation was performed on the DAB channel image region defined by expansion of a bounding box around the connected global segmentation A_{glob} (Fig. 3.4(c)) by a uniform margin m to triple its area in order to allow for sampling of the local region of pixel intensities, including the skeletal tissue considered as background (Fig. 3.4(a)). The automatic local segmentation A_{loc} of each vessel based on Otsu thresholding was defined as the union of the connected skeleton S (Fig. 3.4(e), red and black lines) and the components of the Otsu segmentation connected to S . If A_{loc} lay entirely within the dilated (by disk-shaped structuring element with diameter m) convex hull of A_{glob} , then final segmentation $A = A_{loc}$. Otherwise,

final segmentation $A = A_{glob}$. This last step renders the algorithm robust against Otsu segmentation failures in cases of strong local overstaining of surrounding muscle bundles, which can occur due to within-slide staining variability.

The outline of the outer vessel boundary is trivially defined as the outer boundary of A , the final automatic segmentation. Determination of the outline of the inner vessel boundary is challenged by the fact that vessel lumina can be partially or fully collapsed, causing discontinuities. False lumina, created by holes in the vessel wall arising from weak staining and stain occlusion by nuclei, provide further challenges to finding the true inner vessel boundary. To determine the outline of the inner vessel boundary, the topological skeleton of the filled vessel was computed [17] and pruned to the non-branching skeleton having the longest Euclidean distance between its endpoints. For vessels having an open lumen, the inner vessel boundary was defined as the boundary of the open lumen region that was connected to the pruned skeleton (to retain the true lumen and discard false lumina due to irregularities in the walls as described above). In case of partially collapsed lumina, the inner vessel boundary was defined as union of the pruned skeleton and any lumen which touched the skeleton. For fully collapsed vessels having no open lumen, the pruned skeleton itself was taken to be the locus of the lumen.

3.4 Experimental Design

3.4.1 Evaluation of Segmentation Accuracy

Segmentation and detection validation were performed on a subset of our images consisting of 3 whole mount tissue sections from 3 different mice within the data set (Table 3.1). Within the 3 sections, all vessels were manually identified by a graduate student research assistant with 5 years of experience working with histopathology. 50 vessels were manually delineated on the 3 sections with at least 15 vessels delineated in each section. The manual delineations and automated segmentations were compared pixel wise using the Dice similarity coefficient (DSC), mean absolute boundary distance (MAD), sensitivity, specificity, and precision metrics. These values are described as

$$DSC = \frac{2TP}{FP + 2TP + FN} \quad (3.11)$$

$$MAD(A, M) = \frac{1}{n} \sum_{p \in M} \min_{q \in A} D(q, p) \quad (3.12)$$

$$\text{Sensitivity} = \frac{TP}{TP + FN} \quad (3.13)$$

$$\text{Specificity} = \frac{TN}{TN + FP} \quad (3.14)$$

$$\text{Precision} = \frac{TP}{TP + FP} \quad (3.15)$$

which incorporates the true positive TP , true negative TN , false positive FP and false negative FN regions of the automated segmentations A as compared to the manual segmentations M as well as the distance D between their boundaries (p, q) .

3.4.2 Field of View Sampling Simulation

A simulation of FOV sampling was created to assess the accuracy and variability associated with the current practice, where the user would select FOVs within the whole tissue section on a conventional bright field microscope to estimate vessel measures by extrapolation. In this case there is a trade-off between the FOV and resolution of the images taken due to the inherent nature of the microscope. A selected number of non-overlapping FOVs, ranging from 1 to the total number of FOVs required to cover the whole tissue area, were randomly selected from the whole-slide images and used to measure the vessel density and morphology. The typical system used would be a conventional bright field microscope, thus the parameters from such a system was used in our simulation. The size of the FOVs was based on the image size from the Olympus BX51 Microscope and the Q Imaging Retiga EXi digital camera at $40 \times$ objective magnification (1024 by 1376 pixels or 256 by 344 μm); this represents a typical imaging configuration for this type of study. In order to cover the whole tissue region, the random FOVs were located on a grid. For each selected number of FOVs, random FOV selection was repeated through 100 iterations. This process was repeated 4 times, with the grid position was shifted 32 by 43 μm each time, producing a total of 400 simulations.

3.4.3 Vessel Measurement and Statistical Analysis

Measures of the vessel count and density were calculated for whole tissue sections. The vessel wall area, lumen area (eq. 17), diameter (eq.18), inner perimeter and thickness were calculated for each segmented vessel. Measures of vessel lumen area and diameter were derived from the inner vessel wall perimeter, using a circular geometry. The vessel density was calculated as

$$\text{Vessel density} = \frac{\text{Total number of vessels in FOVs}}{\text{Total tissue area in FOVs}} \quad (3.16)$$

as is the common practice.

$$\text{Lumen Area} = \frac{\text{Perimeter}^2}{4\pi} \quad (3.17)$$

$$\text{Vessel Diameter} = \frac{\text{Perimeter}}{\pi} \quad (3.18)$$

Thickness was measured locally (every $0.25 \mu\text{m}$) along the perimeter as the Euclidean distance between point pairs along inner and outer vessel wall boundaries corresponded using streamlines of the gradient of the solution to the Laplace equation. [21] In Cartesian coordinates the Laplace equation is

$$\Delta f = \frac{\partial^2 f}{\partial x^2} + \frac{\partial^2 f}{\partial y^2} + \frac{\partial^2 f}{\partial z^2} = 0 \quad (3.19)$$

where f is the function, twice differentiated along x , y and z . The streamlines are computed by

$$\mathbf{E} = -\Delta f \quad (3.20)$$

and normalized

$$\mathbf{N} = \mathbf{E} / \|\mathbf{E}\| \quad (3.21)$$

where \mathbf{N} is a unit vector defined along the inner and outer segmentation boundaries. The streamlines between the two boundaries are parameterized by the vector

$$\frac{\partial \mathbf{C}(s)}{\partial s} = \mathbf{N}(\mathbf{C}(s)) \quad (3.22)$$

where the Euclidean distance between $\mathbf{C}(0)$ and $\mathbf{C}(n)$ was taken as the thickness of the vessel. The within-vessel variance in thickness, and the 5th and 95th percentile of the thickness, were also measured to test the extrema for presence of local thinning or thickening of the vessels.

For analysis of the conventional technique of selecting FOV for measurement, no vessel was measured twice; if a vessel appeared in more than one FOV, it was measured only in the first FOV encountered in simulation. For all measures other than vessel count/density, only the FOVs which contained vessels were taken into consideration.

Kolmogorov-Smirnov normality tests were performed using MATLAB 8.5 (The Mathworks Inc., Natick, MA, USA) for all measures. The simulation measures of vessel count per tissue area were compared to the whole tissue vessel density using the paired Wilcoxon sign rank test. The median differences and associated interquartile ranges were measured. Morphological measures of vessels were compared between the automated segmentation and the manual delineations using the paired Wilcoxon signed rank test.

3.5 Experimental Results

The vessel measurements were found to be non-normally distributed ($p < 0.05$); thus, the median and interquartile range (IQR) was reported and non-parametric statistical testing was used. Descriptive statistics including vessel count and media area per section area are reported in Table 3.2, where the vessels were also separated based on the vessel diameter. Descriptive statistics on morphological measures are reported in Table 3.3. The smooth muscle layers and vessel lumen measures were sorted based on the vessel diameter. Aggregated median values for each mouse sample are shown in Fig. 3.5.

Table 3.2: Descriptive statistics of vessel count and density

Vessel Diameter	Vessel Count/ Section Area (mm^{-2})		Media Area/ Section Area ($\mu m^2/\mu m^2$)	
	Median	IQR	Median	IQR
All vessels (n = 69)	6.58	3.01	0.0026	0.0016
0 to 10	2.56	1.49	0.0002	0.0002
10 to 40	3.38	2.18	0.0008	0.0004
40 to ∞	0.71	0.76	0.0017	0.0022

Table 3.3: Automated morphological measures of the smooth muscle layer

Size Range of Vessel Diameter (μm)	N	SM Layer Area (μm^2)		Lumen Area (μm^2)		Lumen Perimeter (μm)		Lumen Diameter (μm)		
		Median	IQR	Median	IQR	Median	IQR	Median	IQR	
0	∞	3391	147.31	251.48	114.41	430.16	37.92	54.37	12.07	17.31
0	2	9	58.38	27.52	2.41	0.43	5.50	0.49	1.75	0.15
2	4	139	50.56	19.48	8.99	3.83	10.63	2.26	3.38	0.72
4	6	419	59.56	33.63	20.22	7.16	15.94	2.84	5.07	0.90
6	8	463	77.50	64.56	37.98	10.24	21.85	2.94	6.95	0.94
8	10	377	90.00	77.67	61.92	15.22	27.90	3.40	8.88	1.08
10	12	280	126.91	107.50	93.47	16.76	34.27	3.06	10.91	0.98
12	14	221	165.38	127.31	128.98	20.40	40.26	3.16	12.82	1.00
14	16	146	179.75	111.38	177.85	22.33	47.28	2.96	15.05	0.94
16	18	166	228.78	111.56	227.61	23.42	53.48	2.75	17.02	0.88
18	20	113	233.88	156.84	279.07	33.13	59.22	3.51	18.85	1.12
20	30	406	325.22	188.38	463.75	200.43	76.34	16.37	24.30	5.21
30	40	140	399.38	266.75	879.54	268.63	105.13	15.80	33.46	5.03
40	50	138	686.69	505.25	1524.44	361.96	138.41	16.22	44.06	5.16
50	100	225	1033.00	1232.00	3980.64	2744.61	223.66	79.22	71.19	25.22
100	150	87	2360.69	4366.14	11039.29	3346.35	372.46	55.24	118.56	17.58
150	200	30	3608.25	3692.38	24175.45	8659.33	551.05	98.81	175.40	31.45
200	∞	32	7740.50	13718.56	98029.76	67131.69	1109.90	419.63	353.29	133.57

Size Range of Vessel Diameter (μm)	N	SM Layer Thickness (μm)									
		5th Percentile		50th Percentile		95th Percentile		Within-Vessel SD			
		Median	IQR	Median	IQR	Median	IQR	Median	IQR	Median	IQR
0	∞	3391	1.67	1.61	3.25	2.17	6.60	5.44	1.39	1.42	
0	2	9	2.02	0.55	3.69	1.34	5.12	1.27	1.02	0.52	
2	4	139	1.52	0.82	2.85	0.77	4.07	1.25	0.82	0.44	
4	6	419	1.43	0.72	2.68	1.05	4.00	1.67	0.75	0.44	
6	8	463	1.49	1.25	2.70	1.75	4.55	2.87	0.93	0.64	
8	10	377	1.58	1.61	2.80	1.71	5.64	3.89	1.13	1.03	
10	12	280	1.79	1.77	3.20	1.95	6.39	3.67	1.34	0.94	
12	14	221	1.82	1.90	3.26	2.13	6.56	3.96	1.39	1.14	
14	16	146	1.77	1.90	3.38	1.73	6.73	3.58	1.52	1.07	
16	18	166	2.12	1.48	3.72	1.69	7.36	4.05	1.61	1.32	
18	20	113	1.82	2.02	3.66	2.11	7.29	4.45	1.53	1.25	
20	30	406	1.91	1.86	3.79	2.08	8.68	4.90	1.99	1.68	
30	40	140	1.44	1.92	3.72	2.48	12.27	5.96	3.19	2.22	
40	50	138	2.40	2.81	4.92	2.28	12.07	7.08	2.90	2.59	
50	100	225	1.90	4.51	4.94	5.43	16.31	12.01	3.51	4.45	
100	150	87	2.30	8.18	6.60	11.48	29.10	25.54	6.58	9.44	
150	200	30	1.59	2.70	10.30	8.04	52.40	76.28	16.25	26.29	
200	∞	32	2.97	8.55	12.54	9.37	89.37	56.02	24.85	18.01	

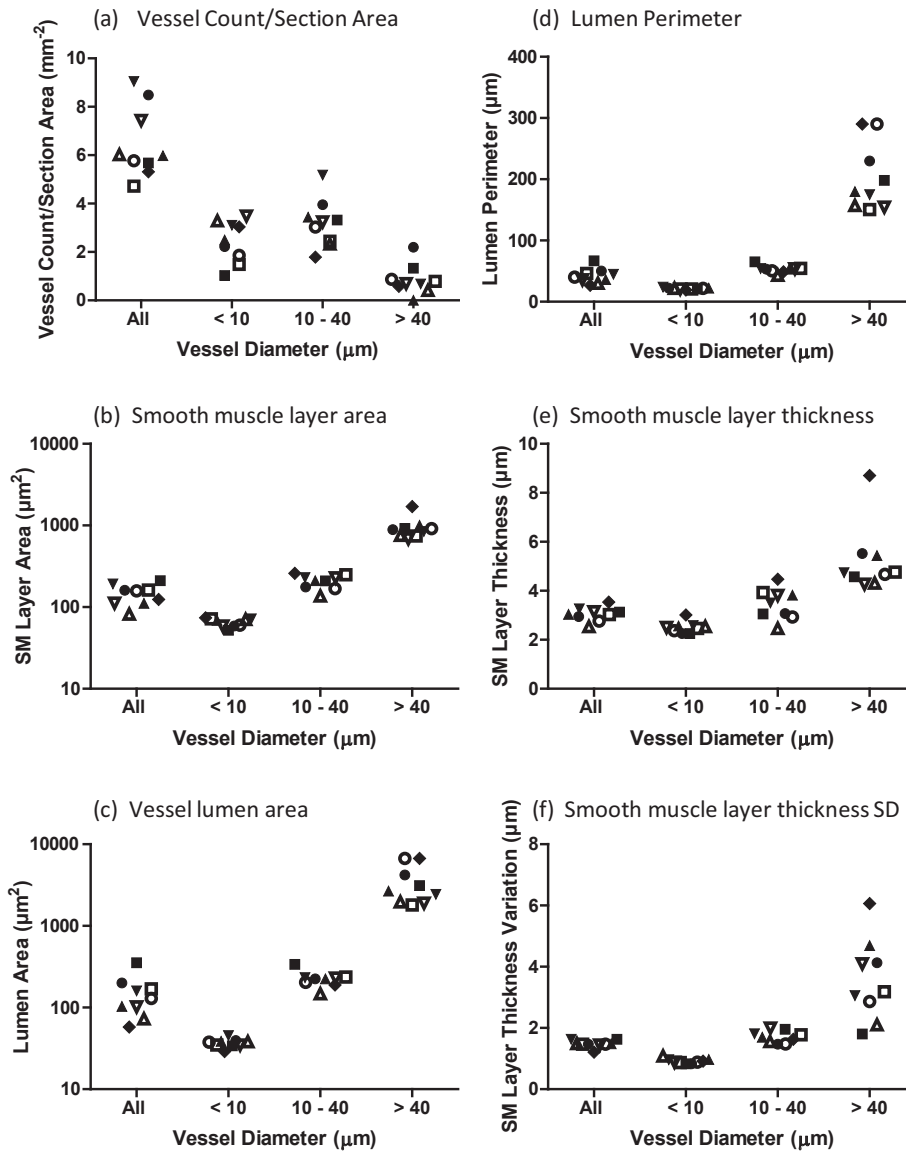


Figure 3.5: Automatic vessel smooth muscle morphological and density measures. The vessel measures were aggregated by median values for each mouse for vessel count per tissue area (a), smooth muscle layer area (b), lumen area (c), lumen perimeter (d), smooth muscle layer thickness (e), and standard deviation (SD) (f) for all vessels and separated by vessel diameter. Each glyph represents one mouse sample.

3.5.1 Segmentation Validation

Table 3.4 shows the segmentation validation measures, indicating good concordance between the manual and automated segmentation methods ($n = 50$) in 3 separate mice (Table 1). The measures were found to be non-normally distributed ($p < 0.05$); thus, the median and interquar-

tile range (IQR) was reported for each vessel size range. The false negative and false positive rates were 3.3% and 9.6% respectively for vessel detection. Fig. 3.6 shows a comparison between manually delineated vessels and the automated segmentation on a small field of the whole slide tissue section. No difference was found between the measures of smooth muscle wall area or thickness ($p > 0.05$) however a bias of $9.75 \mu\text{m}$ was found in the vessel wall inner perimeter ($p < 0.05$). The differences in the measures are demonstrated by the Bland-Altman plots in Fig. 3.7.

Table 3.4: Segmentation validation metrics

n Measure	Size Range of Vessel Diameter (μm)							
	All Vessels		0 to 10		10 to 40		40 to ∞	
	Median	IQR	Median	IQR	Median	IQR	Median	IQR
	50		12		29		9	
Segmentation								
MAD (μm)	0.40	0.28	0.38	0.29	0.39	0.29	0.46	0.28
DSC	0.89	0.06	0.87	0.07	0.89	0.04	0.93	0.05
Jaccard Index	0.81	0.09	0.77	0.12	0.80	0.06	0.87	0.08
Sensitivity	0.91	0.08	0.93	0.09	0.88	0.08	0.94	0.06
Specificity	0.97	0.05	0.90	0.18	0.97	0.04	0.98	0.02
Precision	0.93	0.09	0.88	0.15	0.93	0.09	0.93	0.04

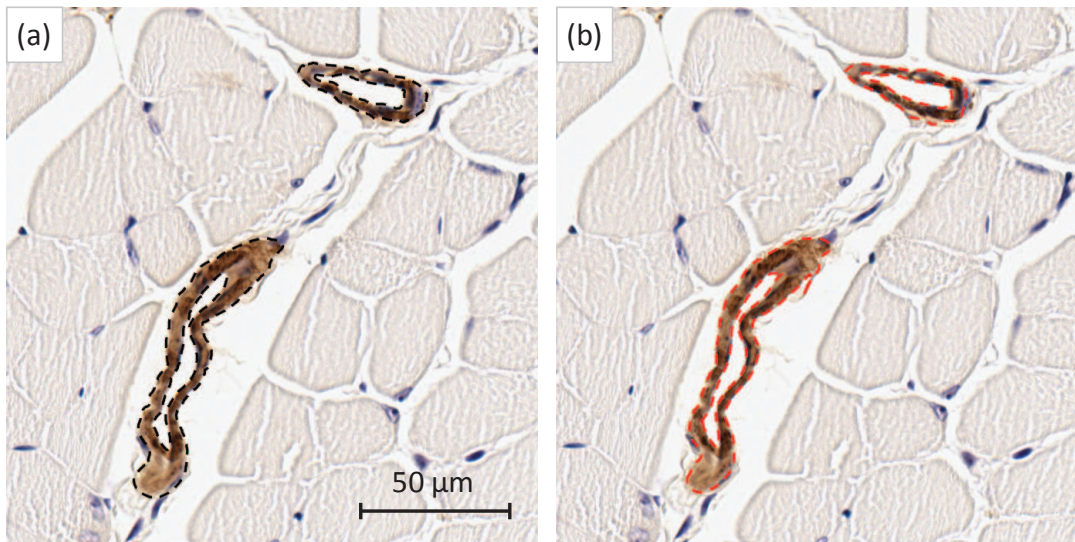


Figure 3.6: Contours of manually delineated (a) and automatically segmented (b) vessel walls in the mouse hind limb stained with DAB for α -actin smooth muscle.

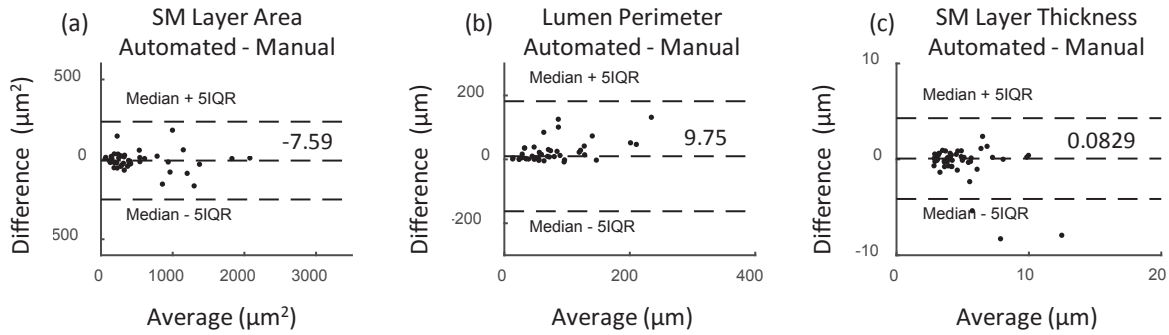


Figure 3.7: Bland-Altman plots depicting the differences between the smooth muscle (SM) layer area, thickness and lumen perimeter measurements derived from manual and automated segmentations. Difference: (automated - manual segmentation measure), Average: (automated + manual segmentation measure)/2.

3.5.2 Field of View Sampling Simulation

The distribution of the differences between the simulated vessel measurements and the whole slide values are shown in Fig. 3.8 for one to 206 FOVs for vessel density and one to 77 FOVs for vessel morphology. The simulation included 400 repeated measures with 4 FOV grid positions, such that the whole tissue region was covered. The variation of the percent difference between the whole slide measure and FOV measures decreases with an increase in the number of FOV incorporated. The numbers of FOVs that needed to be sampled to obtain < 10% and < 20% differences between FOV-estimated and whole-slide measurements for the majority of simulations (those between the 25th and 75th percentiles of the simulations) are shown in Table 3.5.

Table 3.5: Field of view sampling simulation

Measure	Number of FOV to achieve percent difference ranges	
	10%	20%
Vessel count/Section area	103	63
Smooth muscle layer area	30	15
Vessel lumen area	52	30
Lumen perimeter	30	11
Smooth muscle layer thickness	9	3
Smooth muscle layer thickness SD	22	7

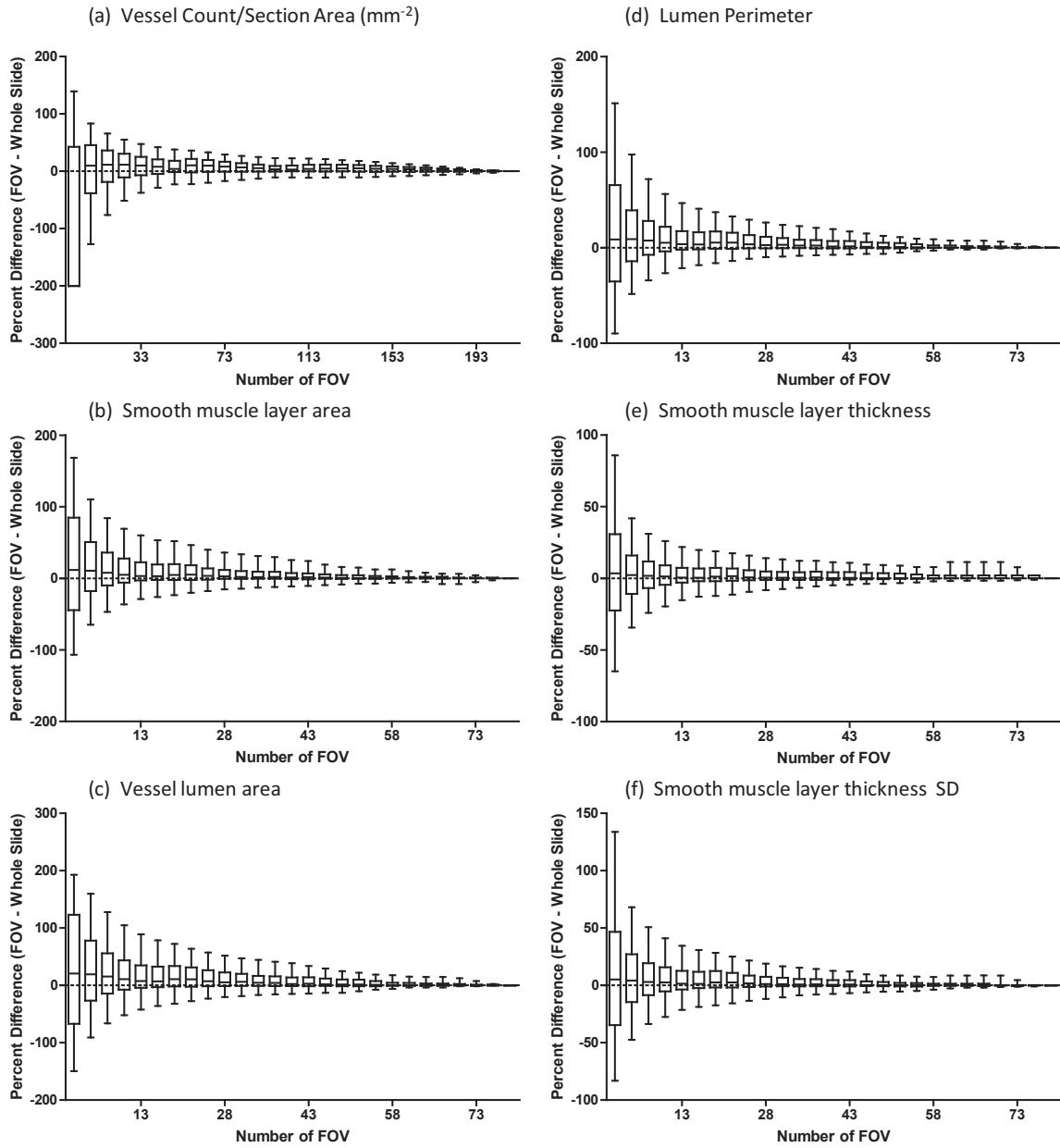


Figure 3.8: The percent difference in vessel measures of the simulated fields of view (FOV) - the whole slide for each tissue section. The vessel measures were aggregated by median values for each FOV for vessel count per tissue area (a), smooth muscle layer area (b), lumen area (c), lumen perimeter (d), smooth muscle layer thickness (e), and variance (f) for all tissue sections ($n = 69$). Boxplots include the median, 25th, 75th percentiles, and whiskers at the 5th and 95th percentiles. Distribution of measurement simulations ($n = 100$) extrapolated from FOVs for each mouse tissue section.

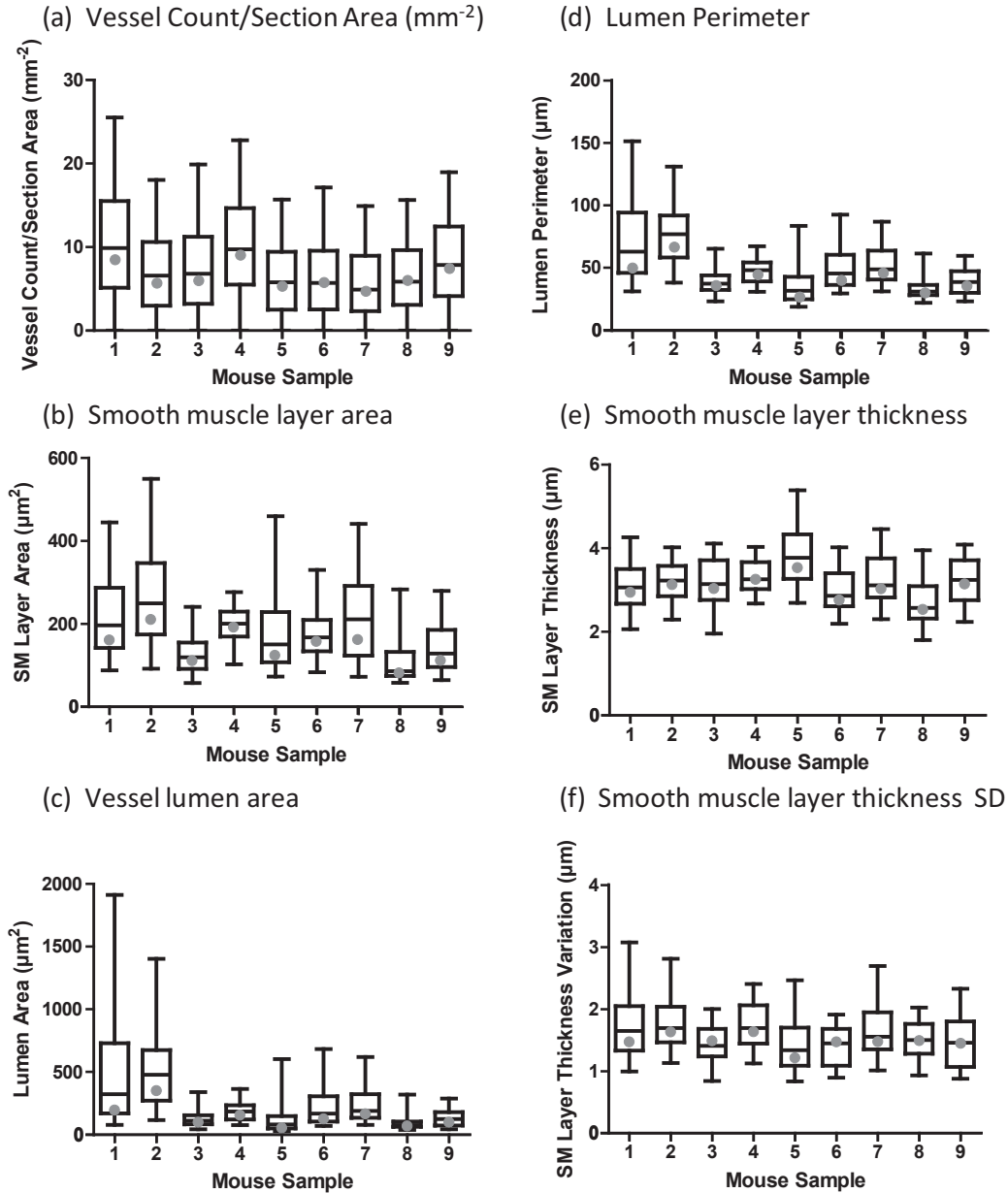


Figure 3.9: The distribution of vessel measures when taking 6 fields of view (FOV) from each tissue section and compared to the whole slide measurement (median shown in grey) for each of the 5 samples. The vessel measures were aggregated by median values for each mouse for vessel count per tissue area (a), smooth muscle layer area (b), lumen area (c), lumen perimeter (d), smooth muscle layer thickness (e), and variance (f) for all tissue sections ($n = 69$). Boxplots include the median, 25th, 75th percentiles, and whiskers at the 5th and 95th percentiles. Distribution of measurement simulations ($n = 400$) extrapolated from 6 FOVs for each mouse tissue section.

A comparison between the median whole slide values within each mouse sample was performed with the measurements from taking 6 fields of view (Fig. 3.9). The boxplots represents the distributions of 400 simulations of the median calculated values as compared to the median whole slide values.

3.6 Discussion

3.6.1 Whole-slide Imaging

Whole-slide imaging allows for the comprehensive quantification of key characteristics of the microvasculature, which contains hundreds of vessels with varying properties. The presented automated algorithm segmented 3391 vessels on 77 sections. Manual quantification on this scale is impractical, requiring the use of subsampling within selected FOVs, and may be subject to operator variability. This system also has the inherent ability to detect vessels with discontinuous vessel walls, which have previously been assessed in tumour vasculature. [22] As demonstrated in Table 3.3, the vessels can be separated into respective sizes for analysis, which is one example of how the vessels can be assessed based on calibre. Whole-slide imaging also allows for the assessment of the density of vessels of different sizes (Table 3.2), and also potentially the location of the vessels with respect to the tissue. This work allows for an automated whole-slide quantification, which allows for high-throughput measurement with concordant accuracy with manual delineations.

3.6.2 Segmentation Validation

The segmentation validation results suggest overall concordance of the automated vessel segmentation with the manual contours resulting in an overall DSC of 0.89 and the resulting vessel measurements (Table 3.4, Fig. 3.5). Vessel detection resulted in balanced false negative and false positive rates of 3.3% and 9.6%. However, a few outlier segmentations did result from unusually faintly stained vessels in some cases, which may be due to the lack of smooth muscle cell wrapping on regions of the vessel. Faintly stained vessels would be difficult even for a user to manually measure; therefore the vessels would likely be counted when considering vessel density but not be measured for morphological features due to the inconsistency of the stain (i.e. detection/counting is more important than segmentation accuracy for very faintly-stained vessels). Non-specific staining of IHC leads to the detection of false positives. This occurred in portions of skeletal muscle with background staining and cells such as myofibroblasts within the tissue also expressing smooth muscle α -actin. The manual and automated measures were

not significantly different for the SM layer area or thickness. There is a bias in the inner lumen perimeter and this may be due to the discrepancy in the delineation of closed lumina when comparing manual to the automated segmentations. Due to the low false negative values and the number of vessels which are detected per slide, one could validate the segmentations by rapid user inspection. The choices could then be used in a machine learning algorithm [23] to train the system to automatically detect the difference between detected vasculature and false positives in future samples.

3.6.3 Field of View Sampling Simulation

The current practice of taking a small number of selected FOVs in order to manually measure the vessel density by extrapolation may yield measurements representative of the whole tissue section, provided that a sufficient number of FOVs is used. Our findings (Fig. 3.8) suggest that with an increasing number of FOVs, there is less variation in the final measurement extrapolated. The variation in morphological values from the fields of view decreases with an increase in the number of FOV taken as there is an increase in the proportion of vessels incorporated into the measurement. To take an example, we compared the measured values at 6 FOV in 400 iterations and compared it to the whole slide value (Fig. 3.9). The median values were not largely different from the whole slide measures but one needs to take into consideration the variation of the measures as represented by the boxplots. A single 6-FOV measurement that would be used in a research study could come from anywhere within the plausible ranges depicted on the box plots. When taking a random sampling, the number of FOVs may affect whether the measure is representative of the whole slide. From Table 3.5, the number of FOVs for the majority of the morphological measurements (those between the 25th and 75th percentiles) to stay within a 20% difference of the whole-slide measure is 3 to 30 fields of view, depending on the measurement. A substantially larger number of FOVs is required for the simulated measures to be within a 20% difference for the measure of vessel density. This is due to the fact that the tissues were uniformly sampled and the spatial distribution of arterioles and venules vary (Fig. 1), and thus a substantially larger number of FOVs is required. Thus, when taking FOV for measurements, bias or misrepresentations may occur when the FOV taken are not representative of the tissues.

Previous segmentation research has been reported for vascular IHC. One example is the capillary-focused method allowing the measurement of vessel density in non-small cell lung cancer developed by Tsou et al. The capillaries were stained using CD31 and the segmentation involved the delineation of the outer vessel wall boundary on FOV. The method was validated using a synthetic dataset, with the lowest reported error rate of 28%. Our method is performed

on whole-slide imaging focused on the smooth muscle wall component, where we are interested in the vessel wall thickness and not only the vessel density, and thus have to take the inner vessel wall boundary into consideration as well. Colour deconvolution for the DAB stain was performed in our method to isolate the stain as compared to a filtering method performed in the method reported by Tsou et al. The two methods have a step which involves Otsu thresholding; however from the resulting error rates it would appear that segmentation could be more challenging at the level of capillaries with CD31 as the target, even if both structures are related to the vasculature and result in a similar brown stain due to IHC.

Taken as a whole, these results are encouraging in that they suggest that if the study hypothesis is concerned only with measuring properties of arterioles and venules in the mouse hind limb, then reliable measures can be obtained with existing extrapolation techniques using a representative number of FOVs which cover a substantial portion of the vessels within the tissue. The random selection of FOVs in our simulation does not reflect any bias, which presents using manual FOV selection by human operators. Accuracy of measures extracted from manually selected FOVs will be affected by inter- and intra-operator variability and may be biased to regions that operators subjectively deem a priori to be representative of the sample. The effective of this bias is described by West as follows: “If the sampling at any level of the scheme is biased, the mean of repeated estimates will systematically deviate from the true value regardless of the amount of sampling performed.” [24] This is especially the case when considering cell counting, which is applied to various biological questions. [25]

3.6.4 Biological Validity

The system can be further validated through an interpretation of the results to determine whether they are concordant with what would be expected from a biological standpoint. The distribution of the number of vessels as a function of vessel diameter (Fig. 3.5(a)) is as expected. Most of the detected vessels are in the 10 - 40 μm range, capturing typical sizes of arterioles and venules. A smaller proportion of the detected vessels are in the <10 μm range; this range contains the smallest arterioles and venules and also contains the capillaries, which are not detected due to a lack of smooth muscle surrounding them (thus they are not stained). The detected vessels in the range of less than 10 μm in Fig. 3.5(a) are small arterioles transitioning into capillaries. The smallest proportion of the vessels are in the > 40 μm range, which contains larger vessels further up in the vessel network above the arteriolar and venular level, where the outliers were samples where the tibial anterior artery was within the tissue section. As expected, the smooth muscle layer area increases with increasing vessel size (Fig. 3.5(b)). There is also an increase in the smooth muscle layer thickness with the increasing vessel size

(Fig. 3.5(e)). This is consistent with the understanding of larger calibre vessels, which need more control of the higher pressure blood flow, and thus require a thicker muscle layer. This is also demonstrated in Table 3.3, where the vessels were further broken down in to sub categories according to vessel diameter, thus one could assess the vascular density and morphology within a certain vessel size range. As a simple self-consistency check, Fig. 3.5(c) reveals that lumen area is directly proportional to vessel diameter. These observations provide evidence, beyond that given by traditional segmentation error measures, that the measurements provided by this algorithm are concordant with expectations; this provides further reassurance regarding the utility of this tool for study of this muscle bundle.

3.6.5 Limitations

The findings of this study need to be considered within the context of its strengths and limitations. The algorithm was applied on a common immunostain, DAB, which results in a brown precipitate; other stains were not tested. Because the colour deconvolution step of the automated segmentation requires a representation of the DAB stain intensity, we believe that the segmentation could be adapted by using a colour deconvolution representation of the stain of interest. The chosen deconvolution method proposed by Ruifrok et al. is a widely cited work, providing stain separation which allow for colour separation in our samples. Should the colour deconvolution involve more than 3 channels or should the method be limited in accuracy due to this process, other colour deconvolution algorithms should be explored and this could be an avenue for future work. [26], [27] Slides may have variability with regard to staining intensity and hue of the stain when performed in different labs with varying reagents, which may in turn affect the intensity of the resulting DAB stain representation from the colour deconvolution. Stain normalization could be applied to the wholes slide images prior to the automated segmentation process if the tissues were processed with varying reagents. This is beyond the scope of this paper but several previous works have studied histology normalization. [26], [28] For segmentation of the vessel wall endothelium, where the inner vessel wall is continuous when void of fenestrations, a hysteresis thresholding approach may lead to increased fidelity in the segmentation and reduce the need for fragment connection. However, in our application, due to the fact that portions of the smooth muscle wall are devoid of DAB stain, a hysteresis threshold method may not reduce the number of fragments.

Currently the implementation is in MATLAB, resulting a total processing time of around 25 minutes per image, however an optimized parallel framework would substantially increase speed. The vessels are quantified in 2D, which does not allow for the assessment of 3D vascular structure. However we have previously addressed this in our work on 3D histology reconstruc-

tion, which could be used in a context where 3D vessel structure is necessary for vascular pathology assessment. [29] Normal mouse samples were used in this dataset and are representative of the tissues processed in our lab. However this may not be representative of tissues processed at a different center, and we have noted this in the limitations paragraph of our manuscript. Our sample size is concordant with sample sizes used in the literature for animal studies, where 3 mice have been used per condition. [30]–[34] Inter- and intra-operator variability is expected, especially in the case of faintly stained tissues, where the variability of manual segmentation will depend on the meticulousness of the operator. The measure of operator variability would consist of several participants and is an under explored area in histology quantification as it is not often performed.

3.7 Conclusion

The vascular smooth muscle component of the microvasculature allows for the control of blood flow and was automatically and accurately segmented on a whole-slide level with the developed software algorithm. The system was shown to be capable of automated quantification of density, vessel wall area, perimeter, and local thickness on several thousand vessels, a task which is well beyond the practical limits of manual quantification. There was no significant difference when comparing manual measurements of vessel wall area and thickness to the measurements in our automated approach. The measurements of normal smooth muscle distribution and morphology demonstrate the biological plausibility of the readouts given by the algorithm and support its utility for comprehensive microvasculature quantification in research studies. We found that traditional vessel density and measurement quantification by extrapolation from manual vessel counting on selected fields of view could be representative of the whole-slide measure; however, the number of required fields of view ranged from 3 to 103, depending on the type of measurement. This system constitutes a valuable tool for scientists requiring high-throughput whole-slide vascular morphology quantification of arteriolar and venular vasculature for disease state comparisons eliminating the need for manual measurements and sparse sampling.

References

- [1] C. Taylor and R. Levenson, “Quantification of immunohistochemistry-issues concerning methods, utility and semiquantitative assessment ii,” *Histopathology*, vol. 49, no. 4, pp. 411–424, 2006.

- [2] M. Barany, *Biochemistry of smooth muscle contraction*. Academic Press, 1996.
- [3] M. J. Frontini, Z. Nong, R. Gros, M. Drangova, C. O’Neil, M. N. Rahman, O. Akawi, H. Yin, C. G. Ellis, and J. G. Pickering, “Fibroblast growth factor 9 delivery during angiogenesis produces durable, vasoresponsive microvessels wrapped by smooth muscle cells,” *Nature biotechnology*, vol. 29, no. 5, pp. 421–427, 2011.
- [4] R. K. Jain, “Determinants of tumor blood flow: A review,” *Cancer research*, vol. 48, no. 10, pp. 2641–2658, 1988.
- [5] M. Gleeson, “Scott-brown’s otorhinolaryngology: Head and neck surgery.,” in G. Browning, Ed. United Kingdom: Hodder Arnold, 2008, pp. 111–112.
- [6] C. C. Reyes-Aldasoro, L. J. Williams, S. Akerman, C. Kanthou, and G. M. Tozer, “An automatic algorithm for the segmentation and morphological analysis of microvessels in immunostained histological tumour sections,” *Journal of Microscopy*, vol. 242, no. 3, pp. 262–278, 2011.
- [7] N. A. Valous, B. Lahrmann, W. Zhou, R. Veltkamp, and N. Grabe, “Multistage histopathological image segmentation of iba1-stained murine microglia in a focal ischemia model: Methodological workflow and expert validation,” *J Neurosci Methods*, vol. 213, no. 2, pp. 250–62, 2013.
- [8] N.-A. Pham, A. Morrison, J. Schwock, S. Aviel-Ronen, V. Iakovlev, M.-S. Tsao, J. Ho, and D. W. Hedley, “Quantitative image analysis of immunohistochemical stains using a cmyk color model,” *Diagnostic pathology*, vol. 2, no. 1, p. 8, 2007.
- [9] J. Van der Laak, J. R. Westphal, L. J. Schalkwijk, M. M. Pahlplatz, D. Ruiters, R. De Waal, and P. De Wilde, “An improved procedure to quantify tumor vascularity using true color image analysis: Comparison with the manual hot-spot procedure in a human melanoma xenograft model,” *J Pathol*, vol. 184, pp. 136–143, 1998.
- [10] M. K. K. Niazi, K. Yao, D. Zynger, S. Clinton, J. Chen, M. Koyuturk, T. LaFramboise, and M. Gurcan, “Visually meaningful histopathological features for automatic grading of prostate cancer,” 2016.
- [11] V. N. Kovacheva, D. Snead, and N. M. Rajpoot, “A model of the spatial tumour heterogeneity in colorectal adenocarcinoma tissue,” *BMC bioinformatics*, vol. 17, no. 1, p. 1, 2016.
- [12] J. N. Kather, A. Marx, C. C. Reyes-Aldasoro, L. R. Schad, F. G. Zollner, and C.-A. Weis, “Continuous representation of tumor microvessel density and detection of angiogenic hotspots in histological whole-slide images,” *Oncotarget*, vol. 6, no. 22, p. 19 163, 2015.

- [13] C.-H. Tsou, Y.-C. Lu, A. Yuan, Y.-C. Chang, and C.-M. Chen, “A heuristic framework for image filtering and segmentation: Application to blood vessel immunohistochemistry,” *Analytical Cellular Pathology*, vol. 2015, 2015.
- [14] A. Belsare, M. Mushrif, M. Pangarkar, and N. Meshram, “Breast histopathology image segmentation using spatio-colour-texture based graph partition method,” *Journal of microscopy*, 2015.
- [15] F. Liu, A. Mackey, R. Srikuea, K. Esser, and L. Yang, “Automated image segmentation of haematoxylin and eosin stained skeletal muscle cross-sections,” *Journal of microscopy*, vol. 252, no. 3, pp. 275–285, 2013.
- [16] A. C. Ruifrok and D. A. Johnston, “Quantification of histochemical staining by color deconvolution,” *Anal Quant Cytol Histol*, vol. 23, no. 4, pp. 291–9, 2001.
- [17] Z. Guo and R. W. Hall, “Parallel thinning with two-subiteration algorithms,” *Communications of the ACM*, vol. 32, no. 3, pp. 359–373, 1989.
- [18] P. S. Aleksandrov, *Combinatorial topology*. Courier Corporation, 1956, vol. 1.
- [19] H. W. Kuhn, “Variants of the hungarian method for assignment problems,” *Naval Research Logistics Quarterly*, vol. 3, no. 4, pp. 253–258, 1956.
- [20] N. Otsu, “A threshold selection method from gray-level histogram,” *IEEE Transactions on Systems, Man and Cybernetics*, vol. 9, no. 1, pp. 62–66, 1979.
- [21] S. E. Jones, B. R. Buchbinder, and I. Aharon, “Three-dimensional mapping of cortical thickness using laplace’s equation,” *Human brain mapping*, vol. 11, no. 1, pp. 12–32, 2000.
- [22] S. Akerman, M. Fisher, R. A. Daniel, D. Lefley, C. C. Reyes-Aldasoro, S. J. Lunt, S. Harris, M. Bjorndahl, L. J. Williams, and H. Evans, “Influence of soluble or matrix-bound isoforms of vascular endothelial growth factor-a on tumor response to vascular-targeted strategies,” *International Journal of Cancer*, vol. 133, no. 11, pp. 2563–2576, 2013.
- [23] C. M. Bishop, *Pattern recognition and machine learning*. springer, 2006.
- [24] M. J. West, “Stereological methods for estimating the total number of neurons and synapses: Issues of precision and bias,” *Trends in neurosciences*, vol. 22, no. 2, pp. 51–61, 1999.
- [25] S. Herculano-Houzel, C. S. von Bartheld, D. J. Miller, and J. H. Kaas, “How to count cells: The advantages and disadvantages of the isotropic fractionator compared with stereology,” *Cell and tissue research*, vol. 360, no. 1, pp. 29–42, 2015.

- [26] A. M. Khan, N. Rajpoot, D. Treanor, and D. Magee, "A nonlinear mapping approach to stain normalization in digital histopathology images using image-specific color deconvolution," *Biomedical Engineering, IEEE Transactions on*, vol. 61, no. 6, pp. 1729–1738, 2014.
- [27] M. Gavrilovic, J. C. Azar, J. Lindblad, C. Wahlby, E. Bengtsson, C. Busch, and I. B. Carlbom, "Blind color decomposition of histological images," *Medical Imaging, IEEE Transactions on*, vol. 32, no. 6, pp. 983–994, 2013, ID: 1.
- [28] M. Niethammer, D. Borland, J. Marron, J. T. Woosley, and N. E. Thomas, "Appearance normalization of histology slides," in *MLMI*, Springer, 2010, pp. 58–66.
- [29] Y. Xu, J. G. Pickering, Z. Nong, E. Gibson, J.-M. Arpino, H. Yin, and A. D. Ward, "A method for 3d histopathology reconstruction supporting mouse microvasculature analysis," *PloS One*, vol. 10, no. 5, e0126817, 2015.
- [30] S. Chen, M. Zhao, G. Wu, C. Yao, and J. Zhang, "Recent advances in morphological cell image analysis," *Computational and mathematical methods in medicine*, vol. 1, 2012.
- [31] W. Xue, S. Chen, H. Yin, T. Tammela, T. Papagiannakopoulos, N. S. Joshi, W. Cai, G. Yang, R. Bronson, and D. G. Crowley, "Crispr-mediated direct mutation of cancer genes in the mouse liver," *Nature*, vol. 514, no. 7522, pp. 380–384, 2014.
- [32] L. Pinto, M. J. Goard, D. Estandian, M. Xu, A. C. Kwan, S.-H. Lee, T. C. Harrison, G. Feng, and Y. Dan, "Fast modulation of visual perception by basal forebrain cholinergic neurons," *Nature neuroscience*, vol. 16, no. 12, pp. 1857–1863, 2013.
- [33] S. Huber, N. Gagliani, L. A. Zenewicz, F. J. Huber, L. Bosurgi, B. Hu, M. Hedl, W. Zhang, W. O'Connor, and A. J. Murphy, "Il-22bp is regulated by the inflammasome and modulates tumorigenesis in the intestine," *Nature*, vol. 491, no. 7423, pp. 259–263, 2012.
- [34] M. T. Heneka, M. P. Kummer, A. Stutz, A. Delekate, S. Schwartz, A. Vieira-Saecker, A. Griep, D. Axt, A. Remus, and T.-C. Tzeng, "Nlrp3 is activated in alzheimer's disease and contributes to pathology in app/ps1 mice," *Nature*, vol. 493, no. 7434, pp. 674–678, 2013.

Chapter 4

Differentiation of Arterioles from Venules in Mouse Histology Images Using Machine Learning

The contents of this chapter were previously published in the Journal of Medical Imaging: Elkerton JS, Xu Y, Pickering JG, Ward AD. Differentiation of arterioles from venules in mouse histology images using machine learning. Journal of Medical Imaging. 2017 Apr 1;4(2):021104. Permission to reproduce this article was granted by SPIE and is provided in Appendix A.

4.1 Introduction

The microvascular network consists of a hierarchical arrangement of arterioles, capillaries and venules. Of these vessel categories, the arterioles and venules are wrapped by vascular smooth muscle cells. They serve vital functions delivering blood to and from the tissue to ensure oxygen and nutrient requirements are met. Assessment of the arteriolar and venular content, wall structure, and network organization is thus essential to our understanding of multiple disease scenarios. For example, in the eye, narrowing of retinal arterioles is related to diabetic macular ischemia [1] and the arteriole-to-venule ratio is associated with hypertensive retinopathy. [2] In the brain, proper arteriolar function is essential to maintaining adequate cerebral blood flow; occlusion of even a single penetrating arteriole connecting the pial network to the subsurface network results in the death of a 0.5 mm cylinder of cortical tissue. [3] In Alzheimer's disease, penetrating arterioles become tortuous whereas the venules do not. [4] Arterioles and venules may also have distinct genetic drivers during embryonic development of the cardiovascular

system as well as angiogenesis in the adult. [5] Importantly however, histologic analysis of the microvasculature is far more complex than for the macrovasculature. The small caliber vessels and their vast content carry a substantial risk of not reliably distinguishing arterioles from venules. Thus, it is critical to have approaches that visualize and quantify microvascular networks that can also distinguish, analyze and compare arterioles and venules.

Brightfield histology provides a wealth of information about vessel wall structure, with a multitude of stains available to capture different structural aspects. For assessing the microvasculature, whole-mount slide scanners for digitization of entire tissue cross sections at $0.25 \mu\text{m}$ pixel size is particularly helpful. [6] However, the volume of the acquired data makes comprehensive analysis very challenging; manual detection and measurement of vessels in tissue requires a prohibitive amount of time. An automated microvessel detection and segmentation algorithm for histological mouse hind limb tissue has been previously reported [7] and other semi-automated approaches have been developed for this task. [8] However, to the best of our knowledge, no automated method has yet been developed to classify arterioles and venules to allow for the separate analysis of arteriolar and venular structure. Such a system would eliminate the need for the laborious and observer-dependent manual classification performed in previous studies. [9]–[11] Our interest is in understanding the cellular structure of the microvascular vessel wall both under normal circumstances and in the post-ischemic and regenerated microvasculature. Such a comparison may yield powerful insights into improving therapeutic regimes after stroke or myocardial infarction. However, in regenerated tissue, the arterioles and venules can be even more difficult to classify, partially due to the fact that newly-generated arterioles often lack a fully-developed vessel wall structure and can have a similar appearance on histology to venules. [12] This leads to a strong dependence on a skilled observer to make the distinction between arterioles and venules.

In this chapter, we addressed this issue by designing, implementing, and testing a software system for automatic classification of arterioles and venules on brightfield histology of the mouse hind limb smooth muscle. The system automatically detects and segments microvessels throughout the whole slide using our method described in. [7] It then extracts texture and morphologic features from all the vessels, performs feature selection to extract the most useful features for classification, and trains a classifier via supervised machine learning. We tested system performance using cross validation on a sample containing tissue samples from normal mice, and from mice previously subjected to hind limb ischemia.

4.2 Materials and Methods

4.2.1 Materials

The experiments were conducted on tissue samples of the upper one third tibialis anterior hind limb muscle from 10 wild type C57BL/J6 mice (1 tissue section per mouse). In 5 of the 10 mice, tissue was collected two weeks after induction of hind limb ischemia by femoral artery excision; these samples were expected to contain regenerated vasculature, where the surgeries were performed under isoflurane anesthesia. The post-ischemic samples are referred to as the regenerated samples. This particular muscle segment was selected because of the consistent development of microvessels of various sizes following hind limb ischemia. The mice were perfused with saline post-mortem to remove the red blood cells from the vessel lumina and then perfusion-fixed at physiological pressure with 4% paraformaldehyde. The tissues were processed and paraffin-embedded after harvesting, then cut into 7 mm by 5 mm blocks and sectioned at 5 μm . All experiments in this study were approved by the Animal Care and Veterinary Service Committee at The University of Western Ontario (Protocol # 2010-244) and were carried out in accordance with their requirements.

To visualize the smooth muscle distribution down to the level of the arterioles and venules, sections were immunostained with smooth muscle α -actin using a monoclonal antibody (DAKO, M0851), and bound primary antibody detected with horseradish peroxidase (HRP)-conjugated secondary antibody and 3,3'-Diaminobenzidine chromogen (DAB, Vector Laboratories, SK-4100). This marked the smooth muscle layer of the vasculature (resulting in the vessel walls being stained with a brown colour) which is shown in Figure 4.1(a). The tissue was then counter stained with hematoxylin, resulting in blue-stained nuclei. The immunostain was performed manually and the samples were processed in two separate batches. The stained sections were then imaged with a ScanScope CS (Aperio Technologies, Vista, CA, USA) bright field slide scanner, at 40 \times objective magnification (achieved on this scanner using a 20 objective with the 2 \times magnification engaged), yielding a 0.25 μm isotropic pixel size. This resulted in whole slide image dimensions ranging between 12341-26398 pixels in height and 9000-17135 pixels in width.

One tissue section was analyzed from each mouse, where each tissue section was known to be either normal or regenerated post-ischemia, with vessels detected and segmented automatically using our previously reported method. [7] Our segmentation algorithm resulted in a Dice similarity coefficient of 0.89 with no bias towards over- or under-segmentation and a detection sensitivity and specificity of 0.91 and 0.97 respectively, and the whole tissue section was automatically extracted from the whole slide scan. A sample vessel and its segmentation are shown in Figure 4.1. Every vessel on the whole slide image was manually classified by the

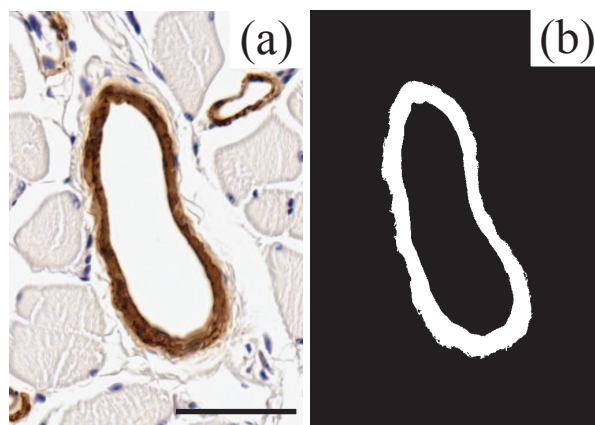


Figure 4.1: Arteriole with the DAB stain (a), and the binary mask (b) output from the automated segmentation. Scale bar is $50 \mu\text{m}$.

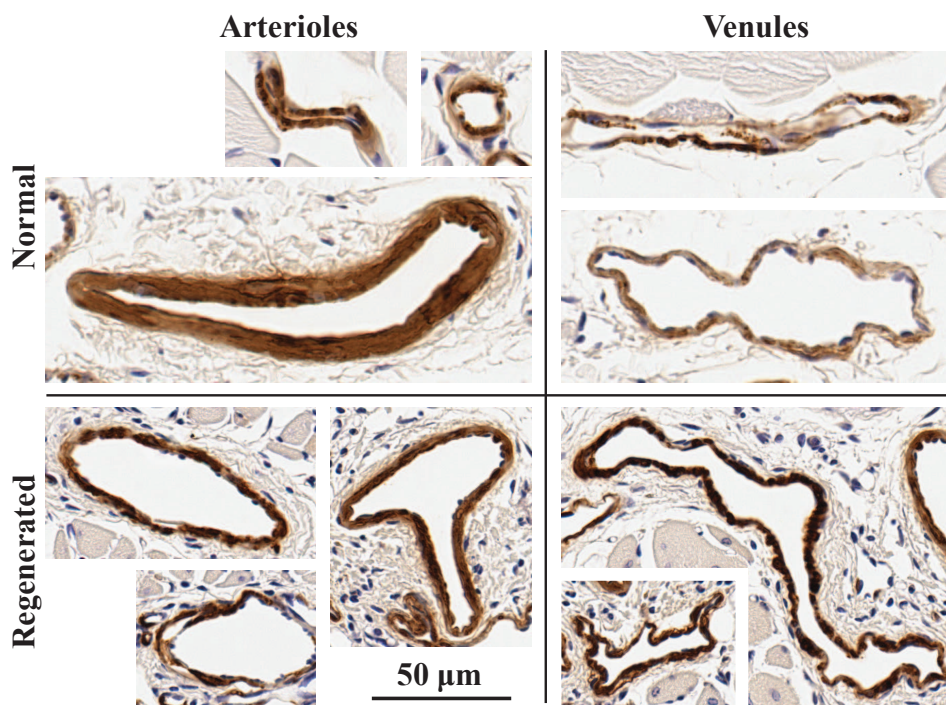


Figure 4.2: Arterioles and venules are shown in the normal and regenerated tissues. The microvessels have distinguishable differences in the normal vasculature where the smooth muscle layer is thicker and more pronounced on the arteriolar side and have a visibly darker stain. Venules also appear to have a more tortuous vessel wall. This difference is less apparent in the regenerated vasculature.

consensus of two observers (i.e. both observers had to be in agreement) into the classes: arteriole, venule, or unknown/other based on vessel size, thickness of the vessel walls, intensity of

the vessel walls, and the relative location of the vessel (Fig. 4.2). Only the arteriole and venule image classes were used for this experiment, with a total of 192 arterioles and 127 venules. This included all vessel sections that the observers were confidently able to classify manually. Each of the 10 mice had a total of 7-66 vessels used from each tissue section.

4.2.2 Methods overview

After automatic vessel detection and segmentation which defined the outer boundary of the vessel wall and the vessel lumen, features were extracted from these vessel walls. This included statistical, texture and morphological features to use for supervised machine learning. Cross validation was used to test the system's ability to differentiate arterioles from venules, with the manual classifications used as the reference standard for comparison (Figure 4.3).

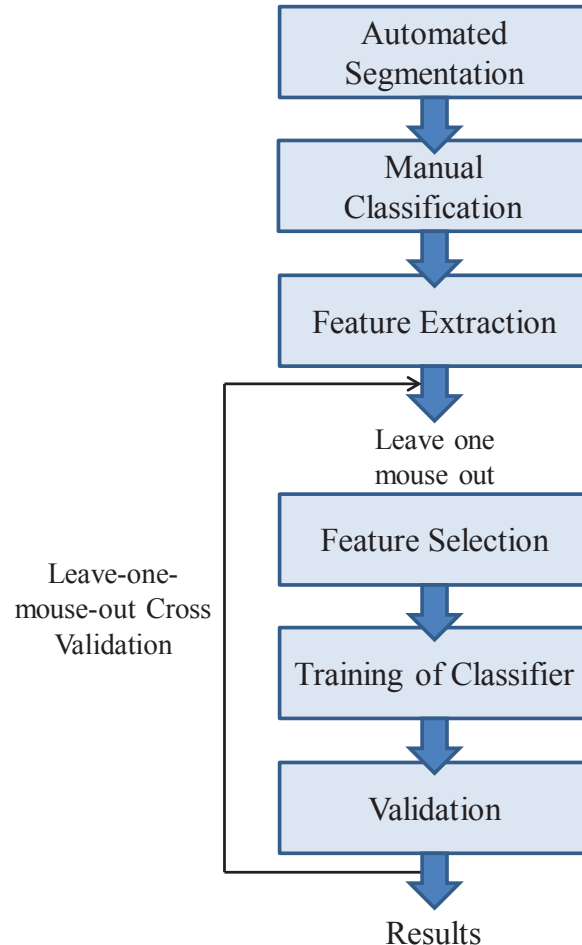


Figure 4.3: Block diagram to demonstrate the method followed in this experiment for a leave-one-mouse-out cross validation.

4.2.3 Feature extraction

First and second-order feature computation was performed within each segmented vessel wall on 10 colour channels separately: 3 red green and blue (RGB), 3 hue saturation and value (HSV), three Lab, and a DAB stain channel extracted by colour deconvolution. [13], [14] The colour images were decomposed into separate channels as they carry different information regarding the stains represented in the image. For example, HSV takes into the account the colour spectrum, saturation of the colour and the brightness of the image and Lab space includes all perceivable colours and approximates human perception of colour differences. Twenty-two first-order features and 22 second-order gray-level co-occurrence matrix (GLCM) texture features [15] were calculated on each colour channel (Table S4.4/5). The GLCM calculations were performed in all 4 neighboring pixel directions, which were then averaged. 19 morphological features were also computed. In total, 459 features were computed for each vessel (Table S4.4/5).

4.2.4 Feature selection

In an effort to select the optimal combination of features, forward feature selection was performed and evaluated using PRTools 5.2.1 (Delft Pattern Recognition Research, Delft, The Netherlands), with an inter-intra class distance criterion. [16] Other forms of feature selection were not explored with our limited sample size in order to avoid overfitting. It is important to note that feature selection was performed only on the training set at each iteration of cross validation. The entire data set was not used to select a single set of features for supervised machine learning. The number of features used for classification was chosen by completing the process for several different numbers of features and comparing the resulting errors and AUCs. It was desired to minimize error and maximize the AUC while keeping the set of features consistent through the cross validations.

4.2.5 Supervised machine learning

We tested the performance of three different machine learning classifiers using the selected features, performed using PRTools. The following classifiers were used: support vector machine (SVM), random forest classifier (RFC), and logistic linear classifier (LOGLC). The SVM calculates the separation by maximizing the margin between the support vectors of the two classes [17], trained with a linear kernel. In the random forest approach, multiple decision trees are created by sampling different feature and data subsets, with classification determined by the majority vote from all the trees. [18] 50 decision trees were trained for each classifier, each

with data subsets chosen by bootstrapping. LOGLC is a linear classifier computed by maximum likelihood estimation using the logistic function. [19], [20]

To optimize the classifier performance, all the features were normalized. This was done by taking each individual feature, subtracting the mean and dividing by the standard deviation. It is important to normalize the features because of classifiers that are sensitive to the scale of the features, such as the SVM. [21] The other classifiers were unaffected by this normalization.

4.2.6 Validation

Two separate analyses were performed in order to validate the resulting classifiers. First, each classifier was tested using a leave-one-mouse-out (LOMO) cross validation (at each iteration, one mouse sample was left out). Feature selection and normalization was performed on the training set at each iteration and the selected features were used to train the classifiers. The classification error rate, false positive rate (FPR), false negative rate (FNR) and area under the receiver operating characteristic curve (AUC) were measured for each classifier. For this experiment, a classification as an arteriole was considered to be a positive classification. In the second experiment, a single classifier was defined using an independent training set and tested on a separate testing set. Six mice were used for training (3 normal, 3 regenerated), and 4 mice were used for testing (remaining 2 normal and 2 regenerated). Aggregation of values in the receiver operating characteristic (ROC) curves by averaging in the first experiment may add a degree of freedom to the analysis; however, there is no such aggregation in experiment two. The performance of the single classifier was validated with the testing set with the same classification errors as the cross validation experiment.

4.2.7 Classifier Confidence

A confidence value was assigned to each vessel ranging from 0 to 1, where the confidence threshold of 0.5 determines the binary classification of each vessel. For the random forest, the confidence was based on the proportion of positive votes from all of the decision trees. For the LOGLC and SVM, confidence was based on distance from the classification boundary which was then scaled by a sigmoid function. [16]

In order to reduce the classification error rates, vessels with varying confidence levels were thresholded and removed. The lowest confidence level is 0.5, representing the situation where the vessel lies on the decision boundary in feature space, and the highest confidence level is 1.0. This enables the system to retain vessels which were classified with high confidence and to eliminate vessels with confidence values near the decision boundary, which have a higher

proportion of false positives. This shrinks the data set, but lowers the error rates, and can be performed depending on the distribution of confidence values in a given sample.

4.2.8 Statistics

To determine statistical significance, a two-way ANOVA test was done. This was performed on the classification error, FNR and FPR with the two factors of vessel type (normal and regenerated) and classifier type (RFC, LOGLC and SVM). A separate ANOVA was done to also test for significant differences in errors between the classifier types and between classifiers trained using different numbers of features.

4.3 Results

4.3.1 Experiment 1

The differences between the three classifiers with respect to the number of features used for each classifier were reported in order to test the sensitivity of each classifier to the number of features. Significant differences in the error rates ($p < 0.05$) were found between the 1-feature and 2-feature classifiers; no other significant differences were found (Fig 4.4b). All classifiers were trained on features from forward feature selection and evaluated using a LOMO cross validation. The AUCs leveled off after 2-3 features at AUCs of > 0.89 for the LOGLC, > 0.89 for the SVM, and > 0.84 for the RFC (Figure 4.4a). Diminishing returns on error rates were observed beyond 2 features, for which the LOGLC had an error rate of 17%, the SVM 16%, and the RFC 21% (Figure 4.4b).

The sets of 3 features chosen from forward feature selection are shown in Figure 4.5. The features chosen consistently at each of the 10 LOMO cross validations were Area Perimeter Ratio (the ratio of the vessel wall area to the outer perimeter squared), and DAB Skewness (skewness in the DAB channel). The third feature chosen was not consistent with every cross validation. The errors resulting from the 2-feature classifiers are discussed for the remainder of the results below.

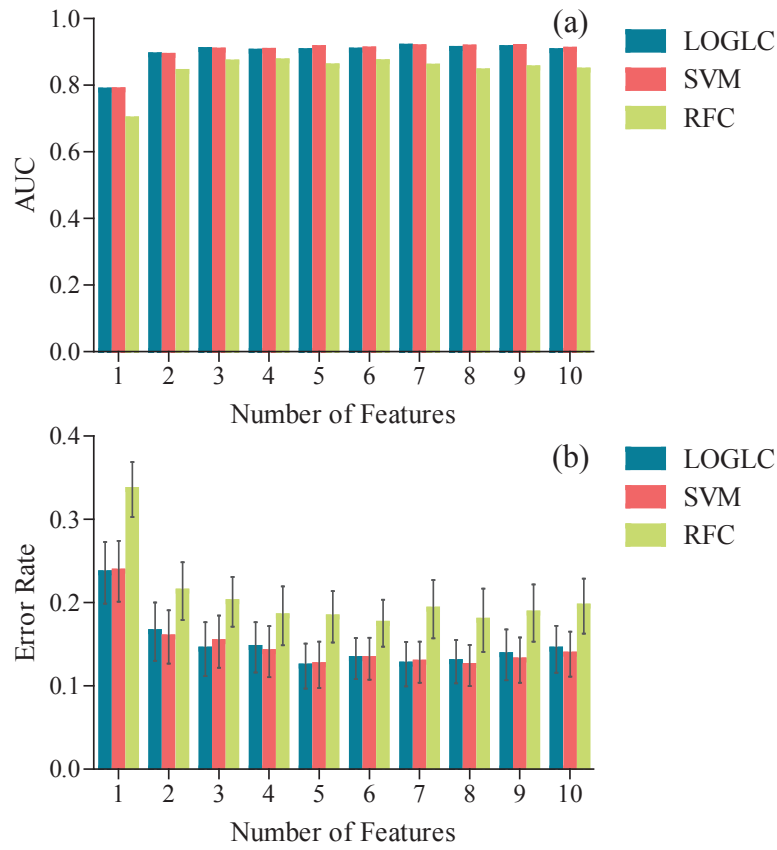


Figure 4.4: AUC (a) and error rate (b) as a function of number of features used for classification. The error bars represent the standard error of the mean. All features were chosen using a forward feature selection and classifiers were trained with a LOMO cross validation.

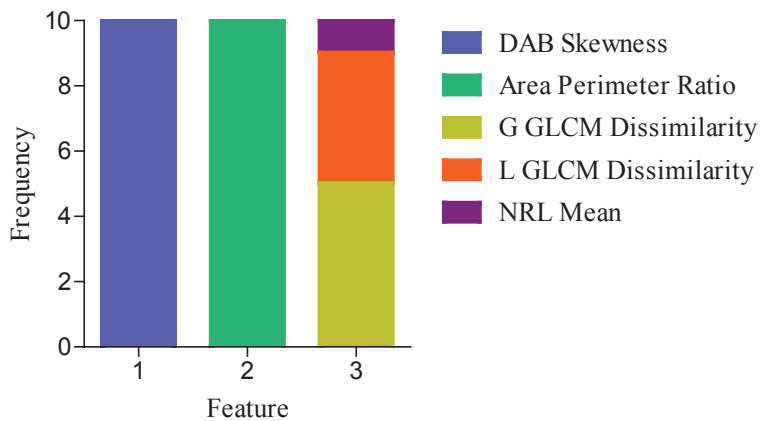


Figure 4.5: Three features chosen from forward feature selection over the 10 cross validations.

The classification performance metrics using 2 features is provided in Table 4.1, where the metrics for normal and regenerated tissues are shown separately. For Table 4.1, all three classifiers performed similarly, with mean classification error rates between 17% and 21%, and AUCs between 0.84 and 0.89. The ROC curves for each classifier type are shown in Figure 4.6, where the curves were averaged over 10 cross validations. Each mouse sample was given equal weightings for the ROC curves. However, ROC curve averaging may add a degree of freedom to the analysis. By contrast, in the second experiment, only one ROC curve was computed using a single classifier and a larger testing set.

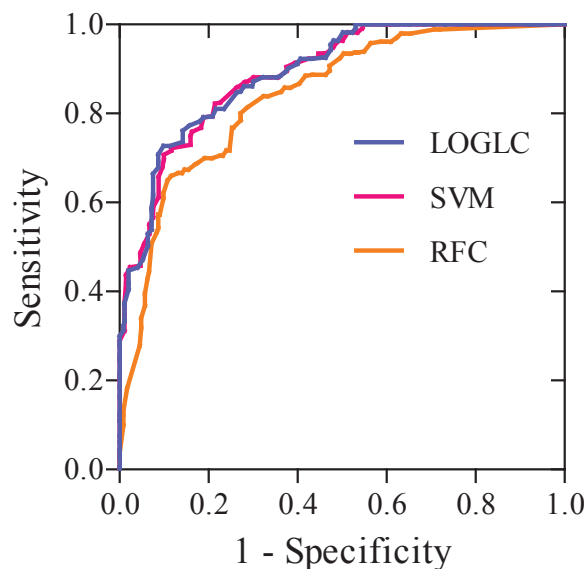


Figure 4.6: Receiver operating characteristic curves for each of the classifiers trained on 2 features. LOGLC AUC: 0.89, SVM AUC: 0.89, RFC AUC: 0.84.

Table 4.1: Performance metrics from cross validation using 2 features from forward feature selection (mean \pm SD) All Vessels

	All Vessels		
	LOGLC	SVM	RFC
Error Rate	0.17 \pm 0.11	0.16 \pm 0.10	0.21 \pm 0.11
False Negative Rate	0.15 \pm 0.24	0.14 \pm 0.22	0.22 \pm 0.27
False Positive Rate	0.26 \pm 0.32	0.26 \pm 0.32	0.25 \pm 0.24
AUC	0.89	0.89	0.84
	Normal		
	LOGLC	SVM	RFC
Error Rate	0.12 \pm 0.11	0.11 \pm 0.11	0.15 \pm 0.10
False Negative Rate	0.04 \pm 0.06	0.04 \pm 0.05	0.12 \pm 0.13
False Positive Rate	0.31 \pm 0.41	0.31 \pm 0.41	0.23 \pm 0.16
AUC	0.94	0.93	0.9
	Regenerated		
	LOGLC	SVM	RFC
Error Rate	0.21 \pm 0.10	0.20 \pm 0.08	0.29 \pm 0.06
False Negative Rate	0.27 \pm 0.31	0.25 \pm 0.28	0.33 \pm 0.36
False Positive Rate	0.21 \pm 0.25	0.21 \pm 0.25	0.33 \pm 0.32
AUC	0.84	0.85	0.81

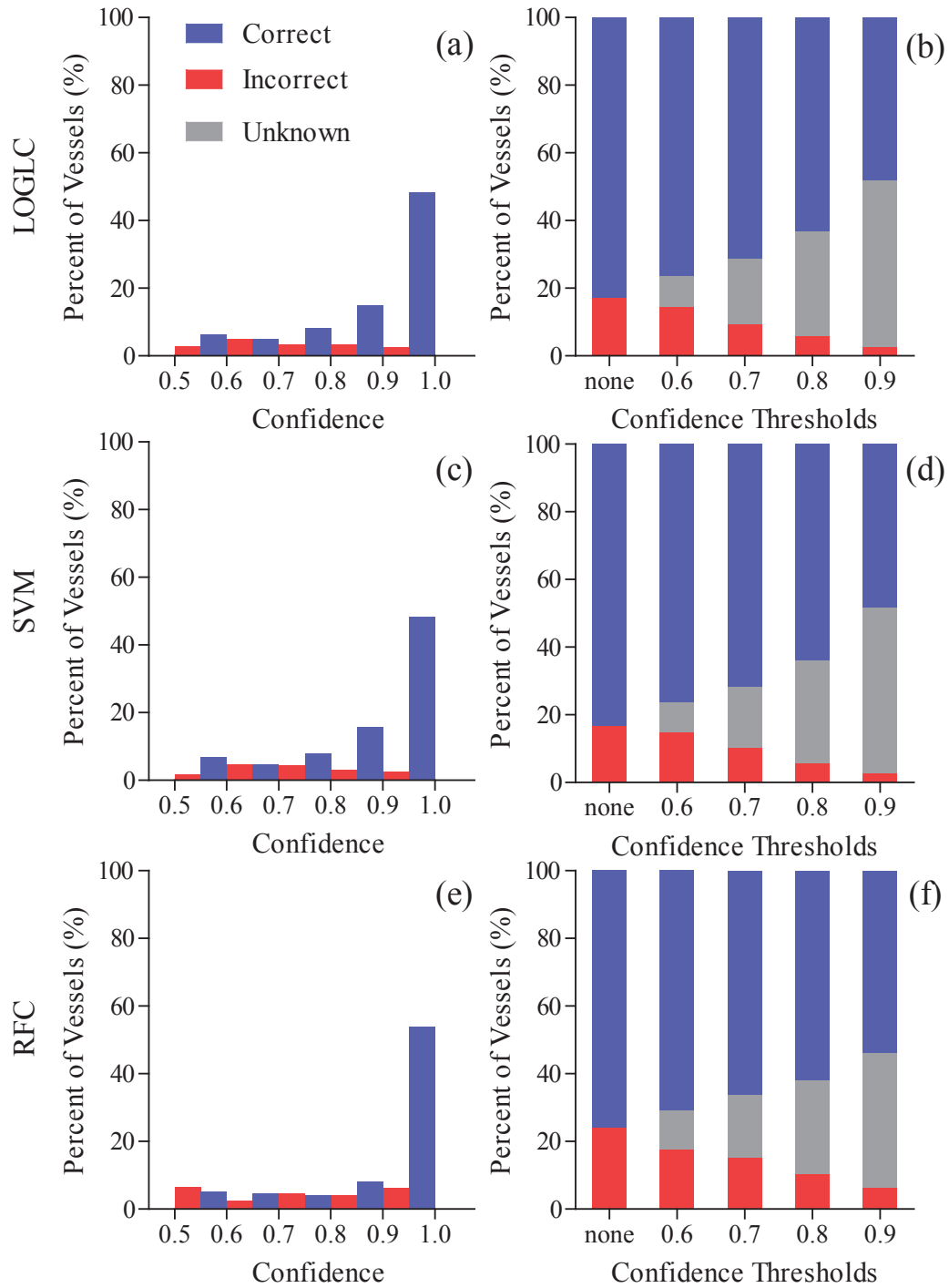


Figure 4.7: Histogram of the confidences from the LOGLC (a,b), SVM (c,d) and RFC (e,f) classification using 2 features with their respective confidence thresholds, where “none” indicates no confidence threshold was applied and all vessels were categorized.

The distribution of correctly and incorrectly classified vessels by the LOGLC, SVM and RFC respectively for different levels of classifier confidence are shown in Figure 4.7 using 2 features. The LOGLC has 48%, SVM has 48%, and RFC has 54% of the vessels being correctly classified with confidence >0.9 . The results from categorizing vessels based on varying confidence thresholds reduced the proportion of incorrectly classified vessels (Figure 4.7), where no removal of vessels or no confidence threshold is denoted by “none”. The error rates of the remaining vessels after the removal of lower confidence vessels after a confidence threshold are shown in Table 4.2. As an example of how this confidence level was used, in Table 4.2, the results reported in the “RFC” row and the “0.9” column show that 39.81% of all the classified vessels had confidence thresholds < 0.9 . Removing those vessels from the analysis resulted in a classification error of 10.42% using an RFC. By contrast, the “none” column shows the classification error when no confidence threshold was applied; this column shows the classification errors using all vessels regardless of their confidence values. A two-way ANOVA test

Table 4.2: The classification errors from the 2 featured forward feature selection with a LOMO cross validation as the confidence threshold increases and vessels are eliminated.

		Confidence Threshold				
		none	0.6	0.7	0.8	0.9
LOGLC	Classification Error	17.24	15.86	11.63	8.6	4.94
	Fraction Removed		9.09	19.12	30.72	49.22
SVM	Classification Error	16.61	16.15	12.26	8.11	4.94
	Fraction Removed		8.78	18.18	30.41	49.22
RFC	Classification Error	24.14	19.86	18.53	14.29	10.42
	Fraction Removed		11.6	18.81	27.59	39.81

was performed to determine statistical significance between the different classifiers and normal versus regenerated tissues. This was performed separately for the error rates, FNRs and FPRs. There was found to be no statistical difference between the three classifiers ($p > 0.05$). There was statistical difference between the normal and regenerated tissue error rates and FNRs ($p < 0.05$) but not the FPRs ($p > 0.05$).

A repeated measures two-way ANOVA was also performed on the different classifiers, and between the errors from using 2 features and 3 features. Again there was found to be no statistical difference between the three classifiers ($p > 0.05$), nor between the errors using 2 and 3 features ($p > 0.05$).

4.3.2 Experiment 2

A single classifier was defined using an independent training set (6 mouse samples; 3 normal and 3 regenerated) and tested on a separate testing set (4 mouse samples; 2 normal and 2 regenerated). In total, there were 206 vessels (84 normal and 122 regenerated) in the training set and 113 vessels (50 normal and 63 regenerated) in the testing set.

The AUCs leveled off after 2 features at AUCs of >0.90 for the LOGLC, >0.91 for the SVM, and >0.89 for the RFC (Figure 4.8a). Diminishing returns on error rates were observed beyond 2 features, for which the LOGLC had an error rate of 15%, the SVM 17%, and the RFC 21% (Figure 4.8b).

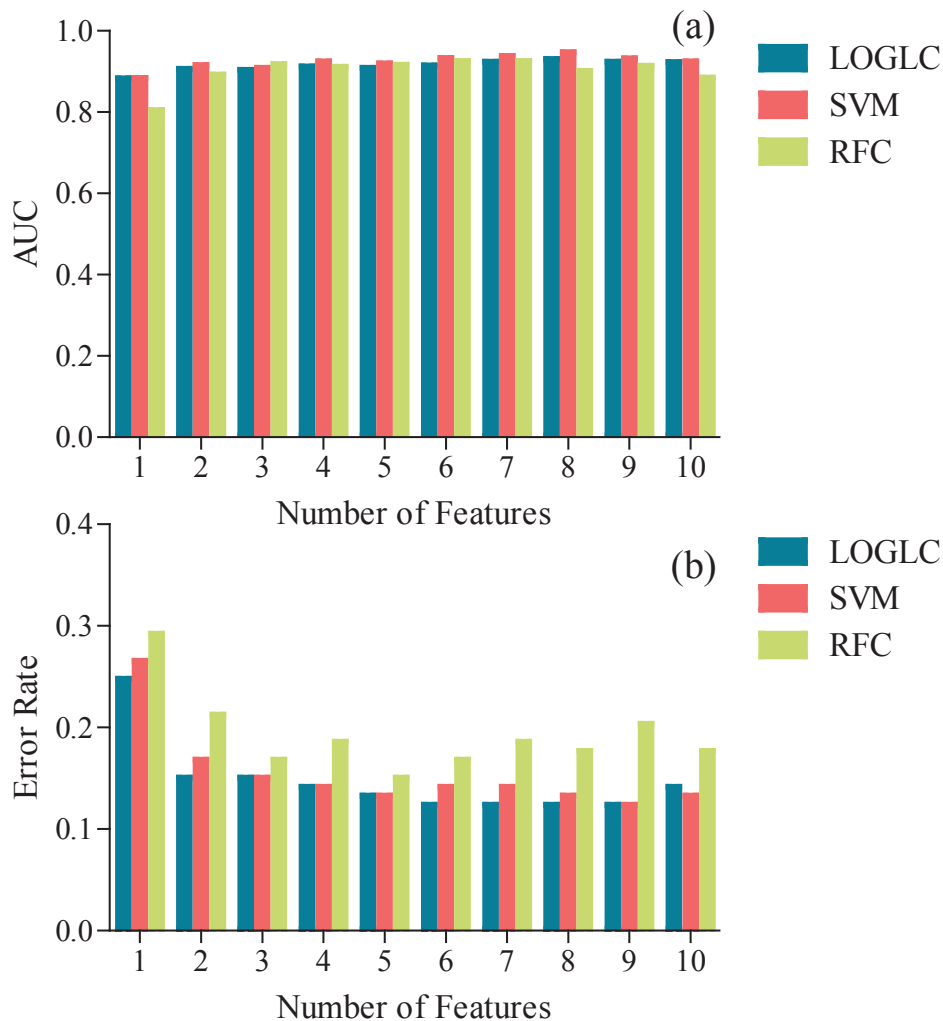


Figure 4.8: AUC (a) and error rate (b) as a function of number of features used for classification. All features were chosen using a forward feature selection and classifiers were trained with an independent training set.

The forward feature selection resulted in the selection DAB Skewness and Area Perimeter Ratio as the top two features. These features chosen were identical those chosen in the LOMO cross validation.

The error metrics are shown in Table 4.3 using those 2 features, and AUC curves are shown in Figure 4.9. The classifier confidence histograms for all the classifiers with confidence threshold levels are shown in Figure 4.10.

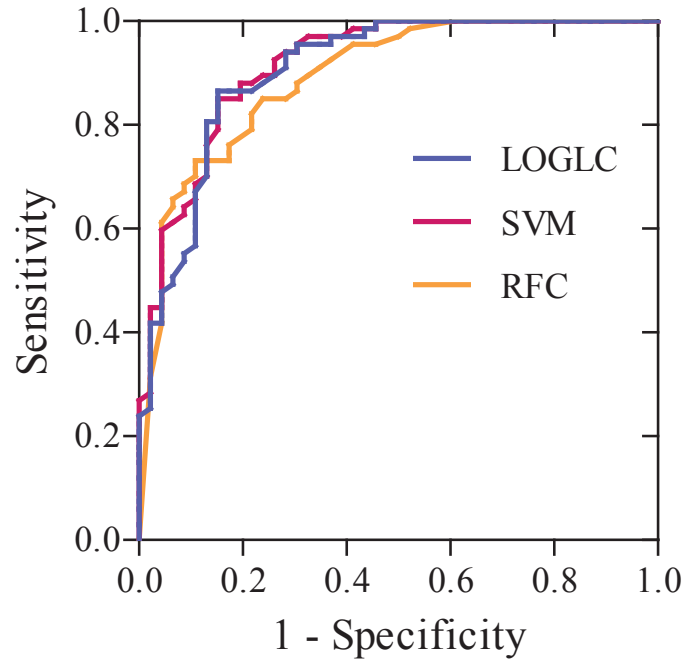


Figure 4.9: Receiver operating characteristic curves for each of the classifiers from classifier trained on 2 features. LOGLC AUC: 0.91, SVM AUC: 0.92, RFC AUC: 0.89.

Table 4.3: Performance metrics using 2 features from forward feature selection.

	All Vessels		
	LOGLC	SVM	RFC
Error Rate	0.15	0.17	0.21
False Negative Rate	0.15	0.15	0.24
False Positive Rate	0.15	0.2	0.17
AUC	0.91	0.92	0.89
	Normal		
	LOGLC	SVM	RFC
Error Rate	0.06	0.1	0.16
False Negative Rate	0.08	0.08	0.23
False Positive Rate	0.04	0.12	0.08
AUC	0.97	0.95	0.92
	Regenerated		
	LOGLC	SVM	RFC
Error Rate	0.22	0.22	0.25
False Negative Rate	0.2	0.2	0.24
False Positive Rate	0.27	0.27	0.27
AUC	0.85	0.84	0.87

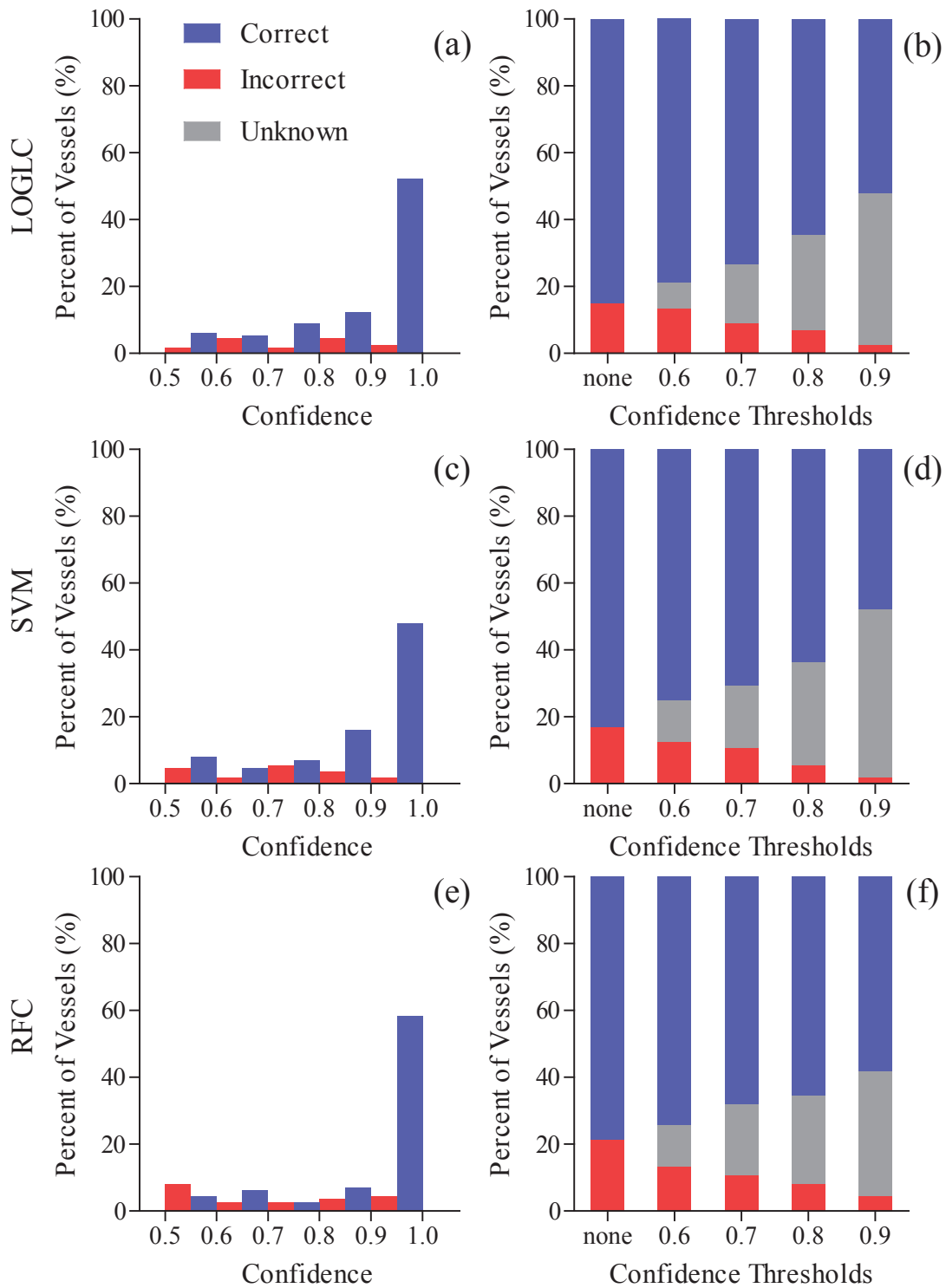


Figure 4.10: Histogram of the confidences from the LOGLC (a,b), SVM (c,d) and RFC (e,f) classifications with their respective confidence thresholds.

4.4 Discussion

Both arterioles and venules contain smooth muscle cells, which are contractile cells that wrap the endothelial cells. We have established that differentiation of these two types of microvessels is feasible with the use of supervised machine learning. All of the tested classifiers provided promising performance, with AUCs between 0.84 and 0.89 determined by cross validation for our two-featured forward feature selection, where the same two features were consistently chosen. Error rate, FNR, and FPR were consistent across classifiers and only two features were required to achieve the reported performance. Variability in vessel size, shape, and staining was observed in our data set. The upper row in Figure 4.11 shows arterioles that were incorrectly classified as venules ($0.6 < \text{confidence} < 0.9$). The lower row shows correctly classified arterioles ($0.6 < \text{confidence} < 1.0$); note the variability in size, shape, and staining tolerated by the LOGLC.

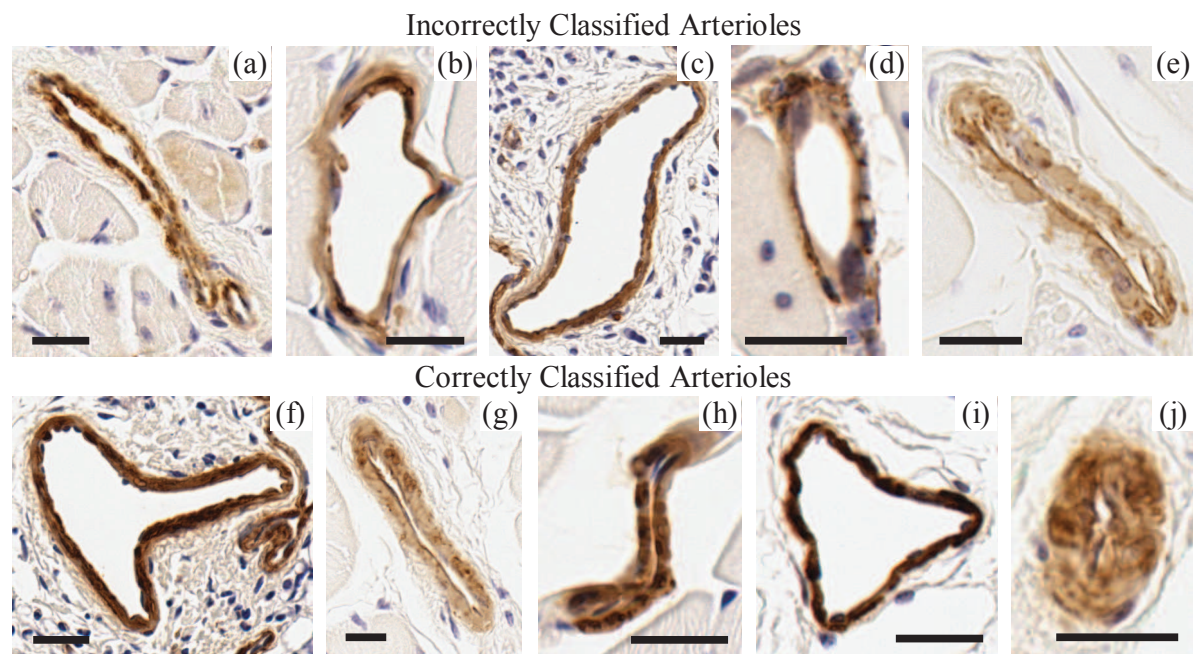


Figure 4.11: Incorrectly (a-e) and correctly (f-j) classified arterioles by the LOGLC. Scale bar is $20 \mu m$

The ability to accurately separate the arterioles from the venules is a key step in analyzing the vascular system. The arterioles control the blood flow directly leading to the capillaries whereas venules are critical to the outflow of blood and tissue waste products. Not only does their function differ but the manner in which they remodel during disease can differ. Accordingly, assessment of diseases characterized by ischemia, injury, and inflammation may be

substantially enhanced by separating the two types of vessels. [1]–[5] Automatic separation allows for fast, high volume analysis that is not user-dependent. This will ultimately be included in a total automated procedure that will include detection and segmentation [7], 3D reconstruction [6], and analysis. The 2 features chosen during forward feature selection were consistent with each round of cross validation. This is promising and suggests generalizability of classifiers trained on these features. Although the error rates were slightly better in the 3-feature system, the inconsistent choice of the third feature across iterations makes this a less favorable solution. The two features chosen included a morphological feature, Area Perimeter Ratio, and vessel wall intensity feature, DAB Skewness, and they were both chosen at every round of cross validation. The utility of the Area Perimeter Ratio feature is concordant with the fact that venules are in general thinner and have less vessel wall area compared to arterioles, which generally have thicker walls. It also may capture the amount of waviness of the vessel walls where the venules in general have more curved walls than arterioles. The other selected feature that was chosen for every cross validation was the DAB Skewness, which is concordant with the fact that in general, arterioles are more darkly stained than the venules since they have more smooth muscle. It is most likely the lack of dark DAB stain on many of the venules, and the original DAB threshold used for segmentation, that causes a positive skewness on many of the venules. The performance based on the type of classifier used was evaluated. There was no significant difference between the errors from each of the classifiers ($p < 0.05$). This indicates that the error rates are independent of the classifier used.

The classification was performed on independent training and testing sets and demonstrated the consistency of the feature selection and classification processes. In order to maintain the generalizability of the classifier with two features, linear and Random Forest classifiers were used to prevent overfitting to our current dataset. The features chosen were consistent with the features chosen during cross validation including one feature based on vessel shape, Area Perimeter Ratio and the other feature based on vessel stain content with regard to intensity in the form of DAB Skewness. The error rates were also comparable to the rates when performing a LOMO cross validation. This suggests the possibility of using a single trained classifier that will be able to separate the vasculature accurately on unseen data.

We observed that in many instances of incorrect vessel classification, errors occurred due to staining variability (e.g. weak staining in Figure 4.11(e)). Lightly stained arterioles tended to be incorrectly classified as venules, and heavily stained venules incorrectly classified as arterioles. This suggests a need for additional preprocessing to normalize the images for the overall level of staining on each slide. Unusually thin-walled arterioles also caused false negatives while thick-walled venules caused false positives. Many of these unusually thick or thin vessels came from the regenerated vasculature. Figure 4.11(a-e) provides a qualitative illustration

of the false negatives. There was significant difference between the normal and regenerated vessel errors for the total error rates and the FNRs. This coheres with the observation that the vessels in the regenerated tissues have less distinct differences between the arterioles and venules and are also more difficult for an operator to differentiate.

The distributions of confidences for each classifier are similar. Between the 2 experiments, the distributions were also similar, suggesting that the smaller training set seems representative of the entire dataset. Thresholding the confidences and eliminating the vessels is a possibility if more accurate classifications are desired. A subset of the vessels with lower confidences would remain unclassified (Fig. 4.7(b,d,f)). The goal is to replicate a human classifier, where a human will likely exclude several vessels based on uncertainty. However, there is a tradeoff between accuracy of the classification and the number of vessels remaining for analysis and this is dependent on the classifier and the distribution of confidences. In this experiment, thresholding the confidence values based on all the classifiers decreased the error rates (Table 4.2). However, the optimal threshold is dependent on the type of classifier used as the distribution of the vessel confidences varies. One needs to take into consideration when analyzing abnormal vasculature that the vessels of interest may lie in the range of lower confidences due to their structure (i.e. interesting discoveries may be found when looking at unusual vasculature occurring in the “low confidence” category). Once the algorithm has separated the vasculature into the three groups (arteriole, venule and unknown), the user can then study the vessels in each category.

This work must be considered in the context of its strengths and limitations. Although we had a large sample size of 192 arterioles and 127 venules of varying sizes, shapes, and staining levels, all of the tissues in this study were prepared in a single laboratory. Additional testing would be required to report on the generalizability of our methods to tissues prepared in different laboratories, allowing for testing of various feature selection and classification techniques without overfitting to the current dataset. Even so, there was still a large staining variability between the mouse samples, including weakly stained vessels which may have been systematically under or over segmented. The technique used for histological slide preparation and immunohistochemistry staining is a standard method for visualizing the microvascular wall. However the classifiers, as trained in our experiments, cannot be directly applied to images using other methods of vessel visualization such as fluorescent staining. This study was also only done on the mouse hind limb tissue and cannot be directly generalized to other tissue types. Although we did not observe substantial improvement in classification performance when more than two features were used, this may have been due to a lack of normalization for staining variability. Our ongoing work includes staining normalization and a subsequent analysis of performance with the inclusion of additional features and more feature selection methods.

4.5 Conclusions

Distinguishing arterioles from venules is an unattained prerequisite to high-throughput, quantitative analysis of the microvascular network morphology. In addition, analysis and morphological comparison of arteriolar and venular sub-networks are essential to our understanding of multiple diseases affecting all vascularized organ systems. We have developed and evaluated the first fully automatic software system for differentiation of arterioles from venules on high-resolution digital histology images of the mouse hind limb. This system eliminates the need for laborious manual classification of the hundreds of microvessels occurring in a typical sample, and paves the way for high-throughput analysis the arteriolar and venular networks in the mouse.

Our software system based on supervised machine learning provided useful classification accuracy for differentiation of arterioles and venules on high-resolution digital histology images of the mouse hind limb immunostained for smooth muscle α -actin. Our system achieved an area under the receiver operating characteristic curve of 0.89. Feature selection was consistent across cross validation iterations, and a small set of two features was required to achieve the reported performance; this augurs well for the generalizability of this system. This system will enable scientists to conduct high-throughput studies of animal models, measuring and comparing arteriolar and venular networks to deepen our understanding of human disease so that improved treatments can be sought.

Table 4.4: List of all the features extracted from each vessel image.

First-Order Features	Second-Order Features	Morphological/Shape Features
Mean $\frac{1}{N} \sum_i x_i$	GLCM Contrast $\sum_{i,j} i - j ^2 g(i, j)$	Max Diameter
Standard Deviation $\sqrt{\frac{\sum_i (x_i - \mu)^2}{N - 1}}$	GLCM Dissimilarity $\sum_{i,j} i - j g(i, j)$	Mean Radial Length
Energy $\sum_i x_i^2$	GLCM Energy $\sum_{i,j} g(i, j)^2$	Spiculation: standard deviation of radial length
Median	GLCM Entropy $-\sum_{i,j} g(i, j) \log_2 g(i, j)$	Aspect Ratio
Maximum	GLCM Autocorrelation $\sum_{i,j} ij g(i, j)$	Waviness $\frac{P_{VesselHull}}{P}$
Minimum	GLCM Homogeneity 1 $\sum_{i,j} \frac{g(i, j)}{1 + i - j }$	Skeleton End Point Count
Range <i>Maximum - Minimum</i>	GLCM Homogeneity 2 $\sum_{i,j} \frac{g(i, j)}{1 + i - j ^2}$	Normalized Radial Length Mean
Mean Absolute Deviation $\frac{1}{N} \sum_i x_i - \mu $	GLCM Correlation $\sum_{i,j} \frac{(i - \mu_i)(j - \mu_j) g(i, j)}{\sigma_i \sigma_j}$	Normalized Radial Length Entropy $-\sum \frac{NRL}{\sum NRL} \log_2 \left[\frac{NRL}{\sum NRL} \right]$
Root Mean Square $\sqrt{\frac{1}{N} \sum_i x_i^2}$	GLCM Cluster Prominence $\sum_{i,j} ((i - \mu_i) + (j - \mu_j))^4 g(i, j)$	Normalized Radial Length Sphericity $\frac{NRL}{SD(NRL)}$
Kurtosis $\frac{1}{N} \frac{\sum_i (x_i - \mu)^2}{\sigma^4}$	GLCM Cluster Shade $\sum_{i,j} ((i - \mu_i) + (j - \mu_j))^3 g(i, j)$	Normalized Radial Length Roughness $\frac{4 \sqrt{(NRL - \overline{NRL})^4 - 2 \sqrt{(NRL - \overline{NRL})^2}}}{\overline{NRL}}$
Skewness $\frac{1}{N} \frac{\sum_i (x_i - \mu)^3}{\sigma^3}$	GLCM Cluster Tendency $\sum_{i,j} ((i - \mu_i) + (j - \mu_j))^2 g(i, j)$	Normalized Radial Length Ratio $\frac{\sum NRL - \overline{NRL} }{\#boundarypoints * \overline{NRL}}$

Table 4.5: List of all the features extracted from each vessel image.

First-Order Features	Second-Order Features	Morphological/Shape Features
Variance $\frac{1}{N-1} \sum_i (x_i - \mu)^2$	GLCM Variance $\sum_{i,j} (i - \mu)^2 g(i, j)$	Area Box Ratio $\frac{A_{Vessel}}{A_{Box}}$
Entropy $-\sum_i IP \log_2 IP$	GLCM Max Probability $\max(g(i, j))$	Area Perimeter Ratio $4\pi \frac{A_{Vessel}}{P_{Vessel}^2}$
Uniformity $\sum_i IP^2$	GLCM Inverse Variance $\sum_{i,j} \frac{g(i, j)}{ i - j ^2}$	Area Convex Hull Ratio $\frac{A_{Vessel}}{A_{VesselHull}}$
1 Percentile	GLCM Sum Average $\sum_{i=2}^{2N} i g_{x+y}(i)$	Median Wall Thickness $\frac{Median\ Thickness}{P_{Lumen}}$
10 Percentile	GLCM Sum Entropy $-\sum_{i=2}^{2N} \log_2 [g_{x+y}(i)] g_{x+y}(i)$	70 Percentile Wall Thickness Ratio $\frac{70\ Percentile\ Thickness}{P_{Lumen}}$
90 Percentile	GLCM Sum Variance $\sum_{i=2}^{2N} i^2 g_{x+y}(i)$	90 Percentile Wall Thickness Ratio $\frac{90\ Percentile\ Thickness}{P_{Lumen}}$
99 Percentile	GLCM Difference Entropy $-\sum_{i=0}^{N-1} \log_2 [g_{x+y}(i)] g_{x+y}(i)$	Wall Thickness SD $\frac{Thickness\ SD}{P_{Lumen}}$
Mean Gradient Value	GLCM Information Measure Correlation 1 $\frac{H_{xy} - H_{xy1}}{\max[HX, HY]}$	
Variance of Gradient	GLCM Information Measure Correlation 2 $\sqrt{1 - \exp[-2(HXY2 - HXY)]}$	
Bimodality Coefficient $\frac{Skewness^2 + 1}{Kurtosis + \frac{3(N-1)^2}{(N-2)(N-3)}}$	GLCM Diagonal Moment $\sum_{i,j} \sqrt{\frac{1}{2}} i - j g(i, j)$	
Median Absolute Deviation $\frac{1}{N} \sum_i x_i - \tilde{x} $	GLCM Inverse Difference Moment $\sum_{i,j} \frac{g(i, j)}{1 + (i - j)^2}$	

* $g(i, j)$ refers to the GLCM, where HX and HY are entropies of g_x and g_y , $HXY = -\sum_{i,j} g_{ij} \log_2 g_{ij}$, $HXY1 = -\sum_{i,j} g_{ij} \log_2 g_x(i)g_y(j)$, $HXY2 = -\sum_i \sum_j g_x(i)g_y(j) \log_2 [g_x(i)g_y(j)]$, μ refers to the mean, \tilde{x} refers to the median, σ refers to the standard deviation, and N refers to the number of pixels. A_x , P_x , and W_x , refer to the area, perimeter, and average width, respectively, of structure x ; Vessel refers to the vessel wall; Box refers to the vessels bounding box; VesselHull refers to the vessels convex hull; and Lumen refers to the inner vessel boundary. NRL is the normalized radial length. The GLCM neighborhood voxel distance was $0.25 \mu\text{m}$ averaged over all directions.

References

- [1] G. Liew, D. A. Sim, P. A. Keane, A. G. Tan, P. Mitchell, J. J. Wang, T. Y. Wong, M. Fruttiger, A. Tufail, and C. A. Egan, "Diabetic macular ischaemia is associated with narrower retinal arterioles in patients with type 2 diabetes," *Acta Ophthalmologica*, vol. 93, no. 1, e45–e51, 2015.
- [2] M. Cavallari, C. Stamile, R. Umeton, F. Calimeri, and F. Orzi, "Novel method for automated analysis of retinal images: Results in subjects with hypertensive retinopathy and cadasil," *BioMed Research International*, vol. 2015, 2015.
- [3] A. Y. Shih, C. Ruhlmann, P. Blinder, A. Devor, P. J. Drew, B. Friedman, P. M. Knutsen, P. D. Lyden, C. Mateo, and L. Mellander, "Robust and fragile aspects of cortical blood flow in relation to the underlying angioarchitecture," *Microcirculation*, vol. 22, no. 3, pp. 204–218, 2015.
- [4] A. Y. Lai, A. Dorr, L. A. Thomason, M. M. Koletar, J. G. Sled, B. Stefanovic, and J. McLaurin, "Venular degeneration leads to vascular dysfunction in a transgenic model of alzheimer's disease," *Brain*, vol. 138, no. 4, pp. 1046–1058, 2015.
- [5] D. Shin, G. Garcia-Cardena, S.-I. Hayashi, S. Gerety, T. Asahara, G. Stavrakis, J. Isner, J. Folkman, M. A. Gimbrone, and D. J. Anderson, "Expression of ephrinb2 identifies a stable genetic difference between arterial and venous vascular smooth muscle as well as endothelial cells, and marks subsets of microvessels at sites of adult neovascularization," *Developmental Biology*, vol. 230, no. 2, pp. 139–150, 2001.
- [6] Y. Xu, J. G. Pickering, Z. Nong, E. Gibson, J.-M. Arpino, H. Yin, and A. D. Ward, "A method for 3d histopathology reconstruction supporting mouse microvasculature analysis," *PloS One*, vol. 10, no. 5, e0126817, 2015.

- [7] Y. Xu, J. Pickering, Z. Nong, and A. D. Ward, "Segmentation of digitized histological sections for quantification of the muscularized vasculature in the mouse hind limb," *Journal of Microscopy*, vol. 266, no. 1, pp. 89–103, 2017.
- [8] C. Taylor and R. Levenson, "Quantification of immunohistochemistry-issues concerning methods, utility and semiquantitative assessment ii," *Histopathology*, vol. 49, no. 4, pp. 411–424, 2006.
- [9] T. Nakagawa, W. Sato, O. Glushakova, M. Heinig, T. Clarke, M. Campbell-Thompson, Y. Yuzawa, M. A. Atkinson, R. J. Johnson, and B. Croker, "Diabetic endothelial nitric oxide synthase knockout mice develop advanced diabetic nephropathy," *Journal of the American Society of Nephrology*, vol. 18, no. 2, pp. 539–550, 2007.
- [10] F. Akhavein, E. J. S.-. Michel, E. Seifert, and C. Rohlicek, "Decreased left ventricular function, myocarditis, and coronary arteriolar medial thickening following monocrotaline administration in adult rats," *Journal of Applied Physiology*, vol. 103, no. 1, pp. 287–295, 2007.
- [11] T. R. Nurkiewicz, D. W. Porter, M. Barger, L. Millecchia, K. M. K. Rao, P. J. Marvar, A. F. Hubbs, V. Castranova, and M. A. Boegehold, "Systemic microvascular dysfunction and inflammation after pulmonary particulate matter exposure," *Environmental health perspectives*, vol. 114, no. 3, pp. 412–419, 2006.
- [12] M. J. Frontini, Z. Nong, R. Gros, M. Drangova, C. O'Neil, M. N. Rahman, O. Akawi, H. Yin, C. G. Ellis, and J. G. Pickering, "Fibroblast growth factor 9 delivery during angiogenesis produces durable, vasoresponsive microvessels wrapped by smooth muscle cells," *Nature biotechnology*, vol. 29, no. 5, pp. 421–427, 2011.
- [13] A. C. Ruifrok and D. A. Johnston, "Quantification of histochemical staining by color deconvolution," *Anal Quant Cytol Histol*, vol. 23, no. 4, pp. 291–9, 2001.
- [14] H. Yin, M. J. Frontini, J.-M. Arpino, Z. Nong, C. O'Neil, Y. Xu, B. Balint, A. D. Ward, S. Chakrabarti, and C. G. Ellis, "Fibroblast growth factor 9 imparts hierarchy and vasoreactivity to the microcirculation of renal tumors and suppresses metastases," *Journal of Biological Chemistry*, vol. 290, no. 36, pp. 22 127–22 142, 2015.
- [15] R. W. Connors and C. A. Harlow, "A theoretical comparison of texture algorithms," *IEE Transactions on Pattern Analysis and Machine Intelligence*, no. 3, pp. 204–222, 1980.
- [16] R. Duin, P. Juszczak, P. Paclik, E. Pekalska, D. de Ridder, D. Tax, and S. Verzakov, "Prtools4. 1, a matlab toolbox for pattern recognition," *Delft University of Technology*, 2007.

- [17] C. Cortes and V. Vapnik, "Support-vector networks," *Machine learning*, vol. 20, no. 3, pp. 273–297, 1995.
- [18] L. Breiman, "Random forests," *Machine learning*, vol. 45, no. 1, pp. 5–32, 2001.
- [19] A. R. Webb, *Statistical pattern recognition*. John Wiley & Sons, 2003.
- [20] J. Anderson, *Logistic discrimination, handbook of statistics. p. r. krishnaiah and In kanal, eds., vol. 2*, 1982.
- [21] R. Herbrich and T. Graepel, "A pac-bayesian margin bound for linear classifiers: Why svms work," in *Advances in Neural Information Processing Systems 13: Proceedings of the 2000 Conference*, vol. 13, MIT Press, pp. 224–230.

Chapter 5

High content analysis of the microvasculature in the post-ischemic skeletal muscle reveals the emergence of abnormally thin-walled arteries and arterioles: Implications for flow reserve in regenerated muscle

*An updated version of the following chapter will be submitted to the journal Angiogenesis:
Xu Y, Ward AD, Yin H, Arpino JM, O'Neil C, Nong Z, Pickering JG.*

5.1 Introduction

Any compromise to the blood supply of organs can lead to impairment of function and tissue loss. This can take the form of many pathologies, including peripheral vascular disease (PVD), which is in the skeletal muscle and can be caused by atherosclerosis. [1], [2] Symptoms of PVD include intermittent claudication, which results in pain during locomotion and in severe cases, pain at rest. [3] There are few approaches to treatment. [4] Pharmacological methods are being developed for therapeutic angiogenesis to combat ischemia. [5] This can result in an increased walking distance of patients of 50%, but increases mortality in patients with heart failure, which is common in PVD patients. [6] Typically, treatment options involve invasive procedures for peripheral vascular disease. Surgical treatments such as endovascular reconstruction and

surgical revascularization are often not an option. [3] This leads to 1.4 million limb amputations annually from dysvascular disease, with diabetes as a main cause of disease. [7] Thus, it is essential to study the composition of the vasculature and the manner in which it can self-repair after an ischemic event.

The body has compensatory mechanisms for organ repair after an ischemic event, such as regeneration of the skeletal muscle, but this does not necessarily result in the successful return of the network to baseline structural and functional status. [8] In the adult, regeneration involves arteriogenesis in the collateral vasculature, which opens and allows for reperfusion of the ischemic tissues. [9], [10] It also involves angiogenesis, when new capillaries develop to compensate for the deficiency of blood flow. [11] Almost all organs have collateral arteries, which can open in the event of severe ischemia, to compensate for the lack of blood flow. [2] Clinically in coronary artery disease, it has been shown that patients who develop a collateral circulation have a reduced mortality rate, with a reduction of 36%. [12] This knowledge of arteriogenesis and angiogenesis after an ischemic event has yet to facilitate the development of new therapies because treatments mediating successful vascular regeneration are unknown. [13] For example, it is not known whether it is best to stimulate the tissues for vascular development, or to allow tissues to repair on their own.

One of the understudied vascular components after regeneration is the change in vascular smooth muscle cell (SMC) wrapping. The SMC component is an integral part of this reperfusion process. [9], [14] It allows for vascular tone control of the upstream vessels by communicating through surrounding vascular components and the sympathetic nervous system. [15] The enlargement of the pre-existing collateral vessels and recruitment of vascular SMCs for stability, through arteriogenesis in adulthood, allow for reperfusion of the ischemic tissues. [9] The arterioles provide peripheral resistance in blood flow to regulate perfusion locally prior to the capillary beds. [16] Previous studies have shown an increase in wrapping of the collateral vessels. [17] However, the structure and content of the SMC wrapping at the distal end of the arterial tree has not been studied comprehensively. Thus, we need comprehensive knowledge of the distal arterial tree through careful examination of vascular histopathology.

In this study, our objective was to quantitatively and comprehensively characterize the arteriolar vasculature after ischemia and regeneration, and model its impact on blood flow function. We recently demonstrated the inefficiency of the regenerated network focused on terminal arterioles. [18] This led us to question the characteristics of the small artery and arteriolar network, incorporating all muscularized microvessels on any given tissue section. The effects of hypoxia on the remodeling of collateral vasculature and increased capillary density have been previously assessed, [17], [19]–[21] capturing differences in steady-state blood flow. However, the structure and functionality of the smooth muscle component after ischemia is not known

in the context of SMC wrapping morphology and the density of the vessels which contain this wrapping. Until recently, methods did not exist for comprehensive analysis for the analysis of microvasculature at the arteriolar level. We recently developed an automated software system for the analysis of microvasculature, [22], [23] to interrogate inherent abnormalities within the network responsible for dynamic regulation. [24], [25] We used our developed method to extensively characterize the arteriolar network. These structural characterizations, such as vessel density and morphology, were used to simulate blood flow function.

To address the need for a comprehensive analysis of SMC content after regeneration of the microvasculature post an ischemic event, we used our developed automated software for vessel measurements and blood flow modeling to infer changes to function. We expect differences in the density and morphology of the muscularized microvasculature in the regenerated skeletal muscle post-ischemia as compared to baseline. The aberrations in SMC content may lead to a decrease in blood flow when the tissue is in a state of perfusion demand, leading to deficient function.

5.2 Methods

5.2.1 Materials

The experiments were conducted on a total of 10 wild type C57BL/J6 mice. Five mice were normal, and five had post-ischemia regenerated vasculature in the hind limb. Between 12 and 19 tissue sections were obtained per mouse; all sections were used for analysis in this study. Mice were subjected to hindlimb ischemia by unilateral femoral artery excision as previously described. [26] Fourteen days after ischemia induction, mice were sacrificed by overdose of isoflurane. After the blood was flushed by intraventricular perfusion with phosphate buffered saline, the tissues were fixed by intraventricular perfusion with formalin. The anterior calf bundles, which contain the tibialis anterior, extensor digitorum longus, and peroneus longus muscles, were isolated from the ischemic and contralateral nonischemic legs and fixed in formalin for another 48 hours. The tissues were processed and paraffin-embedded, and then cut into blocks and sectioned at $5\ \mu\text{m}$. To visualize the smooth muscle distribution within the arterioles and venules, sections were immunostained for smooth muscle (SM) α -actin using the monoclonal antibody (DAKO, M0851), and bound primary antibody detected with horseradish peroxidase (HRP)-conjugated secondary antibody and 3,3'-Diaminobenzidine chromogen (DAB, Vector Laboratories, SK-4100). This marked the smooth muscle layer of the vasculature (resulting in the vessel walls being stained with a brown colour). The tissue was then counter stained with hematoxylin, resulting in blue-stained nuclei. The sections were imaged with a

ScanScope CS (Aperio Technologies, Vista, CA, USA) bright field slide scanner, at 20× objective with 2× magnification engaged, resulting in 0.25 μm isotropic pixels. These yielded images with extents ranging from 11697 - 26398 pixels in the vertical dimension and 9000 - 17135 pixels in the horizontal dimension.

5.2.2 Vessel segmentation summary

The main steps in the automated vessel segmentation algorithm are vessel fragment detection, vessel fragment connection, locally adaptive segmentation refinement, and vessel measurement. [22], [23] The detection and segmentation were validated against manually detected vessels and manually contoured vessels, respectively. Measurements of the vascular smooth muscle layer were compared between the manual and automated segmentations.

5.2.3 Vascular measurements

Measurements of the smooth muscle vascular morphology were performed on all vessels within the tibialis anterior (TA), extensor digitorum longus (EDL) and peroneus longus (PL). This was mediated by an automatic detection and segmentation algorithm we previously developed. [22] The components of the network were separated into the feeder and draining vessels, the arteriole and venules at the level of the microvasculature automatically using a machine learning technique. [23] With the combination of the two techniques, the density and the morphology of the arteriolar smooth muscle distribution was automatically assessed throughout the whole slide images. The positive vessels were detected and then automatically contoured for the smooth muscle wall, resulting in a boundary at the endothelial wall or inner vessel lumen and a boundary around the stained smooth muscle wall component. The density of the arterioles within the tissue was automatically measured. The morphological measurements defined in Table 5.2 were measured for all vessels automatically. The assessments were performed for the normal and regenerated vasculature at day 14 and day 28 post-ischemia.

5.2.4 Blood flow simulation

The parameters involved in the blood flow simulations include the pressure, vessel diameters, and network geometry, which includes the number of vessels, their positions, orientations and baseline diameters. [24], [25] The network geometry was kept consistent, except where additional branches were added to the distal end of the arteriolar tree to reflect the increase in vessel density prior to the perfusion of capillaries. The dimensions of the bounding box containing the arteriolar tree were defined by the extents covering the combined volume of the TA, EDL,

and PL muscles. The inflow and outflow pressures were set to different values to allow for the same baseline flow for the normal and regenerated models, to compare the flow changes when there is a dilation of the vasculature. The maximum dilation was defined as 140% of the baseline diameter for arterioles and was based on the relative dilation of arteriolar vasculature in response to sodium nitroprusside a vasodilator. [25]

The dilations of the vessel diameters (d) were based on the vessel wall thickness values measured in the empirical analysis and ranged from 0 to 1. The vessels in the normal and regenerated networks are defined to have the same diameters at baseline. The regenerated and normal networks both have tree-based network topologies, but has more vessels at the distal end, which have the same diameters as the distal vessels in the normal network. The normal vessel diameters were all dilated to a maximum dilation of 140% of the baseline diameter to model an increase in demand for blood flow. The regenerated vessel diameters were modulated according to differences in their vessel wall thicknesses, as compared to their normal counterparts. The vessel diameters were binned into categories as defined in Table S5.4 and the vessels in the simulation model were dilated with respect to the median thickness of the regenerated vessel wall as compared to the normal, within each vessel diameter range. The dilated vessel diameter d_D in the regenerated model is defined as

$$d_D = d_B \left(1 + D_{max} \times \frac{T_{reg}(d_B)}{T_{norm}(d_B)} \right) \quad (5.1)$$

where D_{max} is the maximum dilation factor of 0.4 dB is the diameter of the vessel segment at baseline, and T_{reg} and T_{norm} are the median vessel wall thickness values for the regenerated and normal vessels respectively for the vessel diameter range containing d_B . (Table S5.4) For example, if the baseline diameter d_B for the vessel is $19 \mu m$, the T_{reg} and T_{norm} are 3.03 and $3.75 \mu m$ respectively. (Table S5.4) Then the dilated diameter d_D would be $(19 \mu m)(1 + 0.4 \times (3.03/3.75)) = (19 \mu m)(1.32) = 25 \mu m$.

5.2.5 Statistical analysis

Kolmogorov-Smirnov normality tests were performed using MATLAB 8.5 (The Mathworks Inc., Natick, MA, USA) for all measures. The null hypothesis was that the median area, perimeter and thickness values were the same for the normal and post-ischemic tissue samples. ANOVA testing was performed using the non-parametric Kruskal-Wallis test with a Bonferroni-corrected significance level of α/n , where n is the number of sections taken from each mouse, to compensate for the potential correlation of vessel measures within each tissue sample. Post-hoc testing was performed on the normal, day 14 and day 28 samples. Aggregate values from each mouse were compared with the significance level of α . In addition, the

measures were grouped with respect to each sample mouse. The median differences and associated interquartile ranges were measured. The difference in regressions of media area and lumen area, as well as media thickness and vessel diameter was measured by the analysis of covariance (ANCOVA).

5.3 Results

All analyses were performed on the small artery and arteriolar vasculature, excluding the venular side from the assessment, [23] in the anterior muscle bundle where we expect vascular regeneration, downstream of the femoral artery excision. Femoral artery excision and vascular regeneration resulted in changes to vasculature with respect to morphology and density.

5.3.1 Increase in density of muscularized vasculature

Through automated analysis, we found an overall increase ($p < 0.05$, $n = 9, 5, 4$ mice) in the small artery and arteriolar density in the regenerated mice, computed as the number of vessels per given tissue region (Table 5.1). Though the quantitative measurements were performed on whole tissues sections, the differences in density can be visualized on portions of the tissue when comparing the normal to the regenerated vasculature. (Fig. 5.1a, b) Most notably, there was a two-fold increase in the vessel density after regeneration at both day 14 and day 28. (Fig. 5.1c) This difference holds when looking at the sub categories of vessels separated with respect to size in the smaller vessel ranges of 5 - 10 μm and 10 - 40 μm .

Table 5.1: Vessel density of the muscularized microvasculature (N indicates number of mice)

Bins	N	Vessel Density (mm^{-2})	
		Median	IQR
Normal	9	4.66	2.49
Day 14	5	10.26	10.93
Day 28	4	9.50	4.13

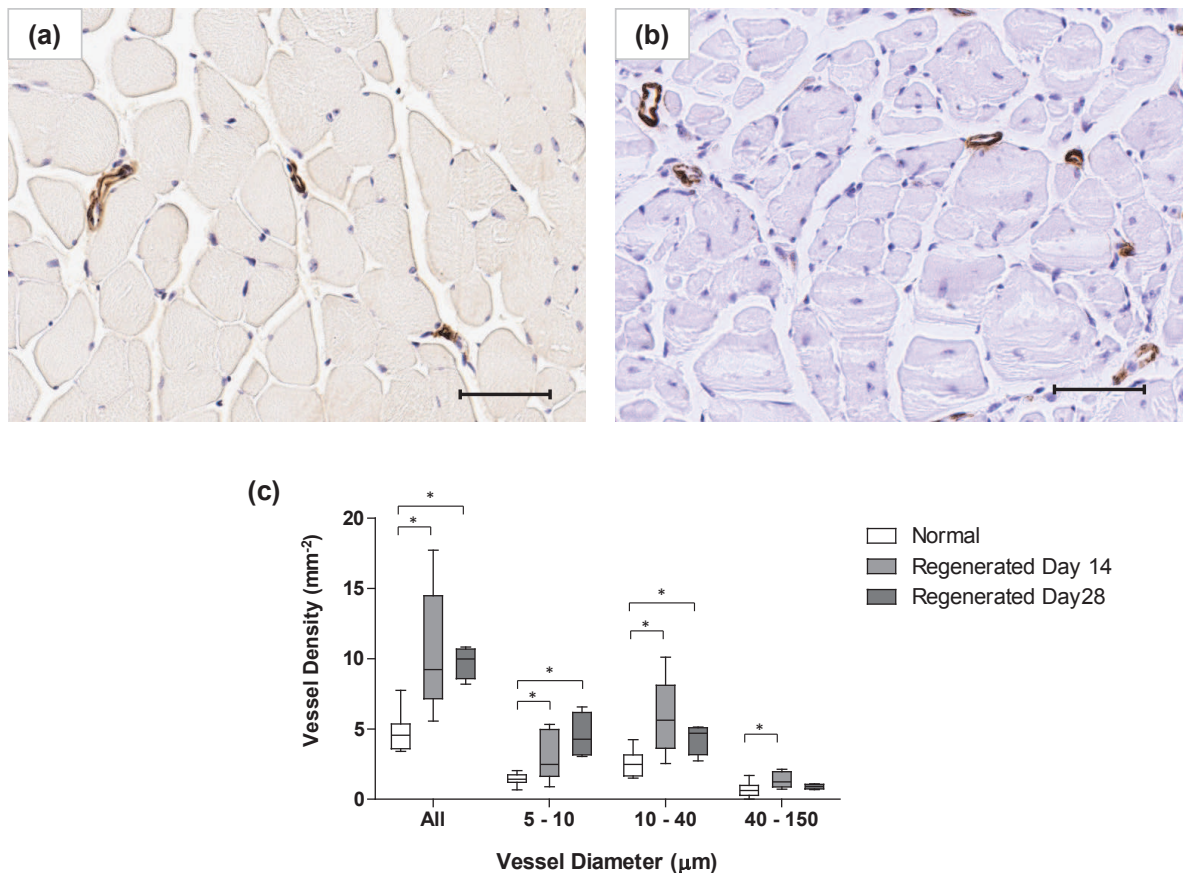


Figure 5.1: Normal (a) and regenerated (day 28) (b) hind limb tissue following ischemic damage, immunostained with an antibody to smooth muscle α -actin and DAB chromogen and counter-stained with hematoxylin. Distribution of density (c) with regards to the vessel diameter where All indicates where the total distribution is represented in the boxplots. The boxes represent the median and interquartile range values and the whiskers are at the 5th and 95th percentile. Significance in the form of a Kruskal-Wallis and post-hoc test is indicated for $p < 0.05$ for density (n for number of mice). Scale bar $50 \mu\text{m}$.

5.3.2 Decrease in vascular SMC wrapping in regenerated skeletal muscle

We were also interested in the effect of the regeneration on the vascular SMC wrapping. The comprehensive morphological measurement also revealed significant differences in the SMC wrapping around the arteriolar vasculature. (Table 5.2) There was a decrease in the vessel wall area and thickness after regeneration. ($p < 0.0001$, $n = 2725, 2164, 374$ vessels, $p = \alpha/n = 0.05/19 = 0.0026$) This is apparent when looking at all vessel sizes, both quantitatively through automated measurements of thousands of vessels and visually examined when comparing selected vessels of similar sizes on the histology section. (Fig. 5.2) The media area decrease

loses statistical significance at day 28 ($p > 0.0026$) when assessing the vasculature at the 5 - 10 μm , 10 - 40 μm , and 40 - 150 μm vessel diameter ranges. (Fig. 5.3) These losses in statistical significance for the size categories of vessels were also observed in the media vessel wall thickness in the day 28 mice. We noted an increase of the median vessel wall thickness from day 14 to day 28 in the 10 - 40 μm vessel diameter range (Fig. 5.3b).

Table 5.2: Morphological measures of the smooth muscle (SM) layer (N indicates number of vessels)

Model	N	SM Layer Area (μm^2)		Lumen Area (μm^2)	
		Median	IQR	Median	IQR
Normal	2400	182.38	291.75	159.24	521.99
Day 14	2037	124.81	186.88	154.96	467.10
Day 28	350	115.22	152.25	97.15	283.89
		Lumen Perimeter (μm)		Lumen Diameter (μm)	
		Median	IQR	Median	IQR
Normal	2400	44.73	58.68	14.24	18.68
Day 14	2037	44.13	53.67	14.05	17.08
Day 28	350	34.94	41.13	11.12	13.09
		SM Layer Thickness (μm)			
		5th Percentile		50th Percentile	
		Median	IQR	Median	IQR
Normal	2400	1.77	1.93	3.38	2.54
Day 14	2037	1.12	1.24	2.61	1.52
Day 28	350	1.25	1.28	2.85	1.84
		95th Percentile		Within-Vessel SD	
		Median	IQR	Median	IQR
Normal	2400	7.29	5.92	1.53	1.47
Day 14	2037	5.46	4.88	1.25	1.46
Day 28	350	6.59	5.39	1.53	1.61

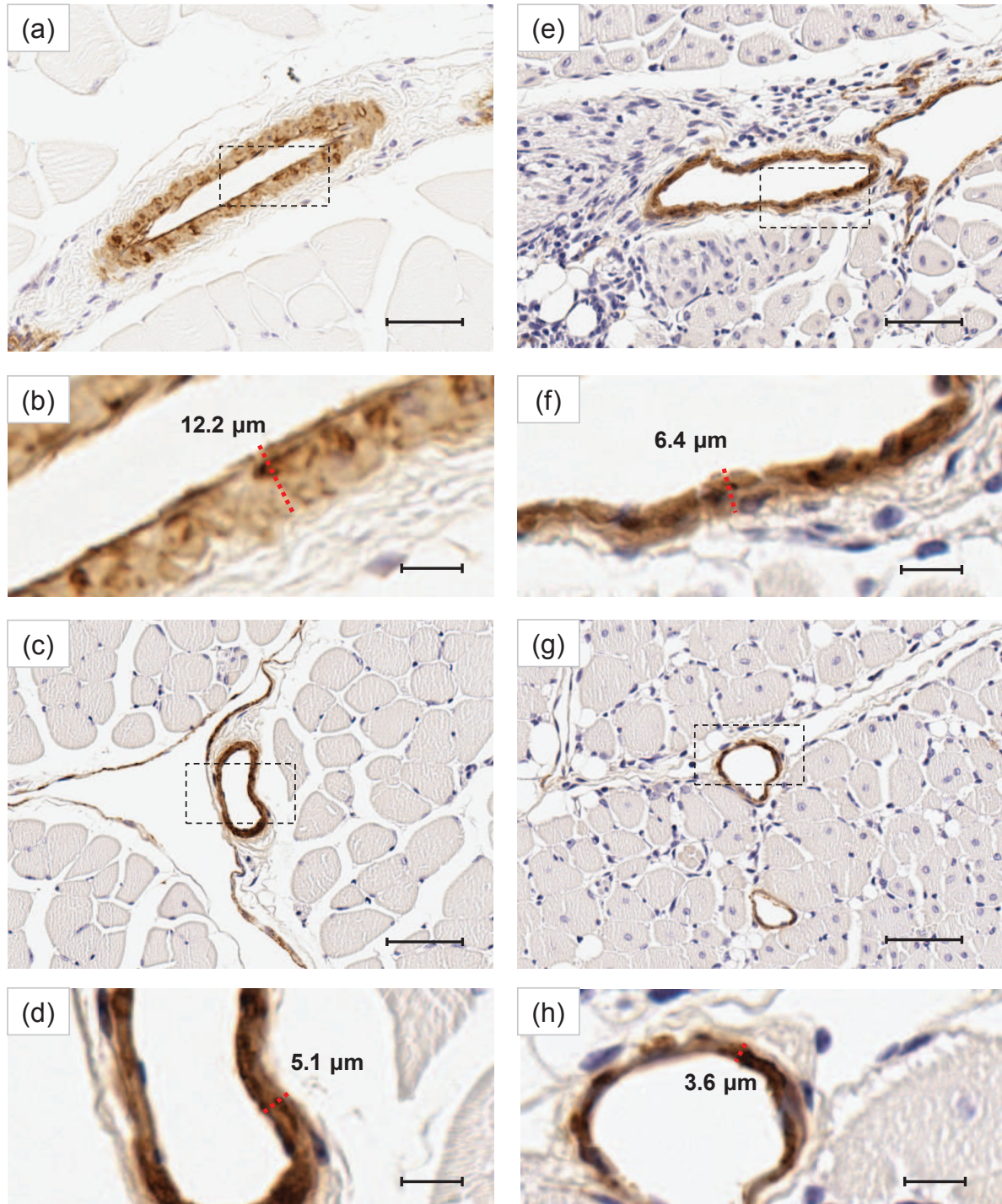


Figure 5.2: Normal (a-d) and regenerated (e-h) hind limb tissue following ischemic damage, immunostained with an antibody to smooth muscle α -actin and DAB chromogen and counterstained with hematoxylin. Scale bar $50 \mu\text{m}$ for full vessels, $10 \mu\text{m}$ for vessel walls.

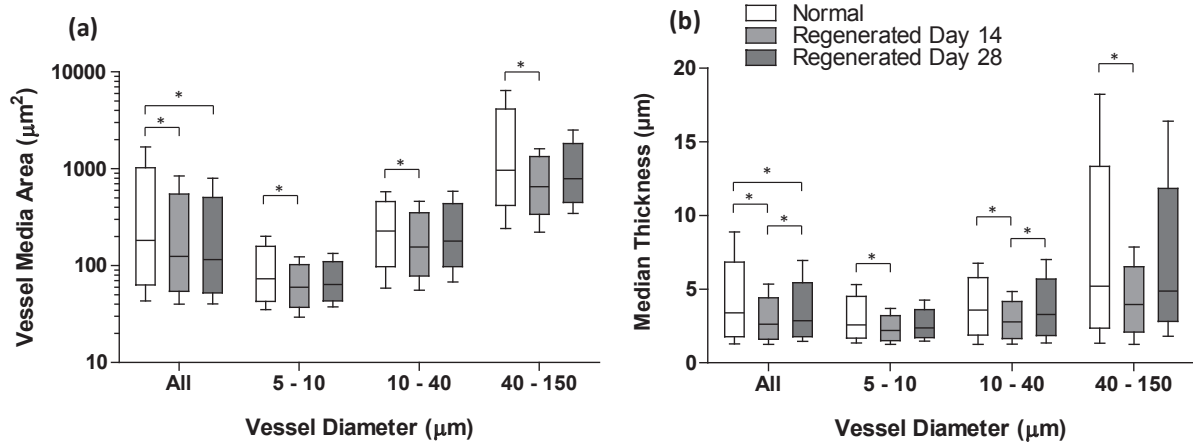


Figure 5.3: Distribution of morphological values with regards to the vessel diameter where All indicates where the total distribution is represented in the boxplots. The boxes represent the median and interquartile range values and the whiskers are at the 5th and 95th percentile. Significance in the form of a Kruskal-Wallis and post-hoc test is indicated for $p < 0.0026$ (n for number of vessels).

We also found an elastic (linear log-log) relationship between the vascular SMC wrapping with respect to vessel calibre, demonstrating less SMC wrapping in the regenerated vasculature compared to the normal. (Fig. 5.4) There were significant differences in the elevation of media area between normal and the regenerated vasculature at days 14 and 28 ($p < 0.0001$), with respect to the lumen area. This is not surprising when looking at the discrepancies in the heights of the correlations in Figure 5.4a. There is a distinct group of vessels in the normal vasculature, surpassing the media area of the regenerated vasculature, visible by the group of blue points above the rest of the points. The overall trend between the lumen area and media area of the vasculature has the same slope for normal, day 14 and day 28 ($p = 0.74$). The regression lines for all groups are parallel, which indicates that within the normal and regenerated vasculature, there is a global effect regarding the SMC component. There is a decrease in SMC wrapping in the regenerated vasculature, regardless of vessel calibre. This correlation between SMC content and vessel size is seen in the vessel diameter and median vessel wall thickness as well. There was no difference between the slopes ($p = 0.33$), but difference in the elevation of the distribution ($p < 0.0001$), where the normal group surpasses that of the regenerated vasculature. (Fig. 5.4b)

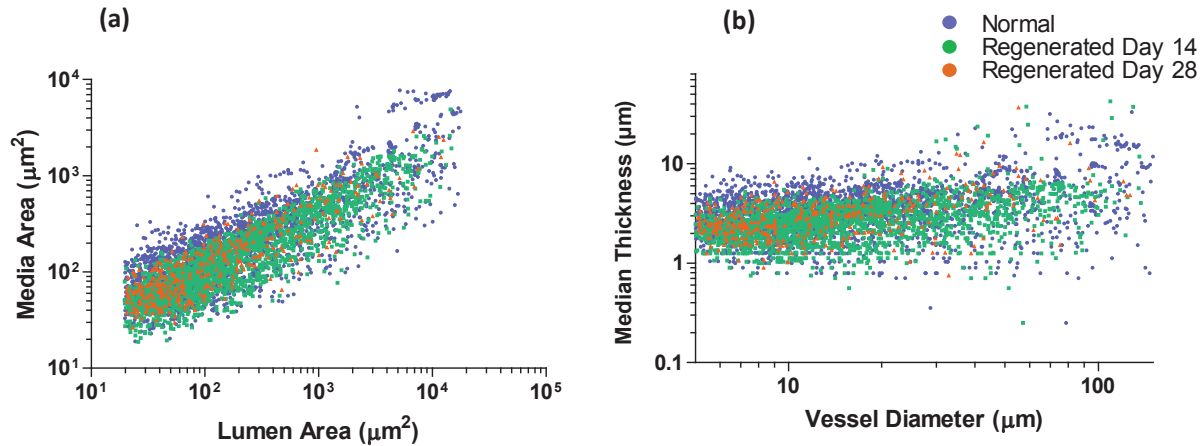


Figure 5.4: Distribution of vessel measurements between the normal and regenerated vessel media at day 14 and day 28 post-ischemia. The media area with respect to the lumen area (a) and the median vessel wall thickness with respect to the vessel diameter (b) are represented with the three distributions.

5.3.3 Lower blood flow in the regenerated arteriolar network

We were interested in the impact of the vessel density and morphology changes on local blood flow control after vascular regeneration. To address this, we performed functional modeling, using the empirical measurements of density and thickness as parameters of the network. [24] All other parameters were constant between the normal and the regenerated vasculature. We modeled a state of perfusion demand between the normal and the regenerated vasculature (Table 5.3). There was 89% (378% - 289%) and 67% (378% - 311%) less flow found in day 14 and day 28 as compared to the control in the dilated state (dilated control - dilated regenerated percent of baseline flow). The distribution of flow is shown in Fig. 5.5, which demonstrates the decrease in flow of the regenerated vasculature. The increase in vessel density is illustrated in Figure 5.5c at the distal end of the arteriolar network, where there is an increase in the number of vessel branches. An increase in the vessel diameter increases the flow in both the normal (Fig. 5.5b) and regenerated (Fig. 5.5d) vascular network. The relative differences in flow of the two models are captured when the tissues are in perfusion demand.

Table 5.3: Simulated blood flow measures and network parameters

	Baseline	Dilated Full	Dilated Reg 14	Dilated Reg 28
Normal Network				
Total Flow (ml/s)	0.009	0.034	0.026	0.028
Max Dilation Factor	0	0.4	0.4	0.4
P_0 (mmHg)	62	62	62	62
P_1 (mmHg)	20	20	20	20
Number of Segments	199	199	199	199
Regenerated Network				
Total Flow (ml/s)	0.009	0.034	0.026	0.028
Max Dilation Factor	0	0.4	0.4	0.4
P_0 (mmHg)	56	56	56	56
P_1 (mmHg)	20	20	20	20
Number of Segments	415	415	415	415
Percent of Baseline Flow	100%	378%	289%	311%
Percent of Normal Dilation Flow	26.47%	100.00%	76.47%	82.35%

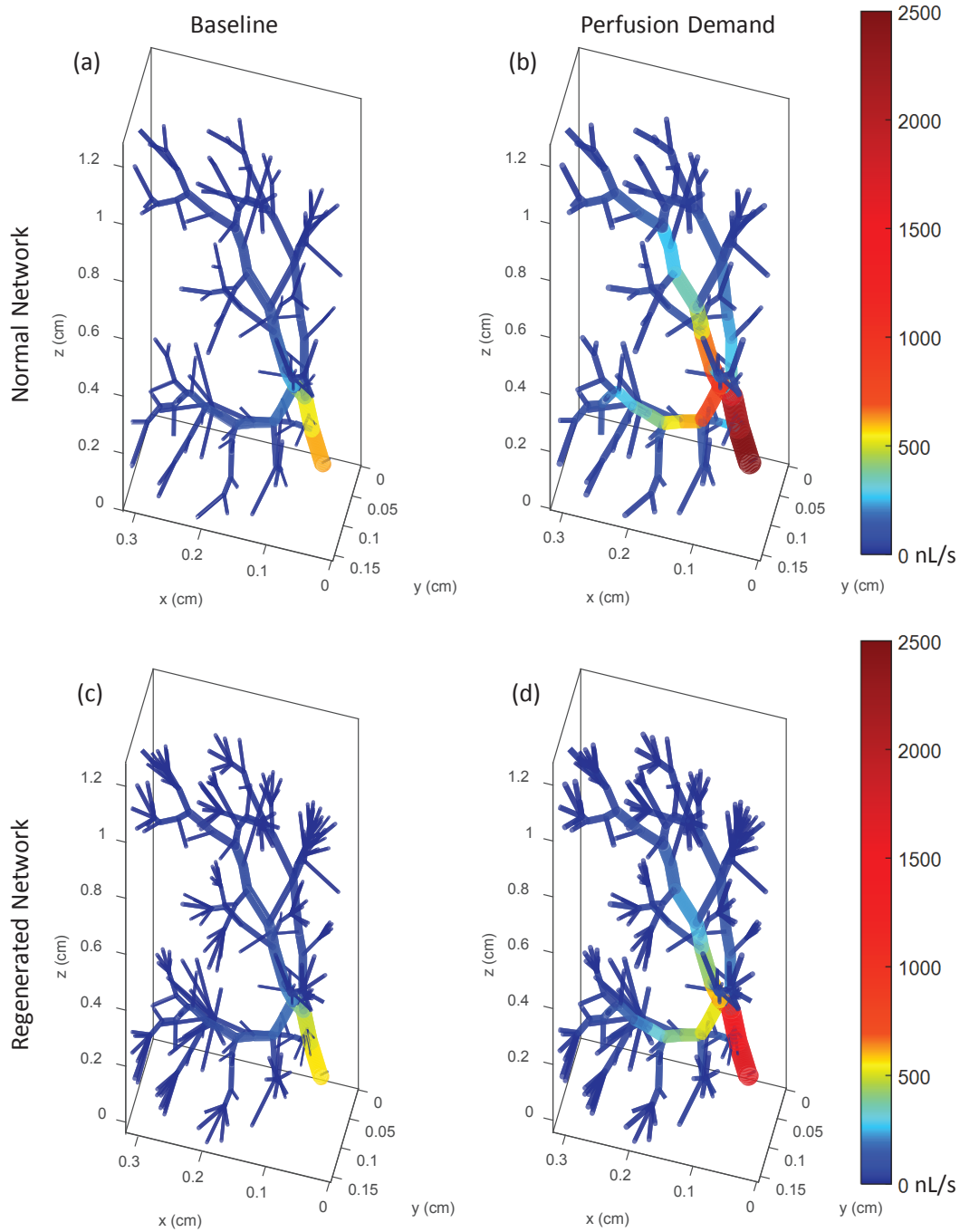


Figure 5.5: Simulated blood flow in the normal (a, b) and regenerated (c, d) networks for vessel diameters at baseline (a, c) and when the tissues are in the state of perfusion demand where the vessel diameter is dilated. Vessel diameter at baseline ranges from 12 to $120\mu\text{m}$.

5.4 Discussion

PVD and compromised blood supplies lead to damage of the vasculature affecting function, which has not been previously studied with respect to SMC wrapping at the distal end of the arteriolar tree for the impact on vascular tone. [27] Through the comprehensive analysis of histology, we have isolated the small artery and arteriole components responsible for local blood flow control, separate from the rest of the vasculature, on whole tissue sections. [22], [23] This led to the discovery of an increase in density of muscularized microvessels in the regenerated vasculature as compared to the control, suggesting compensation of the tissue for lack of tissue perfusion. However, coupled with this was also the finding of a decrease in SMC wrapping in the post-ischemic arteriolar vasculature. Modeling of these aberrations through blood flow simulation identified a lower blood flow in the regenerated arteriolar network as compared to the control, suggesting insufficient restoration of function.

Vascular regeneration can occur after an ischemic injury to the mouse skeletal muscle. [1] This is facilitated by the opening of collateral vessels. [10] Previous studies have demonstrated thickening of the main collaterals through arteriogenesis. [9] The reperfusion of the ischemic tissues stimulates angiogenesis, resulting in an increase in capillary density. [17] The density at the microvascular level not only increases, but surpasses the density in the normal tissue. [17], [19]–[21], [28] This increase in density is not accompanied by normalization in function. Our previous work demonstrated a flawed network structure and function. [18] Although the network structure 14 days after ischemia resembles that of a normal network, the function was not normalized. There was still low oxygen saturation due to arteriolar-venular shunting. [29], [30] These functions and vessel densities have been previously analyzed at the capillary level, but the dynamic vascular smooth muscle component merits further assessment.

Study of the microvasculature has not been comprehensively assessed at the calibre of arterioles, but the understanding of dynamic blood flow control occurs at this level. This is due to the sheer number of microvessels that contain a varying SMC component. Taking a small sample may not represent the full distribution within the skeletal muscles. [22] Thus, most studies at the microvascular level focus on the density of the capillaries and steady-state blood flow. [31], [32] Here, we provided a comprehensive assessment of the artery and arteriolar network captured on high resolution histology, incorporating all sizes of vessels, excluding the venules. [23] This is not feasible to perform by hand, [33] so we developed an automated software system to accurately complete this task. This enabled measurement of vessel density and morphology on the whole tissue section. This is essential because, unlike capillaries, arterioles are not evenly distributed throughout the tissue and vary with regards to their SMC content. [34]

We found an increase in arteriole density in the regenerated vasculature. (Table 5.1) This increase in vessel density is apparent across all vessel sizes. (Fig. 5.1c) This increase is not significant in the 40 - 150 μm diameter vessels at day 28. The vessels incorporated within this range could be collateral vessels, which can regenerate and become larger in size, thus no longer in the below 150 μm diameter range. The arterioles have not been stratified by size in previous studies. The increase in vessel density does correlate with the previously observed increase in capillary density in other studies [17], [19]–[21], [28] and what is visualized on the histology section. (Fig. 5.1) Angiogenesis is occurring to compensate for ischemia. [5], [21], [35]

Assessment was performed on the SMC thickness in the whole tissue section with our developed automated technique. [22], [23] Previous studies have been mainly focused on vessel density at the microvascular level. [31], [32] We measured the thickness of the SMC wrapping along each individual pixel of the vessel perimeter. The microvasculature has yet to be assessed to this extent. There was a decrease in the smooth muscle content around the arteriolar wall in the regenerated vasculature based both on SMC area and thickness. (Table 5.2) There was some incomplete improvement at day 28 compared to day 14 after ischemia. (Fig. 5.3) However, we did not detect a significant difference when compared to the control group. The lack of smooth muscle wrapping may be a contributing factor to the persistent reduction in function after 14 days of regeneration. There could be a fundamental relationship between the vessel size and adequate SMC wrapping, and there is a global effect of ischemia, causing a decrease in vessel wall thickness regardless of vessel calibre. (Fig. 5.4)

We used a blood flow simulation model to evaluate the effect of a decrease in SMC thickness on vascular function as it is essential to study the vasculature's response to stress and exercise, not only at rest. [24], [25] This flow model incorporated the empirical thickness differences at all arteriole sizes. When only accounting for the discrepancy in vessel thickness and density, the flow responsivity was blunted. (Fig. 5.5) As such, the model is very conservative and is likely overestimating the flow response in the regenerated model. Other factors may decrease flow and were not incorporated in the model. [18] These factors include vessel shunting between arterioles and venules, overall network disorganization and different input flow conditions. [30] The hind limb in the regenerated state cannot receive the same amount of flow from collateral vessels, as compared to the control limb from the femoral artery. Even without incorporating those factors, there was still an 89% lower flow in the regenerated limb when compared to the control limb. To further validate this model, we are performing in vivo blood flow analysis using Laser Doppler imaging. This is essential to the understanding of the body's response to stress and exercise.

5.5 Conclusion

Our data describe the morphology and density differences in the arteriolar vasculature after hind limb ischemia and regeneration. Previous analysis techniques have not allowed for the comprehensive measurement for the vasculature at the artery and arteriolar level with regards to SMC content. We characterized features of the arteriolar network with our developed, automated software system. This demonstrated a decrease in SMC wrapping and decreased flow within the regenerated arteriolar network. Thus, even with the increase in vascular density, the regenerated network may not perform efficiently in the state of perfusion demand.

Table 5.4: Smooth muscle (SM) layer thickness binned based on vessel diameter(d_B) in the normal (T_{norm}) and regenerated (T_{reg}) vasculature

Vessel diameter (μm)			SM Layer Thickness (μm)								
			Normal			Regenerated Day 14			Regenerated Day 28		
Bin Min	Bin Max	N	Median	IQR	N	Median	IQR	N	Median	IQR	
4	6	175	2.55	1.27	114	2.02	0.69	36	2.37	0.64	
6	8	350	2.61	1.82	281	2.15	0.84	74	2.33	0.99	
8	10	271	2.57	1.86	241	2.3	1.08	51	2.36	1.73	
10	12	218	3.27	2.15	219	2.36	1.25	26	2.88	1.78	
12	14	174	3.26	2.24	159	2.55	0.96	29	3.26	1.43	
14	16	119	3.26	1.95	130	2.72	1.41	18	3.03	1.41	
16	18	136	3.78	1.92	109	2.93	1.52	15	3.29	0.93	
18	20	96	3.75	2.59	124	3.03	1.27	12	3.09	1.9	
20	30	342	3.9	2.05	223	3.04	1.68	39	3.75	2	
30	40	112	3.78	2.71	148	3.25	1.92	18	4.55	2.66	
40	50	122	5.08	2.27	106	3.23	1.61	11	5.37	3.65	
50	100	208	5.14	5.45	165	4.25	2.5	18	4.66	4.67	
100	150	77	8.1	11.47	18	5.39	7.64	3	4.82	1.36	

References

- [1] T. R. Cardinal, K. R. Struthers, T. J. Kesler, M. D. Yocum, D. T. Kurjiaka, and J. B. Hoying, "Chronic hindlimb ischemia impairs functional vasodilation and vascular reactivity in mouse feed arteries," *Front Physiol*, vol. 2, p. 91, 2011.
- [2] M. A. Ziegler, M. R. Distasi, R. G. Bills, S. J. Miller, M. Alloosh, M. P. Murphy, A. G. Akingba, M. Sturek, M. C. Dalsing, and J. L. Unthank, "Marvels, mysteries, and misconceptions of vascular compensation to peripheral artery occlusion," *Microcirculation*, vol. 17, no. 1, pp. 3–20, 2010.

- [3] W. S. Aronow, “Office management of peripheral arterial disease,” *The American journal of medicine*, vol. 123, no. 9, pp. 790–792, 2010.
- [4] R. Hinchliffe, G. Andros, J. Apelqvist, K. Bakker, S. Fiedrichs, J. Lammer, M. Lepadalo, J. L. Mills, J. Reekers, and C. Shearman, “A systematic review of the effectiveness of revascularization of the ulcerated foot in patients with diabetes and peripheral arterial disease,” *Diabetes/metabolism research and reviews*, vol. 28, no. S1, pp. 179–217, 2012.
- [5] A. Matsakas, V. Yadav, S. Lorca, R. M. Evans, and V. A. Narkar, “Revascularization of ischemic skeletal muscle by estrogen-related receptor- γ ,” *Circulation research*, vol. 110, no. 8, pp. 1087–1096, 2012.
- [6] J. G. Regensteiner and W. R. Hiatt, “Current medical therapies for patients with peripheral arterial disease: A critical review,” *The American journal of medicine*, vol. 112, no. 1, pp. 49–57, 2002.
- [7] V. Y. Ma, L. Chan, and K. J. Carruthers, “Incidence, prevalence, costs, and impact on disability of common conditions requiring rehabilitation in the united states: Stroke, spinal cord injury, traumatic brain injury, multiple sclerosis, osteoarthritis, rheumatoid arthritis, limb loss, and back pain,” *Archives of physical medicine and rehabilitation*, vol. 95, no. 5, pp. 986–995. e1, 2014.
- [8] T. S. Westvik, T. N. Fitzgerald, A. Muto, S. P. Maloney, J. M. Pimiento, T. T. Fancher, D. Magri, H. H. Westvik, T. Nishibe, O. C. Velazquez, and A. Dardik, “Limb ischemia after iliac ligation in aged mice stimulates angiogenesis without arteriogenesis,” *J Vasc Surg*, vol. 49, no. 2, pp. 464–73, 2009.
- [9] M. Heil, S. Wagner, and W. Schaper, “Arterial regeneration by collateral artery growth (arteriogenesis),” *Drug Discovery Today: Disease Models*, vol. 1, no. 3, pp. 265–271, 2004.
- [10] J. E. Faber, W. M. Chilian, E. Deindl, N. van Royen, and M. Simons, “A brief etymology of the collateral circulation,” *Arterioscler Thromb Vasc Biol*, 2014.
- [11] M. Arras, W. D. Ito, D. Scholz, B. Winkler, J. Schaper, and W. Schaper, “Monocyte activation in angiogenesis and collateral growth in the rabbit hindlimb,” *J Clin Invest*, vol. 101, no. 1, pp. 40–50, 1998.
- [12] C. Arnold, A. Feldner, L. Pfisterer, M. Hodebeck, K. Troidl, G. Genove, T. Wieland, M. Hecker, and T. Korff, “Rgs5 promotes arterial growth during arteriogenesis,” *EMBO Mol Med*, vol. 6, no. 8, pp. 1075–1089, 2014.

- [13] P. Madeddu, C. Emanuelli, F. Spillmann, M. Meloni, N. Bouby, C. Richer, F. Alhenc-Gelas, V. Van Weel, D. Eefting, P. H. A. Quax, Y. Hu, Q. Xu, A. L. Hemdahl, J. van Golde, M. Huijberts, Q. de Lussanet, H. S. Boudier, T. Couffinhal, C. Duplaa, S. Chimenti, L. Staszewsky, R. Latini, V. Baumans, and B. I. Levy, "Murine models of myocardial and limb ischemia: Diagnostic end-points and relevance to clinical problems," *Vascular Pharmacology*, vol. 45, no. 5, pp. 281–301, 2006.
- [14] P. Carmeliet, "Mechanisms of angiogenesis and arteriogenesis," *Nature medicine*, vol. 6, no. 4, pp. 389–396, 2000.
- [15] K. A. Dora, "Cell-cell communication in the vessel wall," *Vascular Medicine*, vol. 6, no. 1, pp. 43–50, 2001.
- [16] P. Lacolley, V. Regnault, A. Nicoletti, Z. Li, and J.-B. Michel, "The vascular smooth muscle cell in arterial pathology: A cell that can take on multiple roles," *Cardiovascular research*, vol. 95, no. 2, pp. 194–204, 2012.
- [17] A. Limbourg, T. Korff, L. C. Napp, W. Schaper, H. Drexler, and F. P. Limbourg, "Evaluation of postnatal arteriogenesis and angiogenesis in a mouse model of hind-limb ischemia," *Nature protocols*, vol. 4, no. 12, pp. 1737–1748, 2009.
- [18] J.-M. Arpino, Z. Nong, F. Li, H. Yin, N. W. Ghonaim, S. Milkovich, B. Balint, C. O'Neil, G. M. Fraser, and D. Goldman, "4d microvascular analysis reveals that regenerative angiogenesis in ischemic muscle produces a flawed microcirculation," *Circulation research*, CIRCRESAHA. 116.310535, 2017.
- [19] T. Couffinhal, M. Silver, L. P. Zheng, M. Kearney, B. Witzenbichler, and J. M. Isner, "Mouse model of angiogenesis," *The American journal of pathology*, vol. 152, no. 6, p. 1667, 1998.
- [20] D. Scholz, T. Ziegelhoeffer, A. Helisch, S. Wagner, C. Friedrich, T. Podzuweit, and W. Schaper, "Contribution of arteriogenesis and angiogenesis to postocclusive hindlimb perfusion in mice," *Journal of molecular and cellular cardiology*, vol. 34, no. 7, pp. 775–787, 2002.
- [21] R. A. Brenes, C. C. Jadowiec, M. Bear, P. Hashim, C. D. Protack, X. Li, W. Lv, M. J. Collins, and A. Dardik, "Toward a mouse model of hind limb ischemia to test therapeutic angiogenesis," *Journal of vascular surgery*, vol. 56, no. 6, pp. 1669–1679, 2012.
- [22] Y. Xu, J. G. Pickering, Z. Nong, and A. D. Ward, "Segmentation of digitized histological sections for quantification of the muscularized vasculature in the mouse hind limb," *Journal of microscopy*, vol. 266, no. 1, pp. 89–103, 2017.

- [23] J. S. Elkerton, Y. Xu, J. G. Pickering, and A. D. Ward, “Differentiation of arterioles from venules in mouse histology images using machine learning,” *Journal of Medical Imaging*, vol. 4, no. 2, pp. 021 104–021 104, 2017.
- [24] D. Goldman and A. S. Popel, “A computational study of the effect of capillary network anastomoses and tortuosity on oxygen transport,” *Journal of Theoretical Biology*, vol. 206, no. 2, pp. 181–194, 2000.
- [25] B. K. Al-Khazraji, A. Saleem, D. Goldman, and D. N. Jackson, “From one generation to the next: A comprehensive account of sympathetic receptor control in branching arteriolar trees,” *The Journal of physiology*, vol. 593, no. 14, pp. 3093–3108, 2015.
- [26] M. J. Frontini, Z. Nong, R. Gros, M. Drangova, C. O’Neil, M. N. Rahman, O. Akawi, H. Yin, C. G. Ellis, and J. G. Pickering, “Fibroblast growth factor 9 delivery during angiogenesis produces durable, vasoresponsive microvessels wrapped by smooth muscle cells,” *Nature biotechnology*, vol. 29, no. 5, pp. 421–427, 2011.
- [27] F. Mac Gabhann and S. M. Peirce, “Collateral capillary arterialization following arteriolar ligation in murine skeletal muscle,” *Microcirculation*, vol. 17, no. 5, pp. 333–47, 2010.
- [28] C. L. Duvall, W. R. Taylor, D. Weiss, and R. E. Guldberg, “Quantitative microcomputed tomography analysis of collateral vessel development after ischemic injury,” *American Journal of Physiology-Heart and Circulatory Physiology*, vol. 287, no. 1, H302–H310, 2004.
- [29] S. Mirhashemi, S. Ertefai, K. Messmer, and M. Intaglietta, “Model analysis of the enhancement of tissue oxygenation by hemodilution due to increased microvascular flow velocity,” *Microvascular research*, vol. 34, no. 3, pp. 290–301, 1987.
- [30] N. J. Koning, L. E. Simon, P. Asfar, C. Baufreton, and C. Boer, “Systemic microvascular shunting through hyperdynamic capillaries after acute physiological disturbances following cardiopulmonary bypass,” *American Journal of Physiology-Heart and Circulatory Physiology*, pp. 00 397–2014, 2014.
- [31] W. Chai, Z. Fu, K. W. Aylor, E. J. Barrett, and Z. Liu, “Liraglutide prevents microvascular insulin resistance and preserves muscle capillary density in high-fat diet-fed rats,” *American Journal of Physiology-Endocrinology and Metabolism*, vol. 311, no. 3, E640–E648, 2016.
- [32] W. Zhang, X. Zhao, Y. Xiao, J. Chen, P. Han, J. Zhang, H. Fu, and Y. J. Kang, “The association of depressed angiogenic factors with reduced capillary density in the rhesus monkey model of myocardial ischemia,” *Metallomics*, vol. 8, no. 7, pp. 654–662, 2016.

- [33] C. Taylor and R. Levenson, “Quantification of immunohistochemistry-issues concerning methods, utility and semiquantitative assessment ii,” *Histopathology*, vol. 49, no. 4, pp. 411–424, 2006.
- [34] P. Carmeliet and R. K. Jain, “Molecular mechanisms and clinical applications of angiogenesis,” *Nature*, vol. 473, no. 7347, pp. 298–307, 2011.
- [35] T. Couffinhal, P. Dufourcq, L. Barandon, L. Leroux, and C. Duplaa, “Mouse models to study angiogenesis, vasculogenesis and arteriogenesis in the context of cardiovascular diseases,” *France. Institut National de la Sante et de la Recherche Meidicale*, 2010.

Chapter 6

Conclusions and Future Directions

6.1 Thesis contributions

This thesis addresses an unmet need for technology advancement in automated digital histology analysis involving 3D visualization, segmentation and classification. Methods for whole slide tissue processing and the comprehensive assessment of the microvasculature were developed. Morphological comparisons between normal and regenerated tissues of the vascular smooth muscle were performed using the developed automated system. This contributed to the understanding of blood flow functionality after an ischemic event. The achievement of the objectives (Chapter 1, Section 1.9) and answering of the research questions (Chapter 1, Section 1.9) posed in the introduction led to the following technical contributions and knowledge advancements:

Technological advancements (Chapter 1, Section 1.9):

1. A 3D histology reconstruction algorithm was developed using intrinsic landmarks within the tissue, which results in more accurate registration compared to conventional intensity based registration for tissue reconstruction.
2. An automated segmentation algorithm for the muscularized microvasculature was developed for examining the distribution of vascular morphology in a biological system.
3. A machine learning platform was developed to separate arterioles from the rest of the vasculature automatically for analysis.

Knowledge advancements (Chapter 1, Section 1.9):

1. How does conventional field of view sampling compare to our developed 2D whole tissue section analysis, with respect to vascular assessment?

- Using 2D whole tissue section analysis resulted in different vasculature measurements of morphology and density as compared to conventional field of view sampling.
2. What are the main differences in smooth muscle cell content in the post ischemic and normal arterioles?
 - There are differences in SMC content with respect to density and morphology between post ischemic and normal arterioles.
 3. How do these structural differences affect blood flow and function?
 - The differences in SMC content between post ischemic and normal arterioles effects blood flow and function.

6.1.1 Technological advancements

A 3D histology reconstruction algorithm was developed using intrinsic landmarks within the tissue, which results in more accurate registration compared to conventional intensity based registration for tissue reconstruction.

Chapter 2 describes the developed automated software involving the automated detection of small intrinsic landmarks for the registration of serial histological sections to preserve vessel continuity and geometry. Conventional intensity based algorithms are driven by salient features within the tissues and aim to register components into the same coordinate system. In the context of histology reconstruction, the tissues are serial sections that appear to be visually similar. However, they are technically extracted from different locations in the tissue. Registering the tissue sections using the conventional intensity-based or large feature based algorithms created an accumulation of error due to the “banana-to-cylinder” effect. Larger structures such as arteries and muscle bundles were registered in this case. This registration may not be representative of the original tissue geometry. Previous techniques for histological vascular reconstruction (Chapter 1, Table 1.1) used a combination of manual and intensity based registration techniques, which may result in a bias for straightening large features in the reconstructed planes. To preserve geometry of the reconstruction, we segmented intrinsic landmarks, cell nuclei, which appear in the same spatial location on adjacent serial sections. This resulted in registration of tissues with a target registration error of $3.5 \mu m$. The nuclei are not biased in their orientation and would not drive the registration in a certain direction. The size is thick enough to be bisected at $5 \mu m$ thick sections but thin enough such that the nuclei

are not visible on more than two tissue serial sections at that thickness. *Thus, this thesis contributed to the technological advancement of histology analysis by providing a new technique for 3D reconstruction and introduced the concept of geometry preserving registration in serial histology section registration using intrinsic fiducials.*

An automated segmentation algorithm for the muscularized microvasculature was developed for examining the distribution of vascular morphology in a biological system.

Chapter 3 describes our developed technique for automated adaptive vascular smooth muscle segmentation on whole slide histology, which was validated with respect to manual delineations for detection and segmentation. This validation process involved the assessment of validation measures evaluating detection, resulting in the sensitivity and specificity of 91% and 97% respectively. The segmentation measures of Dice similarity coefficient and mean absolute distance were 89% and 0.40 μm respectively. This was the first work to segment arterioles and venules, in the mouse, with this level of accuracy. Previous methods relating to vessel segmentation were mainly focused at the capillary or artery level, and either extracted the outer boundary of the stained capillary or the vessel lumen of arteries. (Chapter 1, Table 1.2) These validation techniques have been used to assess automated and semi-automated segmentation techniques in many different imaging modalities in 2D and 3D. [1], [2] We took the validation a step further in order to assess the biological validity of the resulting measures from the automated detection and segmentation measure. We assessed the proportion of vessels in each size category and demonstrated that there was the expected number of vessels for each level of vasculature. As the stain targeted the smooth muscle component, we expected there to be many vessels in the 10 to 40 μm range with fewer vessels in the $> 40 \mu\text{m}$ range as there are fewer large caliber vessels. There was also a smaller proportion of vasculature detected in the $< 10 \mu\text{m}$ range as this is at the level of the capillaries. The vessels either contain partial pericyte wrapping or no smooth muscle component at this level of the vasculature. The vessel wall thickness of the vascular smooth muscle was consistent with the size of the vessel. Larger calibre vessels contain a thicker layer of smooth muscle that enables control of higher blood flow. *Thus, the thesis contributed to the technological advancement of quantitative vascular assessment on whole slide histology, which provides a method for measuring the morphology of the microvasculature at the arteriole and venule level with high throughput, independent of user input.*

A machine learning platform was developed to separate arterioles from the rest of the vasculature automatically for analysis.

Chapter 4 presented an automated method for classifying the arteriolar and venular components of the vascular tree through machine learning techniques. This step is crucial for the assessment of the arteriolar portion of the microvasculature that controls the local distribution of blood flow. Accurate representation of the vascular smooth muscle of the arteriolar vascular tree needs accurate classification. Previous classification has been performed manually and can be laborious or observer dependent. The automated classification, which was developed, resulted in AUC of 0.91 and an overall error rate of 15%. The technique resulted in a stable two feature classifier, which results in the separation of the arterioles, and thus the accurate assessment of this portion of the vasculature. Thus, the measurement is not hindered by the pollution of other vessels detected and segmented by the algorithm targeting smooth muscle. *Thus, the thesis contributed to the technological advancement of automatically classifying features, specifically arterioles, within histology using a machine learning platform.*

6.1.2 Knowledge advancements

How does conventional field of view sampling compare to our developed 2D whole tissue section analysis, with respect to vascular assessment?

Chapter 3 measured the difference between field of view (FOV) simulations and whole slide analysis of morphological and density measurements of the vasculature. The analysis of microvasculature density measures at the level of the capillaries has been assessed in many previous studies in order to assess microvascular regeneration and tumour vascular growth. [3] This approach has been performed by using FOV and extrapolating the value to compare the differences in samples. [4] Capillaries are generally evenly distributed and contain one endothelial layer such that a density measure by manual counting on fields of view and extrapolation can be representative of the tissue sections, if they are taken in representative areas of the tissue. However, arterioles are not evenly distributed throughout the tissue section so a count within a FOV will likely not account for the density within the whole slide section. The arterioles also contain a layer of vascular smooth muscle, which varies in thickness down the vascular tree, along with the size of the vessels. The sampling of a select few arterioles within a whole slide image will not be representative of the whole slide image unless a substantial number of FOV are selected, and for one measure up to 30 FOV at 40 times objective magnification. In this case, many manual measurements need to be taken to assess the vasculature. Whole slide analysis enables for a comprehensive assessment of morphology. The amount of vascular

smooth muscle wrapping can be compared between mouse models. The detected aberrations may affect function of the vasculature. *Thus, the thesis advanced knowledge of the effects of selecting fields of view for histological analysis compared to comprehensive measurements on the whole slide using our developed automated detection and segmentation technique.*

What are the main differences in smooth muscle cell content in the post ischemic arteriolar microvasculature compared to the normal tissue?

Chapter 5 evaluated the differences in vascular smooth muscle cell (SMC) morphology and density in the regenerated post-ischemic hind limb as compared to the normal vasculature. The platform described in chapters 3 and 4 involved the comprehensive quantitation of the vascular smooth muscle on a whole slide level. This quantification, in the simplest form, facilitates the comparison of the vessel density of the arteriolar tree. The two-fold increase in the vessel density in the regenerated vasculature correlates with the increase in capillary density described in previous literature and demonstrates regrowth of the vasculature. [5]–[7] Morphological measures, computed by our developed automated technique, included the vessel lumen diameter, perimeter, area of the vessel wall and the vessel wall thickness. A feature of interest was the thickness of the vessel wall as it pertains to the SMC wrapping. Thinner wrapping was found in the regenerated vasculature, which suggests a deficiency in the control of vessel wall diameter for the control of blood flow. Previous literature demonstrated a thickening of the collateral vasculature wall through arteriogenesis. However, the subsequent microvasculature containing SMC is understudied. *Thus, the thesis advanced knowledge in the distribution and morphological differences in the regenerated arteriolar level vasculature post an ischemic event.*

How do these structural differences affect blood flow and function?

Chapter 5 inferred vasotone function at rest and in the state of oxygen demand through blood flow modeling with the input of empirical measures from the automated segmentations of the vasculature. The morphological measures alone do not demonstrate the effects of regeneration on the vasculature. Incorporating comprehensive measurements into a functional model resulted in the ability to demonstrate the functional consequences of structural aberrations. Other complications in the vasculature are visible in the regenerated network through in vivo imaging, were not considered in the blood flow model. These complications such as vascular shunting and disorganization would only add to the deficiency in flow. Even without considering all aberrations in the regenerated network, we found that the deficiency in SMC wrapping caused an 89% reduction in flow, compared to a normal vascular network. *Thus, the thesis ad-*

vanced the knowledge of the arteriolar tree function with regards to blood flow after vascular regeneration.

In summary, we have developed a software platform for: (1) automated 3D histology reconstruction for the visualization of microvasculature with the conservation of geometry and topology, which resulted in the detection of rare aberrations within the tissue volume; (2) automated detection and segmentation of muscularized microvessels within the 2D whole slide histological sections provided high throughput quantification; (3) classification of vascular subtypes automatically through a machine learning platform for separation of the arteriolar network enabled separate analysis; and (4) comprehensive measurement of the arteriolar vascular tree with respect to vascular smooth muscle and simulation of vascular function through blood flow modeling. With the use of the developed software platform, we could detect and model the morphological and functional differences between the normal and regenerated vasculature after an ischemic event.

6.2 Applications and future directions

6.2.1 Vascular analysis in different organs and stains

Reconstruction and segmentation techniques have been applied to tissues with different stains and at different organ sites, thus demonstrates a need for automated vascular analysis. The targeted vessel wall component of our experiments has been the vascular smooth muscle, stained with IHC. The automated reconstruction algorithm developed is reliant on the detection of nuclei, which are present in all cell types. Adaptations of the current algorithms for applications at different organ sites with different stains is feasible with the growth of histology digitization and other advances parallel to the work presented in this thesis. Our work focused on the vasculature within the skeletal muscle of the hindlimb and other works of image registration for reconstruction and segmentation have been performed on organs such as the brain, liver, and glomerulus. [8] Some studies focused on the vasculature; [9]–[13] however other features such as grey and white matter patterns in the brain were of interest. [14], [15] The separation of stains is feasible with colour deconvolution techniques developed for stain separation and thus the developed segmentation can target stains resulting in different colours. [16], [17]

6.2.2 Adaptation of developed techniques for additional applications

Machine learning was used for the classification of vessel subcategories within this thesis but can be used for detection of abnormal pathologies within histology and in combination with

other imaging modalities. Features derived from quantitative histopathology can be used to train a classifier to detect abnormalities within the vasculature or other tissue types. Parameters of the vasculature through automated morphology measurement can potentially be used to train a system to define a classifier for levels of vascular functionality. Applications of machine learning have been previously demonstrated in the literature in combination with image analysis, and were used for cancer prediction and prognosis. [18], [19] This was not only performed in the histological context but with MRI texture and structural morphology as well. [20] Overall, machine learning facilitates users to take advantage of the large numbers of parameters, whether from features of histology or other means, and aids in parsing the dataset to differentiate pathologies.

6.2.3 Potential applications for immunohistochemistry (IHC) analysis

Registration of serial tissue sections in histology can be used for 3D reconstruction, as demonstrated by this thesis, but it can have other application in IHC analysis as well. 3D reconstructions of 2D histology have been used to measure the density of the capillaries in tumour volumes stained for CD31, the endothelial wall component. [9], [21] IHC targets the vasculature and H&E staining enables the visualization of large components within the tissue such as arteries. [22] 3D interpretation of tissue volumes can give the user the ability to assess tissue components without mentally reconstructing through viewing multiple 2D images consecutively. IHC can target specific proteins on a given tissue section. Assessment of different proteins can be performed on serial tissue sections. Colocalizations of proteins are essential to the understanding of interaction within the tissue. Registration of serial sections targeting different stains enables this interpretation of different probes without double IHC procedures. [23]

Automated segmentation within histological tissue enables the comprehensive quantitative assessment of previously user dependent qualitative judgements. Conventional analysis of IHC can involve a “quick eyeball” where the result is based on the individual’s experience. [24] Quantitative analysis involves subsampling fields of view within the tissue section and usually getting a count of the features, essentially calculating a density measure. [25] Segmentation of features in the tissues can aid the field of biological research and eventually in the clinical with implementation of digitized histology. Morphological measurement and automated density counts are performed in the literature and recently, semi-automated commercial software is now available for use in the biological sciences. [25] With further development, automated segmentation will aid scientists and clinicians with the tedious task of cell counting. Automation will also take measures on IHC sections, which were previous unfeasible to perform manually.

One example would be the thickness measurement along each individual pixel of each vessel on sections with hundreds of microvessels as demonstrated by chapter 3 of this thesis.

6.3 Remaining gaps in automated histology analysis

There are several software and hardware advancements that will produce robust histology reconstructions. Registration techniques beyond those described within this thesis need to be developed for robust alignment of different tissue types. Though our algorithm described in chapter 2 resulted in the alignment of serial sections based on cell nuclei present in all tissue types, it was only tested on the skeletal muscle of the mouse hindlimb. To test the robustness of the developed algorithm and the others developed in this field, they need to be tested on different tissue types processed in different labs. Due to the nature of sectioning paraffin embedded tissues on a manual microtome, we can only get a set number of serial sections (under 20) for tissue reconstruction. In order to visualize a large portion of the vascular tree or reconstruct a whole mouse organ, hundreds of serial sections need to be taken. Recently, there has been the development of a system that produces automated serial sectioning of paraffin embedded tissues. [26] This enabled the reconstruction of histology volumes through proof of concept studies. [27] Advancements in histology reconstruction has arisen with the combination of the advancements of software algorithms for accurate registration and hardware for automated serial sectioning.

Segmentation of features within the tissues facilitates morphological measurement and visual pattern quantitation within histological tissues. Within the context of this thesis, the vascular smooth muscle component of the arteriolar vessel tree was quantified with the development of a segmentation algorithm and classification of the vasculature through machine learning. However, this was only performed on one type of tissue and only encompasses one component of the microvasculature. The tissues can be from different regions within the specimen or taken from a patient through a biopsy. For the use of automated segmentation in research and eventually in the clinic, algorithms need to be developed to be robust and site specific with adaptation to different types of stains that may be used. Alongside the advancements of software for segmentation, there needs to be standardization of the IHC process to a degree, within one institution, such that the algorithms can perform accurately. [25] Works are performed for stain normalization from center to center as well as from different batches of the IHC process prior to assessments. [28], [29] However, this can only correct the tissue to a certain degree and in some cases may occlude differences inherently to the tissue section. Thus, advancements and standardized protocols need to be developed hand in hand to accommodate for automated tissue segmentation for assessment.

The field of histology has been incorporating fluorescence microscopy for visualization of multiple probes on one tissue section. Reconstruction and segmentation processes in the field of brightfield histology should take fluorescent images into account with advent of whole slide fluorescent histology scanners and multiplexing. [30] The capability to stain for multiple probes through multiplexing on one tissue section is not yet conventionally available, but is one method for understanding colocalization of proteins. Building algorithms that may be adapted for fluorescence as well as bright field microscopy with site specific analysis of abnormalities will play a role in aiding researchers and clinicians assess features not possible by conventional manual evaluations.

References

- [1] M. G. Linguraru, J. A. Pura, R. L. Van Uitert, N. Mukherjee, R. M. Summers, C. Minniti, M. T. Gladwin, G. Kato, R. F. Machado, and B. J. Wood, “Segmentation and quantification of pulmonary artery for noninvasive ct assessment of sickle cell secondary pulmonary hypertension,” *Medical physics*, vol. 37, no. 4, 2010.
- [2] L. T. Mikalsen, H. P. Dhakal, O. S. Bruland, J. M. Nesland, and D. R. Olsen, “Quantification of angiogenesis in breast cancer by automated vessel identification in cd34 immunohistochemical sections,” *Anticancer Res*, vol. 31, no. 12, pp. 4053–60, 2011.
- [3] N. Weidner, “Current pathologic methods for measuring intratumoral microvessel density within breast carcinoma and other solid tumors,” *Breast cancer research and treatment*, vol. 36, no. 2, pp. 169–180, 1995.
- [4] C. Heeschen, J. J. Jang, M. Weis, A. Pathak, S. Kaji, R. S. Hu, P. S. Tsao, F. L. Johnson, and J. P. Cooke, “Nicotine stimulates angiogenesis and promotes tumor growth and atherosclerosis,” *Nature medicine*, vol. 7, no. 7, pp. 833–839, 2001.
- [5] A. Limbourg, T. Korff, L. C. Napp, W. Schaper, H. Drexler, and F. P. Limbourg, “Evaluation of postnatal arteriogenesis and angiogenesis in a mouse model of hind-limb ischemia,” *Nature protocols*, vol. 4, no. 12, pp. 1737–1748, 2009.
- [6] D. Scholz, T. Ziegelhoeffer, A. Helisch, S. Wagner, C. Friedrich, T. Podzuweit, and W. Schaper, “Contribution of arteriogenesis and angiogenesis to postocclusive hindlimb perfusion in mice,” *Journal of molecular and cellular cardiology*, vol. 34, no. 7, pp. 775–787, 2002.

- [7] T. Couffinhal, M. Silver, L. P. Zheng, M. Kearney, B. Witzensbichler, and J. M. Isner, "Mouse model of angiogenesis," *The American journal of pathology*, vol. 152, no. 6, p. 1667, 1998.
- [8] N. Roberts, D. Magee, Y. Song, K. Brabazon, M. Shires, D. Crellin, N. M. Orsi, R. Quirke, P. Quirke, and D. Treanor, "Toward routine use of 3d histopathology as a research tool," *The American journal of pathology*, vol. 180, no. 5, pp. 1835–1842, 2012.
- [9] J. M. Gijtenbeek, P. Wesseling, C. Maass, L. Burgers, and J. A. van der Laak, "Three-dimensional reconstruction of tumor microvasculature: Simultaneous visualization of multiple components in paraffin-embedded tissue," *Angiogenesis*, vol. 8, no. 4, pp. 297–305, 2005.
- [10] C. F. Chantrain, Y. A. DeClerck, S. Groshen, and G. McNamara, "Computerized quantification of tissue vascularization using high-resolution slide scanning of whole tumor sections," *J Histochem Cytochem*, vol. 51, no. 2, pp. 151–8, 2003.
- [11] C. Sullivan, S. Ghosh, I. Ocal, R. Camp, D. L. Rimm, and G. Chung, "Microvessel area using automated image analysis is reproducible and is associated with prognosis in breast cancer," *Human pathology*, vol. 40, no. 2, pp. 156–165, 2009.
- [12] C. C. Reyes-Aldasoro, L. J. Williams, S. Akerman, C. Kanthou, and G. M. Tozer, "An automatic algorithm for the segmentation and morphological analysis of microvessels in immunostained histological tumour sections," *Journal of Microscopy*, vol. 242, no. 3, pp. 262–278, 2011.
- [13] M. M. Fernandez-Carrobles, I. Tadeo, G. Bueno, R. Noguera, O. Deniz, J. Salido, and M. Garcia-Rojo, "Tma vessel segmentation based on color and morphological features: Application to angiogenesis research," *Scientific World Journal*, vol. 2013, p. 263 190, 2013.
- [14] A. Cifor, L. Bai, and A. Pitiot, "Smoothness-guided 3-d reconstruction of 2-d histological images," *NeuroImage*, vol. 56, no. 1, pp. 197–211, 2011.
- [15] C. D. Markovitz, T. T. Tang, D. P. Edge, and H. H. Lim, "Three-dimensional brain reconstruction of in vivo electrode tracks for neuroscience and neural prosthetic applications," *Frontiers in neural circuits*, vol. 6, no. Journal Article, p. 39, 2012.
- [16] A. C. Ruifrok and D. A. Johnston, "Quantification of histochemical staining by color deconvolution," *Anal Quant Cytol Histol*, vol. 23, no. 4, pp. 291–9, 2001.
- [17] P. Haub and T. Meckel, "A model based survey of colour deconvolution in diagnostic brightfield microscopy: Error estimation and spectral consideration," *Scientific reports*, vol. 5, 2015.

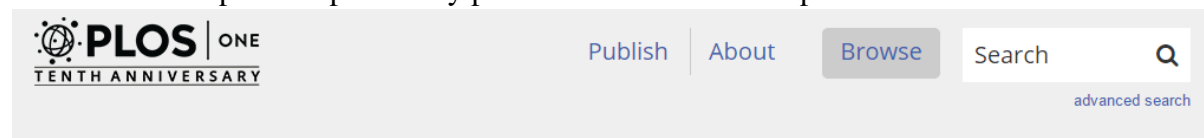
- [18] J. A. Cruz and D. S. Wishart, “Applications of machine learning in cancer prediction and prognosis,” *Cancer informatics*, vol. 2, 2006.
- [19] W. H. Wolberg, W. N. Street, and O. L. Mangasarian, “Image analysis and machine learning applied to breast cancer diagnosis and prognosis,” *Analytical and Quantitative cytology and histology*, vol. 17, no. 2, pp. 77–87, 1995.
- [20] E. I. Zacharaki, S. Wang, S. Chawla, D. Soo Yoo, R. Wolf, E. R. Melhem, and C. Davatzikos, “Classification of brain tumor type and grade using mri texture and shape in a machine learning scheme,” *Magnetic Resonance in Medicine*, vol. 62, no. 6, pp. 1609–1618, 2009.
- [21] H. J. Gilhuis, J. A. van der Laak, J. Pomp, A. C. Kappelle, J. M. Gijtenbeek, and P. Wesseling, “Three-dimensional (3d) reconstruction and quantitative analysis of the microvasculature in medulloblastoma and ependymoma subtypes,” *Angiogenesis*, vol. 9, no. 4, pp. 201–208, 2006.
- [22] M. Schwier, T. Bohler, H. K. Hahn, U. Dahmen, and O. Dirsch, “Registration of histological whole slide images guided by vessel structures,” *Journal of pathology informatics*, vol. 4, no. Suppl, S10–3539.109868. Print 2013, 2013.
- [23] Y. Song, D. Treanor, A. J. Bulpitt, and D. R. Magee, “3d reconstruction of multiple stained histology images,” *Journal of pathology informatics*, vol. 4, no. S7, p. 3539.109864, 2013.
- [24] R. Walker, “Quantification of immunohistochemistry-issues concerning methods, utility and semiquantitative assessment i,” *Histopathology*, vol. 49, no. 4, pp. 406–410, 2006.
- [25] C. Taylor and R. Levenson, “Quantification of immunohistochemistry - issues concerning methods, utility and semiquantitative assessment ii,” *Histopathology*, vol. 49, no. 4, pp. 411–424, 2006.
- [26] M. L. Onozato, S. Hammond, M. Merren, and Y. Yagi, “Evaluation of a completely automated tissue-sectioning machine for paraffin blocks,” *Journal of clinical pathology*, vol. 66, no. 2, pp. 151–154, 2013.
- [27] L. Fonyad, K. Shinoda, E. A. Farkash, M. Groher, D. P. Sebastian, A. M. Szasz, R. B. Colvin, and Y. Yagi, “3-dimensional digital reconstruction of the murine coronary system for the evaluation of chronic allograft vasculopathy,” *Diagnostic pathology*, vol. 10, no. 1, p. 16, 2015.
- [28] M. Niethammer, D. Borland, J. Marron, J. T. Woosley, and N. E. Thomas, “Appearance normalization of histology slides,” in *MLMI*, Springer, 2010, pp. 58–66.

- [29] A. M. Khan, N. Rajpoot, D. Treanor, and D. Magee, “A nonlinear mapping approach to stain normalization in digital histopathology images using image-specific color deconvolution,” *Biomedical Engineering, IEEE Transactions on*, vol. 61, no. 6, pp. 1729–1738, 2014.
- [30] G. M. Clarke, J. T. Zubovits, K. A. Shaikh, D. Wang, S. R. Dinn, A. D. Corwin, A. Santamaria-Pang, Q. Li, S. Nofech-Mozes, and K. Liu, “A novel, automated technology for multiplex biomarker imaging and application to breast cancer,” *Histopathology*, vol. 64, no. 2, pp. 242–255, 2014.

Appendix A

Permission for Reproduction of Scientific Articles

Permission to reproduce previously published material in Chapter 2



Licenses and Copyright

The following policy applies to all PLOS journals, unless otherwise noted.

What Can Others Do with My Original Article Content?

PLOS applies the [Creative Commons Attribution \(CC BY\) license](#) to articles and other works we publish. If you submit your paper for publication by PLOS, you agree to have the CC BY license applied to your work. Under this Open Access license, you as the author agree that anyone can reuse your article in whole or part for any purpose, for free, even for commercial purposes. Anyone may copy, distribute, or reuse the content as long as the author and original source are properly cited. This facilitates freedom in re-use and also ensures that PLOS content can be mined without barriers for the needs of research.

May I Use Content Owned by Someone Else in My Article?

If you have written permission to do so, yes. If your manuscript contains content such as photos, images, figures, tables, audio files, videos, etc., that you or your co-authors do not own, we will require you to provide us with proof that the owner of that content (a) has given you written permission to use it, and (b) has approved of the CC BY license being applied to their content. We provide a form you can use to ask for and obtain permission from the owner. [Download the form \(PDF\)](#).

i If you do not have owner permission, we will ask you to remove that content and/or replace it with other content that you own or have such permission to use.

Don't assume that you can use any content you find on the Internet, or that the content is fair game just because it isn't clear who the owner is or what license applies. It's up to you to ascertain what rights you have—if any—to use that content.

May I Use Article Content I Previously Published in Another Journal?

Many authors assume that if they previously published a paper through another publisher, they own the rights to that content and they can freely use that content in their PLOS paper, but that's not necessarily the case – it depends on the license that covers the other paper. Some publishers allow free and unrestricted re-use of article content they own, such as under the CC BY license. Other publishers use licenses that allow re-use only if the same license is applied by the person or publisher re-using the content.

If the paper was published under a CC BY license or another license that allows free and unrestricted use, you may use the content in your PLOS paper provided that you give proper attribution, as explained above.

If the content was published under a more restrictive license, you must ascertain what rights you have under that license. At a minimum, review the license to make sure you can use the content. Contact that publisher if you have any questions about the license terms – PLOS staff cannot give you legal advice about your rights to use third-party content. If the license does not permit you to use the content in a paper that will be covered by an unrestricted license, you must obtain written permission from the publisher to use the content in your PLOS paper. Please do not include any content in your PLOS paper which you do not have rights to use, and always give proper attribution.

What Are Acceptable Licenses for Data Repositories?

If any relevant accompanying data is submitted to repositories with stated licensing policies, the policies should not be more restrictive than CC BY.

Removal of Content Used Without Clear Rights

PLOS reserves the right to remove any photos, captures, images, figures, tables, illustrations, audio and video files, and the like, from any paper, whether before or after publication, if we have reason to believe that the content was included in your paper without permission from the owner of the content.

How Does One Give Proper Attribution for Use of Content?

When citing a PLOS research article, use the "Vancouver style", as outlined in our [Submission Guidelines](#). For example:

Kaltenbach LS et al. (2007) Huntingtin Interacting Proteins Are Genetic Modifiers of Neurodegeneration. *PLOS Genet* 3(5): e82.
doi:10.1371/journal.pgen.0030082.

When citing non-article content from a PLOS website (e.g., blog content), provide a link to the content, and cite the title and author(s) of that content.

For examples of proper attribution to other types of content, see websites such as [Open.Michigan](#).

Permission to reproduce previously published material in Chapter 3

**JOHN WILEY AND SONS LICENSE
TERMS AND CONDITIONS**

Mar 10, 2017

This Agreement between Yiwen Xu ("You") and John Wiley and Sons ("John Wiley and Sons") consists of your license details and the terms and conditions provided by John Wiley and Sons and Copyright Clearance Center.

License Number	4064980305368
License date	
Licensed Content Publisher	John Wiley and Sons
Licensed Content Publication	Journal of Microscopy
Licensed Content Title	Segmentation of digitized histological sections for quantification of the muscularized vasculature in the mouse hind limb
Licensed Content Author	YIWEN XU,J. GEOFFREY PICKERING,ZENGXUAN NONG,AARON D. WARD
Licensed Content Date	Feb 20, 2017
Licensed Content Pages	15
Type of use	Dissertation/Thesis
Requestor type	Author of this Wiley article
Format	Print and electronic
Portion	Full article
Will you be translating?	No
Title of your thesis / dissertation	Automated vascular segmentation, reconstruction, classification and simulation on whole-slide histology
Expected completion date	Apr 2017
Expected size (number of pages)	250
Requestor Location	Yiwen Xu

Publisher Tax ID	EU826007151
Billing Type	Invoice
Billing Address	Yiwen Xu

Total	0.00 CAD
-------	----------

Terms and Conditions

TERMS AND CONDITIONS

This copyrighted material is owned by or exclusively licensed to John Wiley & Sons, Inc. or one of its group companies (each a "Wiley Company") or handled on behalf of a society with which a Wiley Company has exclusive publishing rights in relation to a particular work (collectively "WILEY"). By clicking "accept" in connection with completing this licensing transaction, you agree that the following terms and conditions apply to this transaction (along with the billing and payment terms and conditions established by the Copyright Clearance Center Inc., ("CCC's Billing and Payment terms and conditions"), at the time that you opened your RightsLink account (these are available at any time at <http://myaccount.copyright.com>).

Terms and Conditions

- The materials you have requested permission to reproduce or reuse (the "Wiley Materials") are protected by copyright.
- You are hereby granted a personal, non-exclusive, non-sub licensable (on a stand-alone basis), non-transferable, worldwide, limited license to reproduce the Wiley Materials for the purpose specified in the licensing process. This license, **and any CONTENT (PDF or image file) purchased as part of your order**, is for a one-time use only and limited to any maximum distribution number specified in the license. The first instance of republication or reuse granted by this license must be completed within two years of the date of the grant of this license (although copies prepared before the end date may be distributed thereafter). The Wiley Materials shall not be used in any other manner or for any other purpose, beyond what is granted in the license. Permission is granted subject to an appropriate acknowledgement given to the author, title of the material/book/journal and the publisher. You shall also duplicate the copyright notice that appears in the Wiley publication in your use of the Wiley Material. Permission is also granted on the understanding that nowhere in the text is a previously published source acknowledged for all or part of this Wiley Material. Any third party content is expressly excluded from this permission.
- With respect to the Wiley Materials, all rights are reserved. Except as expressly granted by the terms of the license, no part of the Wiley Materials may be copied, modified, adapted (except for minor reformatting required by the new Publication), translated, reproduced, transferred or distributed, in any form or by any means, and no derivative works may be made based on the Wiley Materials without the prior permission of the respective copyright owner. **For STM Signatory Publishers clearing permission under the terms of the [STM Permissions Guidelines](#) only, the terms of the license are extended to include subsequent editions and for editions in other languages, provided such editions are for the work as a whole in situ and does not involve the separate exploitation of the permitted figures or extracts**, You may not alter, remove or suppress in any manner any copyright, trademark or other notices displayed by the Wiley Materials. You may not license, rent, sell, loan, lease, pledge, offer as security, transfer or assign the Wiley Materials on a stand-alone basis, or any of the rights granted to you hereunder to any other person.

- The Wiley Materials and all of the intellectual property rights therein shall at all times remain the exclusive property of John Wiley & Sons Inc, the Wiley Companies, or their respective licensors, and your interest therein is only that of having possession of and the right to reproduce the Wiley Materials pursuant to Section 2 herein during the continuance of this Agreement. You agree that you own no right, title or interest in or to the Wiley Materials or any of the intellectual property rights therein. You shall have no rights hereunder other than the license as provided for above in Section 2. No right, license or interest to any trademark, trade name, service mark or other branding ("Marks") of WILEY or its licensors is granted hereunder, and you agree that you shall not assert any such right, license or interest with respect thereto
- NEITHER WILEY NOR ITS LICENSORS MAKES ANY WARRANTY OR REPRESENTATION OF ANY KIND TO YOU OR ANY THIRD PARTY, EXPRESS, IMPLIED OR STATUTORY, WITH RESPECT TO THE MATERIALS OR THE ACCURACY OF ANY INFORMATION CONTAINED IN THE MATERIALS, INCLUDING, WITHOUT LIMITATION, ANY IMPLIED WARRANTY OF MERCHANTABILITY, ACCURACY, SATISFACTORY QUALITY, FITNESS FOR A PARTICULAR PURPOSE, USABILITY, INTEGRATION OR NON-INFRINGEMENT AND ALL SUCH WARRANTIES ARE HEREBY EXCLUDED BY WILEY AND ITS LICENSORS AND WAIVED BY YOU.
- WILEY shall have the right to terminate this Agreement immediately upon breach of this Agreement by you.
- You shall indemnify, defend and hold harmless WILEY, its Licensors and their respective directors, officers, agents and employees, from and against any actual or threatened claims, demands, causes of action or proceedings arising from any breach of this Agreement by you.
- IN NO EVENT SHALL WILEY OR ITS LICENSORS BE LIABLE TO YOU OR ANY OTHER PARTY OR ANY OTHER PERSON OR ENTITY FOR ANY SPECIAL, CONSEQUENTIAL, INCIDENTAL, INDIRECT, EXEMPLARY OR PUNITIVE DAMAGES, HOWEVER CAUSED, ARISING OUT OF OR IN CONNECTION WITH THE DOWNLOADING, PROVISIONING, VIEWING OR USE OF THE MATERIALS REGARDLESS OF THE FORM OF ACTION, WHETHER FOR BREACH OF CONTRACT, BREACH OF WARRANTY, TORT, NEGLIGENCE, INFRINGEMENT OR OTHERWISE (INCLUDING, WITHOUT LIMITATION, DAMAGES BASED ON LOSS OF PROFITS, DATA, FILES, USE, BUSINESS OPPORTUNITY OR CLAIMS OF THIRD PARTIES), AND WHETHER OR NOT THE PARTY HAS BEEN ADVISED OF THE POSSIBILITY OF SUCH DAMAGES. THIS LIMITATION SHALL APPLY NOTWITHSTANDING ANY FAILURE OF ESSENTIAL PURPOSE OF ANY LIMITED REMEDY PROVIDED HEREIN.

- Should any provision of this Agreement be held by a court of competent jurisdiction to be illegal, invalid, or unenforceable, that provision shall be deemed amended to achieve as nearly as possible the same economic effect as the original provision, and the legality, validity and enforceability of the remaining provisions of this Agreement shall not be affected or impaired thereby.
- The failure of either party to enforce any term or condition of this Agreement shall not constitute a waiver of either party's right to enforce each and every term and condition of this Agreement. No breach under this agreement shall be deemed waived or excused by either party unless such waiver or consent is in writing signed by the party granting such waiver or consent. The waiver by or consent of a party to a breach of any provision of this Agreement shall not operate or be construed as a waiver of or consent to any other or subsequent breach by such other party.
- This Agreement may not be assigned (including by operation of law or otherwise) by you without WILEY's prior written consent.
- Any fee required for this permission shall be non-refundable after thirty (30) days from receipt by the CCC.
- These terms and conditions together with CCC's Billing and Payment terms and conditions (which are incorporated herein) form the entire agreement between you and WILEY concerning this licensing transaction and (in the absence of fraud) supersedes all prior agreements and representations of the parties, oral or written. This Agreement may not be amended except in writing signed by both parties. This Agreement shall be binding upon and inure to the benefit of the parties' successors, legal representatives, and authorized assigns.
- In the event of any conflict between your obligations established by these terms and conditions and those established by CCC's Billing and Payment terms and conditions, these terms and conditions shall prevail.
- WILEY expressly reserves all rights not specifically granted in the combination of (i) the license details provided by you and accepted in the course of this licensing transaction, (ii) these terms and conditions and (iii) CCC's Billing and Payment terms and conditions.
- This Agreement will be void if the Type of Use, Format, Circulation, or Requestor Type was misrepresented during the licensing process.

- This Agreement shall be governed by and construed in accordance with the laws of the State of New York, USA, without regards to such state's conflict of law rules. Any legal action, suit or proceeding arising out of or relating to these Terms and Conditions or the breach thereof shall be instituted in a court of competent jurisdiction in New York County in the State of New York in the United States of America and each party hereby consents and submits to the personal jurisdiction of such court, waives any objection to venue in such court and consents to service of process by registered or certified mail, return receipt requested, at the last known address of such party.

WILEY OPEN ACCESS TERMS AND CONDITIONS

Wiley Publishes Open Access Articles in fully Open Access Journals and in Subscription journals offering Online Open. Although most of the fully Open Access journals publish open access articles under the terms of the Creative Commons Attribution (CC BY) License only, the subscription journals and a few of the Open Access Journals offer a choice of Creative Commons Licenses. The license type is clearly identified on the article.

The Creative Commons Attribution License

The [Creative Commons Attribution License \(CC-BY\)](#) allows users to copy, distribute and transmit an article, adapt the article and make commercial use of the article. The CC-BY license permits commercial and non-

Creative Commons Attribution Non-Commercial License

The [Creative Commons Attribution Non-Commercial \(CC-BY-NC\) License](#) permits use, distribution and reproduction in any medium, provided the original work is properly cited and is not used for commercial purposes.(see below)

Creative Commons Attribution-Non-Commercial-NoDerivs License

The [Creative Commons Attribution Non-Commercial-NoDerivs License \(CC-BY-NC-ND\)](#) permits use, distribution and reproduction in any medium, provided the original work is properly cited, is not used for commercial purposes and no modifications or adaptations are made. (see below)

Use by commercial "for-profit" organizations

Use of Wiley Open Access articles for commercial, promotional, or marketing purposes requires further explicit permission from Wiley and will be subject to a fee.

Further details can be found on Wiley Online Library



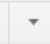

<http://olabout.wiley.com/WileyCDA/Section/id-410895.html>

Other Terms and Conditions:

v1.10 Last updated September 2015

Questions? customercare@copyright.com or +1-855-239-3415 (toll free in the US) or +1-978-646-2777.

Permission to reproduce previously published material in Chapter 4

 **Nicole Harris** [/ia uwoca.onmicrosoft.com](mailto:nharris@uwoca.onmicrosoft.com) 7:04 PM (21 hours ago) ☆  
to Yiwon Xu 

Dear Yiwon Xu,

Thank you for seeking permission from SPIE to reprint material from our publications. Publisher's permission is hereby granted under the following conditions:

- (1) you obtain permission of one of the authors;
 - (2) the material to be used has appeared in our publication without credit or acknowledgment to another source;
- and

- (3) you credit the original SPIE publication. Include the authors' names, title of paper, volume title, SPIE volume number, and year of publication in your credit statement.

Sincerely,

Nicole Harris
Administrative Editor, SPIE Publications

SPIE is the international society for optics and photonics. <http://SPIE.org>

SPIE.

From: Yiwon Xu
Sent: Thursday, March 9, 2017 1:44 PM
To: reprint_permission
Subject: Permission to Use Published Materials for Thesis

...

Good afternoon,

I am requesting permission to use the following journal article as a chapter in my PhD thesis.

Elkertson J, Xu Y, Pickering J, Ward AD; Differentiation of arterioles from venules in mouse histology images using machine learning. J. Med. Imag. 0001;4(2):021104. doi:10.1117/1.JMI.4.2.021104.

Best regards,
Yiwon Xu

Appendix B

Curriculum Vitae

Education

PhD Medical Biophysics - MCISc Clinical Medical Physics (CAMPEP-accredited)

Sept 2012 - May 2017

The University of Western Ontario, London, Ontario

Supervisors: Aaron Ward, PhD and J. Geoffrey Pickering, MD, PhD, FRCPC

BMSc Honours Specialization Medical Biophysics (Western Scholars)

Sept 2008 - Apr 2012

The University of Western Ontario, London, Ontario

Training & Certificates

Jul	2011	Laboratory - Environmental Waste Management Safety Training
Aug	2011	Biosafety Training
Sept	2012	Teaching Assistant Training Program
Aug	2014	Worker Health and Safety Awareness
Mar	2015	Accessibility at Western (AODA) - Accessibility in Service
Dec	2015	Professionalism in Everyday Practice (RSNA)
Jan	2015	Chemical Management Safety Training
May	2016	WHMIS 2015 Edition
Aug	2016	Canada Good Clinical Practice

Technical Training

Software languages: MATLAB, C++, Java, LaTeX

Programs: Slicer3D, IBM SPSS, Microsoft Word, PowerPoint, Excel, Access, GraphPad Prism, TeXnicCenter, TortoiseHg, Camtasia, EndNote, ImageScope, ITK Snap

Memberships

Student member, SPIE Medical Imaging

Student member, The American Association of Physicists in Medicine

Professional Experience

Research Assistant, London Regional Cancer Program and Robarts Research Institute

Sept 2012 - Present

Algorithm development for automating the process of vascular image analysis on digitized histology through programming in the field of image registration, segmentation, and machine learning.

Radiotherapy Quality Assurance, London Regional Cancer Program

Sept 2015 - Dec 2015, Jan 2017 - Present

Weekly quality assurance testing was performed of clinical radiotherapy equipment (Varian iX and TrueBeam linear accelerators).

Teaching Assistant, Department of Medical Biophysics, University of Western Ontario

Sept 2015 - April 2017

4th year undergraduate thesis research course in my department involves teaching a subset of lectures, facilitating the labs, assessing research presentations, lab reports, and the final thesis.

Student Supervisor, London Regional Cancer Program

May 2015 - Aug 2016

Under my supervision and guidance, an undergraduate student was able to use machine learning to automatically differentiate between histological arterioles and venules.

Summer Research Assistant, London Regional Cancer Program and Robarts Research Institute

Jun 2012 - Sept 2012

Developed a registration and reconstruction of mouse cardiac tissue from histology sections through image analysis.

Research Assistant, Department of Biochemistry, University of Western Ontario

May 2010 - Apr 2012 (Undergraduate)

Performed laboratory procedures including DNA preparation, polymerize chain reaction, gel electrophoresis, or yeast/bacterial cloning. This position also involved lab maintenance such as autoclaving, solution and media preparation.

Summer Research Assistant, Robarts Research Institute

Jun 2011 - Sept 2011

Developed a protocol for the quantification of hypoxia levels in histology sections of stained

tissue through image analysis. Contributions to other projects involved genotyping, tissue harvest, immunostaining, microscopy, and image processing software.

Archaeological Interpreter, Museum of Ontario Archaeology

May 2009 - Sept 2009

Assisted in the excavation and interpretation of the 500 Lawson prehistoric Iroquoian archaeological site located beside the Museum of Archaeology. The artifacts recovered were catalogued into a database.

Refereed Contributions

Journal Articles:

1. Xu Y., Pickering J.G., Nong Z., Arpino J.M., Yin H., Ward A.D. (2015) A method for 3D histopathology reconstruction supporting mouse microvasculature analysis. PLOS ONE (DOI: 10.1371/journal.pone.0126817). Impact factor: 3.234.
2. Xu Y., Pickering J.G., Nong Z., Ward A.D. (2017) Segmentation of digitized histological sections for quantification of the muscularized vasculature in the mouse hind limb. Journal of Microscopy, Impact factor: 2.15.
3. Elkerton S.*, Xu Y.*, Pickering J.G., Ward A.D. (2017) Differentiation of Arterioles from Venules in Mouse Histology Images Using Machine Learning. Journal of Medical Imaging. *Shared first authorship.
4. Yin H., Frontini M., Arpino J.M., Nong Z., O'Neil C., Xu Y., Balint B., Ward A.D., Chakrabarti S., Ellis C.G., Gros R., Pickering J.G. (2015) Fibroblast Growth Factor 9 Imparts Hierarchy and Vasoreactivity to the Microcirculation of Renal Tumors and Suppresses Metastases. Journal of Biological Chemistry (DOI: 10.1074/jbc.M115.652222 jbc.M115.652222). Impact factor: 4.573

Patents:

1. Xu Y., Pickering J.G., Ward A.D., Automated segmentation of histological sections for vasculature quantification. U.S. Provisional Patent Application 13353330, filed Feb. 25, 2015.

Regular Presentations:

Medical Biophysics Seminar, Western University (Sept 2012 - current), annually

Medical Physics Journal Club, London Regional Cancer Centre (Sept 2013 - current), biannually

Conference Proceedings (some repeated in presentations):

1. Xu Y., Pickering J.G., Nong Z., Ward A.D. (2016) 3D Morphological Measurement of Whole Slide Histological Vasculature Reconstructions, Proceedings of SPIE Medical Imaging. Paper number: 9791-22; 4 pages. Podium, International
2. Elkerton J., Xu Y., Pickering J.G., Ward A.D. (2016) Differentiation of arterioles from venules in mouse histology images using machine learning, Proceedings of SPIE Medical Imaging. Paper number: 9791-15; 4 pages. Podium, International
3. Xu Y., Pickering J.G., Nong Z., Ward A.D. (2015) Segmentation of digitized histological sections for vasculature quantification in the mouse hind limb, Proceedings of SPIE Medical Imaging. Paper number: 9420-2; 4 pages. Podium, International
4. Xu, Y., Pickering, J.G., Gibson, E., Ward, A.D. (2014) 3D Reconstruction of Digitized Histological Sections for Vasculature Quantification in the Mouse Hind Limb. Proceedings of SPIE Medical Imaging. (Masters work) Paper number: 9041-15; 4 pages. Podium, International

Podium Presentations:

1. Xu Y., Pickering J.G., Goldman D., Nong Z., Elkerton J.S., Ward A.D. (2017) Automated vascular smooth muscle segmentation, reconstruction, classification and simulation on whole-slide histology Presented at Imaging Network Ontario on Mar 16, 2017, London ON
2. Xu Y., Pickering J.G., Goldman D., Nong Z., Ward A.D. (2016) Automated registration and segmentation: an application for vasculature analysis Presented at the London Regional Cancer Program Physics Retreat at on Nov 8, 2016, London, ON
3. Xu Y., Pickering J.G., Nong Z., Ward A.D. (2016) Automated 3D morphometry of the vasculature derived from digital histology Presented at Robarts Research Retreat on June 13, 2016, London, ON
4. Xu Y., Pickering J.G., Nong Z., Ward A.D. (2016) 3D Morphological Measurement of Whole Slide Histological Vasculature Reconstructions, Proceedings of SPIE Medical Imaging. Paper number: 9791-22; 4 pages. Podium, International Presented at SPIE Medical Imaging Mar 3, 2016, San Diego, CA
5. Xu Y., Pickering J.G., Nong Z., Ward A.D. (2015) Automated segmentation of whole-slide histology for vessel morphology comparison Presented at World Congress on Medical Physics and Biomedical Engineering on June 11, 2015, Toronto, ON
6. Xu Y., Pickering J.G., Nong Z., Ward A.D. (2015) Automated segmentation of whole-slide histology for vessel morphology comparison Presented at Imaging Network Ontario on Mar 30, 2015, Toronto ON

7. Xu Y., Pickering J.G., Nong Z., Ward A.D. (2015) Segmentation of digitized histological sections for vasculature quantification in the mouse hind limb, Proceedings of SPIE Medical Imaging. Paper number: 9420-2; 4 pages. Podium, International Presented at SPIE Medical Imaging Feb 25, 2015, Orlando, FL
8. Xu Y., Pickering J.G., Nong Z., Gibson E., Ward A.D. (2014) A method for evaluating normal and regenerated microvasculature using 3D histopathology Presented at Robarts Research Day on June 9, 2014, London, ON
9. Xu Y., Pickering J.G., Nong Z., Gibson E., Ward A.D. (2014) 3D Histology Reconstruction for Microvasculature Quantification in Preclinical Studies Presented at Imaging Network Ontario on Mar 24, 2014, London, ON
10. Xu, Y., Pickering, J.G., Gibson, E., Ward, A.D. (2014) 3D Reconstruction of Digitized Histological Sections for Vasculature Quantification in the Mouse Hind Limb. Proceedings of SPIE Medical Imaging. (Masters work) Paper number: 9041-15; 4 pages. Podium, International Presented at SPIE Medical Imaging Feb 17, 2014, San Diego, CA
11. Xu Y., Pickering J.G., Gibson E., Ward A.D. (2013) 3D Reconstruction of Digitized Histological Sections for Vasculature Quantification in the Mouse Heart Presented at London Health and Research Day Mar 19, 2013, London, ON

Poster presentations:

1. Xu Y., Pickering J.G., Goldman D., Nong Z., Elkerton J.S., Ward A.D. (2017) Automated vascular smooth muscle segmentation, reconstruction, classification and simulation on whole-slide histology, Presented at London Health and Research Day on Mar 28, 2017, London ON
2. Xu Y., Pickering J.G., Nong Z., Elkerton, J.S., Ward A.D. (2016) Automated vascular segmentation, reconstruction and classification on whole-slide histology, Presented at Pathology Visions on Oct 23 - 25, 2016, San Diego, CA
3. Xu Y., Pickering J.G., Nong Z., Ward A.D. (2016) Automated 3D morphometry of the vasculature derived from whole-slide digital histology, Presented at London Image Discovery Day on Jun 17, 2016, London, ON
4. Xu Y., Pickering J.G., Nong Z., Ward A.D. (2016) Automated 3D morphometry of the vasculature derived from whole-slide digital histology, Presented at Robarts Research Retreat on Jun 13, 2016, London, ON
5. Xu Y., Pickering J.G., Nong Z., Ward A.D. (2016) Automated 3D morphometry of the vasculature derived from whole-slide digital histology, Presented at Imaging Network Ontario on Mar 30 - 31, 2016, Toronto, ON
6. Xu Y., Pickering J.G., Nong Z., Ward A.D. (2016) Automated 3D morphometry of the vasculature derived from whole-slide digital histology, Presented at London Health and Research Day on Mar 29, 2016, London, ON

7. Xu Y., Pickering J.G., Nong Z., Ward A.D. (2015) Automated segmentation of whole-slide histology for vessel morphology comparison, Presented at London Health and Research Day on Apr 1, 2015, London, ON
8. Xu Y., Pickering J.G., Nong Z., Ward A.D. (2015) Automated segmentation of whole-slide histology for vessel morphology comparison, Presented at Imaging Network Ontario on Mar 30 - 31, 2015, Toronto, ON
9. Xu Y., Pickering J.G., Nong Z., Gibson E., Ward A.D. (2014) A method for evaluating normal and regenerated microvasculature using 3D histopathology, Presented at London Image Discovery Day on June 26, 2014, London, ON
10. Xu Y., Pickering J.G., Nong Z., Gibson E., Ward A.D. (2014) A method for evaluating normal and regenerated microvasculature using 3D histopathology, Presented at Oncology Research Day on June 20, 2014, London, ON
11. Xu Y., Pickering J.G., Nong Z., Gibson E., Ward A.D. (2014) A method for evaluating normal and regenerated microvasculature using 3D histopathology, Presented at Robarts Research Day on June 9, 2014, London, ON
12. Xu Y., Pickering J.G., Nong Z., Gibson E., Ward A.D. (2014) 3D Histology Reconstruction for Microvasculature Quantification in Preclinical Studies, Presented at Imaging Network Ontario on Mar 24 - 25, 2014, London, ON
13. Xu Y., Pickering J.G., Nong Z., Gibson E., Ward A.D. (2014) A method for evaluating normal and regenerated microvasculature using 3D histopathology, Presented at London Health and Research Day on Mar 18, 2014, London, ON
14. Xu, Y., Pickering, J.G., Gibson, E., Ward, A.D. (2013) 3D Reconstruction of Digitized Histological Sections for the Mouse Hind-Limb Vasculature, Presented at Canadian Cancer Research Conference, Nov 3 - 6, 2013, Toronto, ON
15. Xu Y., Pickering J.G., Gibson E., Ward A.D. (2013) 3D Reconstruction of Histology Sections for Tumour Vasculature Classification, Presented at Oncology Research and Education Day on Jun 17, 2013, London, ON
16. Xu Y., Pickering J.G., Gibson E., Ward A.D. (2013) 3D Reconstruction of Digitized Histological Sections for Vasculature Quantification in the Mouse Heart, Presented at London Image Discovery on Jun 13, 2013, London, ON
17. Xu Y., Pickering J.G., Gibson E., Ward A.D. (2013) 3D Reconstruction of Digitized Histological Sections for Vasculature Quantification in the Mouse Heart, Presented at Imaging Network Ontario on Feb 4 - 5, 2013, Toronto, ON

Co-authored abstracts (*Presenter):

1. Elkerton J. *, Xu Y., Pickering J.G., Ward A.D. (2016) Differentiation of arterioles from venules in mouse histology images using machine learning, Poster Presentation, Presented at London Image Discovery Day on Jun 17, 2016, London, ON

2. Elkerton J. *, Xu Y., Pickering J.G., Ward A.D. (2016) Differentiation of arterioles from venules in mouse histology images using machine learning, Podium Presentation, Presented at Imaging Network Ontario on Mar 31, 2016, Toronto, ON
3. Elkerton J. *, Xu Y., Pickering J.G., Ward A.D. (2016) Differentiation of arterioles from venules in mouse histology images using machine learning, Poster Presentation, Presented at London Health and Research Day on Mar 29, 2016, London, ON
4. Elkerton J. *, Xu Y., Pickering J.G., Ward A.D. (2016) Differentiation of arterioles from venules in mouse histology images using machine learning, Proceedings of SPIE Medical Imaging. Paper number: 9791-15; 4 pages. Podium, International, Presented at SPIE Medical Imaging Mar 3, 2016, San Diego, CA
5. Yin H., Frontini M., Arpino J.M*., Nong Z., O'Neil C., Xu Y., Balint B., Ward A.D., Chakrabarti S., Ellis C.G., Gros R., Pickering J.G. (2015) Generation of Vasoreactive and Hierarchical Tumor Vessels by Fibroblast Growth Factor 9: Implications for Tumor Passivation. Presented at Arteriosclerosis, Thrombosis, and Vascular Biology on May 7 - 9, 2015
6. Watson, A.* , Nong, Z., Xu, Y., Pickering, J. G. (2011) Expression of an NAD+ regenerating enzyme in the developing vasculature. Presented at the American Society for Cell Biology on Dec 3 - 7, 2011
7. Watson, A.* , Nong, Z., Xu, Y., Pickering, J. G. (2011) Expression of an NAD+ regenerating enzyme in the developing vasculature. Presented at the National Canadian Hypertension Congress on Oct 2-5, 2011

Other Contributions

Committee roles:

1. Director, Strong Bones Strong Minds Strong Muscles (Schulich School of Medicine and Dentistry) Sept 2014 - current
Under my guidance, we initiated presentations at the Children's Hospital, and local elementary schools. The role involves volunteer recruitment, internal funding applications, budget tracking, meeting organization, sub-committee task delegation (science presentations at elementary schools, retirement homes, and Children's Hospital), and fundraising event coordination.
2. Executive Committee Member, Robarts Association of Trainees (Robarts Research Institute) Nov 2016 - current
Organize academic and social events for the students within Robarts Research Institute.
3. Imaging Student Representative, Robarts Strategic Planning Committee (Robarts Research Institute) March 2016 - Oct 2016

- Attend meetings, survey the students regarding their concerns and needs, organize discussion and information sessions for students at Robarts. Create the initial Robarts trainee constitution.
4. Student Department Representative, Graduate Students Council (Graduate Studies and Postdoctoral Affairs at Schulich School of Medicine and Dentistry) Apr 2015 - current
Attend committee meetings, coordinate and notify students of various social events, networking opportunities, scholarship applications and interdepartmental events.
 5. Graduate Student Representative, Space Assessment Committee (Schulich School of Medicine and Dentistry) Oct 2015 - current
Represent the graduate student population with regards to facility and amenity needs in the department of Schulich Medicine & Dentistry during monthly meetings.
 6. Medical Biophysics Steward, Public Service Alliance of Canada Local 610 Teaching Assistant Union (Western University) Oct 2015 - current
Attend meetings, keep members up to date with regards to their benefits, and organize department wide social events for teaching assistants.
 7. Co-Chair, Children's Hospital Subcommittee (Schulich School of Medicine and Dentistry) Sept 2012 - Oct 2015
Liaise with Children's Health Foundation, Children's Hospital, and Child Life for Schulich graduate students to present in the inpatient wing, organize activities/presentations, and schedule volunteers.

Outreach Activities:

8. Presenter, Children's Hospital Subcommittee (Schulich School of Medicine and Dentistry) Oct 2015 - current
Present activities to patients in the inpatient wing of the Children's hospital.
9. Student Representative, Schulich information fair (University of Western Ontario) Spring/Fall 2010 - 2012
Outreach educates prospective students on the implications of biophysics, the idea of combining two fields of study, and our departmental developments.
10. Presenter, Good intentions violence prevention (Regional) Winter 2010 & Winter 2011
Presenters educate high school students on the dangers of violent relationships, various methods of intervention and prevention through examples and group activities.
11. Presenter, Biology undergraduate society (University of Western Ontario) Sept 2008 - May 2010
Give presentations and workshops to students in elementary and secondary schools in order to enrich their knowledge in living organisms.

Academic Roles:

12. Session chair, IUPESM World Congress on Medical Physics and Biomedical Engineering, Toronto, June 2015
13. Student consultant, Consult the Experts Session for External Scholarship Applicants, University of Western Ontario, Winter 2014 Advised students on the proposals and applications for external scholarships.
14. Tutor (Regional) Sept. 2007 - 2014 Provide voluntary guidance to elementary, high school and first year undergraduate students. Involvement was generally in the topics of math, physics and chemistry in small groups or individually.
15. Peer mentoring (Regional) 2008 - 2011 Mentors aid in the transition of students from elementary school to high school, was well as prior to post-secondary education. We provided organizational skills, and methods of self-motivation.

Other volunteer positions:

16. See the Line: Concussion Research and Awareness (University of Western Ontario) Aug 10, 2016 Guided individuals throughout the event and aided in the setup and take down procedures.
17. The Thames Valley Science & Engineering Fair (Youth Science Ontario) April 2, 2016 Judge student science projects, grades 6 to 12.
18. Science Olympics (Youth Science Ontario) May 21, 2015 Assist students in the participation of events.
19. Biochemistry Volunteers (Regional) Aug 2012 - Jan 2013 Tuesdays and Saturdays, we prepare and provide a hearty meal to the public in the evening at Rowntree United Church and St. John the Evangelist Anglican Church.
20. Volunteer, Museum of Ontario Archaeology (Doors Open London, Kids Expo, Seasonal Pow Wow) May 2010 - Sept 2012 Educate and present activities to visitors of the museum, and museum booths
21. Studio Assistant (University of Western Ontario) Sept 2009 - May 2010 Assistants aid in the setup of visual or sculptural displays for artists and preparation of materials.

Awards

Sept 2014 - Aug 2017	Natural Sciences and Engineering Research Council of Canada (NSERC) Alexander Graham Bell Canada Graduate Scholarship (CGS) - Doctoral - value \$105,000	National Re- search/Academic
Sept 2012 - Aug 2017	Western Graduate Research Scholarship - value \$2,600/term	Institutional Academic
Oct 16	Pathology Visions - 1st place poster award - value \$250	International Research
Sept 16	Doctoral Excellence Research Awards, University of Western Ontario - value \$10,000	Institutional Research
Oct 15	First Innovation Discloser Award (Vanguard Awards, WORLDdiscoveries)	Regional Re- search
Sept 2014 - Aug 2015	CHIR Strategic Training Fellows (Masters) - value \$24,000	Institutional Re- search/Academic
Jun 15	Norma E. Nixon Marie Ramo Nixon Award, University of Western Ontario - value \$1500	Institutional Re- search/Academic
Apr 15	Western Libraries Open Access Fund, University of Western Ontario - value \$1350	Institutional Research
Feb 15	Robert F. Wagner Best Student Paper Conference Finalists (SPIE Medical Imaging)	International Research
Nov 14	Allen C. Groom Prize Nomination	Institutional Research
Mar 14	Imaging Network Ontario (ImNO) Symposium - 1st place poster award - value \$300	Provincial Re- search
Feb 14	SPIE Medical Imaging Student Grant - value \$200	International Research
Sept 2012 - Aug 2013	Natural Sciences and Engineering Research Council of Canada (NSERC) Alexander Graham Bell Canada Graduate Scholarship (CGS) - Masters - value \$17,500	National Re- search/Academic
Sept 2009 - Apr 2010	Laurene Paterson Estate Scholarship, University of Western Ontario - value \$2,000	Institutional Academic
Sept 2008 - Apr 2009	Scholarship of Excellence, University of Western Ontario - value \$2,000	Institutional Academic
Sept 2008	UWO Science MET, University of Western Ontario - value \$100	Institutional Academic
Sept 2008 - Apr 2012	Dean's Honour List, University of Western Ontario	Institutional Academic
Sept 2008 - Apr 2012	Western Scholars, University of Western Ontario	Institutional Academic